Computational Chemistry Driven Understanding for Group-13 Catalysts in CO_2 Utilisation

Ryan David Lewis

A thesis submitted in partial fulfilment of the requirements of Sheffield Hallam University for the degree of Doctor of Philosophy

May 2025

Candidate Declaration

I hereby declare that:

1. I have not been enrolled for another award of the University, or other academic or professional organisation, whilst undertaking my research degree.
2. None of the material contained in the thesis has been used in any other submission for an academic award.
3. I certify that this thesis is my own work. The use of all published or other sources of material consulted have been properly and fully acknowledged.
4. The work undertaken towards the thesis has been conducted in accordance with the SHU Principles of Integrity in Research and the SHU Research Ethics Policy, and ethics approval has been granted for all research studies in the thesis.
5. The word count of the thesis is 50,647.

Name	Ryan David Lewis
Award	PhD
Date of Submission	30/05/2025
Research Institute	Industry and Innovation
Director of Studies	Dr Thomas Bassindale

Acknowledgements

Dr Alex Hamilton has been a fundamental part of my journey in chemistry. From my academic tutor in university, to my DOS in my PhD. I cannot thank him enough for his never-ending support throughout my time at Sheffield Hallam University and helping me push this thesis over the line. I will be forever grateful for the time he has given me over the years.

I expand this gratitude to Dr Susan Cambell and Dr Thomas Bassindale who both were extremely supportive in helping me get my thesis over the line at a very difficult time in my life.

Thank you to office 722 for making the workplace so enjoyable for the duration of my PhD.

Finally, my biggest thank you goes out to my family. My wife Olivia, and kids Esme and Chessley have been especially important in supporting me in one has been one of the most difficult challenges of my life. I further extend this to thank you to everyone who has helped with childcare to make it possible to complete my PhD.

Abstract

Rising levels of CO_2 is a global challenge as a dominant contributor to rising temperatures. CO_2 utilisation can reduce atmospheric CO_2 levels by converting it into useful products. Of industrial importance, is the cycloaddition of CO_2 and epoxides to form cyclic carbonates, which are used as lubricants, in synthesis and as fuel additives. The stability of CO_2 means the reaction is economically unviable at an industrial scale, therefore, a catalyst needs to be employed.

Lewis acid catalysts are excellent for cyclic carbonate synthesis. Among group 13, aluminium is a popular choice, as it has previously shown high activity for CO_2 and epoxide cycloadditions. This activity has always been attributed to aluminium's stronger Lewis acidity, resulting in better CO_2 activation. As a result, little attention is given to heavier group 13 metal catalysts. This work gives a thorough understanding of the mechanistic action of aluminium, gallium and indium catalysts utilising density functional theory (DFT), quantum theory of atoms in molecules (QTAIM). A review of density functional theory (DFT) methods was conducted in Chapter 2, along with a theoretical introduction to all the methods used.

Bimetallic aluminium salphen is an excellent catalyst for this the conversion of CO_2 and epoxides to cyclic carbonates, whilst the monometallic aluminium salphen was reported as inactive due to the formation of an insoluble precipitate. However, experimentally the Whiteoak group showed In[salphen(Br)] to be highly active. A mechanistic study was conducted to understand why the indium catalyst was active over the aluminium. Furthermore, a ligand abstraction step was needed for the CO_2 insertion to occur and associated with the poor activity of the [Al(salphen)Cl] catalyst.

A mechanistic study on the cycloaddition of 1,2-diphenylaziridine and 1-isopropyl-2-phenyl aziridine with CO_2 catalysed by Ga aminotrisphenolate was undertaken. A temperature selective formation of an oxazolidinone or piperazine product was explored using DFT. Mechanisms were elucidated, and the selectivity attributed to the difference in entropic contributions of the reactants. Importantly, a ligand dissociative ring opening step was seen for the first time between an aminotrisphenolate catalyst and aziridine substrate.

Finally, a comparative study on how the electronic and steric properties affect catalyst activity was undertaken on 12 ML_3 catalysts [M = Al, Ga and In; L = Cl, Br, I, Me*, ^{t}Bu*, Ph* (*Only used with Ga)]. Electronic and steric catalyst properties were elucidated and analysed through quantitative structure-activity relationship models. Results were analysed to see which descriptors could predict a highly active tris-ligated Lewis acidic catalyst.

Table of Contents

List of Figures

List of Tables

List of Schemes

List of Abbreviations

AFIL – Anionic Framework Ionic Liquid

BCP – Bond Critical Point

CPCM – Conductor-like Polarizable Continuum Model

DFT – Density Functional Theory

ΔG – Gibbs Free Energy Change

FIA – Fluoride Ion Affinity

FLA – Fluorescent Lewis Adduct

GEI – Global Electrophilicity Index

HOMO – Highest Occupied Molecular Orbital

LUMO – Lowest Unoccupied Molecular Orbital

MEK – Methyl Ethyl Ketone

ML – Machine Learning

MOF – Metal Organic Framework

MX_3 – Metal Trihalide Catalyst (where M = Al, Ga, In; X = Cl, Br, I)

NCI – Non-Covalent Interaction

NMR – Nuclear Magnetic Resonance

PPNCl – Bis(triphenylphosphine)iminium chloride

QTAIM – Quantum Theory of Atoms in Molecules

QSAR – Quantitative Structure-Activity Relationship

RDG – Reduced Density Gradient

RFE – Recursive Feature Elimination

SCF – Self Consistent Field

TBAI – Tetra-n-butylammonium Iodide

TDI – Turnover frequency Determining Intermediate

TDTS – Turnover Frequency Determining Transition State

TMS – Trimethylsilanefluoride

TS – Transition State

ZPE – Zero Point Energy

Chapter 1 – Introduction

1.1 Introduction to CO_2

Carbon dioxide (CO_2) is one of the leading contributor chemicals to global warming and atmospheric levels continue to rise (Figure 1.1).[1] The high atmospheric level of CO_2 means it is one of the most abundant, renewable carbon resources currently available. This makes it an attractive prospect to utilise and synthesise valuable organic molecules and synthetic building blocks. CO_2 utilisation, as defined by the Intergovernmental Pact on Climate Change (IPCC), is the use of CO2 directly or as a feedstock chemical to produce useful carbon

containing compounds.[2] Utilisation forms a part of a larger research area; carbon capture, utilisation and storage (CCUS), which are discussed in greater depths below.

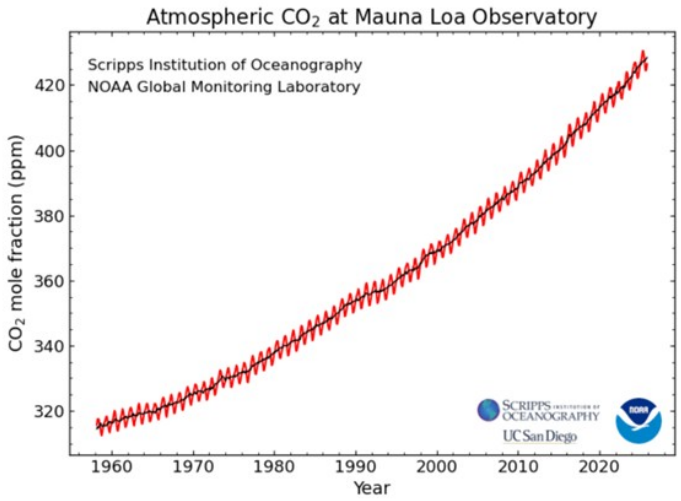

Figure – Introduction.1 - Readings of atmospheric CO_2 levels taken from the Mauna Loa Observatory.[1]

CO_2 (Figure 1.2) is a symmetrical, linear molecule with a sp hybridized carbon bonded to two oxygen molecules. The more electronegative oxygens pull electron density towards themselves creating a dipole. However, due to the symmetry of the molecule there is no net dipole across the molecule, hence the inertness of CO_2.

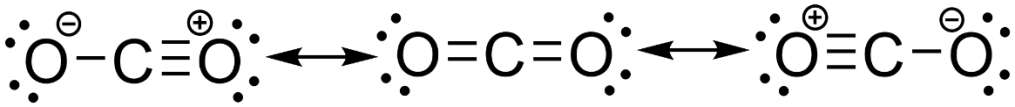

Figure – Introduction.2 - Structure of CO_2 showing the lone pairs and partial charges of the molecule.

CO_2 is a kinetically and thermodynamically stable molecule, generally requiring harsh reaction conditions to undergo reaction. Using the molecular orbital diagram (Figure 1.3), a better understanding of the stability of CO_2 can be obtained. The diagram reveals a large HOMO-LUMO gap, where the HOMO is the 1 p_g orbital and the LUMO the 2 p_u orbital. This makes the nucleophilic properties of CO_2 poor, and its electrophilic nature would require a strong nucleophile or harsh conditions to be activated via donation into the LUMO. Activation by a catalyst can reduce the HOMO-LUMO gap, allowing for the LUMO to be populated, leading to the loss of linearity and allowing a CO_2 reaction to occur. This orbital-based description provides a useful framework for

understanding the subsequent discussion of CO_2 activation and binding modes in catalytic systems.

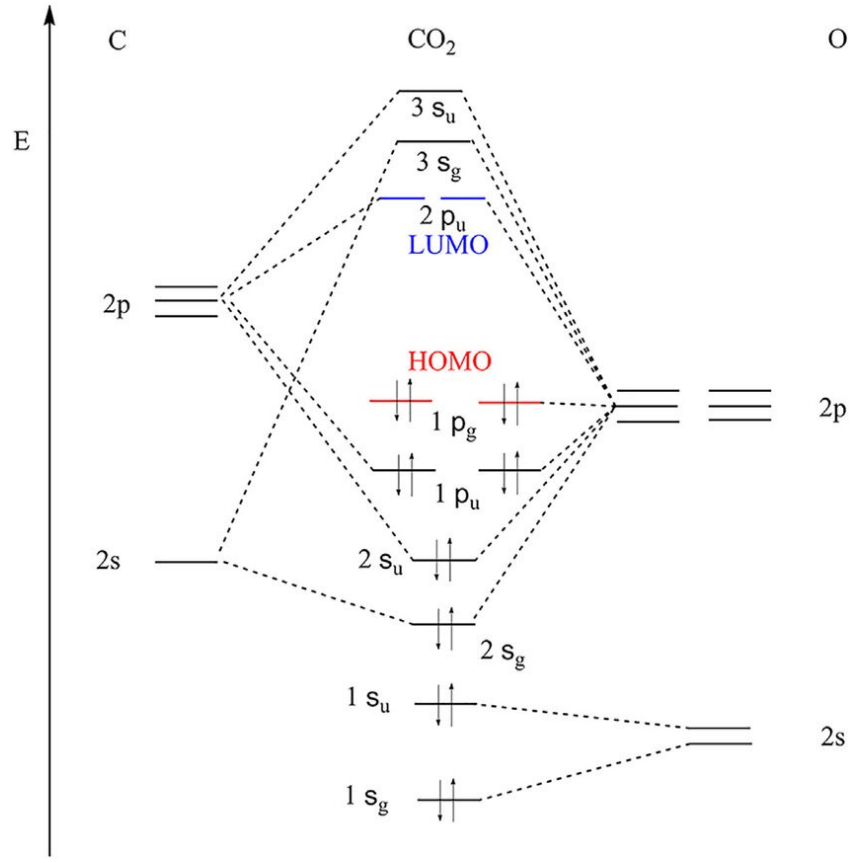

Figure – Introduction.3 - Molecular orbital diagram for CO_2 provided under the referenced licence.[3]

1.1.1 Carbon Capture, Utilisation and Storage

Figure 1.4 shows the net global growth of CO_2 in the atmosphere between the years 2008-2017.[4] Different methods of CCUS and the rate at which this CO_2 dissipates back into the atmosphere are presented. The average net atmospheric change in CO_2 saw a growth of +17 Gt of CO_2 into the atmosphere.

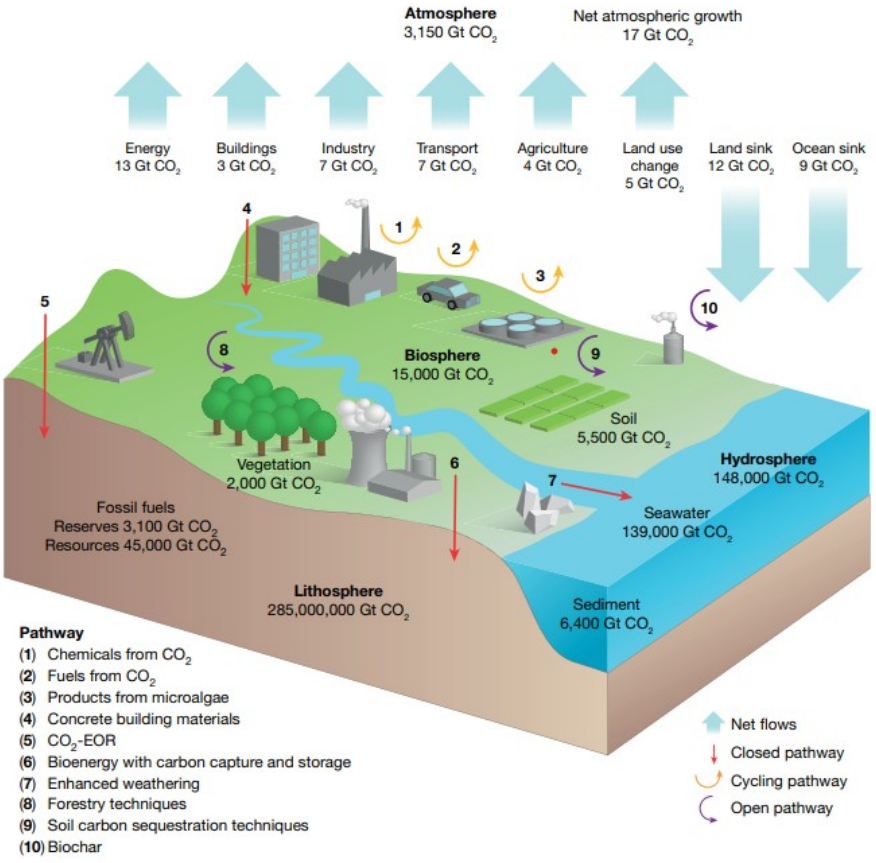

Figure – Introduction.4 - Showing the net atmospheric growth of CO_2 averaged over the years 2008-2017. The numbered arrows represent the methods used of CCUS techniques and the arrows are representative of the type of storage pathway. The large blue arrows are showing the net contribution/reduction of CO_2 in the atmosphere for each sector.[4] Units given in gigatonnes (Gt). From 3.

With such a rise in atmospheric CO_2 levels, it is unsurprising that CCUS is a priority in UK government policy. In the UK, there is an aim to make CCUS an affordable and widely used process by 2030,[5] with many other countries aspiring to be net zero by 2050.[6,7] To achieve these goals, several strategies need to be adopted in each area of CCUS.

1.1.1.1 CO_2 Capture

Whether from an industrial process or directly from the atmosphere, for CO_2 to be stored or utilised, it first needs to be captured and separated from air or the products of combustion. There are three common groups of capture methodologies, pre-combustion, post-combustion and oxy-fuelling.[8] Pre-combustion technologies aim to remove CO_2 that is synthesised as an undesired by-product of combustion. Steam reformation processes are an example of where these technologies are implemented. Current industrial applications include using solvents, polymers and porous organic membranes for CO_2

capture.[9–11] One issue with these capture technologies is that there is an energy penalty related to the desorption of the CO_2 after capture.

Post-combustion processes capture CO_2 after a carbon source has combusted. This type of capture is common in power plants and steelworks. Like pre-combustion capture, solvents, polymers and membranes can also be used in post-combustion capture.[12–14] To assist with post-combustion capture, vacuum/pressure swing absorption can be employed. These work by decreasing/increasing the pressure respectively to aid with the adsorption of CO_2. Upon returning to the normalised pressure, the CO_2 desorbs.[15] Cryogenic absorption can also be employed, which uses the different boiling points of mixtures of gases to separate them. The temperature is dropped to extreme levels and as different gasses condense, they are collected.[16]

Oxy-fuelling aids the capture of CO_2 by burning the fossil fuels in power plants and cement factories with pure oxygen. This produces CO_2 in much higher concentration than if it was burned in just air. Furthermore, it reduces the amounts of nitrous oxides produced allowing for more efficient capture of CO_2.[17] The downside to these processes are they are expensive due to using pure oxygen.

1.1.1.2 CO_2 Transport & Storage

The transport and storage of CO_2 is a highly important link in the CCUS chain. CCUS processes would not be viable if the CO_2 could not be moved/stored after capture and before utilisation. After the capture, CO_2 can be transported via ship, pipeline or truck. These processes can be expensive and lead to a dramatic decrease in the net CO_2 offset from environmental release due to the burning of fossil fuels for transport/infrastructure development. Furthermore, as CCUS processes are a relatively new concept at the industrial level, there is little to no global regulation on CO_2 transportation. This means a lack of consistency across different sectors.[18] Instead, each transportation project is given its own consideration of safety, increasing the cost and hindering progression towards a fully functional CO_2 transportation infrastructure. Regardless, methods are continually developing to work towards this. There are a range of different CO_2 storage methods that are available. A few of them are summarised in Table 1.1.

Table – Introduction.1 - An overview of several different CO_2 storage methods and the pros/cons of each.[19]

Method	Description	Pros	Cons
Saline Aquifers[20]	Deep reservoirs of high salt-content water which the CO_2 is injected and dissolved into for prolonged storage.	Large storage potential, commercially ready, aquifers are well distributed	No economic benefit
Depleted Oil/Gas Reserves[21]	These are underground pores which are empty because of the extraction of oil and gas. They can be repurposed to store CO_2.	Equipment present from oil/gas extraction, conditions suit high pressure gas storage, potential to extract further oil/gas	Technology not at a suitable standard
Coal Beds[22]	These are sheets of coal located in the earth's crust. CO_2 can be injected between the sheets and absorbed into the coal. This displaces and releases methane to the surface.	Close to power plants so less transportation costs, recover methane	Technology not at a suitable standard
Deep Ocean[23]	Under pressure, CO_2 becomes denser than water. Therefore, injecting it deep into the ocean (>2700 m) leaves it trapped in the ocean.	Large storage capacity	Technology not at a suitable standard, no economic benefit, danger to sea life
Deep-sea Sediments[24]	Uses the same concept as the deep ocean but injects below the sediments on the ocean floor.	Large storage capacity, sea life is unaffected	Technology at a suitable standard, no economic benefit, highly expensive

CO_2 storage methods are a viable method to offset CO_2 from entering the atmosphere. However, with technology holding some methods back and very little economic return, the suitability of these methods at present is questionable. As research develops, it is hopeful that storage methods will become more prominent to assist with net carbon neutrality to and from the atmosphere.

1.1.1.3 CO_2 Utilisation

CO_2 utilisation offers an alternative and additional technique to CO_2 storage. It opens the door to synthesising valuable carbon containing products from a renewable C_1 source without the need for fossil fuels. By utilising waste CO_2 to form commodity chemicals, several of Anastas and Eghbali's Green Chemistry criteria are met.[25] These include:

- Using renewable feedstocks.
- Using catalysts for the reactions.
- Using safe reactants which are unlikely to cause damage at a great extent (i.e. explosions, fires and poisoning to local wildlife and water supplies).

Figure 1.5 gives an overview of some of the products that can be synthesised from CO_2 and an overview is provided of the synthesis of a number of these products.[26]

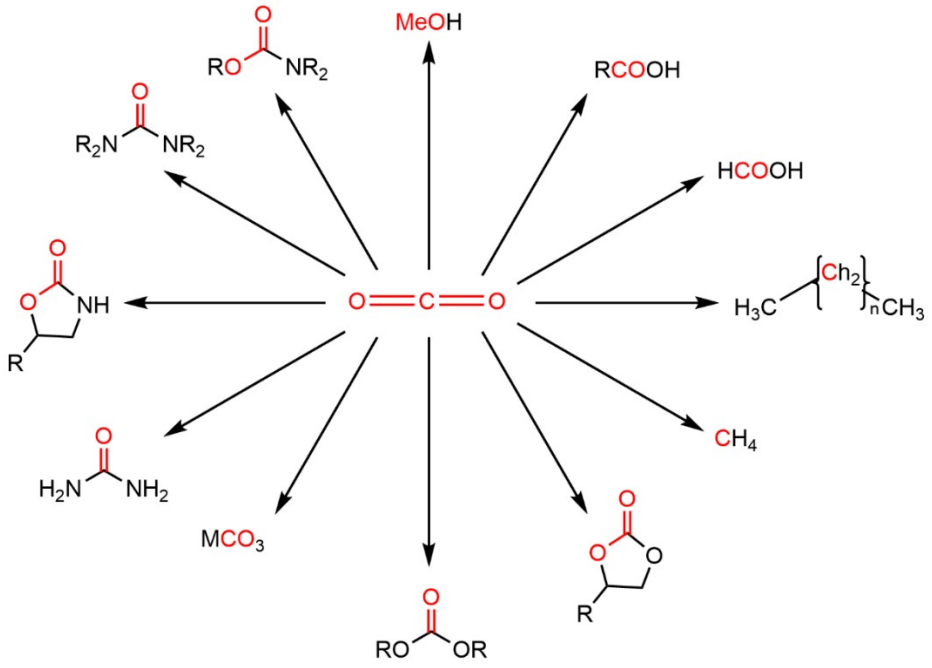

Figure – Introduction.5 - The variety of carbon containing products which can be synthesised utilising CO_2 adapted from Faisal.[26] The components of CO_2 have been highlighted in red.

The products and their uses are summarised below:

Carboxylic Acids (RCOOH)

Carboxylic acids play an extremely important role in chemical synthesis. Of particular interest are phenyl carboxylic acids due to their importance in the pharmaceutical industry.[27] In 1860, Kolbe created an industrially relevant CO_2

utilisation pathway to form phenyl carboxylic acids.[28] This work paved the way to a number of further carboxylic acid synthesis routes including the Kolbe-Schmitt reaction.[29] Finding green synthesis routes is paramount to sustainably meeting demand. More recently, a variety of catalysts including ionic liquids, Lewis acidic catalysts, metal organic frameworks (MOFs) and more have been employed in attempt to synthesise phenyl based carboxylic acids using CO_2, with reduced temperatures, pressures, reaction times and energy costs.[30]

One example of this is the carboxylation of phenol to salicylic acid using an $AlBr_3$ catalyst. This reaction focuses on a one pot direct approach to salicylic acid synthesis in comparison to the high temperature, two-step nature of the original Kolbe-Schmitt procedure.[31] Taking inspiration from the Friedel-Crafts reaction, the Lewis acidic $AlBr_3$ was used to carboxylate phenol with CO_2.[31,32] The proposed mechanism for this reaction is in Figure 1.6.

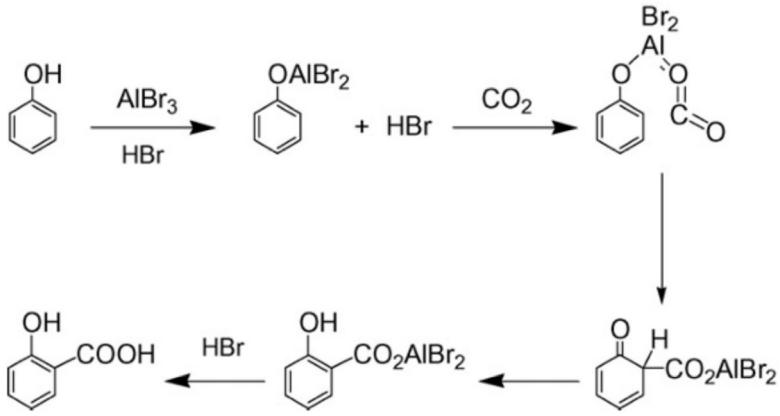

Figure – Introduction.6 - Proposed mechanism for the carboxylation of phenol using CO_2 to form salicylic acid employing an $AlBr_3$ catalyst from 31.[31,32]

Hydrocarbons – Methane (RCH_3)

Methane (CH_4) is a valuable fossil fuel gas both as a fuel and for its potential to synthesise heavier, more useful hydrocarbons. However, CH_4 is second to CO_2 as a damaging and prominent greenhouse gas.[33] This makes it another sought after target for fixation into more useful carbon containing products rather than being released into the atmosphere, with some examples in Figure 1.7.

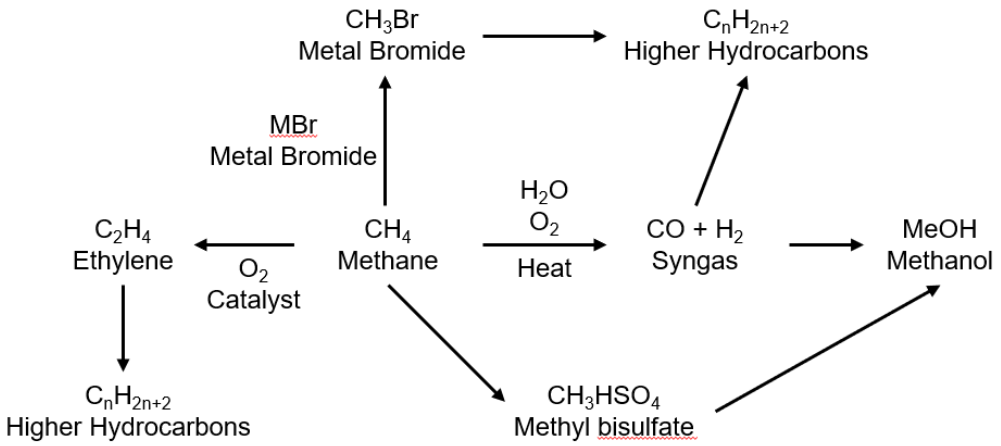

Figure – Introduction.7 - Further synthesis routes of methane for fixation into more useful carbon containing products. Adapted from 34.[34]

CH_4 has been traditionally synthesised from CO_2 via the Sabatier reaction.[35] CO_2 is reacted with H_2 to from CH_4 and H_2O. This reaction required high temperatures (300-400 ^oC) even with the presence of a catalyst, such as a Ni based catalyst supported on Al_2O_3. Despite utilising CO_2 to create a value-added carbon product, the energy penalty minimises the positive effect of utilisation and reduces the net CO_2 used from little to none. To overcome this, a variety of homogeneous and heterogeneous catalysts have been explored for this synthesis.

In 2021, the first homogeneous rhenium catalyst was shown to reduce CO_2 to CH_4 electrochemically at room temperature.[36] The dependence on electricity for this reaction would mean an off-site production of CO_2. However, the fact that the reaction can be conducted at an ambient temperature would be a positive factor for consideration at an industrial scale.

Heterogeneous Ni/Co-MnO nanoparticles have also been shown to be effective for the conversion of CO_2 to CH_4.[37,38] With a conversion rate of >95 % at 150-160 ^oC, these processes offer a huge improvement in comparison to the conditions of the traditional Sabatier reaction.

Large scale industrial production of methane currently exists in the USA and Poland.[39,40] In the USA, heterogeneous based ruthenium catalysts are employed to synthesise CH_4 with the assistance of post-combustion capture solvent (2-EEMPA).[40] 90 % of CO_2 is successfully converted into CH_4. The synergistic capture and utilisation system employed was able to reduce the natural gas price

by 12 %, because of its efficiency.[41] In Poland, a slightly different approach is taken. Hydrogen from water electrolysis was used with CO_2 from flue gas to create a syngas mixture.[39] Despite a 98 % CO_2 conversion, temperatures of 280-350 ^oC, pressures of 1.5-3 bar and electricity to create hydrogen means the process is very energy intensive.

Methanol CH_3OH

Methanol (CH_3OH), is an important chemical commodity as a feedstock for synthesis, as a fuel and as a solvent.[34] CH_3OH can be synthesised from both CH_4 (Figure 1.7) and CO_2. Focussing on synthesis from CO_2, CH_3OH is traditionally synthesised from syngas (a mix of H_2, CO, CO_2 and CH_4) and water reformation.[42] Research has continued to find ways to make CH_3OH synthesis as green as possible through the introduction of homogeneous/heterogeneous catalysts.[34]

Heterogeneous copper nanoparticle-based catalysts have shown promise with high activity and conversion rates. A TiO_2 supported Cu nanoparticle catalyst was able to convert 96 % CO_2 into methanol at 200 ^oC and 30 bar of pressure.[43] In homogeneous catalysts, iron scorpionates and cobalt based catalysts have successfully been employed to synthesise methanol from CO_2 at temperatures as low as 80-90 ^oC. These two catalysts open up a greener synthesis route to methanol, however, as both are air sensitive, using them on an industrial scale is currently not within reach.[44,45]

Commercially, green CH_3OH is currently available in Iceland and China.[34,46,47] CO_2 is captured as a waste product from flue gas and H_2 is generated using water electrolysis using green electricity. Not only are these processes green, but they also generate a greater amount of CH_3OH in comparison to competing processes which utilise natural gas.[34]

Urea H_2NCONH_2

Urea is of great agricultural importance as a prominent fertiliser. The first industrial synthesis of Urea was completed in 1922 by Bosch and Meiser.[48] This process involves the synthesis of carbamate (Eq. 1.1) followed by the decomposition into urea and water (Eq 1.2).

$$2\ NH_3 + CO_2 \rightleftharpoons NH_4CO_2NH_2 \qquad \text{Eq. 1.1}$$

$$NH_4CO_2NH_2 \rightleftharpoons CO(NH_2)_2 + H_2O \qquad \text{Eq. 1.2}$$

The Bosch-Meiser process, although seminal, was at temperatures more than 150 ^{o}C and pressures of 150 bar. Therefore, for the green synthesis of urea, new technologies need to be developed. A recent review on photo/electrochemical synthesis of urea from CO_2 highlighted this point.[49] Yuan *et al*. demonstrate several catalysts capable of synthesising green urea through photo/electrochemical processes including TiO_2, a variety of nanoparticles and binary catalysts. However, a lack of mechanistic understanding and limited research in this area leaves this synthesis very much in its infancy.

Poly/Cyclic Carbonates RC_3O_3

Cyclic and polycarbonates are a sought-after product due to their various applications. Polycarbonates are prominently used in the materials industry. Cyclic carbonates have a variety of uses, one of which is in lithium-ion battery technology, an important field with the increasing onset of electric vehicles (Figure 1.8).[50]

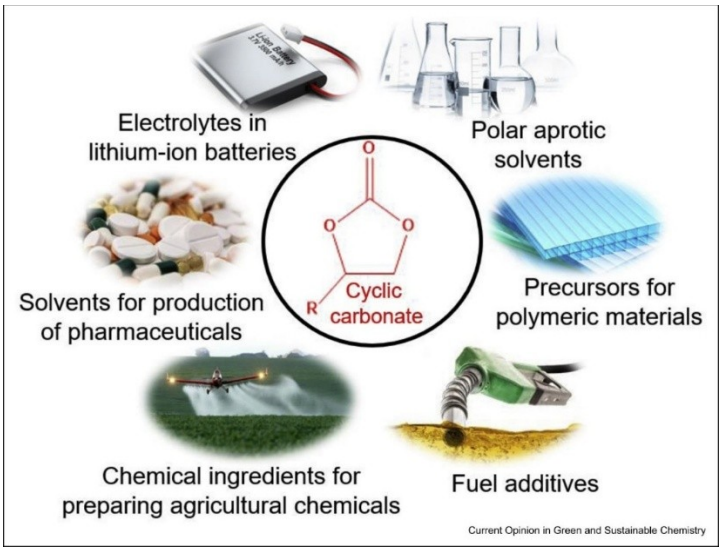

Figure – Introduction.8 - The variety of uses for cyclic carbonates from 50.[50]

Unlike the utilisation products, poly/cyclic carbonates have not been made on an industrial scale with CO_2 as a reagent until much more recently.[51] Again, the high temperatures and pressures required for this reaction meant the process was commercially non-viable. Consequently, the search for new catalysts for this

reaction is a big topic in research with some of the catalysts discussed in section 1.2.

1.1.2 Overcoming CO_2 Inertness

Section 1.1.1 has highlighted the importance of all three research areas of CCUS and how a synergistic approach is needed to progress towards carbon neutrality. It is hard to ignore the overwhelming benefits of CO_2 utilisation. Turning a waste, renewable greenhouse gas into value added carbon containing products without the use of fossil fuels almost seems too good to be true. Despite many green CO_2 utilisation industrial processes already existing, current technologies are not suitable across all desired products and where they are currently being used, more work can be done to swing the net output of CO_2 into the atmosphere to negative. To achieve this goal, the stability of the CO_2 needs to be overcome.

Proposed utilisation processes therefore face economic, environmental, and practical strain leading to many of them never coming to fruition. An example of this was the Joule Unlimited project which aimed to make fuel from sunlight, CO_2 as waste from an industrial process and water mixed with cyanobacteria. The process had a strong theoretical background and was able to raise significant amounts of money and even attract the attention of Audi. However, due to technical failures and economic pressures, the project ceased in 2017.[52]

To overcome the stability, the reaction conditions can be altered. Heating the reaction can lead to an increase in activity but requires a fuel to generate the heat. This releases CO_2 reducing the green benefits of the reaction. Furthermore, fuels are expensive, creating economic pressure on the process being viable. Increasing pressures also leads to greater reactivity in CO_2 utilisation reactions, however the reaction would then require stronger reaction vessels to withstand the conditions; thus, increasing the cost of the process. Increasing both temperature and pressure also increases the risk of the process, heightening the health and safety precautions.

To avoid extreme reaction conditions, a catalyst can be employed to maintain as close to ambient conditions as possible. The CO_2 binds/interacts with the catalyst thereby weakening the strong C=O bonds, by reducing the HOMO-LUMO gap and creating a dipole making CO_2 more susceptible as an electrophile or become

a stronger nucleophile (Figure 1.3).[53] Four common binding modes of CO_2 are displayed in Figure 1.9.

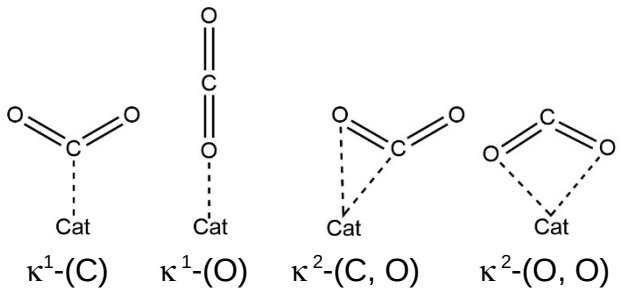

Figure – Introduction.9 - Bonding modes available between catalysts and CO_2.

The κ^1-(C) binding mode shows the catalyst bonding directly to the electrophilic carbon atom. By donating into the LUMO, the CO_2 bends creating a dipole and increasing the reactivity. κ^1-(O) shows CO_2 coordinating to the catalyst through the lone pairs of one of the oxygen atoms. This pulls electron density towards the oxygen atom, creating a dipole for further reaction. The κ^1-(O) mode is commonly seen for Lewis acid catalysts. κ^2-(C, O) sees both an O and C atom coordinated to the catalyst. This weakens the C=O bond thereby making it more able to break and form new bonds. The κ^2-(C, O) mode is seen more typically in transition states and intermediates. Finally, the κ^2-(O, O) binding mode takes advantage of the resonant nature of CO_2. Binding through both oxygens is seen mostly in metal carboxylates and makes the C atom susceptible to nucleophillic attack.

Despite the inherent stability (bond strength around 191 kcal mol^{-1}), CO_2 possesses several desirable properties for use as a feedstock chemical. It is a renewable source of carbon, is non-toxic, odourless and non-flammable.[50] In comparison to traditional synthesis of some of the CO_2 utilisation products, these properties make CO_2 an obvious reagent. For CO_2 as a feedstock chemical to become the normal in society, much work needs to be done on identifying and fully understanding different catalysts available. This requires a co-operative effort between experimental and computational chemists.

1.2 Cycloaddition of epoxides and CO_2 to form cyclic carbonate product

The synthesis of cyclic carbonates, through the cycloaddition of CO_2 and epoxides (Scheme 1.1), affords many benefits. These include:

- 100 % atom economy
- Solvent free, as the epoxide acts as the solvent
- Renewable and green reactants
- High substrate tolerance

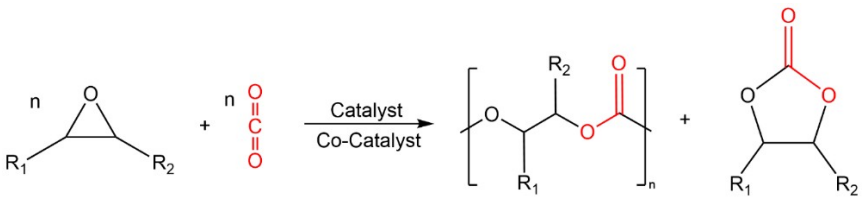

Scheme – Introduction.1 - The reaction of epoxides and CO_2 to afford poly/cyclic carbonates.

The epoxide reactant plays a significant part in allowing this reaction to occur. Once opened, the ring strained molecule releases energy offsetting the kinetic and thermal stability of CO_2. Epoxides are traditionally synthesised using fossil fuels, which reduces the positive impact that this reaction could have, creating a need to find green routes to epoxide synthesis. Recently, several routes have been found to afford “green” epoxides, through natural terpenes, biomass waste and plant oils, adding to the plethora of benefits that this reaction possesses.[54–56]

Considering the above, it is unsurprising that the cycloaddition of CO_2 with epoxides has received a lot of attention over the past decade (Figure 1.10).[57] The importance of cyclic carbonates has driven researchers to find new catalysts and develop a greater understanding of their mechanisms of action, to move closer towards financial viability of mass industrialisation. Density Functional Theory (DFT) and other computational methods are a key component of this research providing insight into potential reaction mechanisms and molecular properties (discussed in Chapter 2). Section 1.2 discusses a variety of catalysts for CO_2 utilisation and their mechanisms of action, if known.

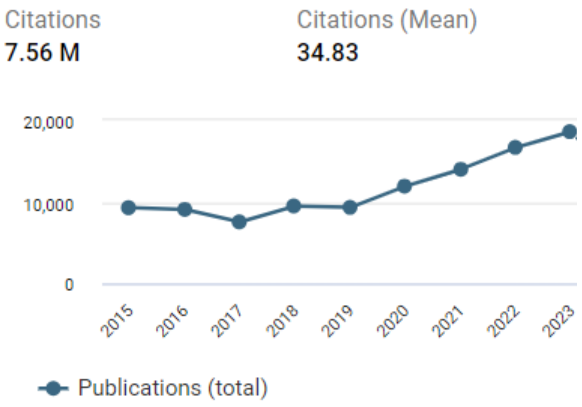

Figure – Introduction.10 - The number of publications relating to the search term "CO_2 Cyclic Carbonates" using the app.dimensions.ai website.[57]

1.2.1 Organocatalysts for Cyclic Carbonate Synthesis

Organocatalysts are metal-free and generally made up of the “organic elements” (H, C, N, O, P and S). Organocatalysts are generally regarded as non-toxic, robust to a variety of reaction conditions, cheaper in comparison to metal-based catalysts and can be synthesised from renewable sources.[58,59] This makes them an attractive prospect as catalysts for this reaction.

1.2.1.1 Boron Based Catalysts

Boron based catalysts are strong Lewis acids due to boron’s high electronegativity. Lewis acidic means that they can accept a pair of electrons. The Lewis acidic nature of boron makes it a sensible target for a catalyst for the synthesis of cyclic carbonates, as the activation of the epoxide and CO_2 both require the donation of a pair of electrons into a catalyst. Scheme 1.2 outlines the general mechanism for a Lewis acid catalyst. The epoxide first associates with the Lewis acid catalyst followed by an epoxide ring opening from an anionic cocatalyst. This is followed by the CO_2 insertion.

The CO_2 insertion involves multiple steps. The O atom associates to the catalyst causing the CO_2 to bend and become polarised. This makes the C atom susceptible to nucleophilic attack from the oxygen of the ring opened epoxide. The electrons of the O of the epoxide are pushed into the π* orbital weakening the C-O π bond. As a result of this, insertion occurs to form the alkoxide intermediate. After the insertion, ring closure occurs affording the cyclic carbonate and reforming the catalyst.

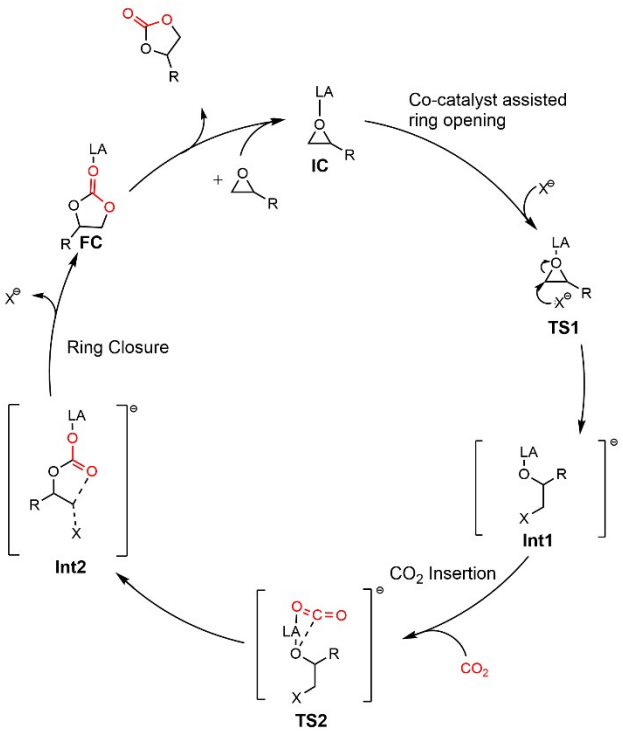

Scheme – Introduction.2 - The generally accepted mechanism for a Lewis acidic catalysed cycloaddition of CO_2 and epoxides to form cyclic carbonates.[60]

One catalyst that followed this mechanism was a BPh_3 catalyst with a Bis(triphenylphosphine)iminium chloride (PPNCl) cocatalyst. The BPh_3 catalyst has high turnover numbers (TON) and turnover frequencies (TOF) in comparison to other organic systems for this cyclisation.[61] The TON is the total number of products a catalyst can produce in its lifetime. The TOF is a calculation of the rate of catalyst cycles per unit of time per catalyst. One set of conditions that stands out is the cycloaddition of glycidyl chloride with 1 bar of CO_2 and a 0.025 % catalyst loading producing a >99 % yield conducted over 24 h. A TON of 3960 and TOF of 165 h^{-1} were reported, which are excellent in comparison to similar catalyst systems.[62,63] However, this reaction was undertaken at 100 ^{o}C, which is higher than some of the temperatures of other systems discussed further in this section.

A bifunctional boron salen catalyst also follows the general Lewis acidic mechanism. This catalyst does not require a co-catalyst due to a triphenyl phosphonium salt as part of the structure. The chloride anion of this salt ring opens the epoxide to allow for CO_2 insertion (Scheme 1.3).[64] For the cyclisation of CO_2 and epichlorohydrin at 100 ^{o}C, with 16 bar of CO_2 and a 0.045 % catalyst loading, a yield of 96.4 % was achieved with a TON of 964 and a TOF of 482 h^{-1}. Despite the increased TOF and shorter reaction time (2 h), this catalyst

demonstrates the effectiveness of the BPh_3 catalyst which produced a higher yield, at an equivalent temperature with a dominant TON.[61,64]

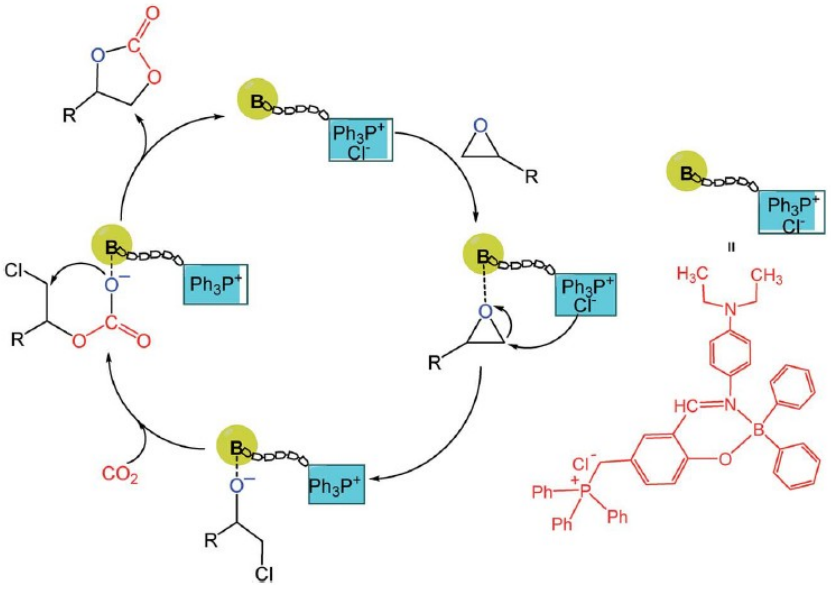

Scheme – Introduction.3 - The proposed reaction mechanism for the cycloaddition of CO_2 and epoxides catalysed by a bifunctional boron salen catalyst from 69.[64]

A heterogeneous BPO_4/KI catalyst was able to successfully catalyse the cycloaddition of CO_2 and propylene oxide. A 98 % yield was achieved at 110 ^oC, 40 bar of CO_2 and 4.5 % catalyst loading over 6 hours.[65] In comparison to the homogeneous catalysts previously discussed, this is extremely poor. The calculated mechanism Figure 1.11 sees the epoxide is first activated by hydrogen bonding to one of the phosphonium groups of the catalyst. This is then ring opened by one of the iodide from the KI co-catalyst followed by a rapid CO_2 insertion. Ring closure then occurs to afford the cyclic carbonate.[66]

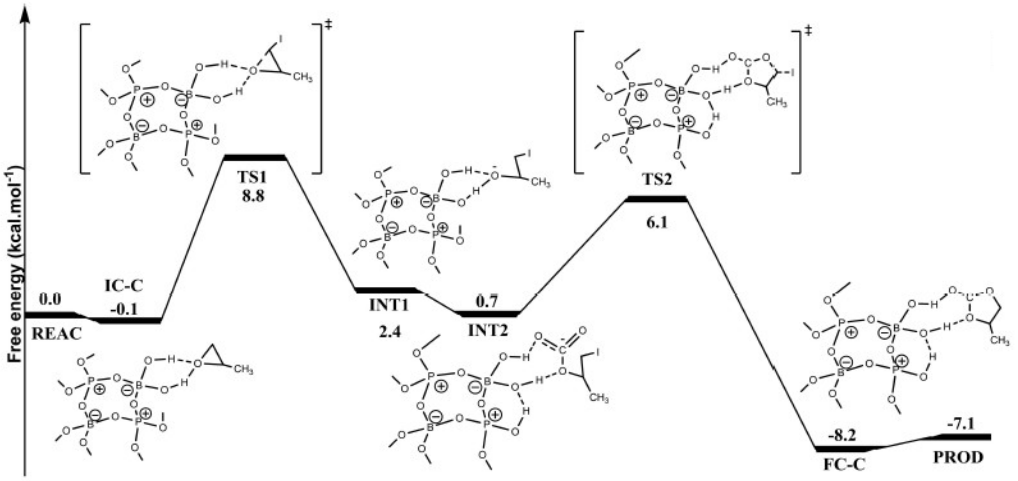

Figure – Introduction.11 – Gibbs free potential energy surface for the cycloaddition of propylene oxide and CO_2 to produce propylene carbonate, catalysed by BPO_4/KI at the B3LYP-D3/6-31G(d) level of theory from 66.[66]

1.2.1.3 H-Bond Donors

H-bond donors (HBDs) are catalysts that are specifically designed to follow the HBD mechanism of activating epoxides and CO_2 through hydrogen bonds. One of the benefits of HBD catalysts is that they many can be obtained naturally. One example of this is Guanidine.[67] Guanidine has two proposed catalytic cycles, pathway A and pathway B (Scheme 1.4). Pathway A follows the generalised HBD mechanism. Pathway B follows a different pathway after the ring opening occurrs. The negative alkoxide weakens the N-H bond, which activated the epoxide in the first instance, allowing for the electrons on the nitrogen to become delocalised with the adjacent amine (G1-IM2-B). As a result, the Lewis basicity of the adjacent amine increases allowing it to activate the CO_2 through the formation of a N-C bond, leaving the delocalised charge on the oxygen. The oxygen then eliminates the iodide from the ring opened epoxide through a nucleophilic attack forming a large ring intermediate (G1-IM4-B). Ring closure then occurs to regenerate the catalyst and form the cyclic carbonate product.[68]

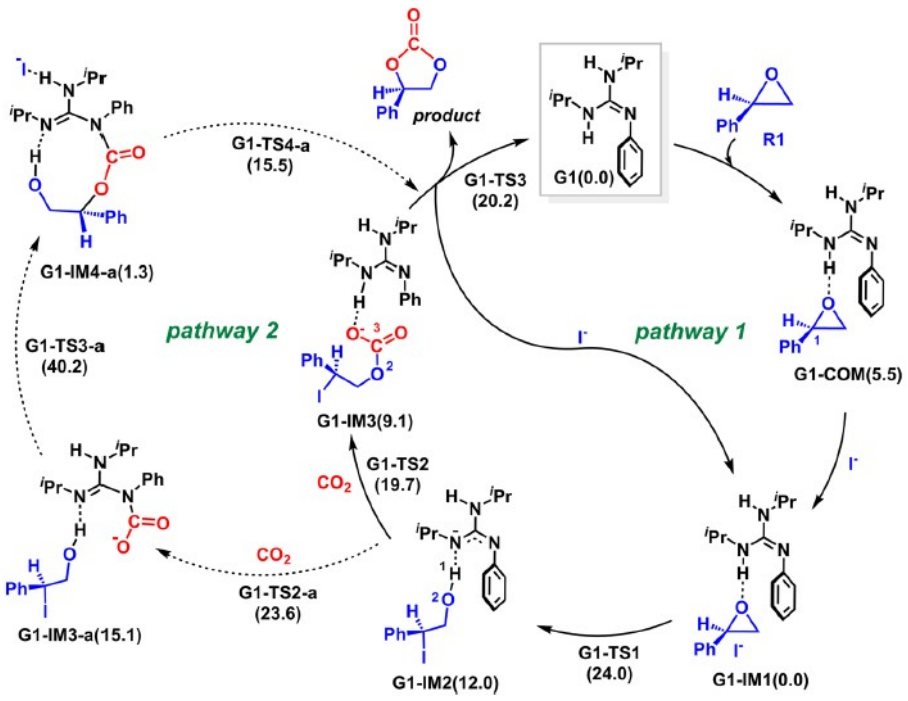

Scheme – Introduction.4 - The proposed catalytic cycles for the cyclisation of epoxides and CO_2 catalysed by guanidine from 68.[68]

Despite the interesting bifunctional nature of pathway B, pathway A was calculated as the active mechanism using DFT. Pathway A was calculated to be 20 kcal mol^{-1} more favourable in comparison to B, with the ring closing step being rate determining for A whilst CO_2 activation was rate determining for B.[68]

Another interesting HBD catalyst is the cyclicpropenium catalyst (Figure 1.12). This catalyst has a cationic ring strained propenium centre, counterbalanced by a halide.[69] The cationic centre draws electron density away from nitrogen of the amine groups creating a dipole between the nitrogen and H-groups around it. Consequently, these catalysts catalyse the cycloaddition of CO_2 and epoxides effectively, producing >95 % yields for a range of epoxides. These conversions occurred in the temperature range 100-120 ^{o}C, in 3 hours, 1 bar of CO_2 and 1 mol % catalyst loading. Despite the temperature being higher than desired, this catalyst performs relatively well in comparison to those previously discussed.

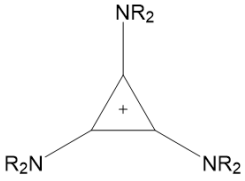

Figure – Introduction.12 - General structure of the cyclopropenium catalyst used for the cycloaddition of CO_2 and epoxides.

The proposed mechanism for the cycloaddition with a Tris(dimethylamino)cyclopropenium Chloride catalyst is displayed in Scheme 1.8. The generalised HBD mechanism is followed. Step A shows the association of the epoxide to the hydrogens promoted by the propenium cation. The epoxide ring is then opened by the Cl^- counterion before CO_2 inserts into the bond. Ring closure of the cyclic carbonate then occurs regenerating the catalyst.

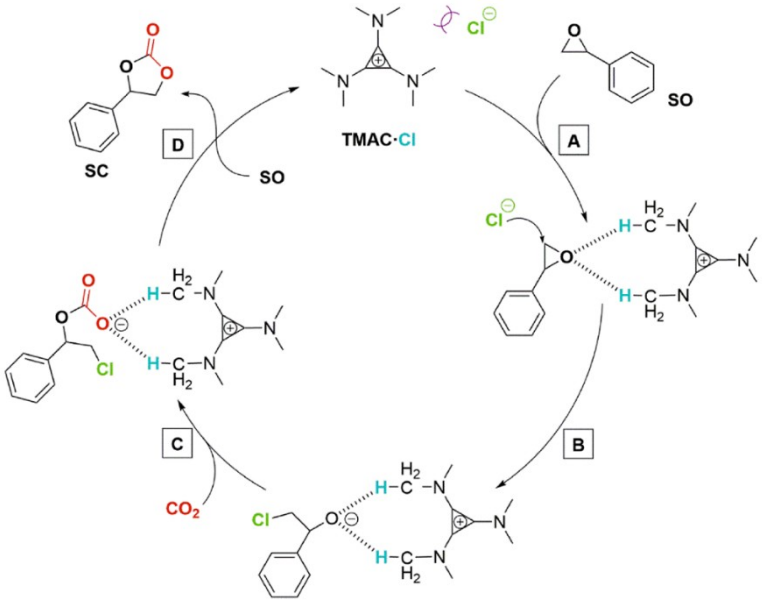

Scheme – Introduction.5 - Proposed mechanism for the cycloaddition of CO_2 and styrene oxide to form styrene carbonate catalysed by Tris(dimethylamino)cyclopropenium Chloride from 69.[69]

1.2.2 Metal Based Catalysts for Cyclic Carbonate Synthesis

Metal based catalysts are simply put, catalysts containing a metal. Compared to organocatalysts, metal catalysts can have more complicated structures due to their ability to form multi-ligand complexes. The nature of metal-ligand bonding also introduces more three-dimensionality into the structures, opening the door to more complex reaction mechanisms. This section discusses a variety of metal complex catalysts and their associated mechanisms. The focus is on catalyst structures which have been related with Lewis acidic catalysis.

1.2.2.1 Salen Based Catalysts

The salen ligand is a tetradentate ligand (Figure 1.13), which is applicable to a variety of metal centres. The large, tuneable backbone creates an opportunity for an array of catalyst structures with different electronic and steric properties, which is useful when searching for new active catalysts. Fe, Co, Al, Zn and Cr have all been used to produce active salen catalysts.[70]

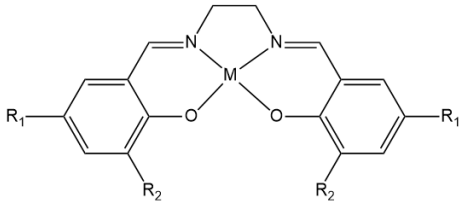

Figure – Introduction.13 - General structure for a salen based catalyst, with ligand κ^2-ONNO coordinated to metal (M) centre.

Ti and V salen (Figure 1.14) are two active catalysts in this field. Both catalysts have shown to catalyse the cycloaddition of CO_2 and epoxides effectively. The titanium complex contains Ti(IV) in a d^0, electron-deficient coordination environment. This provides accessible coordination sites rendering the catalyst reactive. Similarly, the vanadium complex features a V(V) d^0 centre that is likewise electron-deficient, facilitating substrate coordination and subsequent catalytic turnover. Both catalysts have yielded 98 % of cyclic carbonate with a 0.1 mol % catalyst loading, a 0.5 mol % cocatalyst loading at 100 ^oC, 1 bar of CO_2 for 24 hours. In comparison to the organocatalysts, both Ti and V salen show dominant activity. No turnover frequency or numbers were reported.[71]

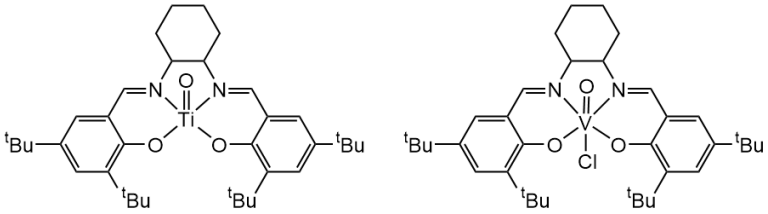

Figure – Introduction.14 - The structures of Ti and V salen in their active form.[71]

It was found that these catalysts produced a racemic mixture rather than being enantiomerically enriched. This means there must be a stereo-inverting step within the mechanism, which is not present in the general Lewis acidic mechanism. Therefore, a Lewis base mechanism was proposed (Scheme 1.6). The CO_2 is activated by the catalyst making one of the oxygens on the CO_2 strongly Lewis basic. This oxygen facilitates the ring opening of the epoxide and is the stereo-inverting step. The oxygen can attack either side of the epoxide because of the distance between the O-C bond.[71] Following this the basic oxygen of the newly formed alkoxide activates a second CO_2 molecule before ring closure occurs and the product is formed.

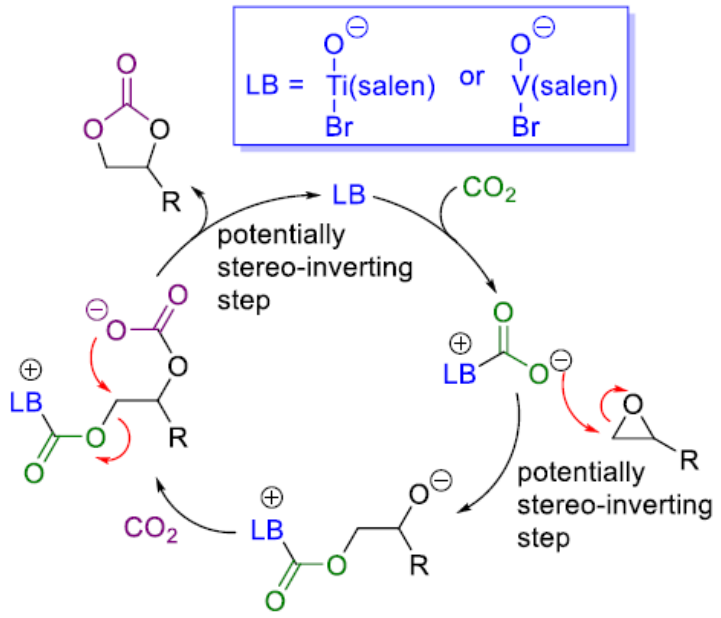

Scheme – Introduction.6 - The proposed catalytic cycle for the cycloaddition of CO_2 and epoxides to form cyclic carbonates catalysed by Ti and V salen from 71.[71]

One study compares a Cr salen and Cr inden ligand (Figure 1.15). In equivalent conditions (0.02 mol % of catalyst and cocatalyst, 80 °C, 20 bar CO_2 for 1 hour) the salen and inden catalysts yielded 25 and 38 % cyclic carbonate respectively and TOFs of 1250 and 1900 h^{-1} respectively. Increasing the cocatalyst concentration to 0.2 mol % for the more active inden increases the yield to 86 % and the TOF to 4300 h^{-1}.[72]

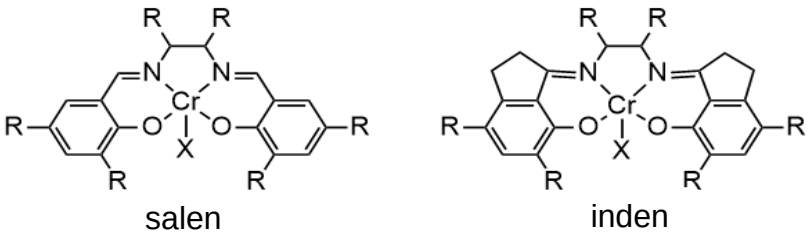

Figure – Introduction.15 - The general structure of the Cr- salen and inden catalysts.

DFT calculations have elucidated the mechanism of both catalysts for the cycloaddition (Figure 1.16). The calculated energy spans are 27.99 and 29.28 kcal mol^{-1} for the inden and salen respectively, showing good agreement with the experimental data. However, no transition state has been quoted for the CO_2 insertion, but rather an association of CO_2 to the alkoxide oxygen.[72] This is an unusual mechanism and considering that the CO_2 insertion step is often rate determining, leaves the calculated energy spans questionable.

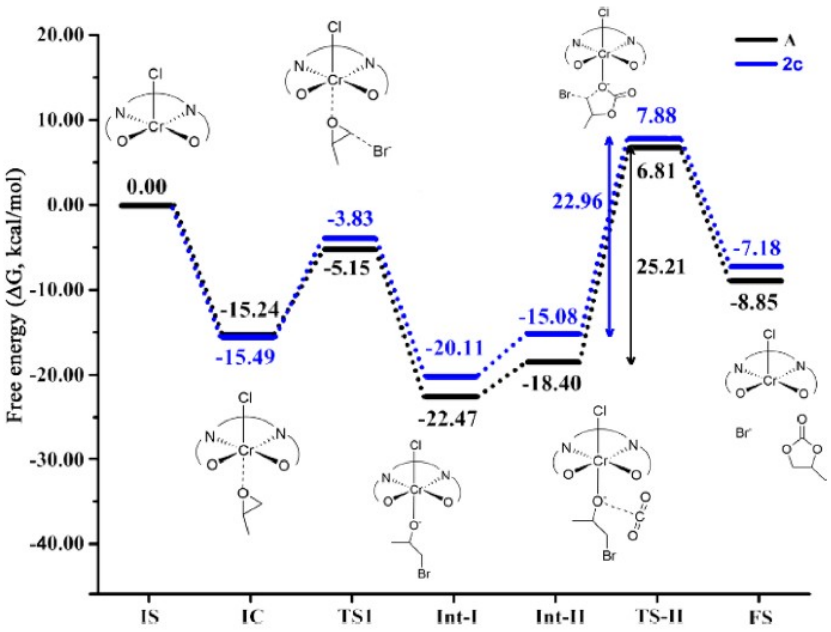

Figure – Introduction.16 - Calculated potential energy surface for the cycloaddition of CO_2 and propylene oxide catalysed by Cr- salen (A; black) and inden (2c; blue) from 72.[72]

Another interesting variation of the salen ligand was North's bimetallic Al salen (Figure 1.17). Considered as highly active among catalysts for this reaction, bimetallic Al salen converted 98 % of styrene oxide to styrene carbonate at ambient conditions (25 ^{o}C, 1 bar CO_2, 2.5 mol % catalyst and cocatalyst in 24 h).[73]

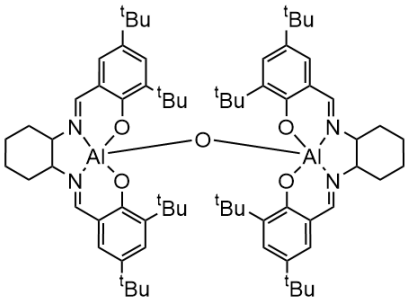

Figure – Introduction.17 - North's bimetallic salen catalyst.[73]

The proposed mechanism by North (Scheme 1.10) suggests a bimetallic mechanism where both Al centres play an active role in the mechanism. The mechanism begins by association of the epoxide to complex **9a**. Following this the tertbutylammoniumbromide (TBABr) assisted ring opening occurs to form the alkoxide complex **11**. A kinetic study found the reaction was second order with respect to TBABr. Then a second active molecule of TBABr assists with the activation of the CO_2 by splitting tributylamine and 1-butylbromide. Tributylamine was shown to have an active role in the mechanism experimentally and is

proposed to react with CO_2 to form a carbamic acid. This then associates with the other Al centre (complex **12**). From **12** the ring opened alkoxide migrates across to the activated CO_2 and eliminates the tributylamine to form **13**. Ring closure then occurs to produce the cyclic carbonate product.

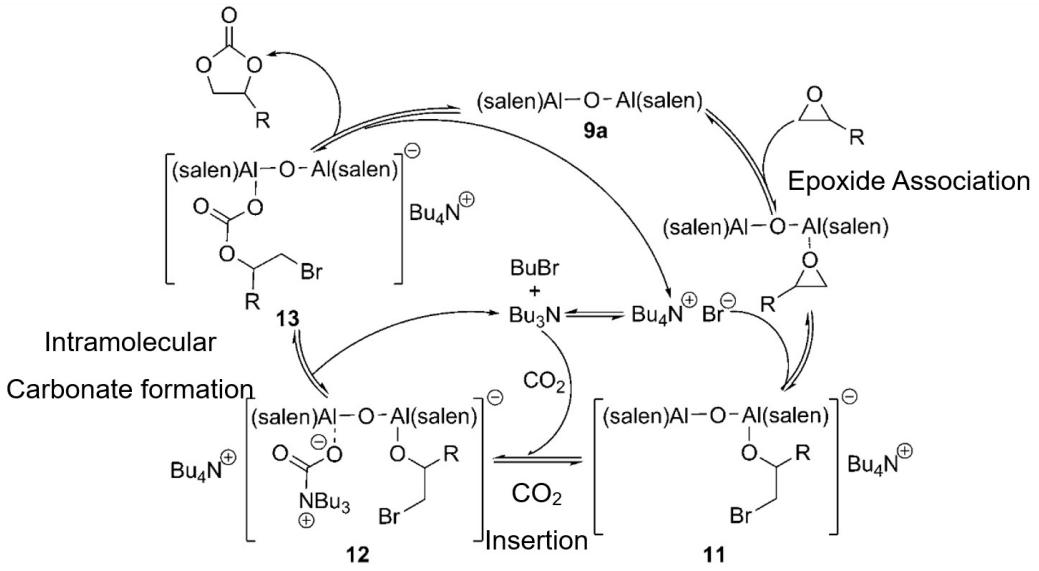

Scheme – Introduction.7 - Proposed mechanism for the cycloaddition of CO_2 and epoxides catalysed by bimetallic Al salen adapted from 74.[73,74]

A DFT study on this catalyst system was undertaken by Deng *et al*.[75] The calculated structure of the catalyst unveiled a potential problem with the bimetallic mechanism proposed in Scheme 1.10. The distance between the opened alkoxide and the activated CO_2, if they were associated to the Al atoms axially, would be too far for elimination of the tributylamine. This means they would need to associate equitorially (Figure 1.18 a). However, an optimised structure for this kind of association could not be calculated.

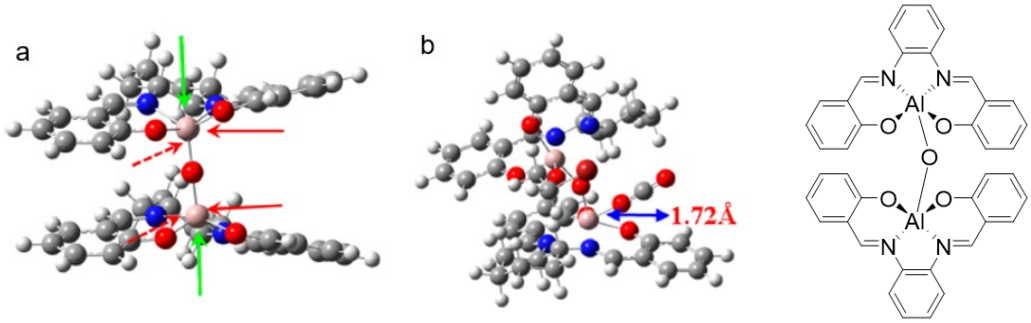

Figure – Introduction.18 – (a) Calculated structure for the bimetallic Al-salen.[75] *The green and red arrows indicate different positions where CO_2 and epoxide could associate to the metal. (b) Showing the starting structure for CO_2 and epoxide association from 75.*[75] *Atom Legend: Red = O, Blue = N, Grey = C, White = H and Peach = Al.*

The red arrows on Figure 1.18a show the positions in which CO_2 and epoxide associate to the catalyst. The starting structure for the optimisation of the association is shown in Figure 1.18b. This optimisation shows the CO_2 dissociating from the metal centre, leading to a proposal and calculation of a monometallic mechanism, which would not agree with the experimental observation of a second order reaction in respect to TBABr. However, notice that in Figure 1.18b, the CO_2 has not been activated by the carbamic acid. Therefore, without the increased negative charge on the oxygen of the CO_2, it is a weaker Lewis base and is less likely to associate with the metal centre. Concluding that the most likely mechanism for this catalyst is the bimetallic.

1.2.2.2 Scorpionate Catalysts

The scorpionate catalyst is a bifunctional catalyst with both Lewis acidic and Lewis basic components. The analogy of the scorpionate catalysts comes from the "pincers" grabbing and holding onto the metal and the "stinger" attacking the "prey" by interacting with the metal from over the top (Figure 1.19).[76] Similar to the salen ligand, the large multidentate ligand structure can be modified to alter the catalyst properties.

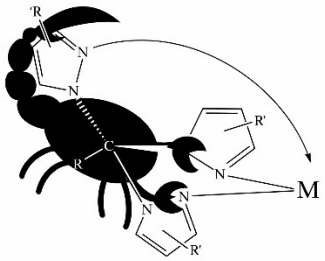

Figure – Introduction.19 - Visual representation of the scorpionate catalyst and how they achieve their name.[76]

An $FeCl_2[\kappa^3\text{-}HC(pz)_3]$ scorpionate catalyst (Figure 1.20 a) in a room temperature ionic liquid solvent. An ionic liquid was chosen as it allowed for a lower concentration of the TBABr co-catalyst to be used in comparison to other similar methods.[76] The Fe catalyst was successfully able to convert 98.3 % of propylene carbonate to propylene oxide with a 0.5 and 0.3 mol % loading of catalyst and TBABr cocatalyst respectively. The reaction took place over 24 hours at 80 ^{o}C and 8 bar of CO_2. The ionic liquid (IL) used for this conversion was $[bmim][N(CN)_2]$ (Figure 1.20 b).

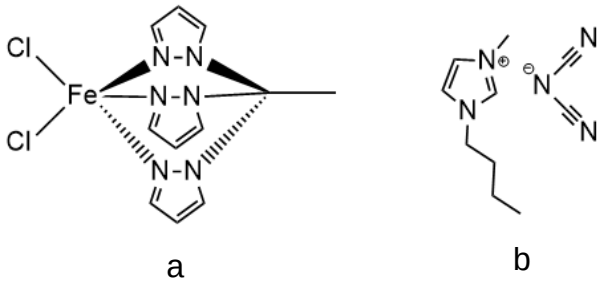

a b

Figure – Introduction.20 – A) $FeCl_2[\kappa^3\text{-}HC(pz)_3]$ catalyst used for the cyclisation of CO_2 and epoxides. B) The IL used as solvent for the reaction.[76]

The mechanism of the conversion using $FeCl_2[\kappa^3\text{-}HC(pz)_3]$ is unknown. Using the IL as a solvent means there are a wide scope of plausible reaction mechanisms for this synthesis. Yet no computational studies have been conducted on this system.

Zinc scorpionates have also shown promise for the cycloaddition of CO_2 and epoxides. A $ZnMe(\kappa^3\text{-}Fphbp^tamd)$ (HFphbptamd = N,N′-di-p-trifluoromethyphenylbis(3,5-di-tert-butylpyrazol-1-yl)acetamidine) catalyst (Scheme 1.8) has been able to achieve a 100 % conversion rate of CO_2 and styrene oxide into styrene carbonate. At 5 mol % of catalyst and co-catalyst (TBABr), a 95 % yield was achieved at room temperature, 10 bar of CO_2 over 18 h. Reducing the loading to 0.2 mol % of each, 100 % conversion was achieved at 50 °C under the same conditions. The TOF achieved in these conditions was 28 h^{-1}. Reducing the time to 8 hours, a 75 % yield was achieved with a TOF of 48 h^{-1}. The TOF could also be increased to 245 h^{-1} by increasing the temperature to 100 °C. This gave a conversion of 98 % with a loading of 0.1 mol % of catalyst and co-catalyst over 4 hours.[77] Versatility across a range of temperatures and loadings can highlight a catalyst as a potential target for industrial usage. The generalised Lewis acid-based mechanism was proposed for this reaction (Scheme 1.2).

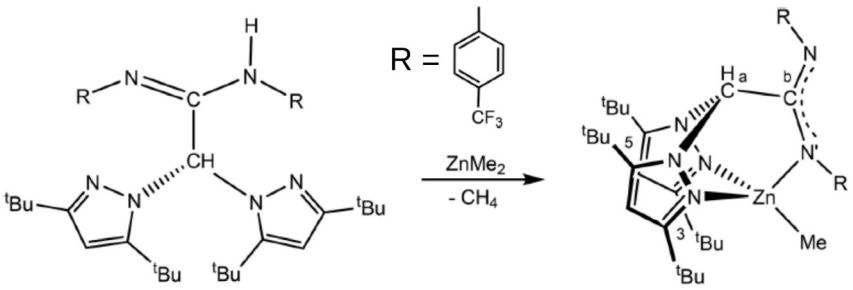

Scheme – Introduction.8 - General structure of the scorpionate ligand and how it is synthesised into the zinc catalyst used for the cycloaddition of CO_2 and epoxides from 77.[77]

An Al scorpionate catalyst (Figure 1.21) has shown catalyst activity equivalent to that of the zinc. For the same cycloaddition, a conversion of 100 % was achieved with a 0.25 mol % catalyst 5 mol % co-catalyst (TBABr) loading, using 10 bar CO_2 at 80 ^{o}C for 3 h.[78] This study also tested the compound on more sterically challenging natural, terpene-based epoxides and the catalyst was able to achieve a 79 % conversion rate to cyclic carbonates at 70 ^{o}C, 10 bar of CO_2, 1 and 3 mol % of catalyst and cocatalyst loading respectively over 66 h.[78] This is a promising find showing the potential of net zero industrial synthesis using 100 % renewable reactants.

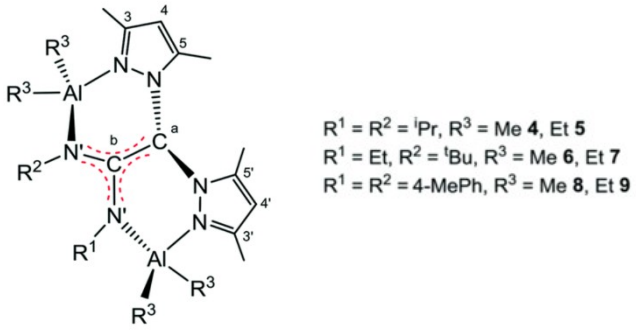

Figure – Introduction.21 - Structure and analogues of the Al scorpionate catalysts tested within the study from 78.[78]

1.2.2.3 Aminotrisphenolate Catalysts

The aminotrisphenolate ligand (Figure 1.22) is a tetradentate ligand consisting of three phenolate arms. This ligand has produced excellent yields for the cycloaddition of CO_2 and epoxides producing some extremely active catalysts.

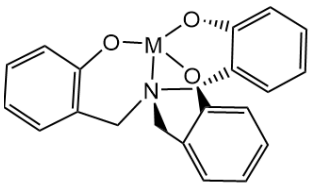

Figure – Introduction.22 - General structure of M(aminotrisphenolate).

A Zr(IV)aminotrisphenolate catalyst is one example of these. It was able to catalyse a wide scope of epoxides to form their respective cyclic carbonates with a 99 % conversion. The catalyst loading was low with 0.05 mol % of the catalyst and 0.25 mol % of the TBABr co-catalyst. The reaction was undertaken at 90 ^{o}C

with 12 bar of CO_2 for 18 h. Impressive TON values between 1900-2000 were reported for this catalyst. The proposed mechanism for this reaction was the general Lewis acidic mechanism (Scheme 1.2).

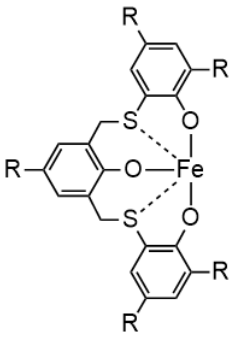

Figure – Introduction.23 - The Fe thioether-triphenolate derivative of the trisaminophenolate ligand.

An Fe thioether-triphenolate derivative (Figure 1.23) shows interesting activity and forms a bimetallic catalyst (Figure 1.24). Using this catalyst a 70 % conversion of epicholorhydrin was achieved at 20 bar of CO_2 and 120 ^{o}C with low catalyst and co-catalyst loadings of 0.01 and 0.1 mol % respectively. This reaction was only carried out over 1 h meaning the catalyst had a reported TOF of 7000 h^{-1}.[79]

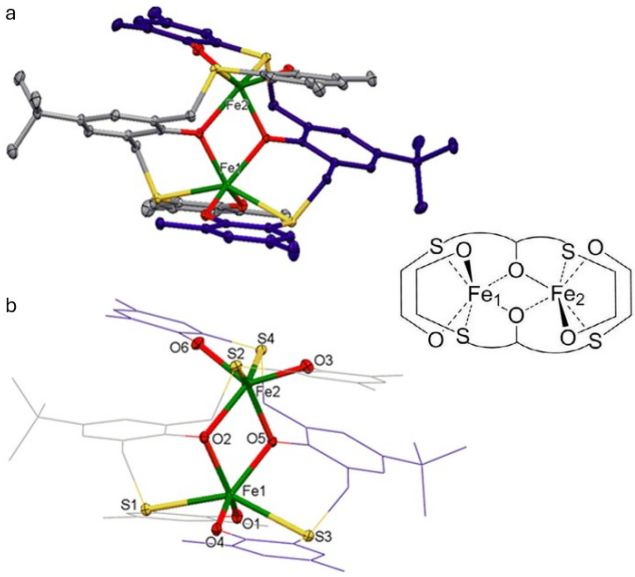

Figure – Introduction.24 - Molecular structure of the dimerised Fe aminotrisphenolate. Hydrogen atoms were omitted from these structures for clarity adapted from 79.[79]

DFT calculations were employed to elucidate the full mechanism of this catalyst. Both a monometallic and bimetallic mechanism were considered (Figure 1.25). The Br from TBABr ring opens the epoxide to form **6-B**. CO_2 can be activated by

the other Fe site and insert (**6-TS-BC'**) or directly insert into the Fe site occupied by the alkoxide (**6-TS-BC**). It is calculated to be 15.7 kcal mol^{-1} more favourable for a direct insertion into the occupied site making the mechanism monometallic. From **6-C**, the cyclic carbonate ring closes and reforms that catalyst.

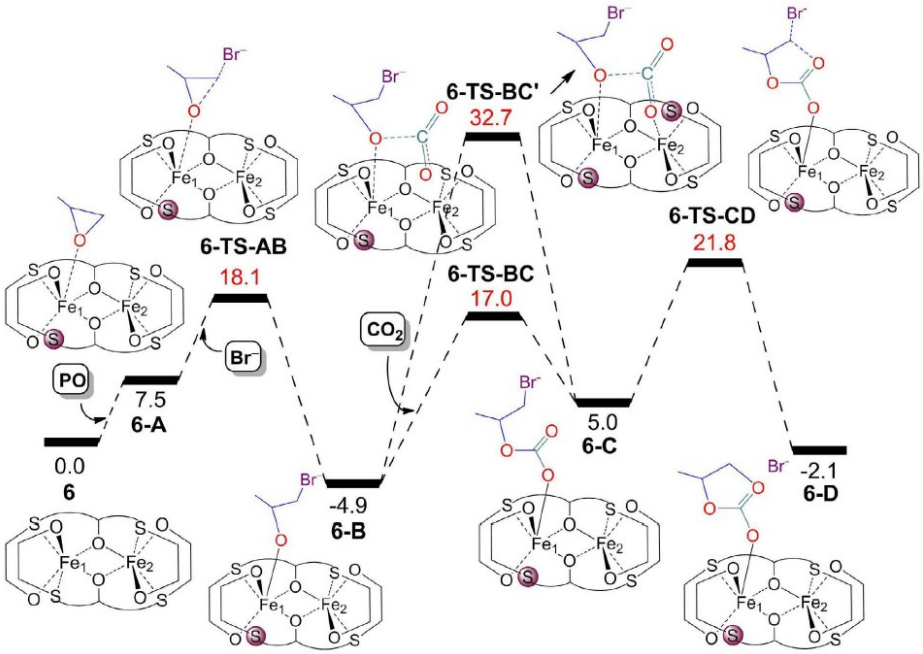

Figure – Introduction.25 - Calculated potential energy surface for the thioester-triphenolate bimetallic Fe catalyst for the cycloaddition of CO_2 and epoxides in kcal mol^{-1} from 79. PO = Propylene oxide[79]

The novel catalysts tested in this study highlight the importance of exploring the chemical space around known ligands. Through the addition of the thiol, a set of catalysts with exemplary TOFs have been identified.

One of the most notable catalysts from the aminotrisphenolate class is the Al variant. This catalyst boasts TOFs of over 10000 h^{-1} with the highest reported TOF being 36000 h^{-1}. This was achieved using 0.0005 mol % Al aminotrisphenolate and 0.05 mol % of PPN-Br cocatalyst. This was conducted at 90 ^{o}C using 10 Bar of CO_2 over 2 hours and the TON of 112000.[80]

Like the Fe catalyst, the Al aminotrisphenolate was found to dimerise. Adding a THF ligand displaces the oxo bridged bonds of the dimer to form the monomeric catalyst which is the active form of the catalyst. The full reaction mechanism was elucidated and compared to an active Zn salphen catalyst (an analogue of the salen catalyst with a phenyl bridge between the amine groups) from the Kleij and Bo groups (Figure 1.26).[81] The salphen catalyst was able to achieve an 80 % yield in the conversion of epoxyhexane to the corresponding cyclic carbonate. This

was done with 10 bar of CO_2 at 45 °C over 18 hours. The catalyst loading was 2.5 mol % and the cocatalyst (TBAI) 1 mol %.[82]

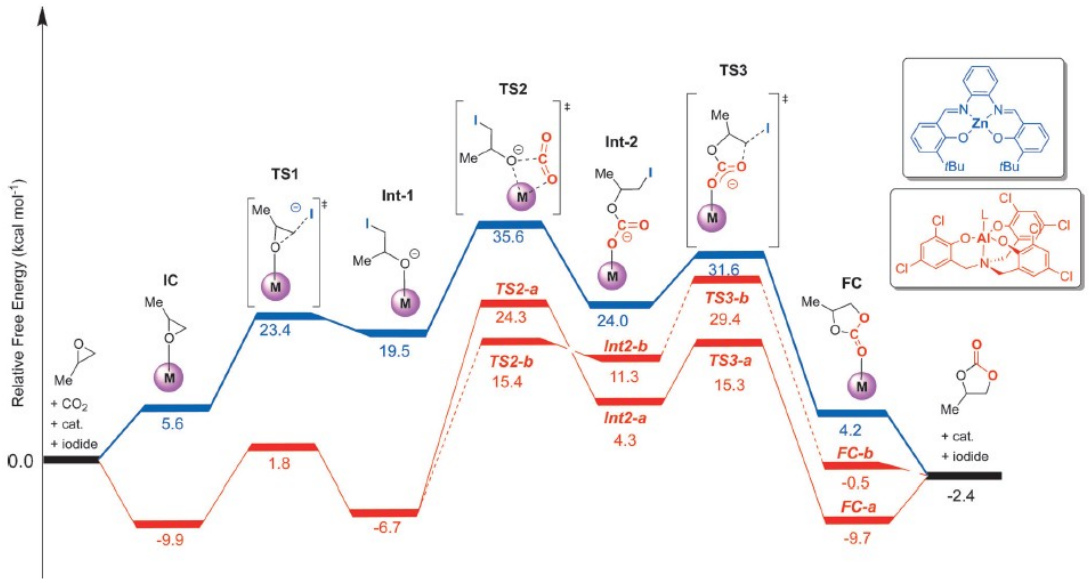

Figure – Introduction.26 - The calculated potential energy surfaces of the cycloaddition of propylene oxide with CO_2 to form propylene carbonate catalysed by Zn Salphen (Blue) and Al aminotrisphenolate (Red). On the red pathway, the CO_2 can insert axially (TS2-a) or equatorially (TS2-b) from 81.[81]

The elucidated mechanisms show that the Zn-salphen catalyst follows the general Lewis acidic mechanism. Using the labels published, the Al aminotrisphenolate first sees a displacement of the THF ligand with the epoxide to form IC-b. [81] This is followed by the ring opening from TBAI-b to form Int-1-b. Following this, CO_2 insertion can either occur axially (TS2-a) or equatorially (TS2-b). The axial insertion barrier is 8.9 kcal mol^{-1} lower in energy so this insertion occurs. At Int-2b, an axial-equatorial isomerisation occurs, and the pathway proceeds via Int-2b. Ring closure of the epoxide then occurs to form the cyclic carbonate and reform the catalyst.[80]

The computational results are in good agreement with their observed experimental results. The Zn salphen catalyst has an energy span of 35.6 kcal mol^{-1} in comparison to a 25.3 kcal mol^{-1} barrier for the Al aminotrisphenolate. The 10.3 kcal mol^{-1} barrier difference explains the dominant activity of the Al aminotrisphenolate catalyst.

1.2.2.4 Porphyrin Catalysts

The porphyrin ligand is a macrocycle, which readily chelates with metals through N lone pair donation into a metal (Figure 1.27). The porphyrin ligand adopts a near-planar geometry, enabling extensive π-electron delocalisation and stable

metal coordination. The metal sits within the centre of the macrocyclic ring. Porphyrins are natural compounds and have been found to play key roles in various biological systems and their biological presence has been dated back to thousands of years ago.[83] Due to their ability to chelate readily to a variety of metals, porphyrins have also played a significant role as catalysts.

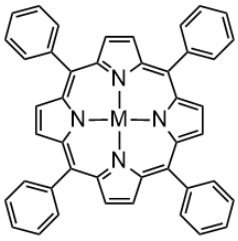

Figure – Introduction.27 - The general structure of a metal (M) porphyrin with κ^4-N_4 coordination.

One of these catalysts is Mn porphyrin (Figure 1.28). Due to the large ring structures of this catalyst, many variations of the catalyst can be made through functionalisation. Figure 1.28 displays a range of different variations of the Mn catalyst. In the optimised experimental conditions, catalyst performed the best, producing a 90 % yield of styrene carbonate. This was undertaken at 90 ^{o}C with 1 bar of CO_2. The catalyst and co-catalyst (TBABr) loadings were 0.02 mol % and 1 mol % respectively. The reported TON was 4529 with a TOF of 126 h^{-1}.

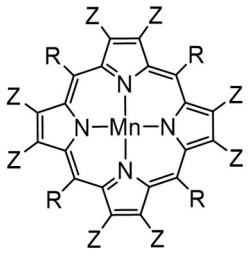

1: R = p-COOH-C_6H_4; Z = H
2: R = p-COOH-C_6H_4; Z = Br
3: R = p-$COOCH_3$-C_6H_4; Z = Br
4: R = –C_6F_5; Z = H
5: R = 2-Cl,6-F-C_6H_4; Z = H
6: R = p-COOH-C_6H_4; Z = 2Br, 6H
7: R = p-COOH-C_6H_4; Z = 4Br, 4H
8: R = p-COOH-C_6H_4; Z = 6Br, 2H

Figure – Introduction.28 - A variety of Mn catalysts used for the cycloaddition of CO_2 and epoxides adapted from 84.[84]

Another active porphyrin catalyst is Mg porphyrin. This catalyst is able achieve a 99 % yield of propylene carbonate at 24 ^{o}C, 14 bar of CO_2 using a catalyst and co-catalyst (TBAI) loading of 0.1 mol % catalyst loading each over 24 hours. This catalyst had a TON value of 1992 and TOF value of 83 h^{-1}.[85] Despite having a lower TON and TOF in comparison to the Mn(III) catalyst, the reaction was undertaken at a much lower temperature with lower co-catalyst loading. However, the catalyst loading was five times higher and the CO_2 pressure significantly higher. A mechanism was proposed for this cycloaddition (Scheme 1.9).

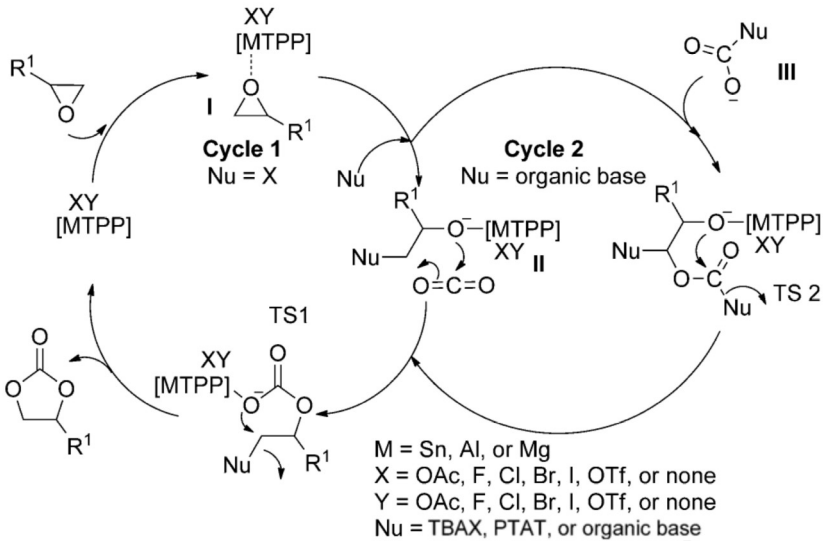

Scheme – Introduction.9 - Proposed mechanism for the cycloaddition of epoxide and CO_2 catalysed by a porphyrin catalyst adapted from 85.[85]

Two different cycles were proposed. Cycle 1 is the standard Lewis acidic mechanism. Cycle 2 sees the nucleophile act as an organic base to first activate the CO_2, which subsequently ring opens the epoxide and then ring closing occurs. Wu *et al*. conducted a computational study into this and found that Cycle A had an energetic span of 18.4 kcal mol^{-1} and Cycle B 40.4 kcal mol^{-1}, hugely favouring the Lewis acidic pathway.[86]

An Al porphyrin catalyst (Figure 1.29) showed incredible activity for this reaction. A 99 % conversion of propylene oxide was achieved at 25 ^{o}C, 1 bar of CO_2 and catalyst and co-catalyst (TBABr) loadings of 0.25 and 2 mol % respectively.[87] This level of activity, in ambient conditions, is a key feature of a potential catalyst for undertaking this reaction at an industrial scale. Further to this, this catalyst is also heterogeneous, another common property sought by industrial scale processes as it reduces the cost of catalyst separation processes.

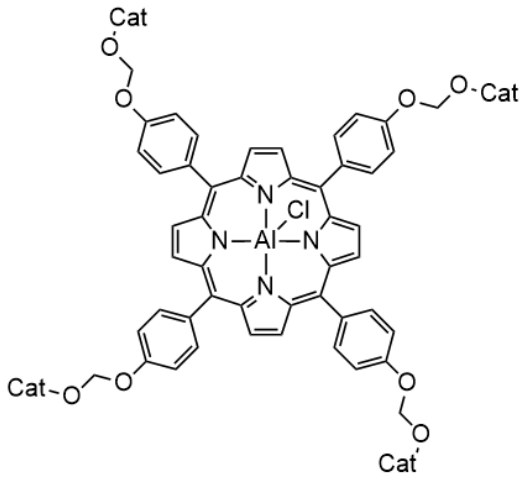

Figure – Introduction.29 - Structure of the Al porphyrin catalyst. The heterogeneous catalyst is built into the scaffold through the O-C-O linkers.[87]

The catalysts TOF values also responded positively to increases in temperature and catalyst concentration. Increasing the temperature from 40 to 100 °C saw the TOF rise from 860 to 5870 h^{-1} using 30 bar CO_2. Similarly, increasing the concentration ratio of propylene oxide to Al porphyrin sees an increase in TOF from 5870 (the 100 °C conditions) to 14880 h^{-1}. The reusability of the catalyst was also tested, and it was found that even after 10 runs a 96 % yield was achieved.[87] The increasing activity and reusability of the catalyst continues to show promise for industrial use.

1.2.3 Heterogeneous Vs, Homogeneous

Homogeneous systems tend to be more active and selective in comparison to heterogeneous systems. Homogeneous catalysts are surrounded by reactants in solution as they are in the same phase. This leads to efficient molecular collisions and uniform access to the active site, which often results in higher catalytic activity and selectivity compared to heterogeneous systems. However, active heterogeneous systems are highly desirable due to lower separation costs and tend to be more stable, thereby making them much more scaleable.[88] The BPO_4 example discussed in subsection 1.2.1.3 demonstrates how changing the structural properties of catalysts can affect the reaction mechanism. Further to this, it examples the difference in activity levels between some homogeneous and heterogeneous systems.[61,62,66]

Currently there is a strong focus on finding novel highly active catalysts that can catalyse this reaction at ambient conditions. As homogeneous catalysts tend to

show a higher rate of activity, this research will focus on the discovery of novel homogeneous catalysts and navigating new chemical space. Furthermore, a developing area of research has emerged in heterogenising homogeneous catalysts by scaffolding them onto silicon surfaces, for example.[89,90] It would be expected that these methodologies will become more prevalent to transfer the higher activity of the homogeneous world into the more durable and industrially relevant heterogeneous world.

1.3 Group 13 Catalysts – Moving into New Chemical Space

Section 1.2 highlights some of the vast choice of catalysts available for the cycloaddition of CO_2 and epoxides. Focussing on the metal, a popular choice is Al due to the high Lewis acidic. It is also readily available and oftentimes cheaper than alternatives.[91] Resulting from the success of Al, the heavier group 13 metals have been far less studied. Furthermore, in 2004, Ga catalysts were reported by Darensbourg *et al.* to be extremely poor catalysts for the copolymerisation of CO_2 and epoxides.[92] This left little motivation for exploration into heavy group 13 complexes for this reaction.

Moving forwards, in 2011 Shibata *et al* reported several In trihalide complexes with a PPh_3 cocatalyst which could successfully catalyse the cycloaddition of CO_2 and a variety of epoxides with yields of greater than 80 %.[93] Although this required high catalyst and cocatalyst loadings (5 and 10 mol % respectively), an insight was provided into the potential of heavier group 13 catalysts.

Following on from this work, in 2021 the Mehrkhodavandi group published a seminal paper showing a clear favourability of both Ga and In trihalide catalysts in comparison to their aluminium counterparts for the cycloaddition of CO_2 and epoxides.[94] In equivalent conditions, $InBr_3$ was found to be more active than all the other group 13 trihalide counterparts (Table 1.2). $InBr_3$ produced a yield of 90 %, whereas $InCl_3$ and InI_3 produced a yield of 70 % and 79 % respectively. All Al and Ga analogues produced yields below 50 %.

Table – Introduction.2 - Yield for the cycloaddition of CO_2 and glycidyl methyl ether epoxide to form glycidyl methyl ether carbonate with a catalyst and co-catalyst loading of 5 and 10 mol % respectively conducted over 1 hour. The reaction was solvent free with 1 bar of CO_2 at 20 ^{o}C.

Catalyst	Yield %
$AlCl_3$	23
$AlBr_3$	41
AlI_3	26
$GaCl_3$	3
$GaBr_3$	39
GaI_3	42
$InCl_3$	70
$InBr_3$	90
InI_3	79

In the same year, a second seminal paper was published by the Hamilton/Whiteoak group showing the dominance of a Ga aminotrisphenolate catalyst over the Al counterpart.[95] The Ga catalyst was able to achieve yields of >99 % at RT with catalyst and co-catalyst loadings of 0.5 and 2 mol % respectively over 16 hours and 8 bar of CO_2. At 90 ^{o}C, the catalyst and co-catalyst loadings were able to be reduced to 0.025 and 0.1 mol % respectively producing a >99 % yield in equivalent conditions. Even more impressive was further reducing the catalyst and co-catalyst loadings to 0.00025 and 0.005 mol % still saw an 86 % yield with equivalent conditions although with a 70-hour reaction time. At these conditions, TON of 344,000 was reported.

The Hamilton/Whiteoak groups published a number of papers highlighting the potential of going beyond Al when considering group 13 homogeneous, a number of which are discussed in later chapters.[96,97] More recently in 2024, the Hamilton/Whiteoak groups showed that the activity of Al, Ga and In aminopyridylbisphenol complexes was In > Ga > Al (Figure 1.30).[98] Not only did the heavier group 13 metals prove to be more active than the Al counterparts, there was also an interesting difference in chemistry with the GaI complex. The GaL-I complex (blue line; Figure 1.30) was able to successfully catalyse the reaction in the absence of a co-catalyst. A yield of >99 % was achieved with 0.6 mol % catalyst loading at 8 bar of CO_2 over 18 hours. This is unusual for this reaction, as in the absence of a co-catalyst there is normally no reactivity or poor yields.[99] It is also interesting that this is specific to the Ga analogue. This reactivity is energetically unavailable to the InL-I analogue (grey line; Figure 1.30).

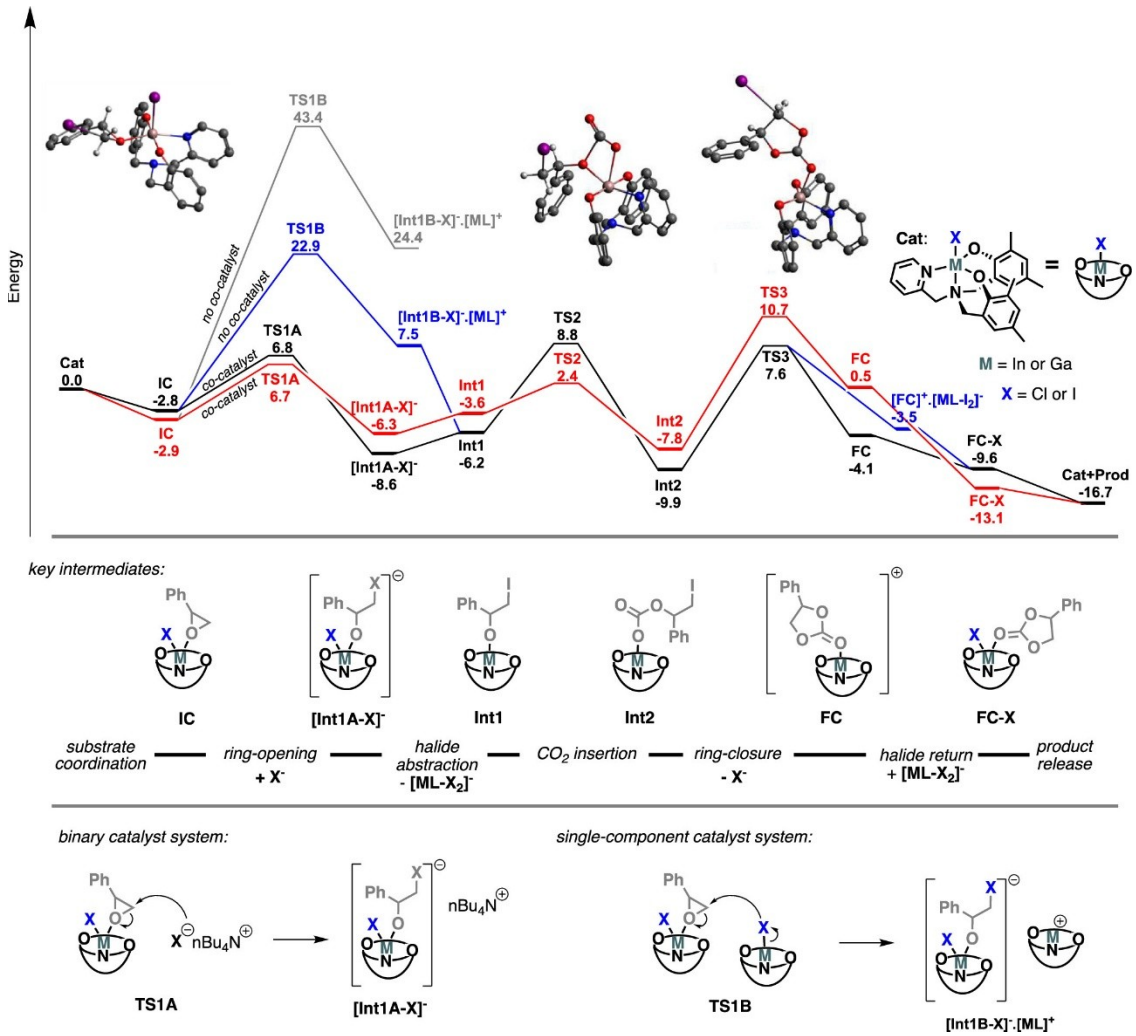

Figure – Introduction.30 – Hamilton's/Whiteoak's calculated free energy surface (ΔG 298 k (kcal mol^{-1})), for the cycloaddition of CO_2 and styrene oxide using catalysts GaL-I/TBAI (black line) and GaL-I (cocatalyst free; blue line), InL-Cl/TBAI (red line), and InL-Cl (cocatalyst free; gray line) from 98.[98]

These recent reports showing the promising nature of the heavier group 13 metal catalysts highlight clearly that a stronger Lewis acidic catalyst does not provide the most active catalyst. Mehrkhodavandi *et al.* addressed this head on with a comparison of cationic In and Ga complex's for the polymerisation of epoxides and ε-caprolactone.[100] Problems with the different methods of measuring Lewis acidity were addressed; namely that a complexes' Lewis acidic strength is related to the environment it is in. This was highlighted through measuring the Lewis acidity using different methods.

The fluorescent Lewis adduct (FLA) method measures the Lewis acidity by measuring the fluorescence emission change when phosphorous oxide is mixed with a Lewis acid. The FLA showed the Lewis acidic strength as Ga^+ complex > In^+ Complex. However, the global electrophilicity index (GEI), which measures

Lewis acidity on a complex's ability to accept electron density through calculating the energies of the frontier molecular orbitals, predicted the opposite.[100]

It is becoming clear that the reactivity of the group 13 catalysts for the cycloaddition of CO_2 and epoxides is not solely governed by the Lewis acidic strength of the complexes. This opens a new area of chemical space which has previously been underexplored that could contain highly active catalysts for CO_2 utilisation. This work aims to explore different regions of this chemical space and test the substrate versatility of the catalysts explored. Further to this, this project aims are to use quantitative structure activity relationships (QSAR) to identify properties beyond Lewis acidic strength responsible for catalyst activity. Finding the underlying electronic and steric properties governing the catalysts activity will better inform catalyst discovery in this field in the future.

1.4 Quantitative Structure Activity Relationships (QSAR)

Quantitative Structural-Activity Relationships (QSAR) are statistical models used to correlate molecular descriptors to activity related descriptors. In terms of chemistry, this could be things like frontier molecular orbital energies and charge relating to the calculated energy span of the reaction. The use of QSAR models increases the efficiency of research and allows for a deeper level of understanding of the relationship between descriptors and the target.[101] The descriptors are the chemical properties that are extracted and tested for correlation to the target. The target is the value that you want to predict using the descriptors, for example, the energetic span is a popular target in computational chemistry.

There are a variety of different methodologies used within QSAR. One method is univariate linear regression. This is a simple $y = mx + c$ model which maps each descriptor to the target. Oftentimes, this is not complex enough for modelling in catalysis as multiple steric and electronic properties contribute towards their reactivity. A more popular choice is multivariate linear regression. This model predicts the correlation between multiple descriptors and the target as each descriptor has its own coefficient ($y = m_1x_1 + m_2x_2\ldots + m_nx_n + c$). The model changes the coefficients until the loss function is minimised, at which point it converges.[102] Both of these methods are examples of liner regression models.

In linear regression, model parameters are determined by minimising a loss function. The loss function measures the difference between predicted and observed values, and regression models optimise their parameters by minimising this error across the dataset. In linear regression, the most common loss function is the sum of squared errors between predicted and actual values. Model performance is commonly evaluated using the coefficient of determination (R^2), which measures how well the model explains variance in the data. When evaluating the R^2 value, the closer it is to 1, the more correlated a model is predicted to be.[101]

However, R^2 increases as more descriptors are added, often leading the user to misjudge the correlation and overfit data. Therefore, an adjusted R^2 value is often preferred as it penalises unnecessary model complexity. Another common metric is the root mean squared error (RMSE), which shows how far, on average, the model's predictions are from the actual values, using the same units as the property being predicted. As RMSE increases when prediction error grows, it can highlight cases where additional descriptors lead to overfitting rather than genuine improvement in model performance.[101]

One example of where QSAR models have been employed in catalysis, is in the study on metallocene catalysts by Yan *et al*.[103] This study demonstrated how catalyst performance can be predicted using a range of descriptors obtained from reaction intermediates and transition states. By correlating these descriptors with catalytic activity, polymer molecular weight, and comonomer insertion rates, machine learning models were able to design improved catalysts that were subsequently validated experimentally, illustrating the potential of QSAR-driven catalyst optimisation.

This study aims to utilise QSAR to begin to explore which catalytic properties are driving the activity of Group 13 homogeneous catalysts. Thereby, providing a platform for future catalyst design.

1.5 Aims and Objectives

This project aimed to break the conventional thinking behind group 13 catalysis. A solid theoretical understanding of heavier group 13 catalysts was obtained by employing computational methodologies (discussed in Chapter 2) such as DFT and quantum theory of atoms in molecules (QTAIM).

In collaboration with the Whiteoak group, two studies focused on catalysts where the Ga and In congeners were more active than smaller Al. The elucidation of the reaction mechanisms for these catalysts provided insight into their differing activity in comparison to Al. Post-DFT analysis and descriptors, in the form of QTAIM, the fluoride ion affinity (FIA), global electrophilicity index (GEI), and more were used to support DFT calculations and give further insight into the calculated energies and observed reactivity. This understanding contributed towards a shift in perception that the more Lewis acidic a catalyst is, the more active it will be.

Expanding on this, a data analysis study utilising quantitative structure-activity relationships (QSAR) provided an increased understanding of the complex links between computed catalyst descriptors and a catalyst's activity (energy span of the reaction). This provided a starting point for the curation of a larger data set of catalysts so that machine learning methodologies could be utilised.

This thesis aimed to provide the following new contributions to knowledge:

1. Utilisation of DFT for elucidation of novel reaction mechanisms for the cycloaddition of CO_2 and strained 3-membered heterocycles catalysed by group 13 catalysts.
2. Use of post-DFT analysis to develop a thorough understanding of the heavier group 13 metals (Ga and In) catalyst activity in comparison to their Al congeners.
3. Utilisation of QSAR to develop a set of catalyst design rules which predict the catalyst properties that contribute the most to the catalytic activity.

1.5 References

1 Global Monitoring Laboratory - Carbon Cycle Greenhouse Gases, https://gml.noaa.gov/ccgg/trends/global.html, (accessed 27 December 2022).

2 B. Metz, O. Davidson, H. de Coninck, M. Loos and L. Meyer, *IPCC Special Report: Carbon Dioxide Capture and Storage*, Cambridge Univ. Press, 2005.

3 Deed - Attribution-NonCommercial-NoDerivatives 4, https://creativecommons.org/licenses/by-nc-nd/4.0/, (accessed 21 January 2026).

4 C. Le Quéré, R. M. Andrew, J. G. Canadell, S. Sitch, J. I. Korsbakken, G. P. Peters, A. C. Manning, T. A. Boden, P. P. Tans, R. A. Houghton, R. F. Keeling, S. Alin, O. D. Andrews, P. Anthoni, L. Barbero, L. Bopp, F. Chevallier, L. P. Chini, P. Ciais, K. Currie, C. Delire, S. C. Doney, P. Friedlingstein, T. Gkritzalis, I. Harris, J. Hauck, V. Haverd, M. Hoppema, K. Klein Goldewijk, A. K. Jain, E. Kato, A. Körtzinger, P. Landschützer, N. Lefèvre, A. Lenton, S. Lienert, D. Lombardozzi, J. R. Melton, N. Metzl, F. Millero, P. M. S. Monteiro, D. R. Munro, J. E. M. S. Nabel, S. Nakaoka, K. O'Brien, A. Olsen, A. M. Omar, T. Ono, D. Pierrot, B. Poulter, C. Rödenbeck, J. Salisbury, U. Schuster, J. Schwinger, R. Séférian, I. Skjelvan, B. D. Stocker, A. J. Sutton, T. Takahashi, H. Tian, B. Tilbrook, I. T. van der Laan-Luijkx, G. R. van der Werf, N. Viovy, A. P. Walker, A. J. Wiltshire and S. Zaehle, *Earth Syst. Sci. Data*, 2016, **8**, 605–649.

5 HM Government, *The UK Carbon Capture Usage and Storage deployment pathway; an Action Plan*, 2018.

6 Y. Yan, T. N. Borhani, S. G. Subraveti, K. N. Pai, V. Prasad, A. Rajendran, P. Nkulikiyinka, J. O. Asibor, Z. Zhang, D. Shao, L. Wang, W. Zhang, Y. Yan, W. Ampomah, J. You, M. Wang, E. J. Anthony, V. Manovic and P. T. Clough, *Energy Environ. Sci.*, 2021, **14**, 6122–6157.

7 F. Nath, M. N. Mahmood and N. Yousuf, *Geoenergy Sci. Eng.*, 2024, **238**, 212726.

8 A. Raza, R. Gholami, R. Rezaee, V. Rasouli and M. Rabiei, *Petroleum*, 2019, **5**, 335–340.

9 G. Ben, D. Guo, Z. Tang, L. Che, M. Zhou, Y. Liu, H. Li, X. Liu, C. Zhang, L. Bai, D. Guo, H. Wang and L. Liu, *Ind. Eng. Chem. Res.*, 2024, **63**, 5889–5900.

10 D. Chakraborty, R. Chatterjee, S. Mondal, S. K. Das, V. Amoli, M. Cho and A. Bhaumik, *ACS Appl. Mater. Interfaces*, 2023, **15**, 48326–48335.

11 H. Pan, C. Yu, X. Suo, L. Yang, X. Cui and H. Xing, *Mater. Chem. Front.*, 2023, **7** 6463–6482.

12 P. Markewitz, W. Kuckshinrichs, W. Leitner, J. Linssen, P. Zapp, R. Bongartz, A. Schreiber and T. E. Müller, *Energy Environ. Sci.*, 2012, **5**, 7281–7305.

13 S. Sung and M. P. Suh, *J. Mater. Chem. A Mater.*, 2014, **2**, 13245–13249.

14 T. Kuramochi, A. Ramírez, W. Turkenburg and A. Faaij, *Prog. Energy Combust. Sci.*, 2012, **38**, 87–112.

15 Z. Qiao, Z. Wang, C. Zhang, S. Yuan, Y. Zhu and J. Wang, *AIChE J.*, 2012, **59**, 215–228.

16 C. Song, L. Run, Q. Liu, S. Deng, H. Li and J. Sun, *Carbon Capture Sci. Technol.* 2024, **13**, 100249.

17 R. M. Cuéllar-Franca and A. Azapagic, *J. CO2 Util.*, 2015, **9**, 82–102.

18 K. R. Simonsen, D. S. Hansen and S. Pedersen, *Renewable Sustainable Energy Rev.*, 2024, **191**, 114149.

19 W. Feng, C. Cao, L. Hejuan, Z. Hou, F. Mehmood and J. Liao, *Energies (Basel).*, 2020, **13**, 1–45.

20 J. T. Birkholzer, Q. Zhou and C.-F. Tsang, *Int. J. Greenhouse Gas Control*, 2009, **3**, 181–194.

21 M. A. Barrufet, A. Bacquet and G. Falcone, *J. Can. Pet. Technol.*, 2010, **49**, 23–31.

22 S. Bachu, *Int. J. Greenhouse Gas Control*, 2007, **1**, 374–385.

23 P. G. Brewer, G. Friederich, E. T. Peltzer and F. M. Orr, *Science (1979).*, 1999, **284**, 943–945.

24 K. Z. House, D. P. Schrag, C. F. Harvey and K. S. Lackner, *Proc. Natl. Acad. Sci.* 2006, **103**, 12291–12295.

25 P. Anastas and N. Eghbali, *Chem. Soc. Rev.*, 2010, **39**, 301–312.

26 P. Styring, D. Jansen, H. de Coninck, H. Reith and K. Armstrong, *Carbon Capture and Utilisation in the green economy*, 2011.

27 M. Faisal, in *Green Sustainable Process for Chemical and Environmental Engineering and Science*, eds. Dr. Inamuddin and T. Altalhi, Elsevier, 2023, pp. 85–118.

28 H. Kolbe, *Justus Liebigs Ann. Chem.*, 1860, **113**, 125–127.

29 R. Schmitt, *J. Prakt. Chem.*, 1885, **31**, 397–411.

30 O. Mohammad, J. A. Onwudili and Q. Yuan, *RSC Sustain.*, 2023, **1**, 404–417.

31 T. Iijima and T. Yamaguchi, *J. Mol. Catal. A Chem.*, 2008, **295**, 52–56.

32 C. Friedel and J. M. Crafts, *C. R. Seances Acad. Sci.*, 1877, **84**, 1392–1395.

33 L. Shen, D. J. Jacob, R. Gautam, M. Omara, T. R. Scarpelli, A. Lorente, D. Zavala-Araiza, X. Lu, Z. Chen and J. Lin, *Nat. Commun.*, DOI:10.1038/s41467-023-40671-6.

34 N. Yusuf, F. Almomani and H. Qiblawey, *Fuel*, 2023, **345**, 128178.

35 S. Wai, Y. Ota, M. Sugiyama and K. Nishioka, *Applied Sciences*, 2020, **10**, 1–12.

36 J. K. Nganga, L. M. Wolf, K. Mullick, E. Reinheimer, C. Saucedo, M. E. Wilson, K. A. Grice, M. Z. Ertem and A. M. Angeles-Boza, *Inorg. Chem.*, 2021, **60**, 3572–3584.

37 W.-G. Cui, X.-Y. Zhuang, Y.-T. Li, H. Zhang, J.-J. Dai, L. Zhou, Z. Hu and T.-L. Hu, *Appl. Catal. B*, 2021, **287**, 119959.

38 J. Barrio, D. Mateo, J. Albero, H. García and M. Shalom, *Adv. Energy Mater.*, 2019, **9**, 1902738.

39 T. Chwoła, T. Spietz, L. Więcław-Solny, A. Tatarczuk, A. Krótki, S. Dobras, A. Wilk, J. Tchórz, M. Stec and J. Zdeb, *Fuel*, 2020, **263**, 116804-.

40 J. Kothandaraman, J. Saavedra Lopez, Y. Jiang, E. D. Walter, S. D. Burton, R. A. Dagle and D. J. Heldebrant, *ChemSusChem*, 2021, **14**, 4812–4819.

41 H. T. Kennedy, *Newstex*, 2021, preprint.

42 B. A. Fayisa, Y. Yang, Z. Zhen, M.-Y. Wang, J. Lv, Y. Wang and X. Ma, *Ind. Eng. Chem. Res.*, 2022, **61**, 10319–10335.

43 S. K. Sharma, A. Banerjee, B. Paul, M. K. Poddar, T. Sasaki, C. Samanta and R. Bal, *Journal of CO2 Utilization*, 2021, **50**, 101576.

44 A. P. C. Ribeiro, L. M. D. R. S. Martins and A. J. L. Pombeiro, *Green Chem.*, 2017, **19**, 4811–4815.

45 F. K. Scharnagl, M. F. Hertrich, G. Neitzel, R. Jackstell and M. Beller, *Adv. Synth. Catal.*, 2019, **361**, 374–379.

46 D. S. Marlin, E. Sarron and Ó. Sigurbjörnsson, *Front. Chem.*, 2018, **6**, 446.

47 G. Ondrey, *Athena Information Solutions Pvt. Ltd*, 2021, preprint.

48 W. Meiser and C. Bosch, 1922.

49 J. Yuan, L. Hu, J. Huang, Y. Chen, S. Qiao and H. Xie, *Appl. Catal. B*, 2023, **339**, 123146.

50 A. A. Marciniak, K. J. Lamb, L. P. Ozorio, C. J. A. Mota and M. North, *Curr. Opin. Green Sustain. Chem.*, 2020, **26**, 100365.

51 J. Nemirowsky, *J. für Prakt. Chemie*, 1883, **28**, 439–440.

52 S. Kirsner, How a biofuel dream turned into a nightmare, https://www.bostonglobe.com/business/2017/09/01/how-biofuel-dream-turned-into-nightmare/rt5ve7mE4YUZUOrqdaTqWK/story.html, (accessed 20 August 2024).

53 S. P. and S. K. Mandal, *Chem. Sci.*, 2020, **11**, 10571–10593.

54 M. F. Mukhtar Gunam Resul, A. Rehman, F. Saleem, M. Usman, A. M. López Fernández, V. C. Eze and A. P. Harvey, *RSC Adv.*, 2023, **13**, 32940–32971.

55 X. Yang, M. Guo, X. Wang, W. Huan and M. Li, *ACS Omega*, 2020, **5**, 28918–28928.

56 E. Louisy, V. Khodyrieva, S. Olivero, V. Michelet and A. Mija, *Chempluschem*, DOI:10.1002/cplu.202200190.

57 Number of publications for the search term ‘CO2 Cyclic Carbonates’, https://app.dimensions.ai/discover/publication?search_mode=content&search_text=CO2 cyclic

carbonates&search_type=kws&search_field=full_search, (accessed 21 August 2024).

58 A. Rehman, F. Saleem, F. Javed, A. Ikhlaq, S. W. Ahmad and A. Harvey, *J. Environ. Chem. Eng.*, 2021, **9**, 105113.

59 V. Mishra and S. C. Peter, *Chem Catalysis*, 2024, **4**, 100796.

60 R. D. Lewis, M. D. G. Billacura, A. Hamilton and C. J. Whiteoak, in *Organometallic Chemistry: Volume 45*, Royal Society of Chemistry, 2024.

61 K. A. Andrea and F. M. Kerton, *ACS Catal.*, 2019, **9**, 1799–1809.

62 R. R. Shaikh, S. Pornpraprom and V. D'Elia, *ACS Catal.*, 2018, **8**, 419–450.

63 G. Fiorani, W. Guo and A. W. Kleij, *Green Chemistry*, 2015, **17**, 1375–1389.

64 A. Kilic, E. Yasar and E. Aytar, *Sustain. Energy Fuels*, 2019, **3**, 1066–1077.

65 Z. Xue, X. Zhao, J. Wang and T. Mu, *Chem. Asian J.*, 2017, **12**, 2271–2277.

66 A. Gonzalez-Vargas, F. Castro-Gómez and P. J. Castro, *ChemistrySelect*, 2021, **6**, 7489–7498.

67 R. G. S. Berlinck, in *Comprehensive Natural Products III*, eds. H.-W. (Ben) Liu and T. P. Begley, Elsevier, Oxford, 2020, pp. 237–243.

68 Y. Fu, Y. Zhang, C. Hu and Z. Su, *New J. Chem.*, 2023, **48**, 920–932.

69 J. Xu, A. Xian, Z. Li, J. Liu, Z. Zhang, R. Yan, L. Gao, B. Liu, L. Zhao and K. Guo, *J. Org. Chem.*, 2021, **86**, 3422–3432.

70 F. Della Monica and C. Capacchione, *Asian J. Org. Chem.*, DOI:10.1002/ajoc.202200300.

71 S. A. Kuznetsova, I. V. Gorodishch, A. S. Gak, V. V. Zherebtsova, I. S. Gerasimov, M. G. Medvedev, D. K. Kitaeva, E. A. Khakina, M. North and Y. N. Belokon, *Tetrahedron*, 2021, **82**, 131929.

72 J. Kiriratnikom, N. Laiwattanapaisarn, K. Vongnam, N. Thavornsin, P. Sae-Ung, S. Kaeothip, A. Euapermkiati, S. Namuangruk and K. Phomphrai, *Inorg. Chem.*, 2021, **60**, 6147–6151.

73 X. Wu and M. North, *ChemSusChem*, 2017, **10**, 74–78.

74 W. Clegg, R. W. Harrington, M. North and R. Pasquale, *Chem. - Eur. J.*, 2010, **16** 6828–6843.

75 T. T. Wang, Y. Xie and W. Q. Deng, *J. Phys. Chem. A*, 2014, **118**, 9239–9243.

76 A. P. C. Ribeiro, P. Goodrich and L. M. D. R. S. Martins, *Molecules*, DOI:10.3390/molecules26041089.

77 M. Navarro, A. Garcés, L. F. Sánchez-barba, D. González-lizana and A. Lara-sánchez, *Dalton Trans.*, 2023, 6105–6116.

78 M. Navarro, L. F. Sánchez-barba, A. Garcés, J. Fernández-baeza and I. Fernández, *Catal.:Sci. Technol.*, 2020, 3265–3278.

79 F. Della Monica, S. V. C. Vummaleti, A. Buonerba, A. De Nisi, M. Monari, S. Milione, A. Grassi, L. Cavallo and C. Capacchione, *Adv. Synth. Catal.*, 2016, **358**, 3231–3243.

80 C. J. Whiteoak, N. Kielland, V. Laserna, F. Castro-Gõmez, E. Martin, E. C. Escudero-Adán, C. Bo and A. W. Kleij, *Chem. - Eur. J.*, 2014, **20**, 2264–2275.

81 F. Castro-Gómez, G. Salassa, A. W. Kleij and C. Bo, *Chem. - Eur. J.*, 2013, **19**, 6289–6298.

82 A. Decortes, M. Martínez Belmonte, J. Benet-Buchholz and A. W. Kleij, *Chem. Commun.*, 2010, **46**, 4580–4582.

83 M. Tahoun, C. T. Gee, V. E. McCoy, P. M. Sander and C. E. Müller, *RSC Adv.*, 2021, **11**, 7552–7563.

84 B. N. Cabral, J. L. S. Milani, A. M. Meireles, D. C. da S. Martins, S. L. da S. Ribeiro, J. S. Rebouças, C. L. Donnici and R. P. das Chagas, *New Journal of Chemistry*, 2021, **45**, 1934–1943.

85 D. Bai, S. Duan, L. Hai and H. Jing, *ChemCatChem*, 2012, **4**, 1752–1758.

86 Q. Wang, C. H. Guo, J. Jia and H. S. Wu, *J. Mol. Model.*, 2015, **21**, 1–9.

87 Y. Chen, R. Luo, Q. Xu, W. Zhang, X. Zhou and H. Ji, *ChemCatChem*, 2017, **9**, 767–773.

88 K. Wang, J. Horlyck, N. An and A. Voutchkova-Kostal, *Green Chemistry*, 2024, **26** 3546–3564.

89 S. E. Maier, T. Nagel, M. Turan, E. Kaya, W. Frey, M. Dyballa and D. P. Estes, *Organometallics*, 2024, **43**, 233–241.

90 R. Ye, A. V. Zhukhovitskiy, C. V. Deraedt, F. D. Toste and G. A. Somorjai, *Acc. Chem. Res.*, 2017, **50**, 1894–1901.

91 T. A. Zevaco, A. Janssen, J. Sypien and E. Dinjus, *Green Chemistry*, 2005, **7**, 659–666.

92 D. J. Darensbourg and D. R. Billodeaux, *Comptes Rendus Chimie*, 2004, **7**, 755–761.

93 I. Shibata, I. Mitani, A. Imakuni and A. Baba, *Tetrahedron Lett.*, 2011, **52**, 721–723.

94 H. A. Baalbaki, H. Roshandel, J. E. Hein and P. Mehrkhodavandi, *Catal. Sci. Technol.*, 2021, **11**, 2119–2129.

95 L. Álvarez-Miguel, J. D. Burgoa, M. E. G. Mosquera, A. Hamilton and C. J. Whiteoak, *ChemCatChem*, 2021, **13**, 4099–4110.

96 M. D. G. Billacura, R. D. Lewis, N. Bricklebank, A. Hamilton and C. J. Whiteoak, *Adv. Synth. Catal.*, 2023, **365**, 3129–3137.

97 D. J. Cabrera, R. D. Lewis, C. Díez-Poza, L. Álvarez-Miguel, M. E. G. G. Mosquera, A. Hamilton and C. J. Whiteoak, *Dalton Trans.*, 2023, **52**, 5882–5894.

98 J. Damián Burgoa, L. Álvarez-Miguel, M. E. G. Mosquera, A. Hamilton and C. J. Whiteoak, *Inorg. Chem.*, 2024, **63**, 15376–15387.

99 D. J. Cabrera, R. D. Lewis, C. Díez-Poza, L. Álvarez-Miguel, M. E. G. G. Mosquera, A. Hamilton and C. J. Whiteoak, *Dalton Transactions*, 2023, **52**, 5882–5894.

100 C. Goonesinghe, H. Jung, I. O. Betinol, J. R. Gaffen, C. N. Garrard, J. Chang, K. Hosseini, H. Roshandel, K. Nyamayaro, B. Patrick, M. Ezhova, C. B. Caputo, T. Baumgartner, J. P. Reid and P. Mehrkhodavandi, *ACS Catal.*, 2023, **13**, 16148–16157.

101 K. Fenner and P. G. Tratnyek, *Environ. Sci. Process. Impacts*, 2017, **19**, 185–187.

102 A. F. Zahrt, S. V. Athavale and S. E. Denmark, *Chem. Rev.*, 2020, **120**, 1620–1689.

103 B. Yan, S. Wang, X. Gui, X. Xing, Q. Guo, C. Cao, J. Li and T. Jiang, *J. Catal.*, 2025, **452**, 116447.

Chapter 2 – Methodology

2.1 Density Functional Theory

2.1.1 Theoretical Introduction

Since the foundational work of Hohenberg, Kohn and Sham in 1964-65,[1,2] Density Functional Theory (DFT) has become a versatile tool within chemistry. DFT elucidates the ground state energy (E_0) of a many-bodied system through approximation of the Schrödinger equation (Eq. 1). The Schrödinger equation is a fundamental expression in quantum mechanics providing insight into the electronic structure of atoms and molecules. In DFT, the many electron wavefunction is replaced by the electron density, which depends only on three spatial variables rather than the 3N variables required for N electrons, greatly reducing computational complexity.

Despite a reduction in complexity, DFT calculations can produce accurate results at a relatively low computational cost, even for larger molecular systems. The computational simplicity allows for the lower cost, however DFT is able to maintain an acceptable level of accuracy by incorporating exchange and correlation effects through carefully developed functionals that approximate electron–electron interactions.[1,3] This nature of DFT makes it applicable to a broad range of problems in chemistry, from elucidating reaction mechanisms,[4] predicting spectroscopic properties,[5] in materials science,[6] to understand biological systems,[7] astrochemistry[8] and for applied machine learning.[9]

$$H\varphi = E_0\varphi \qquad \text{Eq. 1}$$

Hohenberg-Kohn-Sham DFT was derived from Hartree-Fock (HF) theory.[10–12] HF theory takes an exact non-empirical approach, where the wavefunction is represented as a N slater determinant's for every N electrons a molecule contains. As a slater determinant only accounts for exchange energy (without modification) HF theory does not account for correlation energy. The Exchange energy arises because electrons with the same spin tend to avoid each other,

reducing electron repulsion. Correlation energy accounts for the additional avoidance between electrons due to their mutual repulsion that is not captured in simpler models. This leads to inaccuracies in calculations making it unsuitable for most chemical systems.[13] To overcome this, several post-HF calculations were developed. Below are descriptions of three theories:

Møller-Plesset (MP) pertubation theory - MP perturbation theory expands on HF theory by taking a perturbative approach to include the electron correlation. This means, the theory first takes a simple approximation and takes small stepwise corrections leading to a more accurate prediction. This method provides a bridge between the lesser accurate HF and the higher-level methods discussed next.[14]

Configuration Interaction (CI) theory – CI theory takes a more accurate approach towards the exact wavefunction by calculating the correlation energy through a linear combination of Slater determinants. The correlation energy can be calculated with single excitations (CIS), single and double excitations (CISD) and all excitations in the full configuration (FCI). While this method can be extremely accurate, the combinatorial nature of it makes it very expensive for larger systems.[15,16]

Coupled Cluster (CC) theory – CC theory expands on CI theory by adding an exponential term into the wavefunction. This provides a more accurate description of the correlation energy. CC theory, like CI theory, can compute the correlation energy with respect to single and double excitations (CCSD) and also single, double and triple excitations (CCSD(T)); where the “T” is bracketed due to triple excitations are calculated perturbatively.[17] CCSD(T) is renowned as the “golden standard” in computational chemistry.[18]

Due to the higher accuracy of these methods, the computational cost for an increasing number of electrons/atoms becomes exponentially large. As a result, an alternative method was needed which provided a reasonable level of accuracy at low computational cost; Hohenberg, Kohn and Sham solved this problem. Hohenberg and Kohn produced two theorems to describe how the electron density could be used as a function to derive the ground state energy. This led towards the subsequent Kohn-Sham equations.

The first theory presented by Hohenberg and Kohn stated that all the ground state properties of a system could be determined by the electron density ($\rho(r)$) (Eq. 2). Therefore, both the ground-state wavefunction and ground-state energy are uniquely determined by the electron density.

$$\rho(r)_0 \propto \varphi_0 \propto E_0 \qquad \text{Eq. 2}$$

The second theory of Hohenberg and Kohn feeds directly into the practical application of DFT. It is known as the variational principle and states that E_0 is minimized by the ground state electron density ($\rho(r)_0$) across an external potential ($v_{ext}\rho$), meaning the calculated energy is always higher than the exact energy $E_0 > E_{exact}$. Practically, this means the ground state energy can be calculated by iteratively lowering $\rho(r)_0$ across the external potential. Following this, the Kohn-Sham equation were developed (Eq. 3).[1,19]

$$E_0 ¿ E(\rho)_{min} = T_0(\rho) + \int v_{ext}\rho + J(\rho) + E_{xc} \qquad \text{Eq. 3}$$

The equation consists of the kinetic energy ($T_0(\rho)$), the interaction energy with the external potential ($v_{ext}\rho$), the classic Coulomb electron repulsion energy ($J(\rho)$) and the exchange-correlation energy (E_{xc}). The E_{xc} term is the negative energy relating to electron correlation energy (E_c) and electron exchange energy (E_x). The E_x term is the dominant term and represents the energy which arises because of the Pauli exclusion principle. The E_c term arises from the dynamic correlations between electrons which induces repulsion and means electrons avoid each other. This repulsion between the electrons typically lowers the energy of the system but less so than E_x.[19–21]

Although E_{xc} can theoretically be calculated exactly, in the same way as the Schrödinger equation, it would be impractical for most chemical problems even with large computing resources. For this reason, approximations need to be made to be able to calculate E_{xc} at a good accuracy to cost ratio. These approximations are one of the fundamentals which gives DFT its accuracy and low cost. The approximations are called density functionals.

2.1.2 Density Functionals

Density functionals provide an approximation to E_{xc}. The functionals are grouped by accuracy according to their accuracy in a hierarchical Jacob's ladder (Figure 2.1).[20] The accuracy of the approximations increases as you climb the ladder through computational systematic improvements by adding additional physical parameters. However, this comes with a penalty of computational cost. When choosing a method, considerations of accuracy, cost and suitability for the system of interest need to be kept in mind. A basic overview of each rung of the ladder is presented below.

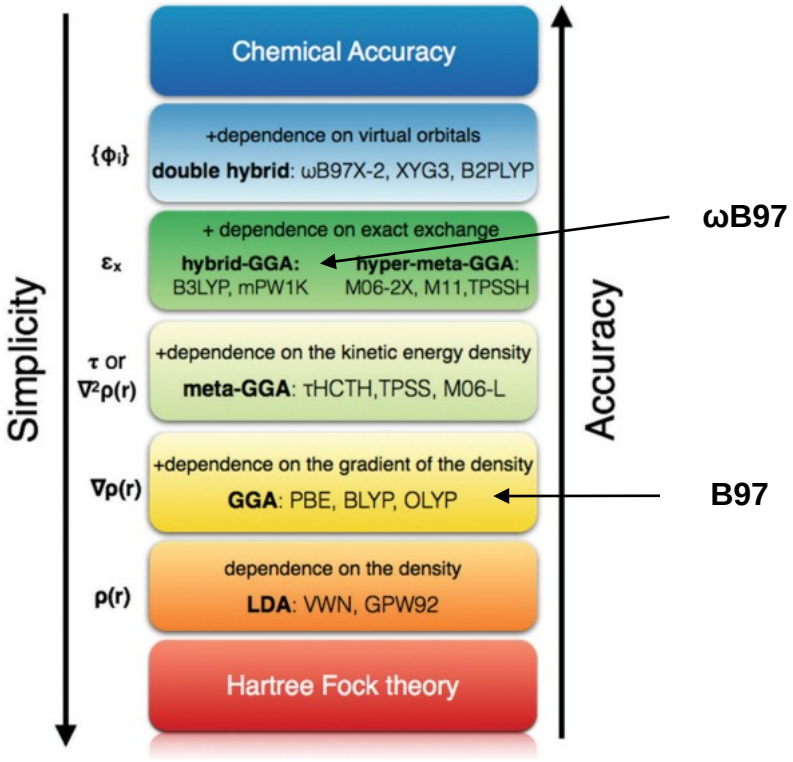

Figure – Methodology.31 - Jacob's ladder of hierarchy of density functionals adapted from 26. The B97 and ωB97 functional are used in the work presented in chapters 3-5.[20,22–25]

Despite the systematic improvements offered by higher rungs of Jacob's ladder, density functional approximations still exhibit known limitations. Many functionals suffer from self-interaction error, which can lead to incorrect electron delocalisation and inaccurate reaction energies. In addition, dispersion interactions are poorly described without empirical correction schemes, and systems involving strong electron correlation or charge transfer can remain challenging to model accurately. Consequently, careful functional selection and validation remain essential when applying DFT to catalytic systems.[26]

2.1.2.1 Local Density Approximation

The local density approximation (LDA) is the simplest group of density functionals. Kohn-Sham developed this approximation in their seminal paper.[1] The premise of these functionals is calculating E_{xc} by using the exchange-correlation energy density of a uniform electron gas (Eq. 4).

$$E_{xc}^{LDA}[\rho] = \int \rho \epsilon_{xc}(\rho) d^3 r \qquad \text{Eq. 4}$$

Two approximations other than the original Kohn-Sham functional are the Perdew-Zunger (PZ81) and the Vosko-Wilk-Nusair (VWN) functionals.[27,28] As these methods are fairly primitive, their accuracy remains low when describing larger systems because density does not stay uniform across a molecule, but in fact varies. As it does not account for this, it therefore leads to a poor approximation.

2.1.2.2 Generalised-Gradient Approximation

To address the issue of non-uniformity in LDAs, generalised gradient approximations (GGA) include density gradients to calculate E_{xc} (Eq. 5). The LDA approximation only considers the local electron densities ($p_\uparrow(r), \rho_\downarrow(r)$), whereas the GGA approximation includes the gradients of these densities ($\nabla p_\uparrow(r), \nabla \rho_\downarrow(r)$). The accuracy of GGA functionals significantly increases on LDA functionals for bonding. This is because density varies heavily in regions of bonding, therefore measuring this gradient is significant. Despite the inclusion of this extra term, there is no dramatic increase in computational cost, making this a good class of functionals for geometry optimisation.

$$E_{xc}^{GGA}[p_\uparrow, \rho_\downarrow] = \int \rho(r) \epsilon_{xc}(p_\uparrow(r), \rho_\downarrow(r), \nabla p_\uparrow(r), \nabla \rho_\downarrow(r)) d^3 r \qquad \text{Eq. 5}$$

There are a number of notable GGA approximations commonly employed in DFT calculations. The non-empirical Perdew-Burke-Ernzerhof (PBE) functional is known to give a good accuracy to computational cost balance.[29] This functional was an extension of the Perdew-Wang (PW91) functional.[30] PBE was superior to PW91 as it could better describe the uniform electron gas and modelled the correct behaviour under uniform scaling.

Another popular GGA functional is Becke's B97.[31] This takes a semi-empirical approach to solving E_{xc}. The semi-empirical approach makes B97 an excellent functional to predict certain properties such as ionisation energies, however, as

the functional is partly fitted to a set of empirical data, some systems yield poor results if they are beyond the scope of the empirical parameters.

The Becke exchange functional (B88) and Lee-Yang-Parr correlation functional (LYP) account for the E_x and E_c terms individually.[32,33] The terms for this reason are normally partnered with each other or another exchange/correlation functional. The combination of B88/LYP functionals is not an overly common choice. However, these functionals laid the foundation for the highly popular B3LYP hybrid functional.

2.1.2.3 Meta-GGA

At the third rung, Meta-GGA approximations improve on GGA through the inclusion of additional parameters such as the kinetic energy density (Eq. 6). Like the LDA to GGA jump, there is good increase in the level of accuracy with a minimal penalty on computational cost. The increase in accuracy makes this set of functionals more applicable for calculation of atomisation energies and barrier heights. A few examples of common functionals are given below:

$$E_{xc}^{GGA}\left[p_{\uparrow},\rho_{\downarrow},\tau\right]=\int \rho(r)\epsilon_{xc}\left(p_{\uparrow}(r),\rho_{\downarrow}(r),\nabla p_{\uparrow}(r),\nabla \rho_{\downarrow}(r),\tau(r)\right)d^3r \qquad \text{Eq. 6}$$

Tao-Perdew-Staroverov-Scuseria developed the TPSS functional.[22] This is a non-empirical functional inclusive of the kinetic energy term. It is commonly used in reaction mechanism chemistry with good calculated molecular structures and energy spans.

There are a family of meta-GGA functionals known as the Minnesota functionals developed by Truhlar and Zhao.[34]. They were developed to have a balanced performance across all aspects of computational chemistry such as thermochemistry, kinetics, noncovalent interactions and transition metal chemistry and benchmarked against large datasets.[35] They have a specific coded naming system (MX-Y) where M represents that it is part of the Minnesota family. X is the year it is developed and Y represents optional modifiers to the functional.[36]

A few common examples are the M06-L which is a meta-gga functional. The L tells us it is only a local functional with 0% HF exchange. Another variation is the M06 functional which is a hybrid meta-GGA functional and without the L modifier

contains around 27% HF exchange. The Minnesota functionals appear across all rungs of the Jacob's ladder and are a popular choice in computational chemistry.

2.1.2.4 Hybrid Functionals

Hybrid functionals begin to move into different territory. Unlike the previous rungs, hybrid functionals utilise both exact and approximate solutions to E_{xc}. As a result of this, the computational cost significantly rises for these functionals with a jump in accuracy. It is worth noting that despite the increase in computational costs, hybrid functional calculations remain cheaper than high-level ab-initio methods.

Hybrid density functionals incorporate a fraction of exact exchange energy from Hartree–Fock (HF) theory into the DFT exchange–correlation functional. In single hybrid functionals, HF exchange is mixed with DFT exchange, while the correlation part remains entirely DFT-based. In contrast, double hybrid functionals go further by also incorporating a portion of second-order perturbation theory correlation energy, in addition to exact exchange, thereby improving the accuracy of both the exchange and correlation components.[37]

PW6B95 is a single hybrid functional based on empirical parameters.[38] It is notable in areas of thermochemistry and kinetics. This functional uses the Perdew-Wang exchange approximation coupled with exact Hartree-Fock exchange. The functional calculates the correlation energies using approximation from the B95 functional.

One of the most popular functionals used in computational chemistry is the B3LYP single hybrid functional. which became popular due to its reliable performance across many molecular systems while maintaining moderate computational cost. However, although B3LYP remains widely used for historical and comparative reasons, it is known to struggle with dispersion interactions and some transition-metal and noncovalent systems, meaning newer functionals are often preferred for modern catalytic studies.[39] A combination of the Becke exchange energy with the Lee-Yang-Parr correlation energy is used to calculate E_{xc}.[40] Similar to PW6B95, this functional uses 28% Hartree-Fock exchange energy.

The ωB97X-D functional, developed by Head-Gordon *et al*. is a range separated single hybrid functional. It accounts for long range and short-range exchange energies with different methods.[41] Short range exchange energies are dealt with

DFT and longer-range interactions with HF. The functional also makes use of a dispersion correction which is discussed in section 2.1.2.6.

Finally, B3PLYP is a double hybrid functional that combines single hybrid methodology (part DFT exchange energy; part HF exchange energy) with a second order perturbation correlation energy.[42] This method can accurately describe barrier heights and non-covalent interactions, but at a high computational cost.

2.1.2.5 Higher Level Methods

While high-level methods like CCSD(T) have historically been too computationally intensive for routine mechanistic studies, recent developments such as the domain local pair natural orbital coupled cluster (DLPNO-CCSD(T)) framework have significantly reduced the cost.[43] By utilising pair natural orbitals to include triple excitations DLPNO-CCSD(T) is able to retain the accuracy of CCSD(T) but at a scaling of N^3-N^4 in comparison to N^7.

2.1.2.6 Additional Considerations

DFT methods have limitations with describing Van der Waals forces. Van der Waals forces are weak attractive interactions between molecules or atoms that arise from temporary or induced dipoles by a shift in electron distribution. For large structures that are reliant on these forces to work, some functionals alone would not be accurate enough. The Grimme dispersion correction can help overcome these inadequacies. Grimme's dispersion correction is an empirical method added to density functional calculations to account for long-range dispersion interactions that are not well described by many standard density functionals. Grimme's dispersion correction accounts for long-range dispersion interactions by adding an empirical energy term that decays with interatomic distance, typically proportional to $1/r^x$, between pairs of atoms, allowing weak van der Waals attractions missing from many density functionals to be included.[42]

Initially, Grimme developed a set of dispersion functions which contain pairwise additive corrections to account for dispersion forces (D1 & D2).[42] To build on this and make a more accurate dispersion correction, Grimme added a three-body non-additive term (D3). This term incorporates both atomic coordination and bonding effects.[39,44] The D3 correction is a popular choice for DFT calculations providing a good cost to accuracy balance.

There is also the more advanced D4 term which incorporates charge-scaling within the calculation of polarizabilities. While it is more accurate than D3, it comes at a greater cost and is more suitable for heterogeneous and charged systems.[45] On top of this, the Becke-Johnson (BJ) damping term can also be added to the calculation to increase the accuracy. This adjusts for short-range dispersion corrections to avoid overestimation of these forces in high regions of electron density.[39,44]

Another class of dispersion corrections is the Vydrov-Van Voorhis 2010 correction (VV10). Unlike Grimme's corrections which use pairwise additives, this correction takes a non-empirical approach by incorporating the dispersion correction into the E_{xc} calculation using a non-local term.[46] This treatment of the dispersion correction makes the correction more accurate for weak interactions making it much more accurate. However, this comes at a larger computational cost rendering these corrections unsuitable for larger systems. Dispersion interactions may be treated through empirical pairwise corrections, non-local dispersion functionals, or functionals parametrised to reproduce dispersion effects. In this work, empirical dispersion corrections are employed.

Using the Orca 4.0 computational chemistry program, there is a predefined choice of the integration grid used in calculations.[47] The integration grid provides a spatial map between atoms so that a numerical value of the E_{xc} and its potentials between atoms can be calculated. Within Orca, as the grid number increases it becomes denser with less space between grid points. A higher grid number provides a more accurate approximation of E_{xc}.[48]

To reduce the computational cost, different integration grids can be employed for different parts of the calculation, using the notation "GridX FinalGridY". GridX would be smaller than FinalGridY. Grid X is the integration grid that is used for the early SCF iterations while the structure is converging. Once converged, the larger FinalGridY is employed to provide a more accurate final energy.[48]

Another consideration is how to account for the different solvent environments that a reaction takes place in. Solvent models can either be explicit or implicit. Explicit solvent models include molecules of solvent within the calculation. This makes them particularly useful when mechanisms include proton transfers, ion

pairing or solvent mediated reactions. These calculations, however, are computationally very expensive, so should only be utilised where necessary.[49]

Implicit solvent models are used more routinely than explicit solvent models. Two popular models are the conductor-like polarizable continuum model (CPCM) and the solvation model based on density (SMD). The CPCM model creates a solvent cavity which the solute fits within. The polarisation of the solvent is measured using a reaction field which interacts with the solute based on its charge distribution. The reaction field strength is determined by the dielectric constant of the solvent that is being modelled.[50,51] The SMD model is built on the CPCM model by including the electron density to model solute-solvent interactions and more empirical parameters.[52] This means the SMD model is more accurate than the CPCM model but comes at greater computational cost. As the CPCM model is sufficient for modelling reaction mechanisms, this will be utilised in this work.

2.1.2.7 Concluding Remarks

Section 2.1.2 has demonstrated the broad range of DFT methodology available to the user. As discussed, the main considerations taken when choosing the level of theory used are:

- Computational cost.
- Accuracy of method.
- Empirical/non-empirical – Is there a functional that is empirically designed to fit a system?
- Overall reliability – Are results consistently reliable?

While the functional is an integral part of DFT methodology for describing E_{xc}, it needs to be accompanied by a basis set. The basis set is the second important part of DFT methodology. Careful considerations need to be given to the basis set in the same way as the functionals.

In this work, the B97 and range-separated hybrid ωB97 functionals were employed together with Grimme's dispersion corrections to account for long-range van der Waals interactions. These functionals have been shown in benchmarking studies to provide reliable performance across thermochemistry, reaction energetics, and noncovalent interactions, making them suitable choices for modelling the catalytic systems investigated here. They also provide a good balance between accuracy and computational cost.[35,39]

2.1.3 Basis Sets

2.1.3.1 Theoretical Introduction

Basis sets are a set of functions which describe the molecular orbitals. Two types of basis sets exist, Slater Type Orbitals (STOs) and Gaussian Type Orbitals (GTOs) (Figure 2.2). STOs are the more accurate of the two representations of orbitals. STOs analytically solve the Schrödinger equation for 1 electron atoms (hydrogen) to achieve an exact description of the molecular orbitals. Albeit accurate, the computational demands of using STOs for DFT calculations on large systems means GTO basis sets are first choice.[53]

GTOs use a set of primitive Gaussian functions for each basis function, to represent the molecular orbitals as close as possible to STOs. Despite there being more basis functions to solve for the GTOs, they are comparatively much simpler than the STO basis functions and therefore have a lower computational cost.[53]

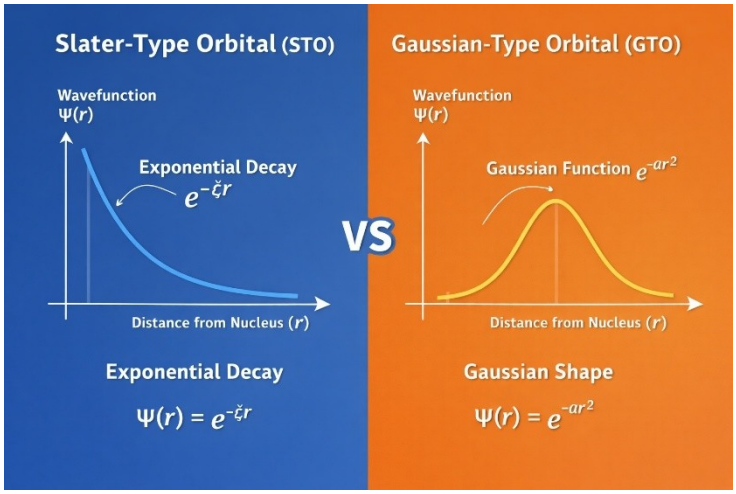

Figure – Methodology.32 - A graphical representation of the differences between an STO and GTO.

The most basic type of basis set is the minimal basis set where a single Gaussian function is used to represent each occupied atomic orbital. This representation is problematic as it does not account for orbital breathing, polarisation effects or weak interatomic interactions. Therefore, for GTO basis sets to be accurate enough for meaningful results, more sophisticated basis sets are needed to describe these effects.

Orbital breathing is the name given to the expansion and contraction of orbitals because of their chemical environment.[54] With only one Gaussian function per atomic orbital, the orbital can only be represented with a single shape. To

overcome this, more than one Gaussian function can be employed per atomic orbital. Within basis sets, this is denoted as double-zeta (two Gaussian functions), triple-zeta (three Gaussian functions) and so on.

With the addition of extra Gaussian functions per orbital, the computational cost would rapidly increase. To mitigate for this, split-valence basis sets can be employed. Using a split-double-zeta basis set as an example, the valence atomic orbitals would be described by two Gaussian functions, and the inner orbitals would be described minimally by one Gaussian function. The reduced number of functionals decreases computational cost. As the inner orbitals do not expand/contract as much as the valence orbitals, having only one Gaussian function describing them does not affect the accuracy of the calculation.[55]

Polarisation effects see orbitals deviate from an axis, which passes through the centre of an atom due to interaction with other orbitals or bonds. These functions are typically denoted by additional higher angular momentum terms, such as d or f functions, in basis set notation (e.g., 6-31G(d,p)). So, additional functions need to be added with higher angular quantum numbers. Basis sets that have these parameters are known as polarised basis sets. Diffuse functions are another parameter that can be added to basis sets, denoted by the prefix “(+)aug”. These functions allow for a better description of systems where electrons are weakly partaking in weak interactions, are not tightly bound to the nucleus or anions. These functionals include higher radial quantum numbers. They can do this as the basis functions have very small exponents, meaning the function extends far out from the nucleus. Where an atom is an anion or has weakly bound electrons, the electron density will extend further away from the nucleus than a neutral atom. Therefore, they are an important class of functions employed to increase accuracy in these cases.

A consideration when heavier atoms are included in calculations, such as transition metals, is to utilise electron core potentials (ECPs) or pseudopotentials within a basis set. ECPs are used to treat the core electrons implicitly as a potential rather than explicitly. This reduces the number of basis functions within a calculation and therefore the cost. Furthermore, they account for some relativistic effects, which is helpful for elements such as gallium and indium.[56] For this reason, ECP basis sets are to be used within this research.

A careful choice of basis set is needed to ensure the atomic orbitals are described accurately, but at a suitable computational cost. To consider the choice of basis sets, an overview of four common families of basis sets is given.

2.1.3.2 Pople's Basis sets

The Pople basis sets were one of the earlier families of basis sets, with the STO-3G was one of the earliest minimal basis set developed. It uses three Gaussian functions to approximate the Slater orbital.[57] As this is a minimal basis set, it is not accurate enough for computational calculations of complex systems. However, it paved the way for the more commonly used split valence 3-21G and 6-31G. The nomenclature of these functionals denotes how many Gaussian functions are used for each set of orbitals (X-YZG), where X is the number of functions for the core orbitals and YZ are the number of functions for the valence orbitals. These functions can also be extended to include diffuse and polarisation functions for increased accuracy.[58,59]

2.1.3.3 Dunning's Basis Sets

The Dunning correlation consistent split basis sets are designed to work with correlated wavefunctions. They systematically increase the number of functions as the size of the basis set increases to converge electron correlation effects. Dunning basis sets have the following notation CC-pVXY where XY can be DZ, TZ, QZ and 5Z. These are double, triple, quadruple and quintuple zeta basis sets respectively. Each one of these basis sets contains a set of polarisation functions and can also have additional diffuse functions if required.[60–62]

2.1.3.4 Jensen's Basis Sets

Jensen's polarisation consistent basis sets (PC-X), where X ranges from 0-4, focus on a systematic approach towards the complete basis set (CBS) limit through the consistent treatment of polarisation effects by polarisation functions. The CBS limit is the theoretical point whereby the highest accuracy a basis set has been achieved through representing a "true" solution to the Schrödinger equation. The Dunning basis sets are also set up in this manner. Jensen's basis sets can also be augmented to include diffuse functions.[63–65]

2.1.3.4 Ahlrichs Basis Sets

The split valence Ahlrichs basis sets are a popular choice in chemistry. They can adopt polarisation and diffuse functions to increase accuracy. Like Dunning's and

Jensen's basis sets, there is a hierarchy of basis set accuracy towards the CBS limit. Using the form of the more accurate second-generation basis sets, the general connotation used is def2-XVP where X = single (S), triple zeta (TZ) and quadruple zeta (QZ). As with previous mentioned basis sets, diffuse functions can be added when necessary.[66–69]

2.1.3.5 Auxiliary Basis Sets

There is a class of basis sets that exist to reduce the computational cost to accuracy ratio. These are auxiliary basis sets and are known as the resolution of identity (RI). They work by approximating the two-electron integrals more efficiently by reducing from four-centre integrals down to three. For larger molecules, where the number of integrals increases exponentially with the number of atoms, using three-centre integrals per two-electron integral reduces the computational cost significantly.[66,70]

The simplest format of RI is used regularly in DFT and MP2 calculations.[70,71] Building on this form, RI can be combined with a chain of spheres (RIJCOSX). The addition makes the method applicable for hybrid DFT functionals. Using both RI and COSX methodology, RIJCOSX reduces the cost of the calculation of the Hartree-Fock exchange.[71]

RI-K is another development of RI designed to approximate the Hartree-Fock coulomb term used in hybrid DFT calculations and can be used alongside other computational methods.[72] The goal of using auxiliary basis is to make DFT calculations more scalable for larger systems

2.1.3.6 Concluding Remarks

When choosing a basis set, it is critical that careful consideration is taken. Choosing a basis set too small could result in poor calculations with non-meaningful results. On the other hand, choosing a basis set too large could come at a large penalty of computational cost with very little to show for it in the accuracy of the results.[73] Taking this into account, where possible, the choice of DFT methodology should be made logically based on benchmarking studies and past performance on similar systems.

n this study, the def2-TZVPP basis set was employed throughout to provide a balanced and reliable description of electronic structure while maintaining manageable computational cost for the catalytic systems investigated. The triple-

ζ valence description combined with additional polarisation functions allows accurate modelling of bonding environments and reaction intermediates, making def2-TZVPP well suited for the transition-metal and main-group systems examined in this work.[68,69,74]

2.1.4 DFT Applications For This Work

2.1.4.1 Reaction Mechanism Elucidation

The elucidation of reaction mechanisms is one of the most popular applications of DFT. This is due to the benefits of synergistic research between experimental and computational chemistry. Experimental insight from computational calculations can reduce time and waste, as well as providing new insights into what is happening at the atomic level. This section briefly outlines the general methodology used to elucidate a reaction mechanism.

To calculate a reaction mechanism, the lowest energy geometries of all reactants, intermediates, transition states and products are identified through conformational searches on the structure. Optimisation and analytical frequency calculations are undertaken on all complexes. For non-transition states, only real vibrational modes should be present in the frequency calculation. This signals that a minima have been found. Different conformations can yield different minima and the one with the lowest energy is considered the global minima/ground state energy. For transition states, there should be a single imaginary frequency that relates to the bond that is being formed/broken.[49] Avogadro 2.0 is used to visualise calculated structures for this work.[75]

Once a correct structure has been optimised, single point energy calculations including frequency, higher level methods for energetics or solvent effects can be done on the optimised structure. Solvent calculations provide a correction to account for the experimental effect of the solvent. Following the solvation calculation, the final ΔG_{solv} can be evaluated through Eq. 7:

$$\Delta G_{solv} = \Delta G_{gas} + (\Delta E_{solv} - \Delta E_{gas}) \qquad \text{Eq. 7}$$

Where ΔG_{gas} is calculated from the frequency calculation and the solvent correction term ($\Delta E_{solv} - \Delta E_{gas}$) is the solvated energy minus the gaseous energy. Once ΔG_{solv} has been calculated, considerations of the concentration of the intermediates needs to be incorporated.[49]

DFT calculations calculate the energy of a system using a gas phase standard of 1 atm. When looking at solution-phase energies, this can cause discrepancies between experimental and computational results especially when modelling catalytic reactions where the catalyst concentration is many times lower compared to the reagents.

A concentration correction can be applied to consider all reactants and products at equal concentration (1 mol dm^{-3}), rather than at equal pressures. For concentrations of 1 M at 298 K this equates for 1.89 kcal mol^{-1} energy correction per molecular unit. As concentrations change this value changes. The correction with varied concentrations is calculated by the addition of the term in Eq. 8 to the final Gibbs free energy. Equation 8 can be broken down into the ideal gas constant (R), the temperature (T), the species concentration at standard state (C^0) and the concentration at 1 atm (C^{1atm}).

$$RTln\left(\frac{C^0}{C^{1\,atm}}\right) \qquad \text{Eq. 8}$$

Another form of the concentration correction is by considering the reaction quotient. Eq. 9 shows the correction where R is ideal gas constant, T is the temperature and Q is the reaction quotient. The correction considers the concentration gradient of the limiting reagent ($[R]$) with respect to the product ($[P]$) through the reaction quotient ($Q = [P]/[R]$). Although this method is not exact, applying it can more accurately represent experimental results.[49,76,77]

$$Concentration\,Correction = RTln(Q) \qquad \text{Eq. 9}$$

Once the concentration correction has been applied, the relative energies between the reactants, intermediates and transition states are calculated. These are plotted into a potential energy surface to represent the reaction mechanism. Within this work, both the 1 mol dm^{-3} correction and reaction quotient correction have been used depending on which method better models the experimental work.

While elucidated reaction mechanisms are the foundational to understanding a reaction pathway, further DFT based descriptors are needed to compliment them for a thorough understanding. This is particularly important when comparing

multiple reaction pathways and varying catalysts/reactants. Several DFT based descriptors that will aid this research are described in the following subsections.

2.1.4.2 Fluoride Ion affinities

Fluoride ion affinity (FIA) calculations provide a measure of the Lewis acidic strength of different complexes. Fluoride binds directly to the electron-deficient metal centre, and because it is small and highly basic, it readily coordinates to Lewis acids, making it an ideal benchmark of Lewis acid strength. Furthermore, its small size means steric, dispersion and charge transfer effects are negligible.[78] Greb *et al.* compare two different FIA reference systems, the isodesmic-anchored trimethylsilanefluoride (TMS) system,[79,80] and the COF_3^- system (Figure 2.2).[81] Due to the reference, COF_3^-, being anionic, the TMS system becomes more favourable. This smaller charge to size ratio of the COF_3^- ion in comparison to the Me_3Si^+ ion means that more errors are present due to a more in-depth treatment of the dynamic electron correlation.[78]

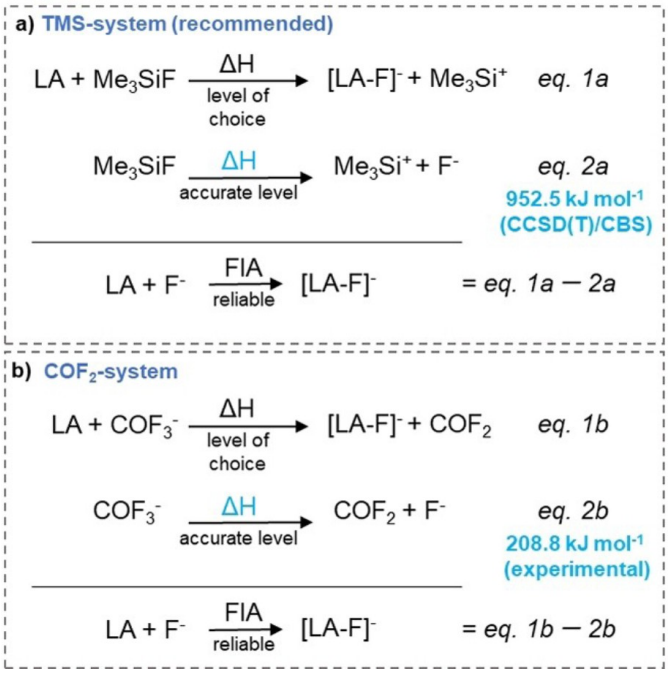

Figure – Methodology.33 - The two reference systems presented by Greb et al. for the calculation of the FIA of different complexes from 82.[78]

In this work, the TMS system will be employed utilising the methodology provided by Greb *et al.*.[78]

2.1.4.3 Global Electrophilicity Index

The Global Electrophilicity Index (GEI) is another measure of the Lewis acidic strength. Unlike FIA calculations, the GEI is derived solely from the molecular

structure. This approach was developed by Stephan *et al*. as other measurements of Lewis acidity were currently based on the computed affinity to a Lewis base, rather than a complexes affinity to accept electrons. To calculate the GEI, the HOMO-LUMO energies of the complex in question need to be applied into Eq. 10.

$$GEI = \omega = \frac{\mu^2}{2\eta} \qquad \text{Eq. 10}$$

Where $\mu = \frac{1}{2}\left(E_{HOMO} + E_{LUMO}\right) \wedge \eta = \left(E_{LUMO} - E_{HOMO}\right)$

The chemical potential (μ), reflects the molecule's electron affinity. The larger the value of the chemical potential, the more Lewis acidic a molecule is.[82] The chemical hardness (η) is a measure of the resistance to charge transfer. The smaller the value of η, the more able a molecule is to change its electron count and therefore is a stronger Lewis acid.[83] The different approach of the GEI for measuring Lewis acidic strength means that it can be used in conjunction with the FIA to provide an alternative view of Lewis acidic strength.

2.2 Post-Wavefunction Analysis

MultiWFN is a software package that is designed for analysing molecular structures in more detail after DFT calculations have taken place.[84] A thorough quantitative and qualitative description of bonding and non-covalent interactions can be achieved through this analysis. Two of the more popular analyses which will be employed within this work are quantum theory of atoms in molecules (QTAIM) and non-covalent interaction analyses (NCI). These methods are widely used as an extra computational tool for added-value explanations of mechanistic systems.[85,86]

2.2.1 Quantum Theory of Atoms in Molecules Analysis

Bader's QTAIM is a post-wavefunction analysis method that provides additional insights into the electronic structures of molecules. Using optimised DFT structures, QTAIM can produce several topological descriptors of the molecule to describe bonding and non-covalent interactions (NCI) from the electron density of the molecule, defining bonding interactions directly from the electron density rather than relying on predefined chemical bonds.[87,88]

Utilising the electron density, QTAIM can identify bond paths between different atoms. Bond paths are paths of maximum electron density connecting two different atoms. If a bond is present between two different atoms, there will be a bonding critical point (BCP) within the bond path. The BCP (Figure 2.3) is the point at which density is at a minimum in the same plane as the bond path but at a maximum in the perpendicular plane.

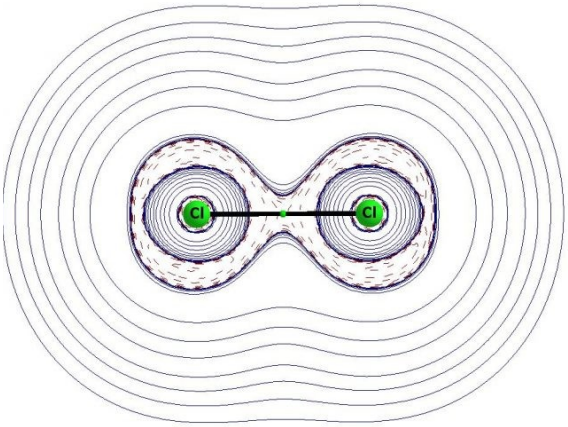

Figure – Methodology.34 - A molecular graph depicting the Laplacian of electron density lines depicting the BCP (green dot) between a pair of bonded chlorine atoms.[89]

The BCP is the point at which topological data is extracted to give more information about the bonds. Some of the topological features that can be extracted include:

Electron Density $\rho(BCP)$ – The electron density at the bonding critical point is a positive value correlating to the bond strength. The stronger the bond, the larger the $\rho(BCP)$ value.

Potential Energy $V(BCP)$ – The potential energy value is a negative value providing a measure of the bond strength. The more negative the $V(BCP)$ value, the stronger the bond is.

Laplacian of Electron Density $\nabla^2\rho(BCP)$ – The Laplacian of electron density gives an indication to the nature of the bond. A negative $\nabla^2\rho(BCP)$ value suggests a bond that is covalent in nature, whereas a positive value indicates a bond which is ionic in nature. This parameter does not always give a correct answer.

Energy Density $H(BCP)$ – The energy density of at the BCP is another indication of the nature of the bond. Like $\nabla^2\rho(BCP)$, a negative $H(BCP)$ indicates covalent bonding and positive indicates non-covalent. This value is also known to not give

a perfect indication of the type of bonding present, so it is important to apply chemical intuition and use the $\nabla^2\rho(BCP)$ parameter as a second indication.[90]

Other topological parameters can be derived that can give indication to whether the reaction is open/closed shell, the bond degree and bond ellipticity. QTAIM parameters do not only give quantitative information on strong bonds, but also on some weak interactions. NCI analysis can give a qualitative understanding of these weaker interactions.

2.2.2 Non-Covalent Interaction Analysis

NCI analysis allows the user to visualise the weaker interactions within a molecule. These interactions include hydrogen bonds, weak interactions such as Van der Waals and dispersion forces, weak repulsive forces and strong steric repulsion. Through MultiWFN, NCI plots and reduced density gradient (RDG) plots can be created. The NCI plots show a representation of the molecule with interactions being shown with a colour scale and as planes between atoms. Figure 2.4 is an example of an NCI plot taken from Chapter 5. The red represents the steric repulsions, the dark green represents the weak repulsive forces, the light green represents Van der Waals and dispersion forces, and blue represents strong attractive forces.

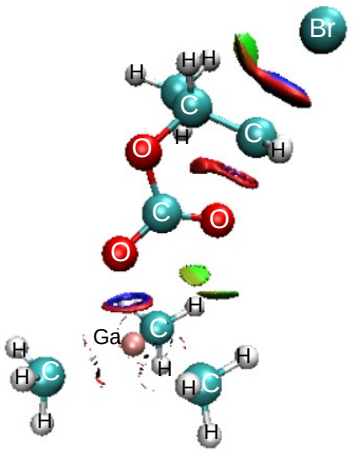

*Figure – Methodology.35 - Example of an NCI plot using **TS3** from the $GaMe_3$ pathway of Chapter 5.*

RDG plots give a graphical representation of the weaker interactive forces (Figure 2.4). The RDG plots use the same key as the NCI plots. To analyse the RDG the depth and concentration of the colour needs to be considered. Figure 2.5 shows a

deep and concentrated light green (-0.0025 to -0.0075 au) and dark green area (0.0025 to 0.0075 au) indicating the presence of weak attractive and repulsive forces. The red region also moves towards the base of the graph (~0.0375 au) but is much less concentrated than the green regions, meaning that steric repulsion forces are present but lesser so than the attractive forces.

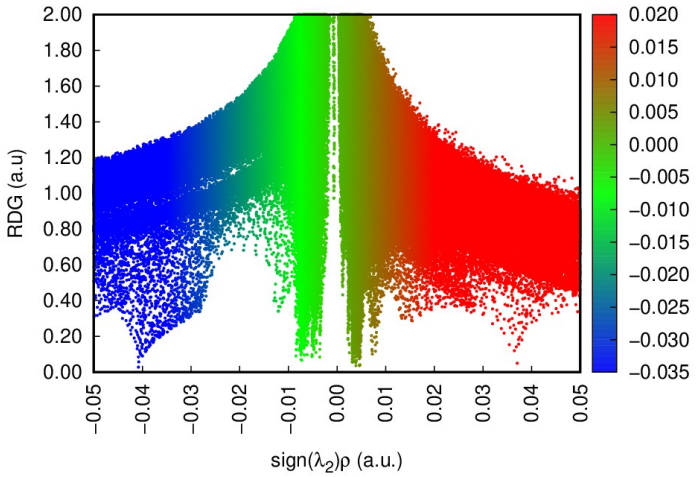

*Figure – Methodology.36 - An example RDG plot of **TS3** for the Ga^{t}Bu$_3$ catalyst from Chapter 5.*

Combining the RDG and NCI plots provides a good understanding of the intra-atomic interactions within a molecule. This increased understanding provides good rationale for elucidated mechanism and the pathways followed.

2.2.3 Concluding Remarks

Post-wavefunction analysis is an extremely useful tool for computational chemists to achieve a deeper understanding of the electronic and steric properties of different molecules. The quantitative nature of QTAIM partnered with the qualitative nature of NCI analysis means well-rounded conclusions can be made on interesting mechanistic steps. This methodology will be employed throughout this work to assist in such explanations.

2.3 Conclusion

DFT has fast evolved over the past 30 years, from the primitive Hartree-Fock theory to the multifaceted DFT functionals that are available today. The range of DFT tools available allows for a basic estimation of a problem right to a calculation close to chemical accuracy. This range gives the user a vast toolbox enabling the choice of a convenient method to best approach the problem that is trying to be

solved. For this reason, it has become a paramount tool in research, playing a key role in mechanistic elucidation and catalyst development.

DFT calculations will be performed using the Orca 4.2.1 computational program.[47] Benchmarking studies highlighted Becke's B97-D3 functional and Head-Gordon's ωB97X-D3 hybrid functional as efficient for mechanistic evaluations.[74,91,92] Grimme and Goerigk's GMTKN55 (general main-group thermochemistry, kinetics, and noncovalent interactions) database contains 55 different benchmark datasets. As they are main group, it makes the benchmark studies on these data sets highly applicable for the chemistry included in this thesis.

Both the B97-D3 and ωB97X-D3 were benchmarked on this database using Orca as the computational program of choice. In the paper, the WTMAD-2 (Weighted Total Mean Absolute Deviation) (Eq. 11) is used to measure a functional's computational performance. The WTMAD is an extension of the MAD (Mean Absolute Deviation). The MAD gives the average error per reaction for a dataset; however, it is limited to one dataset as it cannot account for datasets of different energy scales. The WTMAD accounted for this by weighting the scale of each data set so that no category unfairly dominates and the errors of the benchmark could be combined into one number. Moving into this study, a second iteration (WTMAD-2) was developed such that an average weight factor is applied across all data sets. This is seen in Eq. 11 and the 56.84 kcal mol^{-1} energy is the average energy scale across all GMTKN55 data sets.

$$WTMAD-2=\frac{1}{\sum N_i}\sum_i^{\square} N_i\cdot\frac{56.84}{|\Delta E|_i}\cdot\frac{1}{N}\sum|E_{calc}-E_{ref}| \qquad \text{Eq.11}$$

Where $\frac{56.84}{|\Delta E|_i}$ is the average energy scale across the database.

The WTMAD-2 values for B97-D3 and ωB97X-D3 are 8.55 kcal mol^{-1} and 4.77 kcal mol^{-1} respectively. This places B97-D3 as one of the strongest GGAs in the group making it suitable for geometry optimisations in this study. The improved WTMAD-2 value of ωB97X-D3 renders it as one of the best in the hybrid functionals and confirms it's applicability as the functional of choice for final energy evaluations in this study.

With the inclusion of Grimme's dispersion correction, the B97-D3 and ωB97X-D3 functionals have also shown to perform well on group 13 catalyst systems and thus will be the focus in this work.[93] The Ahlrichs basis sets will also be utilised throughout this work due to their performance on similar systems and in benchmarks. The specific basis set will be the def2-svp for geometry optimisations and def2-TZVPP for final energy evaluations.[92,93] Auxiliary basis sets will be employed to reduce the computational cost throughout. Exact methodologies utilised in each study will be provided within the appropriate chapter, with a summary below (Table 2.1)

Table – Methodology.3 - Summary of the different computational methodologies used in the research Chapters 3, 4 and 5.

Chapter	Summary of DFT methodology	Additional methodologies
3	Geometry optimisation and frequency calculations performed using RI-B97-D3/def2-SVP, with single-point energy refinement at RIJCOSX-ωB97X-D3BJ/def2-TZVPP including CPCM solvation corrections.	QTAIM and NCI post-wavefunction analysis, together with concentration and thermochemical free-energy corrections.
4	Geometry optimisation and frequency calculations performed using RI-B97-D3/def2-SVP with energetic refinement at RIJCOSX-ωB97M-D3BJ/def2-TZVPP including CPCM solvation corrections.	Temperature-dependent free-energy calculations and concentration corrections applied for comparison of competing reaction pathways.
5	Geometry optimisation and frequency calculations performed using RI-B97-D3/def2-TZVPP with energetic refinement at RIJCOSX-ωB97X-D3BJ/def2-TZVPP including CPCM solvation corrections.	QTAIM and NCI analyses, fluoride ion affinity and global electrophilicity index calculations, and QSAR modelling via linear regression and feature selection methods.

2.4 References

1 W. Kohn and L. J. Sham, *Phys. Rev.*, 1965, **140**, 1133–1138.

2 P. Hohenberg and W. Kohn, *Phys. Rev.*, 1964, **136**, 864–871.

3 C. Lee, W. Yang and R. G. Parr, *Phys. Rev. B*, 1988, **37**, 785–789.

4 C. F. Sun, Q. Liu, L. Meng and X. Li, *J. Comput. Chem.*, 2024, **45**, 331–340.

5 A. S. Dumon, H. S. Rzepa, C. Alamillo-Ferrer, J. Bures, R. Procter, T. D. Sheppard and A. Whiting, *Phys. Chem. Chem. Phys.*, 2022, **24**, 20409–20425.

6 H. Rajapaksha, L. J. Augustine, S. E. Mason and T. Z. Forbes, *Angew. Chem.*, 2023, **135**, e202305073.

7 S. Khatun, R. P. Bhagat, S. A. Amin, T. Jha and S. Gayen, *Comput. Biol. Med.*, 2024, **175**, 108468.

8 Q. Liao, J. Wang, P. Xie, E. Liang and Z. Wang, *Res. Astron. Astrophys.*, 2023, **23** 122001.

9 G. R. Schleder, A. C. M. Padilha, C. M. Acosta, M. Costa and A. Fazzio, *JPhys Mater.*, 2019, **2**, 032001.

10 L. H. Thomas, *Mathematical Proceedings of the Cambridge Philosophical Society*, 1927, **23**, 542–548.

11 E. Fermi, *Rend. Accad. Naz. Lincei*, 1927, **6**, 32.

12 P. A. M. Dirac, *Math. Proc. Cambridge Philos. Soc.*, 1930, **26**, 376–385.

13 Y. Shikano, H. C. Watanabe, K. M. Nakanishi and Y. ya Ohnishi, *Eur. Phys. J.:Spec. Top.*, 2021, **230**, 1037–1051.

14 Chr. Møller and M. S. Plesset, *Phys. Rev.*, 1934, **46**, 618–622.

15 S. F. Boys, in *Proceedings of the Royal Society of London. Series A, Mathematical and Physical Sciences*, The Royal Society, 1950, vol. 200, pp. 542–554.

16 C. C. J. Roothaan, *Rev. Mod. Phys.*, 1951, **23**, 69–89.

17 J. Čížek, *J. Chem. Phys.*, 1966, **45**, 4256–4266.

18 K. Raghavachari, G. W. Trucks, J. A. Pople and M. Head-Gordon, *Chem. Phys. Lett.*, 2013, **589**, 37–40.

19 A. D. Becke, *J. Chem. Phys.*, 2014, **140**, 18A301.

20 J. P. Perdew, *MRS Bull.*, 2013, **38**, 743–750.

21 K. Burke, *J. Chem. Phys.*, 2012, **136**, 150901.

22 J. P. Perdew, A. Ruzsinszky, J. Tao, V. N. Staroverov, G. E. Scuseria and G. I. Csonka, *J. Chem. Phys.*, 2005, **123**, 62201.

23 V. Van Doren, C. Van Alsenoy and P. Geerlings, in *Proceedings of the International Conference on 'Density Functional Theory and its Applications to Materials' held in Antwerp, June 8-10, 2000, American Institute of Physics, Conference Proceedings, Volume 577, Melville, New York, 2001, 220*, 2001.

24 X. Liao, R. Lu, L. Xia, Q. Liu, H. Wang, K. Zhao, Z. Wang and Y. Zhao, *Energy Environ. Mater.*, 2022, **5**, 157–185.

25 Q. Peng, F. Duarte and R. S. Paton, *Chem. Soc. Rev.*, 2016, **45**, 6093–6107.

26 A. J. Cohen, P. Mori-Sánchez and W. Yang, *Chem. Rev.*, 2012, **112**, 289–320.

27 J. P. Perdew and A. Zunger, *Phys. Rev. B*, 1981, **23**, 5048–5079.

28 S. H. Vosko, L. Wilk and M. Nusair, *Can. J. Phys.*, 1980, **58**, 1200–1211.

29 J. P. Perdew, K. Burke and M. Ernzerhof, *Phys. Rev. Lett.*, 1996, **77**, 3865–3868.

30 J. P. Perdew and Y. Wang, *Phys. Rev. B*, 1992, **45**, 13244–13249.

31 A. D. Becke, *J. Chem. Phys.*, 1997, **8560**, 8554–8560.

32 C. Lee, W. Yang and R. G. Parr, *Phys. Rev. B*, 1988, **37**, 785–789.

33 A. D. Becke, *Phys. Rev. A*, 1988, **38**, 3098–3100.

34 Y. Zhao and D. G. Truhlar, *Acc. Chem. Res.*, 2008, **41**, 157–167.

35 N. Mardirossian and M. Head-Gordon, *Mol. Phys.*, 2017, **115**, 2315–2372.

36 Y. Zhao and D. G. Truhlar, *Acc. Chem. Res.*, 2008, **41**, 157–167.

37 L. Goerigk and S. Grimme, *Wiley Interdiscip. Rev. Comput. Mol. Sci.*, 2014, **4**, 576–600.

38 Y. Zhao and D. G. Truhlar, *J. Phys. Chem. A*, 2005, **109**, 5656–5667.

39 S. Grimme, J. Antony, S. Ehrlich and H. Krieg, *J. Chem. Phys.*, 2010, **132**, 154104.

40 A. D. Becke, *J. Chem. Phys.*, 1993, **98**, 5648–5652.

41 J. Da Chai and M. Head-Gordon, *Phys. Chem. Chem. Phys.*, 2008, **10**, 6615–6620.

42 S. Grimme, *J. Chem. Phys.*, 2006, **124**, 034108.

43 C. Riplinger, B. Sandhoefer, A. Hansen and F. Neese, *J. Chem. Phys.*, 2013, **139** 134101.

44 S. Grimme, S. Ehrlich and L. Goerick, *J. Comput. Chem.*, 2011, **32**, 1456–1465.

45 E. Caldeweyher, S. Ehlert, A. Hansen, H. Neugebauer, S. Spicher, C. Bannwarth and S. Grimme, *J. Chem. Phys.*, 2019, **150**, 154122.

46 O. A. Vydrov and T. Van Voorhis, *J. Chem. Phys.*, 2010, **133**, 244103.

47 F. Neese, *Wiley Interdiscip. Rev. Comput. Mol. Sci.*, 2012, **2**, 73–78.

48 B. Helmich-Paris, B. de Souza, F. Neese and R. Izsák, *J. Chem. Phys.*, 2021, **155**, 104109.

49 H. Ryu, J. Park, H. K. Kim, J. Y. Park, S. T. Kim and M. H. Baik, *Organometallics*, 2018, **37**, 3228–3239.

50 B. Mennucci, R. Cammi and J. Tomasi, *J. Chem. Phys.*, 1998, **109**, 2798–2807.

51 S. Sinnecker, A. Rajendran, A. Klamt, M. Diedenhofen and F. Neese, *J. Phys. Chem. A*, 2006, **110**, 2235–2245.

52 A. V Marenich, C. J. Cramer and D. G. Truhlar, *J. Phys. Chem. B*, 2009, **113**, 6378–6396.

53 J. Harvey, *Computational Chemistry*, Oxford University Press, 2018.

54 P. C. Hiberty and S. Shaik, *Theor. Chem. Acc.*, 2002, **108**, 255–272.

55 F. Jensen, *Wiley Interdiscip. Rev. Comput. Mol. Sci.*, 2013, **3**, 273–295.

56 X. Xu and D. G. Truhlar, *J. Chem. Theory Comput.*, 2012, **8**, 80–90.

57 W. J. Hehre, R. F. Stewart and J. A. Pople, *J. Chem. Phys.*, 1969, **51**, 2657–2664.

58 P. C. Hariharan and J. A. Pople, *Theor. Chim. Acta*, 1973, **28**, 213–222.

59 W. J. Hehre, R. Ditchfield and J. A. Pople, *J. Chem. Phys.*, 1972, **56**, 2257–2261.

60 Jr. Dunning Thom H., *J. Chem. Phys.*, 1989, **90**, 1007–1023.

61 R. A. Kendall, Jr. Dunning Thom H. and R. J. Harrison, *J. Chem. Phys.*, 1992, **96** 6796–6806.

62 K. A. Peterson and Jr. Dunning Thom H., *J. Chem. Phys.*, 2002, **117**, 10548–10560.

63 F. Jensen, *J. Chem. Phys.*, 2001, **115**, 9113–9125.

64 F. Jensen, *J. Chem. Phys.*, 2002, **116**, 7372–7379.

65 F. Jensen, *J. Chem. Phys.*, 2002, **117**, 9234–9240.

66 F. Weigend, M. Häser, H. Patzelt and R. Ahlrichs, *Chem. Phys. Lett.*, 1998, **294**, 143–152.

67 A. Schäfer, H. Horn and R. Ahlrichs, *J. Chem. Phys.*, 1992, **97**, 2571–2577.

68 F. Weigend, *Phys. Chem. Chem. Phys.*, 2006, **8**, 1057–1065.

69 F. Weigend and R. Ahlrichs, *Phys. Chem. Chem. Phys.*, 2005, **7**, 3297–3305.

70 F. Neese, *J. Comput. Chem.*, 2003, **24**, 1740–1747.

71 F. Neese, F. Wennmohs, A. Hansen and U. Becker, *Chem. Phys.*, 2009, **356**, 98–109.

72 K. Eichkorn, O. Treutler, H. Öhm, M. Häser and R. Ahlrichs, *Chem. Phys. Lett.*, 1995, **242**, 652–660.

73 N. Mardirossian and M. Head-Gordon, *Mol. Phys.*, 2017, **115**, 2315–2372.

74 L. Goerigk and S. Grimme, *Phys. Chem. Chem. Phys.*, 2011, **13**, 6670–6688.

75 M. Hanwell, D. Curtis, D. Lonie, T. Vandermeersch, E. Zurek and G. Hutchison, *J. Cheminform.*, 2012, **4**, 17.

76 J. N. Harvey, F. Himo, F. Maseras and L. Perrin, *ACS Catal.*, 2019, **9**, 6803–6813.

77 J. Jover, *Phys. Chem. Chem. Phys.*, 2017, **19**, 29344–29353.

78 P. Erdmann, J. Leitner, J. Schwarz and L. Greb, *ChemPhysChem*, 2020, **21**, 987–994.

79 H. Böhrer, N. Trapp, D. Himmel, M. Schleep and I. Krossing, *Dalton Transactions* 2015, **44**, 7489–7499.

80 I. Krossing and I. Raabe, *Chem. - Eur. J.*, 2004, **10**, 5017–5030.

81 K. O. Christe, D. A. Dixon, D. McLemore, W. W. Wilson, J. A. Sheehy and J. A. Boatz, *J. Fluor. Chem.*, 2000, **101**, 151–153.

82 R. G. Parr, R. A. Donnelly, M. Levy and W. E. Palke, *J. Chem. Phys.*, 1977, **68**, 3801–3807.

83 R. G. Parr and R. G. Pearson, *J. Am. Chem. Soc.*, 1983, **105**, 7512–7516.

84 T. Lu and F. Chen, *J. Comput. Chem.*, 2012, **33**, 580–592.

85 P. S. V. Kumar, V. Raghavendra and V. Subramanian, *J. Chem. Sci.*, 2016, **128**, 1527–1536.

86 R. A. Alharis, C. L. McMullin, D. L. Davies, K. Singh and S. A. Macgregor, *Faraday Discuss.*, 2019, **220**, 386–403.

87 F. Cortés-Guzmán and R. F. W. Bader, *Coord. Chem. Rev.*, 2005, **249**, 633–662.

88 R. F. W. Bader, *Chem. Rev.*, 1991, **91**, 893–928.

89 C. T. López, The Chemical Bond, https://mappingignorance.org/2015/08/20/the-chemical-bond-is-this-term-still-useful-or-it-should-be-replaced-by-another-one/, (accessed 15 April 2025).

90 D. Cremer and E. Kraka, *Angew. Chem., Int. Ed. Engl.*, 1984, **23**, 627–628.

91 L. Goerigk, A. Hansen, C. Bauer, S. Ehrlich, A. Najibi and S. Grimme, *Phys. Chem. Chem. Phys.*, 2017, **19**, 32184–32215.

92 M. Bursch, J. M. Mewes, A. Hansen and S. Grimme, *Angew. Chem.*, 2022, **134**, e202205735.

93 L. Álvarez-Miguel, J. D. Burgoa, M. E. G. Mosquera, A. Hamilton and C. J. Whiteoak, *ChemCatChem*, 2021, **13**, 4099–4110.

Chapter 3 – Beyond Al: Group 13 salphen Catalysts for Efficient CO_2 Utilisation. Insight from DFT calculations.

This work was published: D. J. Cabrera, R. D. Lewis, C. Díez-Poza, L. Álvarez-Miguel, M. E. G. G. Mosquera, A. Hamilton and C. J. Whiteoak, Group 13 salphen compounds (In, Ga and Al): a comparison of their structural features and activities as catalysts for cyclic carbonate synthesis *Dalton Trans.*, 2023, **52**, 5882–5894.[1]

3.1 Introduction

Salen ligands (Scheme 3.1) are synthesised by the condensation of salicylaldehyde and ethylenediamine. They are a versatile class of tetradentate Schiff base ligands in which the steric and electronic properties can be modulated with a variety of metal centres. This makes them popular in coordination chemistry and homogeneous catalysis. The salens have also been shown to be effective catalysts for the cycloaddition of CO_2 and epoxides. Particularly, Cr[salen] has shown to achieve high turnover frequencies and yields in a range of reaction conditions.[2]

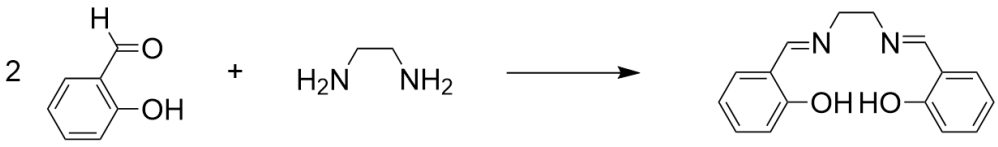

Scheme – Beyond Al: Group 13 salphen Catalysts for Efficient CO2 Utilisation. Insight from DFT calculations..10 - The general reaction scheme for the synthesis of the salen ligand.

Group 13 metal complexes of salens, particularly those incorporating aluminium and gallium, have attracted interest due to the earth abundance, low toxicity, and ability to catalyse a range of organic transformations of Al and Ga. Group 13 salens have been reported for catalytic use for cyclic carbonate formation as early as 2002 by He *et al.*.[3] These reports showed promise highlighting enhanced activity compared to other metal based salens.[2] However, catalyst solubility has been shown to hinder the potential of this class of catalysts.[3]

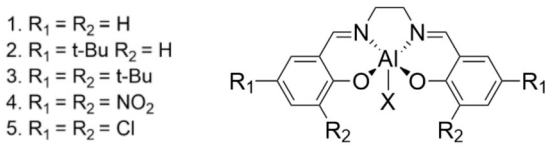

Figure – Beyond Al: Group 13 salphen Catalysts for Efficient CO2 Utilisation. Insight from DFT calculations..37 - Aluminium salen structure studied by He et al.[3] The R-positions represent the positions that were functionalised, and X is the position of the negative halide ligand.

A lesser explored analogue of the salen ligand is the salphen ligand (Figure 3.2 a). The salphen ligand has a phenyl bridge between the two amine groups. They share the same versatility as the salen ligand and can be easily functionalised and used with a variety of metals. The versatility of the salphen ligand makes it highly applicable in catalysis as it gives the user a range of functionalisation points to tune catalyst properties for appropriate use. Currently, uses include optical sensors for amines produced by bacteria in the food industry,[4] as cancer drugs[5] and as catalysts.[6]

North *et al.* highlighted Al-salphen was not very active due to arising solubility issues during the reaction. Therefore, a dimeric Al-salphen complex (Figure 3.2b) was synthesised which would go on to be a highly active and prominent catalyst. [7,8] Continued research produced another highly active bimetallic salphen derivative (Figure 3.2c).[9] To put this into perspective, yields of 27-70v% were observed using the monomeric catalyst (Figure 3.2a) compared to 85-94 % yields observed with the dimeric analogue (figure 3.2c) across varying reaction conditions.[9] The higher 70 % yield was achieved with double the concentration of the monomeric salphen compared to the dimeric salphen, confirming the number of metal sites available to catalyse the reaction was not proportional to the yield.

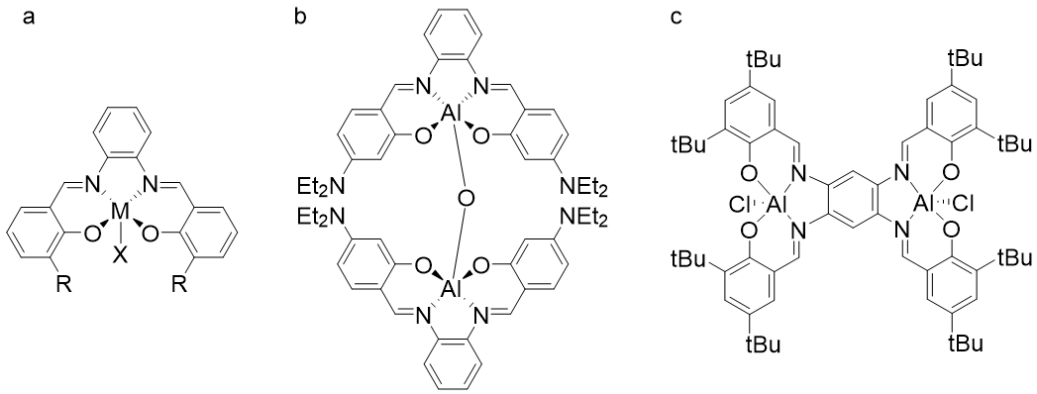

Figure – Beyond Al: Group 13 salphen Catalysts for Efficient CO2 Utilisation. Insight from DFT calculations..38 – a) The general structure of a group 13 monomeric salphen catalyst where X is usually a

halide and R the position of functionalisation. b and c) Two dimeric variations of the Aluminium salphen catalyst developed by North.[7–9]

Since the realisation of monomeric aluminium salphens solubility issues by He, North and Kleij, there has been little attention given to the monomeric group 13 salphens.[8] As already discussed in Chapter 1, the generally accepted mechanism for the cycloaddition of CO_2 and epoxides with a Lewis acidic catalyst is shown in Scheme 1.2. Due to them being softer Lewis acids, it was traditionally assumed that they would not be able to activate the epoxide and CO_2 as effectively and therefore would not being as active. Consequently, zinc and chromium have been the first choice for metal centres of monomeric salphen catalysts, with both showing over 90 % yields for the conversion of propylene oxide to propylene carbonate.[8,10] Furthermore, the full reaction mechanism of zinc salphen has been elucidated by Kleij and Bo *et al*. (figure 3.3). [11]

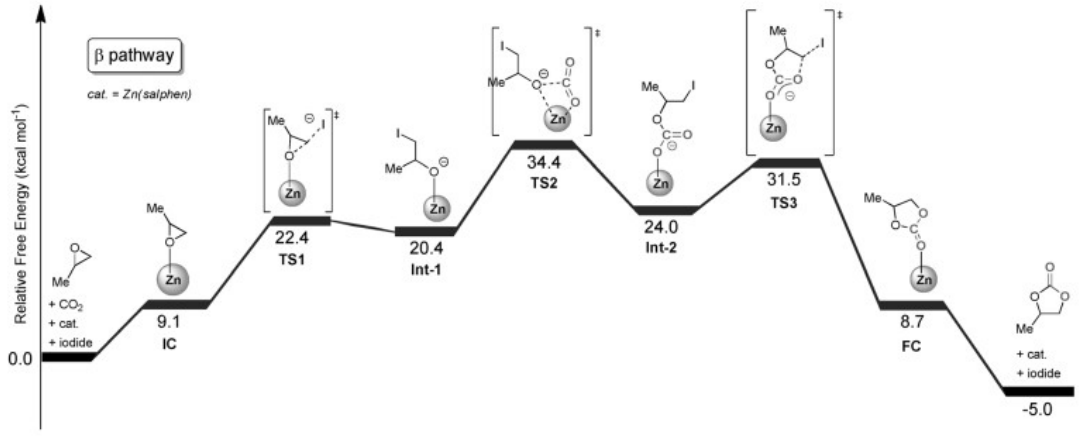

Figure – Beyond Al: Group 13 salphen Catalysts for Efficient CO2 Utilisation. Insight from DFT calculations..39 – Calculated solvated free energy surface (kcal mol^{-1}) for the cycloaddition of CO_2 and propylene oxide catalysed by Zn[salphen], to form propylene carbonate at the BP86 level of theory from 11. [11]

The outlined mechanism (Figure 3.3) begins at **IC** where propylene carbonate associates with the metal centre. The epoxide ring is then opened at **TS1** (22.4 kcal mol^{-1}) by the iodide of tertbutylammonium iodide (TBAI) to form **Int-1**. CO_2 insertion occurs at **TS2** (34.4 kcal mol^{-1}) to form **Int-2**. Two possible ring closing mechanisms are available after **Int-2** (Figure 14) but the lowest energetically is displayed in Figure 3.4. A direct cyclic carbonate ring closure over **TS3** (31.5 kcal mol^{-1}) affords the cyclic carbonate product exergonically bound to the catalyst (**FC**).[11] The contrary ring closure method first sees a conformation changed followed by the ring closure at 37.9 kcal mol^{-1}.

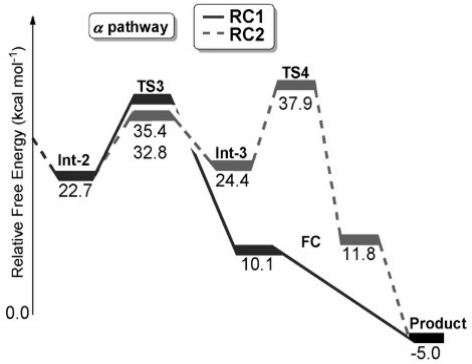

Figure – Beyond Al: Group 13 salphen Catalysts for Efficient CO2 Utilisation. Insight from DFT calculations..40 - DFT calculated potential energy surface for the two competing cyclic carbonate ring closures from Castro Gomez et al from 11.[11]

Recent work from the Hamilton and Whiteoak groups showed that gallium catalysts were more active compared to the aluminium counterparts.[12] While aluminium remains a cheaper option for catalyst processes, more expensive catalysts could be used as alternatives if there is a suitable improvement in reaction conditions. Due to the success of the heavier group 13 elements using the aminotrisphenolate catalyst, the Whiteoak group undertook preliminary experimental investigations on gallium and indium monomeric salphens. Table 3.1 showed that both the Ga and In[salphen(X)] catalysts were more active than the aluminium counterpart and did not suffer the same solubility issues. The In[salphen(X)] catalyst was the most active; even seeing high yields at room temperature and low catalyst loading (0.125 %).

Table – Beyond Al: Group 13 salphen Catalysts for Efficient CO2 Utilisation. Insight from DFT calculations..4 - Catalytic activity of selected M[L(X)] (where M = Al, Ga and In, X = Br, Cl, and I and L = salphen) catalysts in the cycloaddition of CO_2 to styrene oxide.

Catalyst	Catalyst loading (mol %)	T (°C)	Yield (%)
Al[L(Cl)]	0.25	50	47
Al[L(Br)]	0.25	50	65
Ga[L(Cl)]	0.25	50	67
Ga[L(Br)]	0.25	50	86
Ga[L(I)]	0.25	50	95
In[L(Cl)]	0.25	50	98
In[L(Br)]	0.20	50	98
In[L(Br)]	0.125	60	95
In[L(Br)]	0.15	60	>99
In[L(I)]	0.125	50	62

Catalyst	Catalyst loading (mol %)	T (°C)	Yield (%)

As seen with the aminotrisphenolate catalyst study,[12] the Whiteoak group have again shown that the heavier group 13 elements can produce active catalysts. As this follows a Lewis acid-based mechanism (Scheme 3.1), many expect the catalyst activity is proportional to the strength of Lewis acidity. This is one of the reasons why little attention has been paid to the heavier group 13 elements.[13] In the case of the salphens, it was assumed that due to the precipitant formed by the Al[salphen(X)] catalyst hindering its activity, the heavier, weaker Lewis acidic group 13 catalysts would still not be as active. So, in collaboration with the Whiteoak group, this work aims to build an understanding of the observed experimental results.

3.1.2 Aims

- Outline the reaction mechanisms for each M[salphen(X)] catalyst, where M = Al, Ga and In, and X = Cl, Br and I, using DFT calculations. Ensure calculated energies are in good agreement with experimental results.
- Use QTAIM and NCI analysis to elucidate topological descriptors and kinetic differences to explain experimental findings.
- Identify a cause for the insoluble precipitate that forms over the duration of the reaction with Al[salphen(x)] and explain why this isn't seen in the heavier group 13 elements.

3.2 Mechanistic Investigations

Calculated energies were used to elucidate the free energy surfaces for each M[salphen(Cl)] catalyst (M = Al, Ga and In) (Figure 3.6). Based on the calculations, the general outline of the mechanism is as follows. In the first instance, ethylene oxide associates with the M[salphen(Cl)] species to form the initial complex (**IC**). Iodide from tertbutylammonium iodide (TBAI), attacks the lesser substituted carbon of ethylene oxide to open the epoxide ring and form **Int1**. The chloride ligand is then abstracted by a second catalyst to form **Int1+Di** and a dihalide catalyst complex ($M[salphen(Cl)_2]^-$). This allows the metal to protrude from the ligand structure and interact more strongly with CO_2 (Figure 3.5). This allows for a stronger interaction between the oxygen of CO_2 and the metal centre, creating a C-O dipole, reducing the HOMO-LUMO gap.

Subsequently, CO_2 insertion occurs at **TS2+Di**, the turnover frequency determining transition state (TDTS), to form an alkoxide structure at **Int2+Di**.

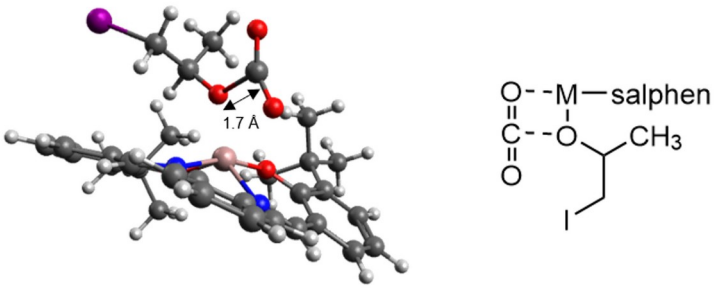

*Figure – Beyond Al: Group 13 salphen Catalysts for Efficient CO2 Utilisation. Insight from DFT calculations..41 - The insertion of CO_2 at **TS2** for [Ga(salphen)X]. Red = O, Grey = C, Purple = I, Blue = N and Peach = Ga.*

At **Int2+Di**, there are slight variations in the mechanisms for the different metals as stated below. For aluminium and gallium salphen, the chloride reassociates with the active catalyst from the dihalide species at **Int2+Di**, prior to both ring closing mechanisms. The reassociation of the ligand for indium salphen can occur in two separate places depending on which ring closing mechanism pathway is taken. Reassociation can occur at **Int2+Di** if ring closure pathway 1 one takes place (**R1**) and at **Int3R2+Di** if ring closure pathway 2 takes place (**R2**). For indium salphen, isomerisation is not possible once the chloride has reassociated. The general mechanism for **R1** sees the carbonyl oxygen of the alkoxide form a bond (1.7 Å) with the unsubstituted carbon, eliminating the iodide, to form propylene carbonate associated to the catalyst via the carbonyl oxygen (**FCR1**).

The general mechanism for **R2**, first undergoes an isomerisation via **TS3R2** to align the alkoxide oxygen bound to the metal centre with the carbon bearing the Iodide (**Int3R2**). **Int3R2** is proceeded by a ring closure to eliminate the iodide and forms **FCR2** where propylene carbonate is associated to the catalyst by the intra-ring oxygen that is bonded to the unsubstituted carbon. Upon propylene carbonate dissociating from the final complexes, the active catalyst is regenerated.

The energy span for the aluminium, gallium and indium pathways is 29.8, 36.1 and 29.0 kcal mol^{-1} respectively. The computed results suggest that the catalytic activity would be In ≈ Al > Ga. However, experimental results (Table 3.1) do not directly agree with this showing the catalytic activity as In > Ga > Al. As discussed,

aluminium salphen catalysed reactions can have solubility related issues and this was also seen in this reaction through the formation of a precipitate over the duration of the reaction.[1] As the aluminium was the least active, yet had a similar reaction barrier height to that of indium, the formation of the precipitate in this reaction must have impacted the overall yield. This could indicate the presence of an off-cycle intermediate forming during the reaction. Due to the size of the potential precipitants, molecular mechanics would need to be employed, although some basic structures are explored in Section 3.4.

Al has numerous intermediate energies across the potential energy surface where an off-cycle intermediate could be forming. From **Int1α** to **Int1β** all 3 group 13 metals show an exergonic energy difference for the abstraction of the halide. For aluminium, there is a 6.3 kcal mol^{-1} energy drop between the intermediates. This is significant compared to a 3.4 and 1.0 kcal mol^{-1} energy drop for gallium and indium respectively. The aluminium dihalide complex is significantly more stable. Furthermore, the stability of the dihalides ($M[salphen(Cl)_2]^-$) is inversely proportional to the experimental activity of the catalyst.

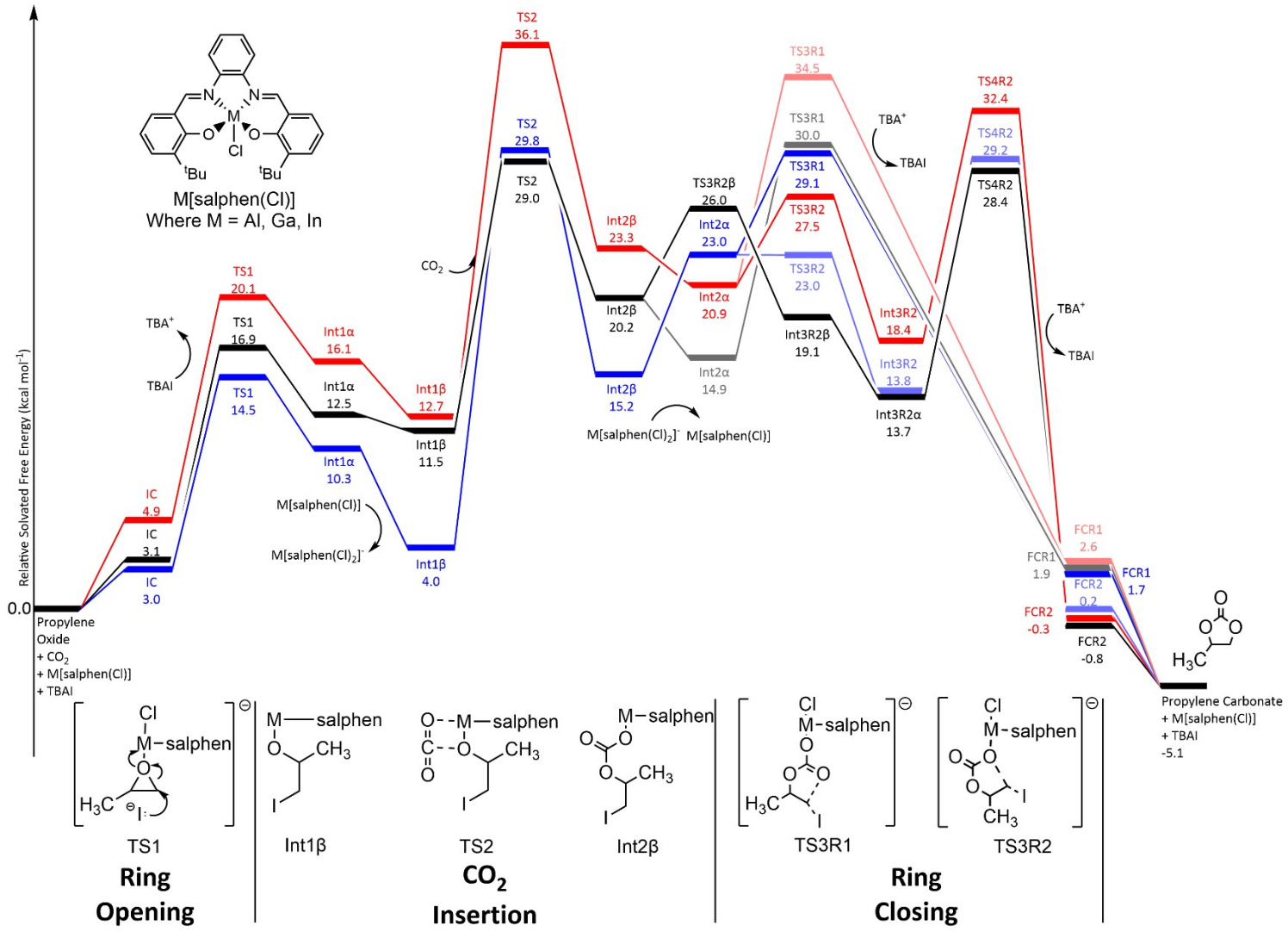

Figure – Beyond Al: Group 13 salphen Catalysts for Efficient CO2 Utilisation. Insight from DFT calculations..42 – Calculated solvated free energy surface in kcal mol^{-1} (ΔG 298 K) for the cycloaddition of CO_2 and propylene oxide catalysed by M[salphen(Cl)] (where M = Al, Ga and In), to form propylene carbonate at the ωB97-D3BJ/def2-tzvpp/def2/j level of theory. Blue = Al, Red = Ga and Black = In.

Proceeding **Int1β** is **TS2,** which is the rate determining transition state. The energy barrier for aluminium, gallium and indium is 25.8, 23.4 and 17.50 kcal mol^{-1} respectively, which is inversely proportional to the experimental activity. Another energetic difference in the aluminium pathway is between **Int2β** and **Int2α**. For gallium and indium, the reassociation of Cl^- is exergonic by 2.4 and 5.4 kcal mol^{-1} respectively. However, for aluminium, the reassociation is endergonic by 7.7 kcal mol^{-1}. Considering the inverse relationship of the dihalide complex stability and the **TS2** free energy barriers, between **Int1α** and **TS2** is a reaction coordinate in which an off-cycle intermediate could be formed. This is supported by the endergonic dissociation of Cl^- from the $Al[salphen(Cl)_2]^-$ complex.

Although insightful, experimental results are not in direct agreement with the calculated energy spans Al > In > Ga. The unknown precipitant formed over the duration of the reaction is responsible for this. DFT calculations were able to identify that the dihalide catalyst complex was much more stable for Al than the other group 13 metals. To compliment the DFT calculations, quantum theory of atoms in molecules (QTAIM), has been employed to investigate the different electronic properties of the catalysts and the contribution to the catalyst activities.

3.2.1 QTAIM Analysis of M[salphen(Cl)] Complexes

Bonding descriptors of M[salphen(Cl)] complexes are presented in Table 3.2. Table 3.2 highlights differences for H(r) (differences bolded for clarity). For the Al–O bonds, H(r) is positive, however, the Ga–O and In–O bonds have is negative. A positive H(r) is indicative of a more ionic interaction, whereas a negative value suggests stronger covalent bonding character. Fundamentally, this shows there is a difference in bonding between the Al and Ga/In catalysts with O bonding atoms of salphen. This would be expected as the Al^{3+} ion is much smaller and harder than Ga^{3+}/In^{3+} and so more likely to be involved with ionic bonds. The Al–N bonds also are very close to a positive H(r) value showing similar behaviour. The difference in bonding means that the Al[salphen(X)] complexes are more likely to form ionic aggregates or oligomers. If these structures were thermodynamically stable, they would be able to precipitate out of solution. This agrees with the $Al[salphen(X)_2]^+$ ionic complex being more stable than the Ga and In counterparts and provides insight into why precipitate is observed with the Al catalyst reaction system.

Table – Beyond Al: Group 13 salphen Catalysts for Efficient CO2 Utilisation. Insight from DFT calculations..5 – QTAIM topological data for each M[salphen(Cl)] performed using wavefunctions obtained at the ωB97-D3BJ/def2-tzvpp/def2/j level of theory. Topological analysis was carried out using the Multiwfn package. Structure below the table highlights which bonds are A and B, red = oxygen, peach = metal, grey = carbon, white = hydrogen, blue = nitrogen and green = chlorine.

Catalyst	Bond	ρ(ea^{-3})	V(r) (E$_h$a^{-3})	G(r) (E$_h$a^{-3})	H(r) (E$_h$a^{-3})	∇^{2}ρ(r) (ea^{-3})
	Al–Cl	0.0604	-0.0871	0.0764	-0.0106	0.263
	Al–O(A)	0.0685	-0.120	0.127	**0.00688**	0.535
Al[salphen(Cl)]	Al–O(B)	0.0676	-0.118	0.125	**0.00679**	0.528
	Al–N(A)	0.0520	-0.0749	0.0737	-0.00121	0.290
	Al–N(B)	0.0534	-0.0774	0.0764	-0.00104	0.301
	Ga–Cl	0.0815	-0.0975	0.0721	-0.0254	0.187
	Ga–O(A)	0.0902	-0.138	0.128	**-0.00938**	0.475
Ga[salphen(Cl)]	Ga–O(B)	0.0884	-0.134	0.125	**-0.00897**	0.465
	Ga–N(A)	0.0756	-0.0972	0.0797	-0.0175	0.249
	Ga–N(B)	0.0778	-0.101	0.0833	-0.0179	0.262
	In–Cl(B)	0.0700	-0.0752	0.0637	-0.0115	0.209
	In–O(A)	0.0752	-0.105	0.105	**-0.000440**	0.418
In[salphen(Cl)]	In–O(B)	0.0753	-0.105	0.104	**-0.000641**	0.415
	In–N(A)	0.0654	-0.0774	0.0716	-0.00583	0.263
	In–N(B)	0.0644	-0.0755	0.0699	-0.00566	0.257

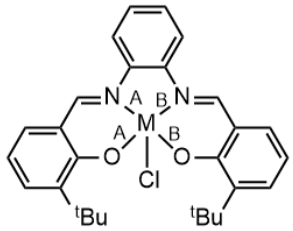

Laplacian maps of the electron density ($\nabla^2\rho$) were generated for the M[salphen(Cl)] complexes to visualise regions of electron density concentration and depletion within the catalyst (Figure 3.7). In these maps, negative values of $\nabla^2\rho$ (blue regions) correspond to areas of electron density concentration, typically associated with lone pairs or shared interactions, whereas positive values (yellow–red regions) indicate closed-shell interactions.

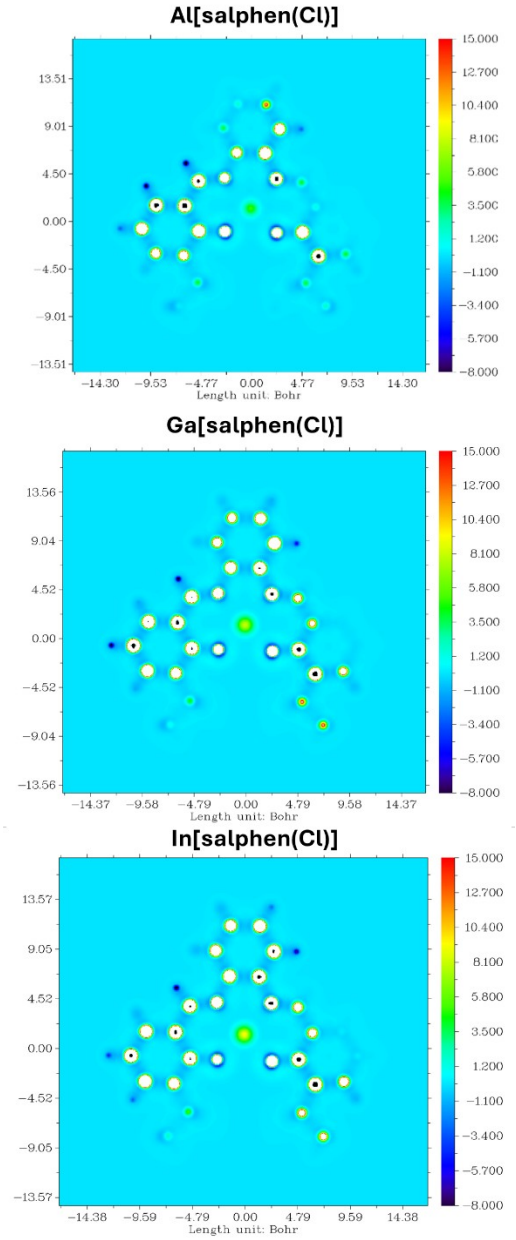

Figure – Beyond Al: Group 13 salphen Catalysts for Efficient CO2 Utilisation. Insight from DFT calculations..43 - Laplacian maps of the electron density ($\nabla^2\rho$) for the M[salphen(Cl)] complexes (M = Al, Ga, In). Regions of electron density concentration (negative $\nabla^2\rho$) are shown in blue, while regions of electron density depletion (positive $\nabla^2\rho$) are shown in yellow. $\nabla^2\rho$ measured in ea^{-3}.

Comparing the Laplacian maps reveals a trend in the distribution of electron density across the series Al → Ga → In. The aluminium complex exhibits the most

electron depletion around the metal centre and strong density concentration at the ligand donor atoms. This is consistent with the QTAIM analysis in Table 3.2, where the Al–O interactions display positive H(r) values. The gallium complex shows reduced metal-centred depletion and slightly more diffuse ligand density, while the indium complex displays the most diffuse electron density around the metal centre. H(r) values reflect this trend, with the Ga–O interactions exhibiting negative values and the In–O interactions approaching zero, suggesting increasing shared interaction character down the group. Together, the Laplacian maps and bond critical point analysis indicate a gradual reduction in the polarity of the metal–ligand interactions from aluminium to indium, consistent with increasing metal size and decreasing Lewis acidity across the series.

3.3 In-depth Mechanistic Analysis

3.3.1 Halide Abstraction/Reassociation

At **Int1** the halide ligand can be abstracted from the active catalyst by TBA^+ or a second catalyst. Calculations show that the catalyst-based abstraction is energetically favourable compared to TBA^+ (Table 3.3). The relative stability of the dihalide complex decreases as the size of the metal increases, explaining why Cl^- abstraction is less exergonic for the larger metals.

Table – Beyond Al: Group 13 salphen Catalysts for Efficient CO2 Utilisation. Insight from DFT calculations..6 - The relative free energetic stability (kcal mol^{-1}) when the halide ligand is abstracted by either the catalyst (entries 1-3) or TBA+ (entries 4-6). The relative stability for the catalyst abstraction is between M[salphen(Cl)] vs. M[salphen(Cl)$_2$]. The relative stability of the TBA^+ abstraction is between TBA^+ being a free ion in solution vs. being neutralised by abstraction of the halide ligand.

Entry	Abstracted By	Relative Stability (kcal mol^{-1})
1	Al[salphen(Cl)]	-6.3
2	Ga[salphen(Cl)]	-3.4
3	In[salphen(Cl)]	-1.0
4	TBA^+ (Al Salphen Pathway)	-2.1
5	TBA^+ (Ga Salphen Pathway)	-1.4
6	TBA^+ (In Salphen Pathway)	+8.2

For the gallium and indium salphen complexes, the reassociation of the halide ligand is exergonic by 2.4 and 5.4 kcal mol^{-1} respectively. However, the reassociation for the aluminium salphen it is endergonic by 7.7 kcal mol^{-1}. These energies agree with the dihalide stability (Table 3.3), as these show a stabilisation energy in this region without considering the energy of the intermediate.

The indium pathway also sees the chloride reassociate at a different point in the mechanism. Rather than the reassociation of the halide ligand occurring at **Int2**, it occurs at **Int3R2,** after the isomerisation. To try and justify the halide reassociation differences seen in the indium pathway, non-covalent interaction (NCI) analysis was undertaken on **TS3R2,** for each catalyst using Multiwfn.[14] NCI analysis highlights areas of non-covalent repulsion and attraction via the form of reduced density gradients. These can be portrayed graphically, where areas of repulsion are highlighted by a red colour, weak interactions (Van der Waals forces) by a green colour and strong interactions (i.e. H-Bonds) by a blue colour. Some further examples of inte 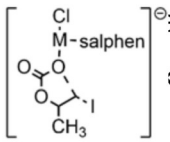

TS3R2
e steric hinderance, ring strain, electrostatic repulsion/attraction a
king interactions.[14]

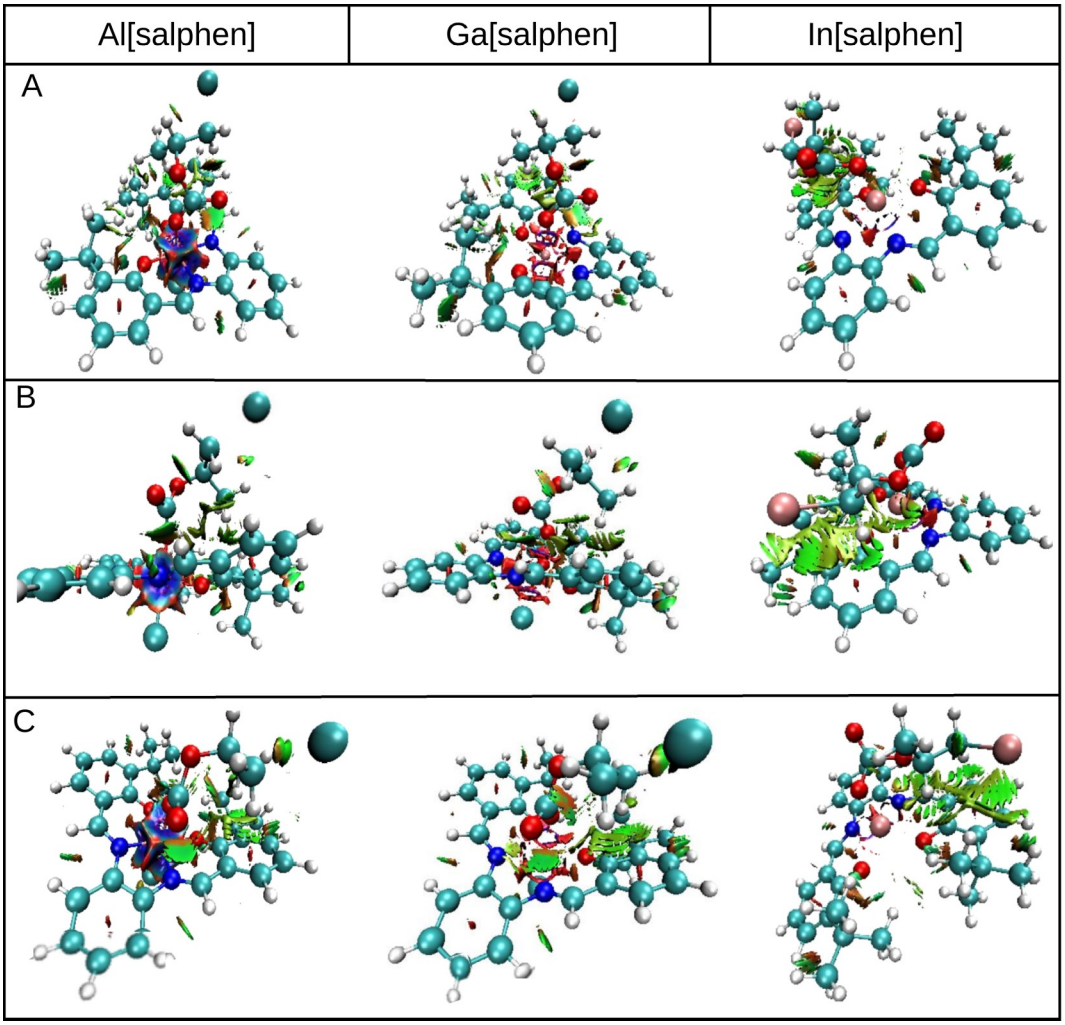

Figure – Beyond Al: Group 13 salphen Catalysts for Efficient CO2 Utilisation. Insight from DFT calculations..44 - Reduced density gradient isosurfaces for Al, Ga and In[salphen] (from left to right respectively) at ***TS3R2****.*

Figure 3.8 displays the reduced density gradient (RDG) isosurfaces produced by NCI analysis. Row A shows each salphen metal centre and how it is interacting with the ligand at **TS3R2**. The In[salphen] does not bear a halide ligand in this figure as it does not recoordinate until **Int3R2**. Row A shows the interaction of each metal centre with the ligand. Rows B and C provide two different perspectives of the alkyl halide bound to the metal centre and how it is interacting with the salphen ligand structure. Row A shows differences in how the metal is interacting and positioned around the ligand. Aluminium salphen has a blue region surrounding the salphen ligand and metal centre. Therefore, the aluminium is bonding with the ligand more ionically. Conversely, a blue region is not present for the gallium and indium suggesting they share more covalent interactions.

The second notable difference displayed in row A is the indium atom is protruding from the centre of the salphen ligand towards the alkyl halide substrate, whereas the gallium and aluminium atoms are sat in the centre of the salphen ligand (a more detailed discussion of the calculated τ_5 geometry indexes is in Section 3.5). As the ionic radii size of the metal increases from aluminium to gallium, a significant amount of red appears on the RDG isosurface between the metal and the ligand, because of increased steric hinderance. Furthermore, the continued increase in size between gallium and indium would create even more repulsion if the indium was in the centre of the salphen ligand. A combination of this factor, as well as the bulky alkyl halide isomerising above the metal, means the indium salphen requires the halide ligand to remain dissociated until **Int3R2**, to allow the indium atom to protrude the ligand and reduce the amount of steric hinderance during the isomerisation.

Rows B and C show very similar interactions for all three metal salphens. For the aluminium and gallium salphen complexes there is a van der Waals interaction between the carbonyl oxygen and one of the nitrogen of the salphen ligand. The indium on the other hand, shows a similar interaction, but with the oxygen originating from propylene oxide. All three salphens show Van der Waals interactions between the alkyl halide chain and the centre of the phenyl ring of the salphen. However, in the indium salphen structure, there is an extra Van der Waals interaction between the iodide and bulky tert-butyl group.

The graphical representations of the RDGs (Figure 3.9) allow an alternative way to analyse the different intra-atomic interactions. The depth and concentration of

points, particularly below 1 arbitrary unit, give measurement of the amount of each force present.

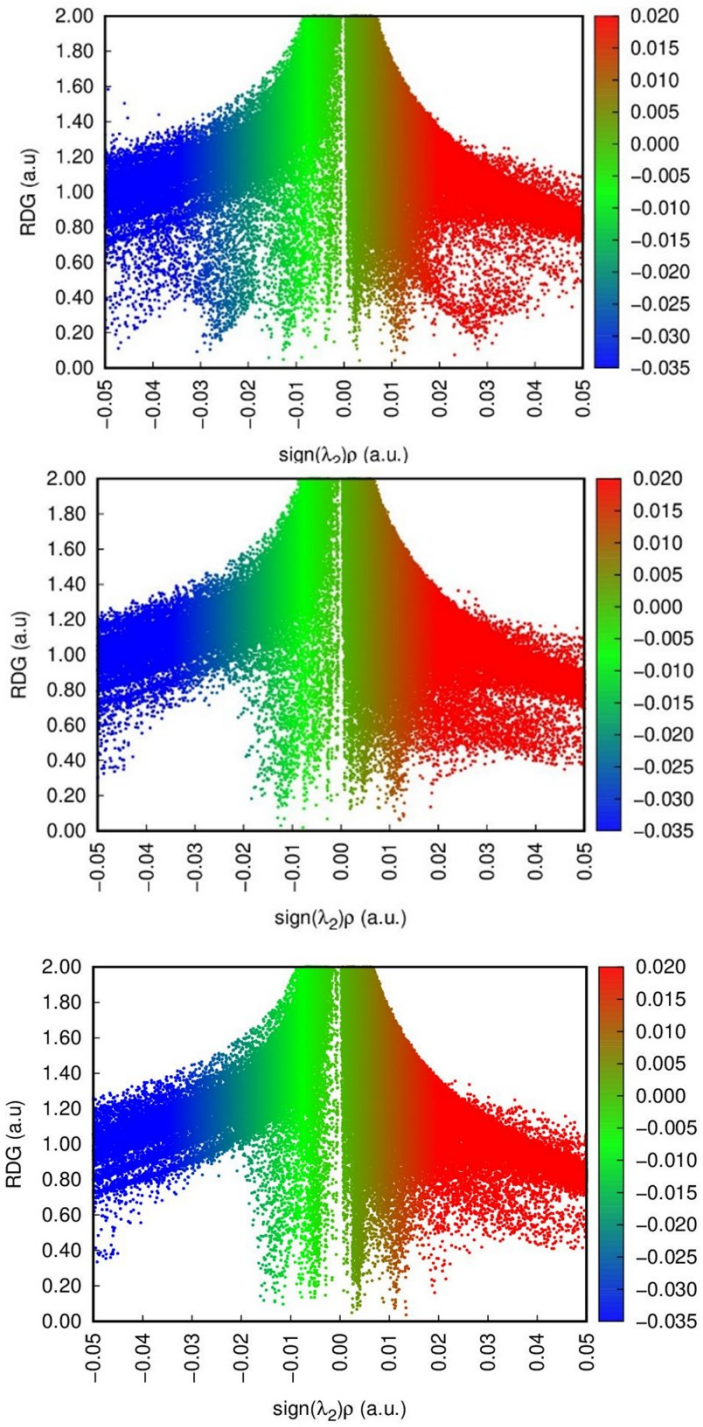

*Figure – Beyond Al: Group 13 salphen Catalysts for Efficient CO2 Utilisation. Insight from DFT calculations..45 - Graphically represented RDGs of **TS3R2** for Al[salphen] (top), Ga[salphen] (middle) and In[salphen] (bottom). RDG values are dimensionless and sign(λ_2)ρ values are reported in atomic units of electron density (ea_0^{-3}), as produced by Multiwfn.*

Figure 3.9 shows an obvious increase in the concentration and depth of the red region of the graph between the aluminium and gallium. Between gallium and indium, the red region becomes less intense due to the indium sitting off centre of

the salphen ligand. The green regions for all three metals look very similar in depth and intensity, showing that there are similar levels of Van der Waals forces present, indicating that all the alkyl halides are interacting with similar part of the salphen ligands whilst isomerising. Finally, the aluminium complex shows a strong blue presence compared to the gallium and indium complexes, highlighting the more ionic nature of the metal to ligand interaction, as discussed above.

3.3.2 Ring Closing Mechanisms

The different pathways to ring closing of the alkoxide to form the cyclic carbonate see variations between the three catalysts. For Al[salphen(Cl)], both pathways, **R1** and **R2** (Scheme 3.2), are energetically equivalent with only a 0.1 kcal mol^{-1} energy difference in barrier height. Consequently, both pathways would happen simultaneously without being distinguished as there are no product isomers. The Ga[salphen(Cl)] shows a clear preference for **R2** by 7.0 kcal mol^{-1}. Although **R2** is more energetically favourable in this case, **R1** is still energetically accessible but it will occur at a much lower rate. Previous studies by Kleij and Bo on Zn-salphen, show a clear preference for **R1** with a 2.8 kcal mol^{-1} favourability over **R2**.[11]

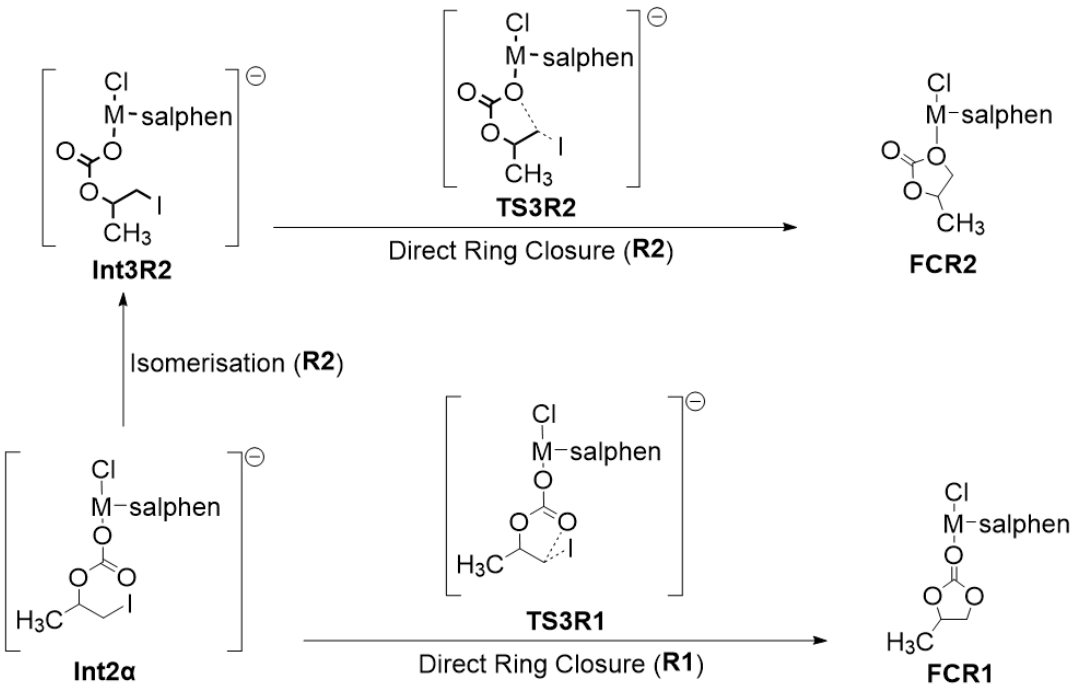

*Scheme – Beyond Al: Group 13 salphen Catalysts for Efficient CO2 Utilisation. Insight from DFT calculations..11 - Reaction scheme showing the two different ring closure mechanisms, **R1** and **R1**.*

Similarly, to Ga[salphen(Cl)], the **R2** route is preferred for In[salphen(Cl)]. However, this is much less significant to the gallium catalyst with **R2** only being favourable by 1.6 kcal mol^{-1}, because of the reassociation of the halide ligand at **Int3R2**, lowering the pathway after the transition state.

3.4 Solubility Issues

Identifying the structure of an off-cycle intermediate can be extremely difficult computationally. In the case of the insoluble aluminium precipitate, experimental analysis has been inconclusive as to the exact nature of the precipitate. Consequently, with little experimental insight, computational investigations become time-consuming due to the number of structural possibilities of the compound. To narrow this down, the previously discussed mechanistic differences in Figure 3.8 are a good starting point to look for an off cycle intermediate.

One difference between aluminium salphen to the gallium and indium adducts is the stability of the dihalide complexes. The energies in Table 3.4 show the free energy changes between the intermediates where the chloride dissociates and reassociates to the active catalyst. The order of stability is Aluminium > Gallium > Indium. The aluminium dihalide formation is 3.9 kcal mol^{-1} more stable than gallium and 5.3 kcal mol^{-1} more stable than Indium. The reassociation of the chloride to the active catalyst which a +11.1 kcal mol^{-1} difference in energy for aluminium compared to the gallium, sees a 13.2 kcal mol^{-1} difference in free energy compared to indium. It is also endergonic for the aluminium product compared to exergonic for gallium and indium, showing a difference in stability of the aluminium dihalide structure.

The stability of the dihalide complexes is inversely correlated to the catalyst activity shown experimentally and could explain the solubility effects shown in the aluminium pathway. Due to it being an anion, an ion pair would be an obvious candidate for the precipitate.

*Table – Beyond Al: Group 13 salphen Catalysts for Efficient CO2 Utilisation. Insight from DFT calculations..7 - Free energy changes between the dissociation of the chloride at **Int1α** and the reassociation of the chloride at **Int2β** for Al-Salphen and **Int3R2β** for In- and Ga-salphen salphen.*

	Free Energy for Cl^- Dissociation (kcal mol^{-1})	Free Energy for Cl^- Reassociation (kcal mol^{-1})
Al	-6.3	+7.7
Ga	-2.5	-3.3
In	-1.0	-5.4

3.4.1 [TBA^+] [$Dihalide^-$]

The [TBA^+][$Dihalide^-$] complex became of interest due to work from North's group.[10] They proposed a dihalide structure as the starting point for the mechanism for Cr[salophen(Br)] (Figure 3.10).

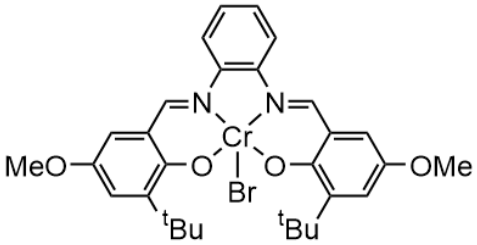

Figure – Beyond Al: Group 13 salphen Catalysts for Efficient CO2 Utilisation. Insight from DFT calculations..46 – Cr[salophen(Br)] structure which begins the mechanistic cycle in the dihalide form by abstraction of Br from TBABr.[10]

The dihalide is formed by the catalyst abstracting I^- from TBAI, to form a cationic complex, Cr[salophen]$^+$. This led to investigations into this complex due to it being a potential candidate for causing the solubility issues. It was hypothesised that if the aluminium complex was to be significantly lower in energy compared to the other metal complexes, it had potential to be precipitating out of solution and hindering the reaction. However, Table 3.5 shows that this would not be applicable for this system. In all cases the formation of [TBA^+][$Dihalide^-$] is more endergonic than the epoxide associating to the catalyst (**IC**). As a result, it would be more thermodynamically favourable to form **IC** than [TBA^+][$Dihalide^-$].

Table – Beyond Al: Group 13 salphen Catalysts for Efficient CO2 Utilisation. Insight from DFT calculations..8 - The relative free energy difference between the starting point (the reactants in solution) and the formation of the [TBA+][Dihalide-] complex. L = salphen.

Complex	[TBA^+][$Dihalide^-$] Free Energy of Formation (kcal mol^{-1})	IC Free Energy of Formation (kcal mol^{-1})
Al	+ 5.9	+ 1.6
Ga	+ 7.8	+ 3.5
In	+ 2.6	+ 1.8

3.4.2 Catalyst Dimer

Another potential candidate studied was a dimeric catalyst structure (Figure 3.11). It has already been proven that a second catalyst can abstract the halide ligand from the

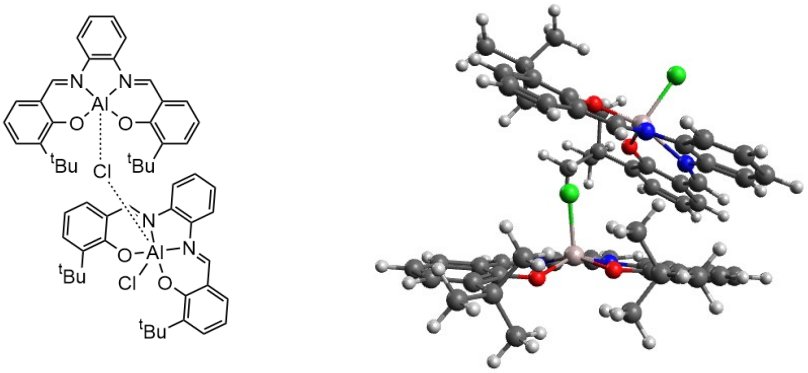

mechanistically active catalyst.

Therefore, it would be a suitable prediction that the monomeric catalyst complexes could be forming oligomeric chains which lead to it precipitating out of the reaction.

Figure – Beyond Al: Group 13 salphen Catalysts for Efficient CO2 Utilisation. Insight from DFT calculations..47 – Chemdraw and the calculated optimised structure of the catalyst dimer structure for [Al(salphen)(μ-Cl)]$_2$. Red = oxygen, blue = nitrogen, green = chloride, grey = carbon, white = hydrogen and peach = aluminium.

Table 3.6 shows that the free energy needed for dimer formation all dimers is more than 30 kcal mol^{-1} rendering this energetically unfeasible. This can be accounted for due to the Lewis acidic nature of the salphen complex wanting to accept electrons. The sharing of the halide ligand from the second catalyst makes it more cationic in nature and increases the energy of the complex.

Table – Beyond Al: Group 13 salphen Catalysts for Efficient CO2 Utilisation. Insight from DFT calculations..9 - The relative free energy difference between the starting point (the reactants in solution) and the formation of the catalyst dimer complex.

Catalyst	[Dihalide^{-}][Cationic Catalyst^{+}] Free Energy of Formation (kcal mol^{-1})
AlCl	36.5
GaCl	37.9
InCl	33.1

While no exact structure of the insoluble intermediate could not be identified, **Int1β** is a target area of the mechanism where this could be forming. At this point of the mechanism Al is stabilised significantly more than Ga and In. As this is the point at which the halide ligand is abstracted, it would be predicted that an insoluble, ionic complex is seeding from the anionic dihalide complex. This would also agree with the QTAIM calculations which showed Al to have more ionic bonds.

3.5 Exchanging of Halide Ligand

The halide ligand clearly plays a significant role in the mechanism of the reaction. Therefore, DFT calculations were undertaken to predict the effects of changing the halide ligand. Cl, Br and I were all studied computationally and the optimised structures of the M[salphen(X)] complexes can be seen in Figure 3.12.

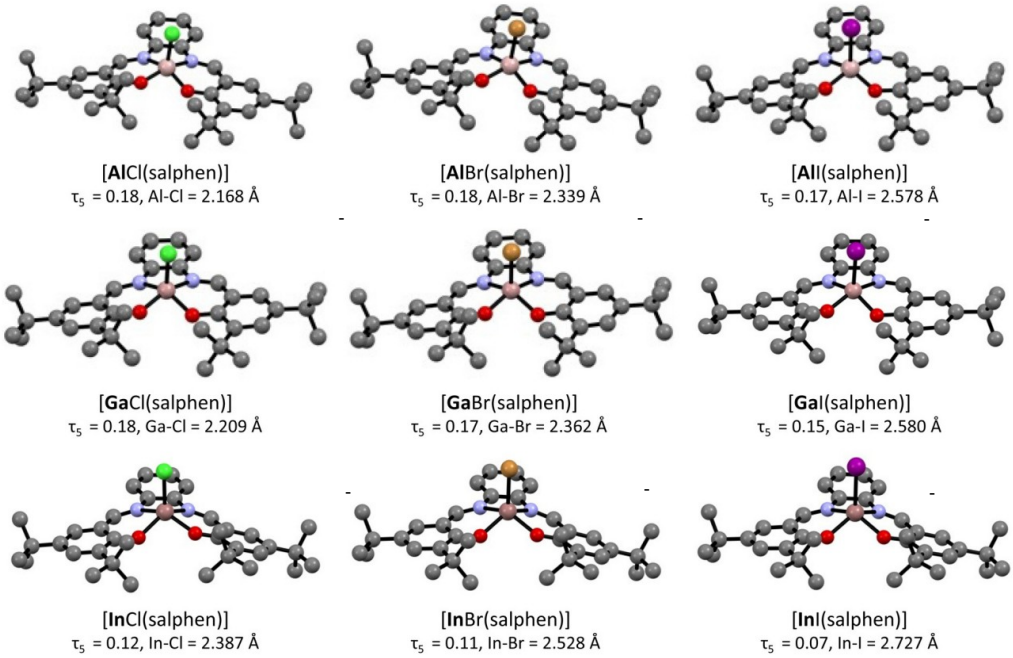

Figure – Beyond Al: Group 13 salphen Catalysts for Efficient CO2 Utilisation. Insight from DFT calculations..48 – Calculated structures (RI-B97-D3/def2-SVP) of the [MX(salphen)] compounds (M = Al, Ga and In; X = Cl, Br and I) with τ5 values and M–X bond lengths. Hydrogen atoms omitted for clarity from Ref. 1.
[1]

Geometry optimisations were performed for all nine [MX(salphen)] complexes to enable direct comparison of structural distortion across the series. The calculated τ_5 values reveal that, for the aluminium complexes, the halide identity has minimal influence in the gas phase, with $\tau_5 \approx 0.17–0.18$ for AlCl, AlBr and AlI. This contrasts with the available solid-state data, where [AlCl(salphen)] exhibits a lower distortion ($\tau_5 = 0.10/0.12$) and [AlBr(salphen)] shows a significantly higher value ($\tau_5 = 0.32$), likely influenced by intermolecular hydrogen bonding in the crystal lattice. In the case of the gallium analogues, the calculated τ_5 values (0.15–0.18) are more consistent with experimental trends and indicate only modest geometric variation across the halides.[1] For the indium systems, where no solid-state structures are available, the calculated geometries show a clear reduction in distortion down the group, with τ_5 decreasing from 0.12 (InCl) to 0.07 (InI). The particularly low τ_5 value for [InI(salphen)] suggests an almost ideal square pyramidal geometry, which can be rationalised by the increased ionic radius of indium relative to aluminium and gallium, allowing reduced ligand strain and more favourable coordination geometry.

Figures 3.13-3.15 show the potential free energy surfaces of $M[(salphen)(X)_2]^-$ where M = Al, Ga and In and X = Cl, Br and I. The reactions were studied between the point of dissociation and reassociation of the halide ligand, as this is the place in which halide effects will have the greatest impact on the reaction free energies. For all metals, changing the halide ligand does not change the general mechanistic pathway.

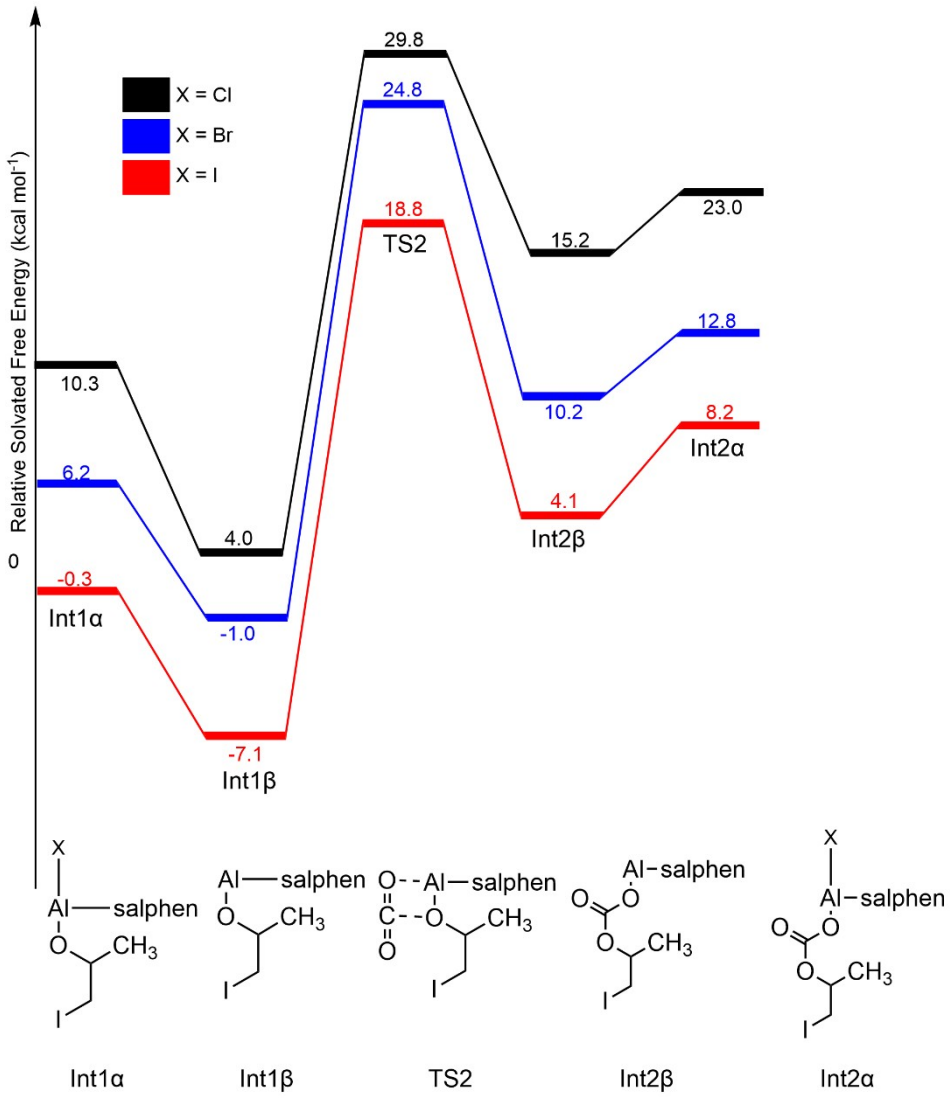

*Figure – Beyond Al: Group 13 salphen Catalysts for Efficient CO2 Utilisation. Insight from DFT calculations..49 – Calculated solvated free energy surface in kcal mol^{-1} (ΔG 298 K) for Al[(salphen)(X)$_2$]$^-$ (X = Cl, Br and I) between **Int1α** and **Int2α** at the ωB97-D3BJ/def2-tzvpp/def2/j level of theory. The relative zero is the reactants in solution.*

Figure 3.13 shows that there is a general periodic trend for the different halides for ga aluminium. As the size of the halide increases, energies generally decrease across all intermediates and transition states. The stability of the dihalide complex also increases, the dissociation step becomes more exergonic and the reassociation more endergonic.

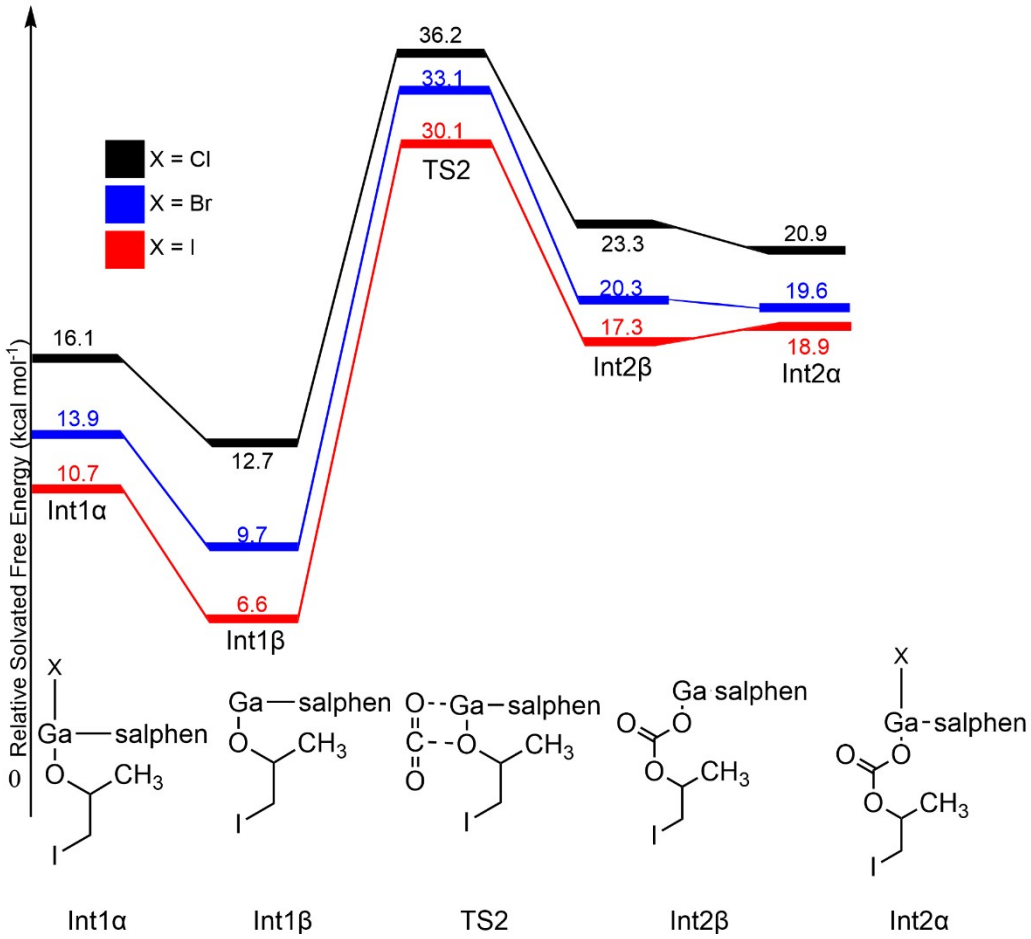

*Figure – Beyond Al: Group 13 salphen Catalysts for Efficient CO2 Utilisation. Insight from DFT calculations..50 – Calculated solvated free energy surface in kcal mol^{-1} (ΔG 298 K) for Ga[(salphen)(X)$_2$]$^-$ (X = Cl, Br and I) between **Int1α** and **Int2α** at the ωB97-D3BJ/def2-tzvpp/def2/j level of theory. The relative zero is the reactants in solution.*

Figure 3.14 shows the effects of changing the halide for the Ga[salphen(X)] complex. The dissociation for the bromide and iodide pathways happens with a 4.2 kcal mol^{-1} and 4.1 kcal mol^{-1} drop in free energy respectively. In comparison, the chloride pathway sees a 3.4 kcal mol^{-1} decrease. This follows the same pattern as the aluminium. The reassociation iodide becomes endergonic and consequently **Int2α** is higher in free energy than **Int2β**. This behaviour is identical to that initially observed in the Al[salphen(X)] mechanisms and can be attributed to the increased stability of M[salphen(X)$_2$] complexes.

Figure 3.15 shows that indium does not follow this general halide trend. Instead, there is a minimal effect on the overall reaction energetics, with the only exception being the dissociation (**Int2α**) and reassociation of the iodide being endergonic. However, it has already been established that halide reassociation does not occur at **Int2β** for the indium pathway, consequently this step was not investigated in

detail. In summation of Figure 3.14, based on the calculations the Br and Cl complexes are equally active catalysts with the iodide ligand being less active. The iodide complex shows a +1–2 kcal mol^{-1} energy difference across the mechanism compared to the other two complexes.

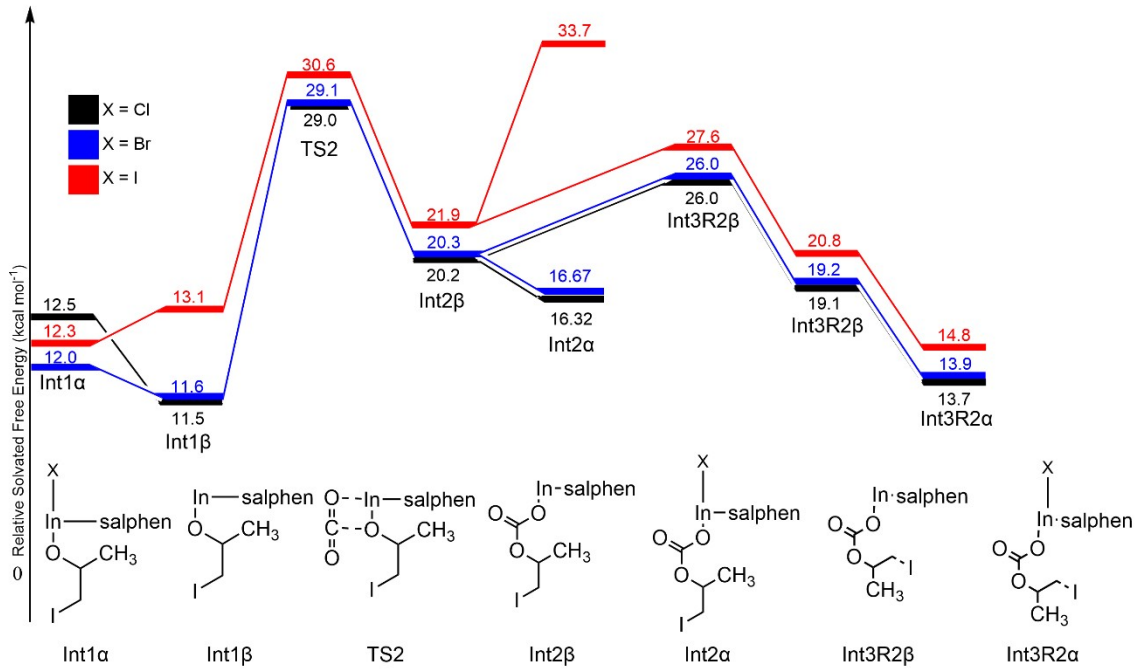

*Figure – Beyond Al: Group 13 salphen Catalysts for Efficient CO2 Utilisation. Insight from DFT calculations..51 – Calculated solvated free energy surface in kcal mol^{-1} (ΔG 298 K) for In[(salphen)(X)$_2$]$^-$ (X = Cl, Br and I) between **Int1α** and **Int3R2α** at the ωB97-D3BJ/def2-tzvpp/def2/j level of theory. The relative zero is the reactants in solution.*

3.5.2 FIA Calculations

Using the methodology described in section 2 by Erdmann *et al.*,[15] the FIA values were calculated for all nine catalyst complexes (Figure 3.16). The higher the FIA value, the greater the Lewis acidic strength of the catalyst.

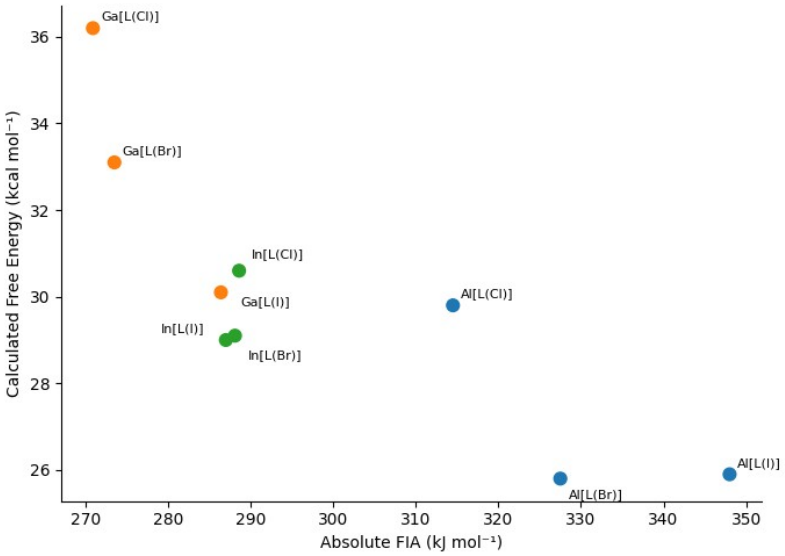

Figure – Beyond Al: Group 13 salphen Catalysts for Efficient CO2 Utilisation. Insight from DFT calculations..52 - The calculated reaction free energy barrier (kcal mol^{-1}) vs. the FIA (kJ mol^{-1}) for the M[L(X)] catalysts where M = Al, Ga and In; X = Cl, Br and I and L = salphen.

Figure 3.16 shows the relationship between the FIA and calculated reaction free energy barrier. For the aluminium and gallium salphens, the heavier the halide the more Lewis acidic the catalyst becomes. This is in line with the computational data showing lower energy pathways for the heavier halide complexes. The indium complexes do not follow the trend of the other two metals and despite changing the halide ion the Lewis acidic strength is similar. The general trend shows that as the Lewis acidic strength increases the calculated reaction free energy barrier decreases. However, this does not translate into a better catalyst experimentally due to solubility issues. As a result, it could be proposed that there is an optimum Lewis acidic strength within the range. This is further supported by the most active catalyst experimentally, In[salphen(Br)], falling in the mid-range of Lewis acidity and calculated free energy barrier height.

Comparing the chloride complexes for each salphen, the trend in Lewis acidic strength is Al > In > Ga. This agrees with the computed energy pathways showing the catalytic activity of Al ≈ In > Ga. If aluminium salphen did not encounter solubility issues, it would be reasonable to assume that it would be a highly active catalyst. Although the strength of Lewis acidity can provide a good indication of catalyst activity, other factors, such as solubility and solution dynamics of the catalyst, are not considered in the computational model. The over reliance on Lewis acidity as a descriptor for catalyst activity has been noted in the literature.[12,16] In this case, it appears that there is an optimal Lewis acidity region, rather than a proportional measure of activity.

3.6 Conclusion

This work successfully explains the experimental findings of the Whiteoak group for the cycloaddition of propylene oxide and CO_2 to form propylene carbonate, catalysed by aluminium, gallium and indium salphen. The full operative mechanism for each M[salphen(X)] (where M = aluminium, gallium and indium and X = Cl, Br and I) has been elucidated. The energies would predict the activity of the catalysts to be In ≈ Al > Ga disregarding the known solubility issues with aluminium. The barrier between **Int1** and **Int2** was highlighted as the origin of the insoluble Al complex forming, as the free energy barrier is 25.8 kcal mol^{-1} for Al, compared to gallium and indium which have an energy barrier of 23.4 and 17.5 kcal mol^{-1} respectively. Additionally, more in-depth analysis of the stability of dihalide complexes shows the aluminium dihalide, Al[salphen$(X)_2$], is the most stable. This further reinforces the formation of the dihalide structure originating at **Int1+Di**.

Several potential ion pairs, [TBA^+][$Dihalide^-$] and [$Dihalide^-$][Cationic $Catalyst^+$], were studied to identity the insoluble species seen in the Al-salphen pathway. In both cases, the reaction energetics favoured the formation of **IC** compared to the ion pair, leaving the insoluble complex unidentified. Therefore, this remains an area of interest for future work.

Due to the chloride ligand playing a role in the mechanism, it was exchanged with Br^- and I^- to see how it affected the free energy of the reaction. The mechanisms between **Int1** and **Int2** for gallium and indium, and between **Int1** and **Int3R2** for indium, were fully elucidated.

The energies showed a clear preference for the heavier halides with aluminium or gallium salphen adducts. This would suggest that as the halide becomes heavier, the aluminium and gallium catalysts would become more active, (discounting solubility issues). FIA calculations conclude that the heavier halide adducts were also more Lewis acidic. Therefore, the lower calculated free energy Br^- and I^- analogues of the catalysts have been attributed to their greater Lewis acidity. Indium salphen showed no real change in free energies or Lewis acidic strength when the halide changed, suggesting that there would be little change in activity when the halide is changed. Again, this was mirrored in the FIA calculations showing a direct link to the Lewis acidic strength of each catalyst.

This work demonstrates the importance of exploring wider chemical space. An unreactive Al catalyst initially led to the heavier group 13 elements being discounted as potential catalysts. This computational study shows this was not the case and the In[salphen(Br)] catalyst is extremely active. Furthermore, understanding why a catalyst is inactive is extremely important. This study shows that Al's harder Lewis acidity leads to ionic interactions. The formation of the insoluble precipitant has been closely associated with this difference, against the conventional understanding that a stronger Lewis acid is more active. To build on this, the substrate versatility (Chapter 4) and transferability to other catalysts (Chapter 5) will be explored.

3.7 Methodology

Computational calculations were undertaken using Orca 4.2.1.[17,18] Optimisation and frequency calculations were performed at the RI-B97-D3/def2-svp/j level of theory.[19–25] Final single point energies and solvent corrections were calculated at the RIJCOSX-ωB97-D3BJ/def2-tzvpp/j level of theory.[22–24,26,27] Solvation corrections were implemented with a dielectric constant of ε = 16.0 for the epoxide using the CPCM model.[27] Analytical frequencies were calculated for inclusion of the Zero Point Energy (ZPE) correction and entropic contributions to the free energy term (ΔG 298.15 K) as well as confirming all intermediates were true with no imaginary modes and all transition states exhibited a single imaginary frequency corresponding to the expected bond-forming and bond-breaking motions along the reaction coordinate. All thermodynamic parameters were calculated in the standard state (298.15 K and 1 atm). A larger numerical integration "grid 4" was used for the SCF steps of the calculation with grid5 being applied to the final energy evaluation step. Concentration correction for the individual species was applied as a free energy correction based on RT $\ln(c_i/c_{atm})$ [28] where c_i is the experimental concentration of the relevant species. Avogadro 1.2.0 was utilised to perform all structural analysis and graphical visualisations.[29] Post-wavefunction analysis methods (QTAIM and NCI) were performed using the Multiwfn package.[14]

3.8 References

1 D. J. Cabrera, R. D. Lewis, C. Díez-Poza, L. Álvarez-Miguel, M. E. G. G. Mosquera, A. Hamilton and C. J. Whiteoak, *Dalton Trans.*, 2023, **52**, 5882–5894.

2 A. Decortes, A. M. Castilla and A. W. Kleij, *Angew. Chem., Int. Ed.*, 2010, **49**, 9822–9837.

3 X. B. Lu, X. J. Feng and R. He, *Appl. Catal. A Gen.*, 2002, **234**, 25–33.

4 M. A. Sahudin, M. S. Su'ait, L. L. Tan, Y. H. Lee and N. H. Abd Karim, *Anal. Bioanal. Chem.*, 2019, **411**, 6449–6461.

5 S. Xu, J. Liu, D. Li, L. Wang, J. Guo, C. Wang and C. Chen, *Biomaterials*, 2014, **35**, 1676–1685.

6 J. A. Castro-Osma, M. North and X. Wu, *Chem. - Eur. J.*, 2016, **22**, 2100–2107.

7 M. North and R. Pasquale, *Angew. Chem.*, 2009, **121**, 2990–2992.

8 A. Decortes, M. Martínez Belmonte, J. Benet-Buchholz and A. W. Kleij, *Chem. Commun.*, 2010, **46**, 4580–4582.

9 X. Wu and M. North, *ChemSusChem*, 2017, **10**, 74–78.

10 J. A. Castro-Osma, K. J. Lamb and M. North, *ACS Catal.*, 2016, **6**, 5012–5025.

11 F. Castro-Gómez, G. Salassa, A. W. Kleij and C. Bo, *Chem. - Eur. J.*, 2013, **19**, 6289–6298.

12 L. Álvarez-Miguel, J. D. Burgoa, M. E. G. Mosquera, A. Hamilton and C. J. Whiteoak, *ChemCatChem*, 2021, **13**, 4099–4110.

13 J. Damián Burgoa, L. Álvarez-Miguel, M. E. G. Mosquera, A. Hamilton and C. J. Whiteoak, *Inorg. Chem.*, 2024, **63**, 15376–15387.

14 R. F. W. Bader, *Chem. Rev.*, 1991, **91**, 893–928.

15 P. S. V. Kumar, V. Raghavendra and V. Subramanian, *J. Chem. Sci.*, 2016, **128**, 1527–1536.

16 T. Lu and F. Chen, *J. Comput. Chem.*, 2012, **33**, 580–592.

17 P. Erdmann, J. Leitner, J. Schwarz and L. Greb, *ChemPhysChem*, 2020, **21**, 987–994.

18 H. Plommer, L. Stein, J. N. Murphy, N. Ikpo, N. Mora-Diez and F. M. Kerton, *Dalton Trans.*, 2020, **49**, 6884–6895.

19 F. Neese, *Wiley Interdiscip. Rev. Comput. Mol. Sci.*, 2018, **8**, 4–9.

20 F. Neese, *Wiley Interdiscip. Rev. Comput. Mol. Sci.*, 2012, **2**, 73–78.

21 S. Grimme, S. Ehrlich and L. Goerick, *J. Comput. Chem.*, 2011, **32**, 1456–1465.

22 F. Neese, *J. Comput. Chem.*, 2003, **24**, 1740–1747.

23 S. Grimme, *J. Comput. Chem.*, 2006, **27**, 1787–1799.

24 A. Schäfer, H. Horn and R. Ahlrichs, *J. Chem. Phys.*, 1992, **97**, 2571–2577.

25 F. Weigend, *Phys. Chem. Chem. Phys.*, 2006, **8**, 1057–1065.

26 F. Weigend and R. Ahlrichs, *Phys. Chem. Chem. Phys.*, 2005, **7**, 3297–3305.

27 A. D. Becke, *J. Chem. Phys.*, 1997, **8560**, 8554–8560.

28 F. Neese, F. Wennmohs, A. Hansen and U. Becker, *Chem. Phys.*, 2009, **356**, 98–109.

29 S. Sinnecker, A. Rajendran, A. Klamt, M. Diedenhofen and F. Neese, *J. Phys. Chem. A*, 2006, **110**, 2235–2245.

30 J. N. Harvey, F. Himo, F. Maseras and L. Perrin, *ACS Catal.*, 2019, **9**, 6803–6813.

31 M. Hanwell, D. Curtis, D. Lonie, T. Vandermeersch, E. Zurek and G. Hutchison, *J. Cheminform.*, 2012, **4**, 17.

Chapter 4 – Oxazolidinones *vs.* Piperazines: The Temperature Dependant Conundrum For The Cycloaddition Of Aziridines And CO_2

This work was published: M. D. G. Billacura, R. D. Lewis, N. Bricklebank, A. Hamilton and C. J. Whiteoak, *Adv. Synth. Catal.*, 2023, **365**, 3129–3137.[1]

4.1 Introduction

While it is essential to develop catalysts that are built for purpose and are highly efficient for specific reactions, it is also important that they remain versatile to a wide scope of similar substrates. A catalyst that can be applied across multiple related reactions is more cost-effective and resource-efficient than one that must be specifically tailored for each individual transformation. Mechanistic investigations with a variety of different substrates are also essential for further catalytic development. Novel binding modes, unseen mechanistic pathways and general information about a catalyst can be deduced from such investigations. Thereby informing the future of catalyst development. Figure 4.1 shows a range of substrates that would be suitable for a reaction akin to the cycloaddition of CO_2 and epoxides.

Figure – Oxazolidinones vs. Piperazines: The Temperature Dependant Conundrum For The Cycloaddition Of Aziridines And CO2.53 - Alternative substrates which, in theory, could be used to produce 5-membered heterocyclic rings through Lewis acidic catalysis.

The analogous aziridine (C_2H_4NH) substrate is of particular interest. Similarly to epoxides, the ring strained nature of the aziridine substrate means that the ring opening is significantly exergonic. Although both epoxides and aziridines are three-membered heterocycles and therefore highly strained, they differ significantly in their electronic and steric properties. Epoxides contain an electronegative oxygen atom, which strongly polarises the C–O bonds and renders the adjacent carbon centres electrophilic. In contrast, aziridines contain nitrogen, which is less electronegative and possesses a lone pair that can donate electron density into the ring, reducing overall bond polarisation. As a result, aziridines are generally less electrophilic than epoxides but can display greater coordination flexibility through nitrogen–metal interactions. Sterically, nitrogen substituents in aziridines are often bulkier and more variable than the typically smaller substituents found on epoxides, which can influence ring-opening pathways and metal coordination geometry. Consequently, while both systems are strain-activated, their reactivity profiles are governed by distinct electronic and steric contributions.

Ring opening of the aziridine relieves significant angle strain, stabilising the ring-opened intermediate. As the transition state involves partial C–N bond cleavage and geometric relaxation toward this lower-energy structure, the associated strain release lowers the free energy barrier for CO_2 insertion.[2] Cycloaddition between CO_2 and aziridines is an attractive prospect due to the formation of 5, 6 and 7-membered heterocyclic compounds.[3] These compounds are of high pharmaceutical and industrial importance.

The 5-membered ring predominantly formed is oxazolidinone ($C_2H_4NO(CO)$). Oxazolidinones were traditionally formed using phosgene ($COCl_2$) precursors.[4–6] This method of synthesis was not atom economical, and the substrates limited the reaction scope. Therefore, the 100% atom economical synthesis while using

CO_2 as a C_1 carbon feedstock at reasonable temperatures and pressures is of interest (Figure 4.2).

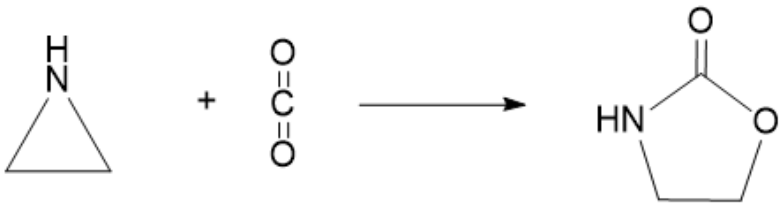

Scheme – Oxazolidinones vs. Piperazines: The Temperature Dependant Conundrum For The Cycloaddition Of Aziridines And CO2.12 - General reaction scheme for the synthesis of oxazolidinone from CO_2 and aziridine.

Oxazolidinones are a desirable product due to their uses. They have been prominently utilised as a chiral precursors for further synthesis to produce valuable carbon products.[7] Furthermore, oxazolidinones are used in antibiotic drugs (Figure 4.2).[8] This makes the aziridine a desirable target for cycloaddition with CO_2 to form oxazolidinones.

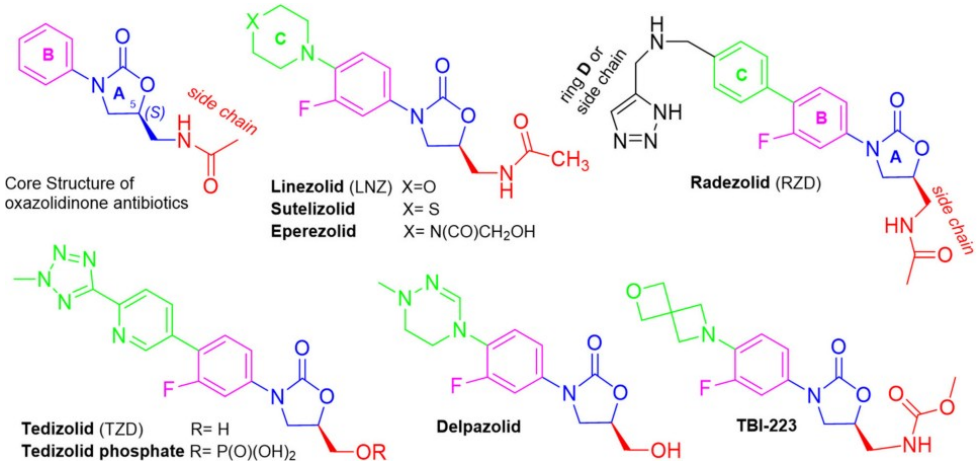

Figure – Oxazolidinones vs. Piperazines: The Temperature Dependant Conundrum For The Cycloaddition Of Aziridines And CO2.54 - A variety of antibiotics with the oxazolidinone motif in blue from 9.[9]

Interest in this field is growing, particularly with transferring the knowledge of epoxide systems to aziridine reaction systems. The North group were able to utilise their highly active bimetallic aluminium catalyst for a conversion of 98 % to oxazolidinone.[10] Another catalyst with translatable usage across the epoxide and aziridine substrate is a Cu_{12} metal organic framework (MOF) catalyst (**$\{[Cu_2(L^{4-})(H_2O)_2] \cdot 3DMF \cdot 2H_2O\}_n$**, where H_4L = 2′-fluoro-[1,1′:4′,1″-terphenyl]-3,3″,5,5″-tetracarboxylic acid (**A**)).[11,12] This catalyst was able to achieve yields of up to 98 % at 333 K with a 0.5 MPa CO_2 for 12 hours. With both the aziridine and epoxide being similar substrates, it was expected that the mechanisms would be

analogous. Calculations showed that both substrates followed the standard Lewis acidic mechanism (Scheme 3.2) with association of the 3-membered ring substrate to the metal centre, followed by co-catalyst assisted ring opening. The CO_2 insertion then occurred followed by ring closure to afford the product (Scheme 4.2).[11,12]

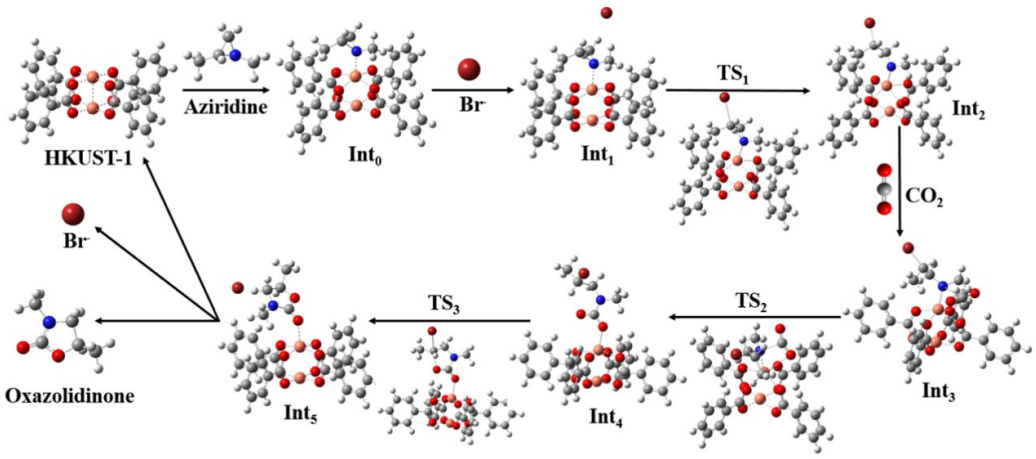

*Scheme – Oxazolidinones vs. Piperazines: The Temperature Dependant Conundrum For The Cycloaddition Of Aziridines And CO2.13 - A schematic representation of the elucidated mechanism for the cycloaddition of aziridine and CO_2 with a Cu_{12} MOF catalyst **A**. Grey = C, white = H, blue = N, pink = Cu and brown = Br from 11.*[11]

Although the mechanism presented in Scheme 4.2 is probable, other mechanisms for the synthesis of oxazolidinones were identified. A Lewis acidic chromium salen catalyst was found to catalyse the reaction via an adduct associative mechanism (Figure 4.3).[13,14] This associative route cycle begins with CO_2 associating to the catalyst, followed by the aziridine associating to CO_2. Then, an intramolecular concerted ring opening/closing occurs to form the oxazolidinone. This mechanism would be one to consider due to the utilisation of a Lewis acidic catalyst.

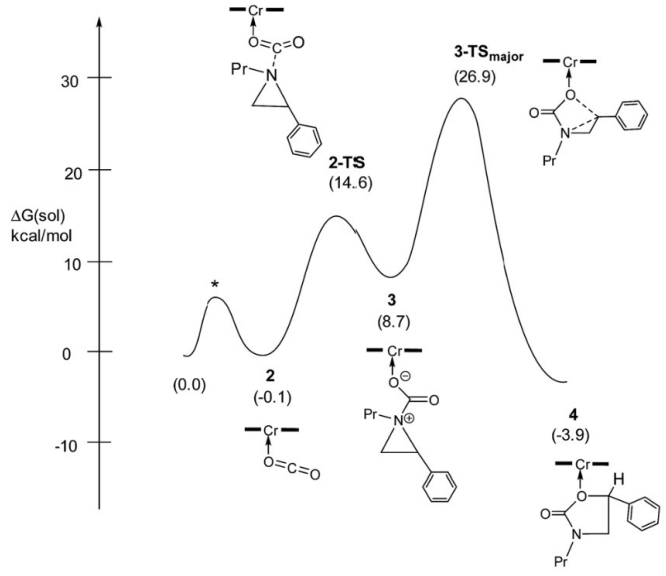

*Figure – Oxazolidinones vs. Piperazines: The Temperature Dependant Conundrum For The Cycloaddition Of Aziridines And CO2.55 - The calculated mechanism (M06/cc-pVTZ(-f)//M06/LACVP**) by Adhikari et al. following an adduct associative pathway using a Cr[salen] catalyst from 14.*[14]

Kleij *et al.* reported another mechanism of interest. This was for the cyclisation of epoxides and CO_2 using a V aminotrisphenolate catalyst.[15] The calculated mechanism saw a ligand cooperative ring opening of the epoxide. The general outline of the mechanism (Scheme 4.3) sees the epoxide associate to the catalyst. The oxygen of the ligand arm dissociates from the gallium to ring open the epoxide. CO_2 insertion then occurs to form an alkoxide. The halide from NBu_4X then eliminates the oxygen of the ligand arm allowing it to reassociate to the catalyst. Ring closure eliminates the halide, forming the cyclic carbonate product.

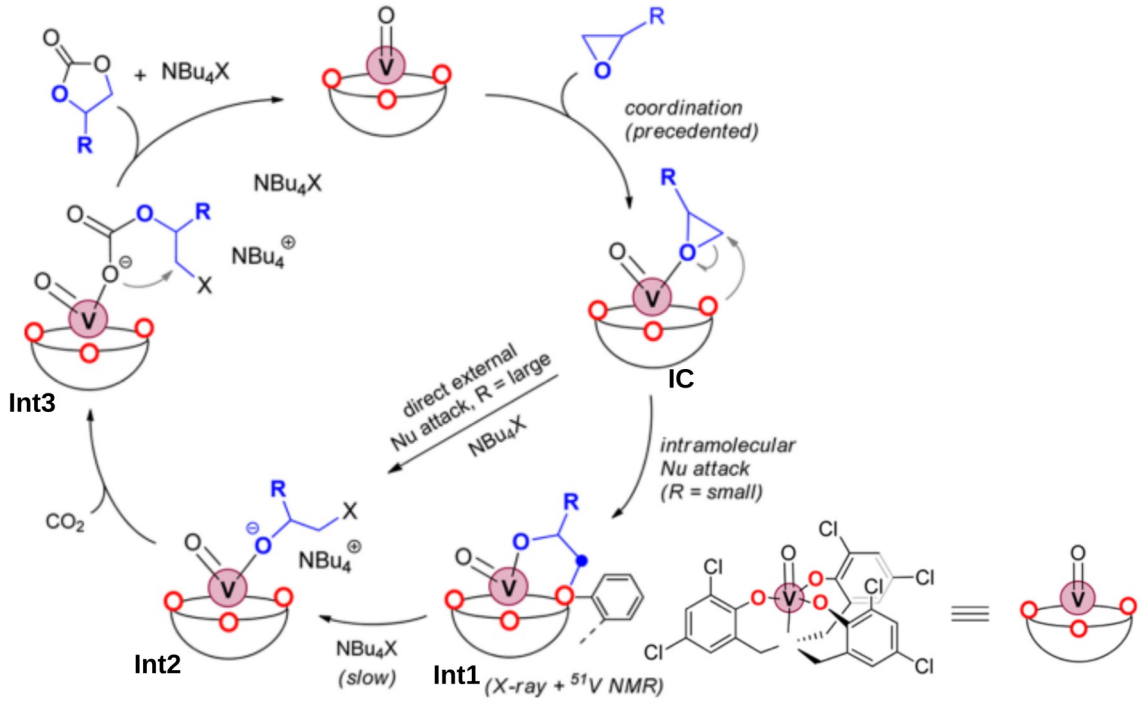

Scheme – Oxazolidinones vs. Piperazines: The Temperature Dependant Conundrum For The Cycloaddition Of Aziridines And CO2.14 - The mechanistic cycle for a ligand cooperative cycloaddition of CO_2 and epoxide using a V(aminotrisphenolate) catalyst and NBu_4X cocatalyst by Kleij et al. Key showing what the cone shape represents. Adapted from 15.[15]

A crystal structure was isolated for an intermediate from this pathway (Figure 4.4) thereby confirming the mechanism as viable option to consider for this study. The crystal structure, **Int1**, (Scheme 4.3) was the ring opened epoxide (OC_2Me) coordinated to the V metal centre and to one of the O^- donor atoms of the aminotrisphenolate ligand.

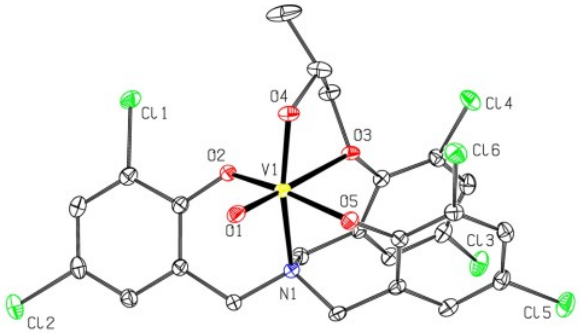

*Figure – Oxazolidinones vs. Piperazines: The Temperature Dependant Conundrum For The Cycloaddition Of Aziridines And CO2.56 - Crystal structure of **Int1** (V(aminotrisphenolate) with the ring opened epoxide (OC_2Me) coordinated to the V metal centre and to one of the O^- donor atoms of the aminotrisphenolate ligand.) obtained by Kleij et al from 15.*[15]

The use of group 13 Lewis acidic catalysts, beyond aluminium, for this cycloaddition is even more limited than that of the epoxides, as discussed in Chapter 3. Therefore, in continuation with the collaboration of the Whiteoak group

work, a gallium aminotrisphenolate catalyst was employed to look at the cycloaddition of aziridines and CO_2. The Ga aminotrisphenolate catalyst has already proven successful at catalysing the cycloaddition of epoxides and CO_2.[16] Ga aminotrisphenolate is a tetradentate aminotrisphenolate ligand comprising three anionic phenolate donors and a neutral amine donor. The ligand is formally trianionic and binds gallium(III) in a κ^4-N,O,O,O fashion, providing strong σ-donation and stabilising the Lewis acidic metal centre. In this study, two different aziridine substrates, 1,2-diphenylaziridine (**1a**), and 1-isopropyl-2-phenylaziridine (**1b**), were used to synthesise their respective oxazolidinones, 3,5-diphenyloxazolidin-2-one (**2a**) and 3-isopropyl-5-phenyloxazolidin-2-one (**2b**) respectively (Figure 4.5).

Experimental work by the Whiteoak group unravelled a temperature dependant reaction for **1a** which meant that a selective formation of a piperazine product could be achieved for the **1a** (Figure 4.5). At 333 K the **1a** forms the piperazine product and the **1b** forms the oxazolidinone product. At 373 K both aziridines form the oxazolidinone product. Substrates **1a** and **1b** translate to the respective labelled products. To the best of our knowledge, the selective formation of piperazines by alteration of the temperature has not been reported, although numerous groups see the presence of a piperazine byproduct in reactions.[17–19] The selective formation of piperazine is an attractive prospect due to its' importance as a motif in antiviral drugs for HIV and as an NK-1 antagonist which reduces nausea and vomiting in chemotherapy patients. The motif also accounts for a third of The United States Food and Drug Administration's (FDA's) approved nitrogen heterocycle drugs.[20,21]

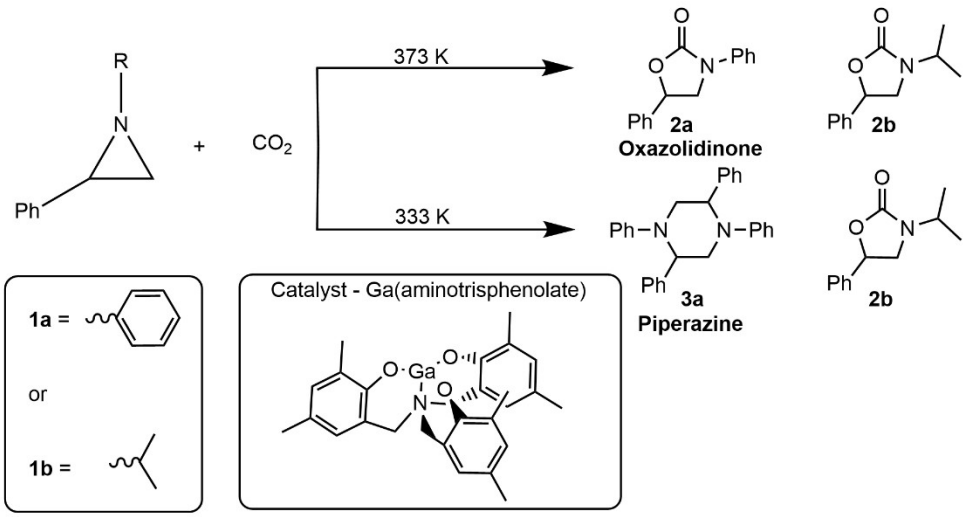

Figure – Oxazolidinones vs. Piperazines: The Temperature Dependant Conundrum For The Cycloaddition Of Aziridines And CO2.57 - The reaction between aziridines and CO_2 for the formation of piperazines and oxazolidinones catalysed by gallium aminotrisphenolate in methylethylketone (MEK).

Table 4.1 breaks down the experimental results observed by the Whiteoak group. **1b** only produced the oxazolidinone substrate at 333 K and 373 K. However, at 333 K, **1a** produced the piperazine product with 81 % with no oxazolidinone present. However, increasing the temperature to 373 K produces the oxazolidinone at a 75 % yield with a 15 % yield of the piperazine.

*Table – Oxazolidinones vs. Piperazines: The Temperature Dependant Conundrum For The Cycloaddition Of Aziridines And CO2.10 – Experimental results by the Whiteoak group for the cycloaddition of **1a** and **1b (**6.2 mmol) with CO_2 at the following conditions Ga-catalyst (0.5 mol %, TBAI (2.0 mol %), 1 ml MEK, CO_2 (15 bar) in a sealed 50 mL high-pressure reactor.*

	Oxazolidinone Yield		**Piperazine Yield**	
Substrate	**333 K**	**373 K**	**333 K**	**373 K**
1a	0 %	75 %	81 %	16 %
1b	>99 %	>99 %	0 %	0 %

4.1.1 Aims of this work

- Employ DFT to elucidate the reaction mechanism for the synthesis of oxazolidinone and piperazine from aziridine and CO_2 with a Ga aminotrisphenolate catalyst.
- Why temperature leads to selective formation of oxazolidinone or piperazine product for **1a** but not **1b**.

- Discuss the feasibility of expanding the product selectivity to other aziridine substrates.

4.2 Results and Discussion

4.2.1 Oxazolidinone Mechanism Investigations

In the same sense the fact that Ding and Hu reported that this mechanism translated from the epoxide to the aziridine, it would be sensible to propose this as the mechanism for Ga aminotrisphenolate as this follows the same mechanism for epoxide cyclisation (Scheme 1.2). The proposed mechanism for the aziridine cyclisation (Scheme 4.4) starts with the aziridine associating to the gallium centre followed by a ring opening from the iodide of TBAI to form **Int1**. CO_2 insertion occurs to form **Int2** followed by a ring closure to form the oxazolidinone product.

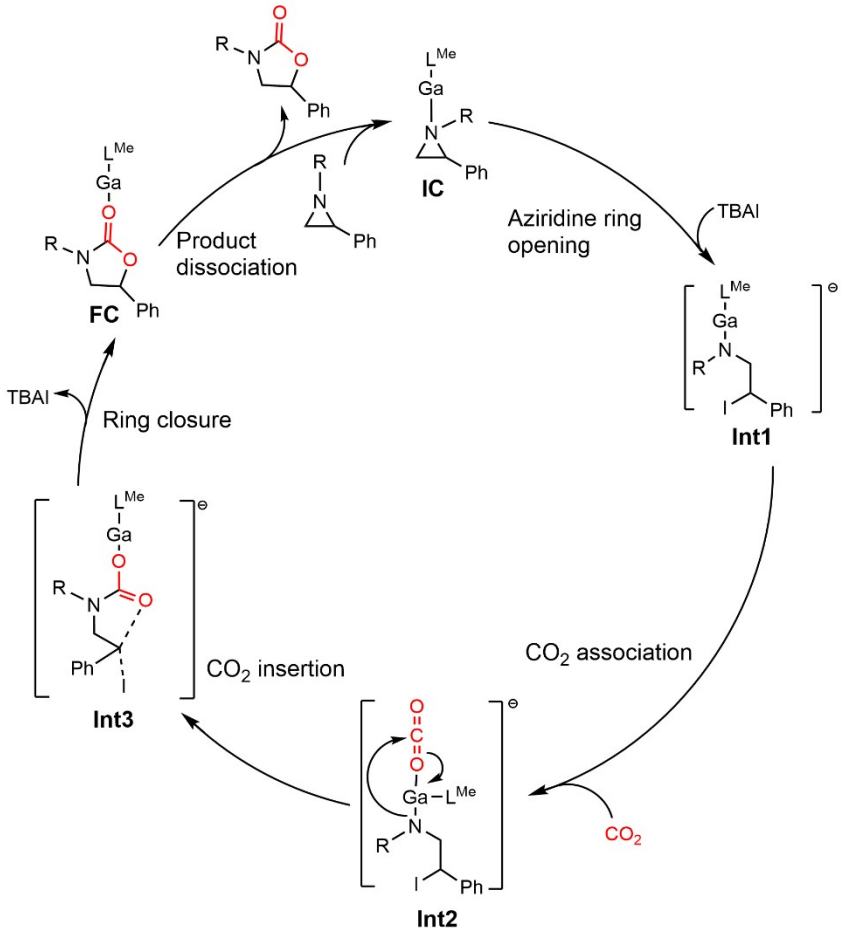

Scheme – Oxazolidinones vs. Piperazines: The Temperature Dependant Conundrum For The Cycloaddition Of Aziridines And CO2.15 - Proposed mechanism for the cycloaddition between aziridines (R = Ph and iPr) and CO_2 with a gallium trisaminophenolate catalyst (LMe = aminotrisphenolate).

DFT calculations (RIJCOSX-ωB97M-D3BJ/def2-TZVPP) in this study showed that this pathway was not viable. The energies of **Int1** were higher than their

proceeding transition state after optimisation (Figure 4.6). As a result, the conductor-like polarizable continuum model (CPCM) was also employed in optimisation and frequency calculations, accounting for the electrostatic contributions of methyl ethyl ketone (MEK).[22] By inclusion of solvation effects in the optimisation, it was predicted that this would stabilise **Int1** and optimise it to a lower energy conformation. However, **Int1** could not be optimised for **1b**. The optimised structure of **Int1** was elucidated for **1a** (without the optimisation of **TS1**), but the following CO_2 insertion step (**TS2**) was calculated at a free energy of 47.5 kcal mol^{-1} (Figure 4.6). This energy would be inaccessible in the reaction conditions; therefore, this mechanism can be ruled out.

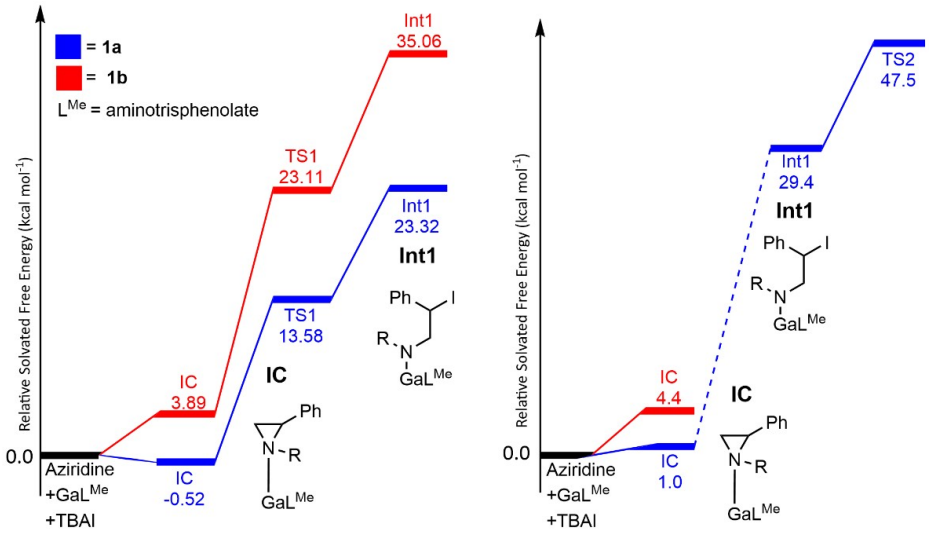

Figure – Oxazolidinones vs. Piperazines: The Temperature Dependant Conundrum For The Cycloaddition Of Aziridines And CO2.58 - Calculated free energy surface (ΔG333 K), RIJCOSX-ωB97M-D3BJ/def2-TZVPP, for the early intermediates for the synthesis of oxazolidinones from CO_2 and aziridines. Optimisation and frequency calculations were undertaken at a RI-B97-D3/def2-SVP level of theory with CPCM not included (left) and included (right).

The computed energy profile places the intermediate above the subsequent transition state, suggesting that this region of the surface does not correspond to a viable mechanistic sequence.[23,24] Consequently, further exploration of this pathway was not pursued.[14] Additional targets for the start of the mechanism were identified so that this pathway would still be followed (Scheme 4.5) These were a CO_2-aziridine adduct (**Add**) and a CO_2-catalyst adduct (**CO_2·Cat**).

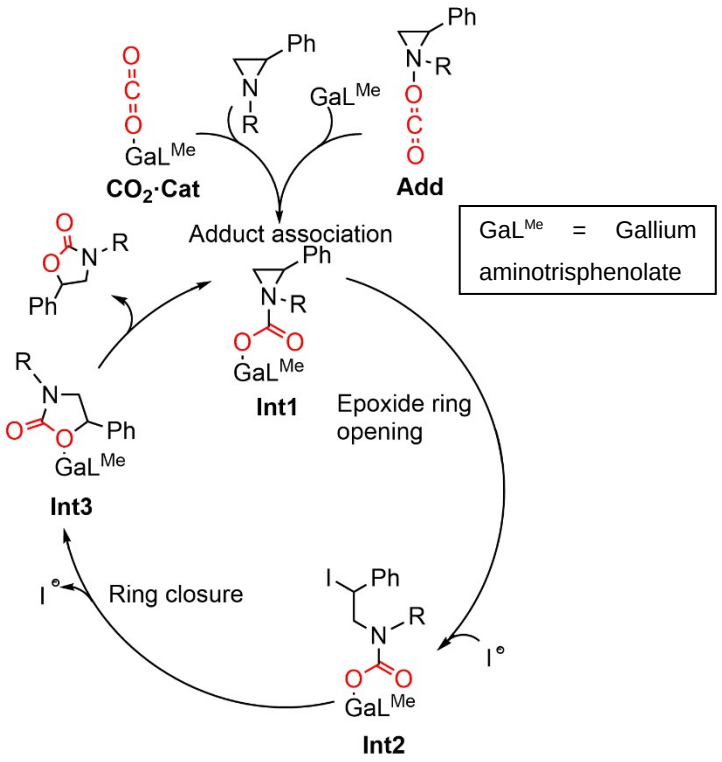

*Scheme – Oxazolidinones vs. Piperazines: The Temperature Dependant Conundrum For The Cycloaddition Of Aziridines And CO2.16 - Proposed catalytic cycle for a potential mechanism whereby a CO_2 forms an adduct with the GaL^{Me} catalyst (**CO_2·Cat**) or with the aziridine (**Add**) before ring opening occurs (L^{Me} = aminotrisphenolate).*

The experimental data in this work shows that the **TBAI** cocatalyst is an active species within the reaction and must be present to produce suitable yields. To account for this, the mechanism would need to include a ring-opened halide alkoxide intermediate. The proposed structure of this intermediate would be **Int2** in Scheme 4.5 and is denoted by I^- in the mechanism.

To understand if this route was energetically feasible, the energies of **CO_2-Cat** and **Add** needed to be compared with the initial complex (**IC**). The energies showed the formation of **IC** was favourable for both aziridine substrates in comparison to **CO_2-Cat** and **Add** (Figure 4.7). While this does not discount the adduct associative pathway, there would be competition between the association of **Add** and the aziridine. To confirm if this mechanism was viable, it was attempted to calculate a CO_2 insertion between the Ga-$NRC_2H_3(C_6H_6)$ bond of **IC** to obtain **Int1**; Figure 4.7. No optimised structure could be found for this transition state suggesting the structure was unfeasible/didn't exist. Therefore, alternative pathways needed to be investigated.

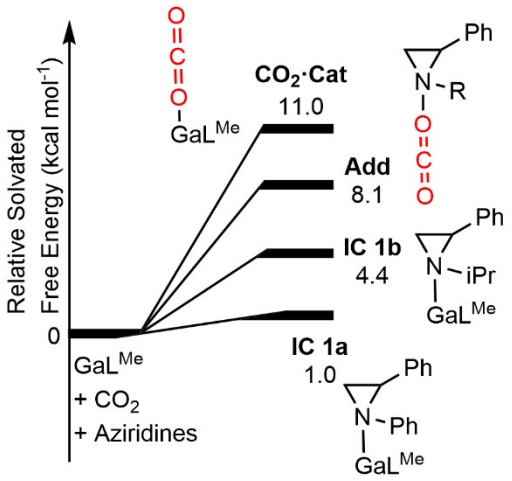

Figure – Oxazolidinones vs. Piperazines: The Temperature Dependant Conundrum For The Cycloaddition Of Aziridines And CO2.59 - Calculated free energy surface (ΔG 333 K), RIJCOSX-ωB97M-D3BJ/def2-TZVPP, for the initial targets of the adduct associative proposed mechanism (L^{Me} = aminotrisphenolate).

As the adduct associative pathway was deemed unfeasible, the ligand cooperative ring opening proposed by Kleij for the V(aminotrisphenolate) complex was consulted.[15] The proposed mechanism for this reaction is seen in Scheme 4.6.

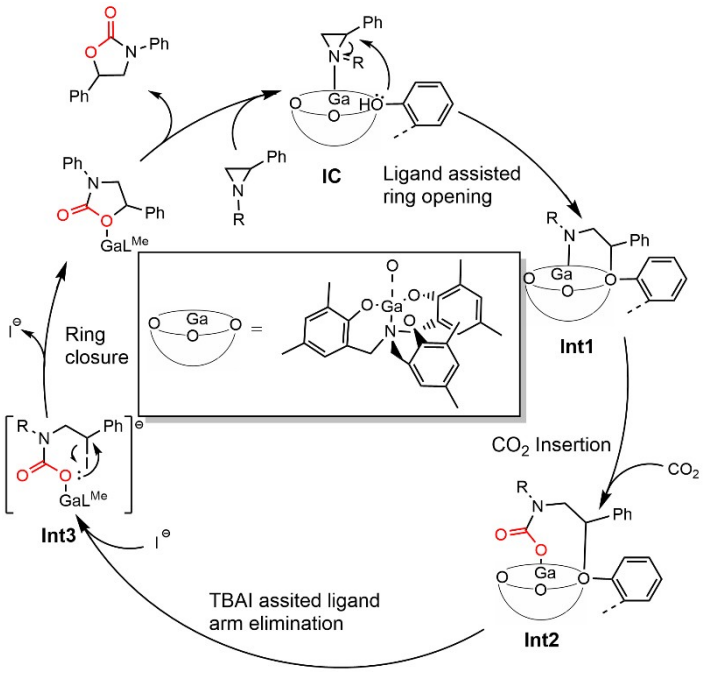

Scheme – Oxazolidinones vs. Piperazines: The Temperature Dependant Conundrum For The Cycloaddition Of Aziridines And CO2.17 - The proposed mechanism for the formation of oxazolidinones for the cycloaddition of CO_2 and aziridines catalysed by Ga aminotrisphenolate. The mechanism was derived from the work of Kleij et al.

The proposed mechanism in scheme 4.6 was successfully fully elucidated for both **1a** and **1b** with reasonable energy spans (Figures 4.9 and 4.10). The calculated mechanism starts from **IC**, where the aziridine associates to the catalyst. This agrees with the energies calculated in Figure 4.8. Following **IC**, the

phenoxy ligand arm dissociates from the catalyst and ring opens the aziridine at the more sterically hindered position to afford **Int1** (**TS1**).

The ring opening occurs at the more sterically hindered position because aziridines are functionalised on the N atom. By opening at the more sterically hindered position, there is less steric repulsion as the distance increases between the R-groups bound to the nitrogen and carbon due to the bond breaking. Ring opening at the non-substituted position (C_2) would mean the R-groups are adjacent and feel steric repulsion. The energies for the aziridine ring opening for **1a** and **1b** at the substituted position were around 40 kcal mol^{-1} and the substituted position could not be calculated as a structure would not converge.

Once the aziridine ring is opened, CO_2 interacts with the metal centre and donates a lone pair of electrons from the oxygen. This creates a dipole between the C=O bond, lowering the HOMO-LUMO gap and making C electrophilic. Insertion then occurs between the N atom and the metal centre, with the metal centre activating the CO_2 (**TS2**) to form **Int2**. At **Int2**, the halide co-catalyst eliminates the phenoxy group from the ligand and the o-donor coordinates to the metal centre (**TS3**) to form **Int3**. From **Int3** ring closure occurs to produce the oxazolidinone (**TS4**).

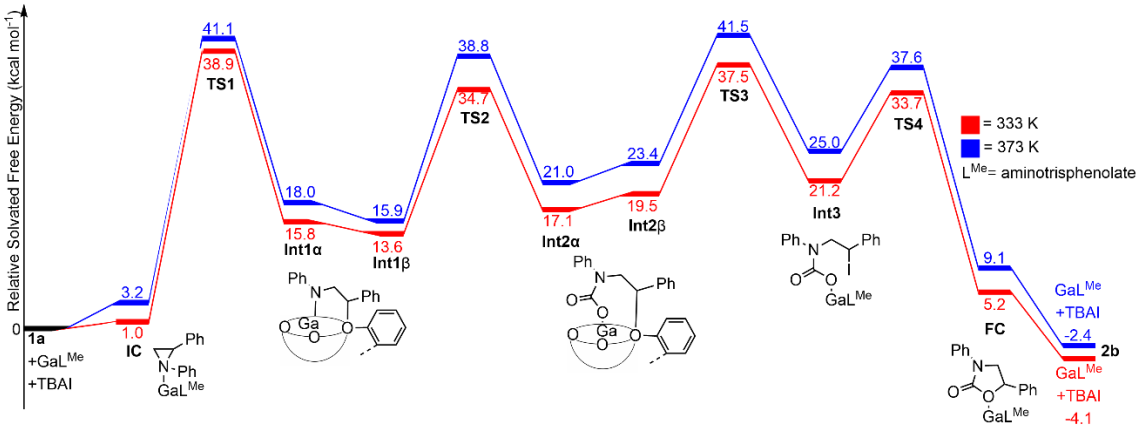

*Figure – Oxazolidinones vs. Piperazines: The Temperature Dependant Conundrum For The Cycloaddition Of Aziridines And CO2.60 - Calculated free energy surface (Red = ΔG 333 K, Blue = ΔG 373 K) RIJCOSX-ωB97M-D3BJ/def2-TZVPP, for the synthesis of oxazolidinones from CO_2 and **1a** catalysed by Ga(aminotrisphenolate) and TBAI.*

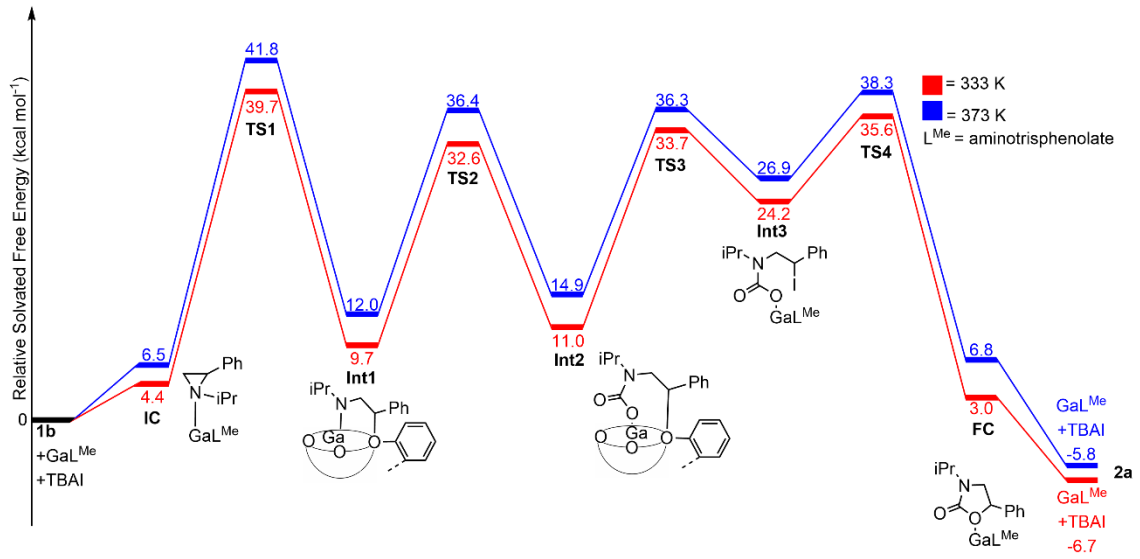

*Figure – Oxazolidinones vs. Piperazines: The Temperature Dependant Conundrum For The Cycloaddition Of Aziridines And CO2.61 - Calculated free energy surface (Red = ΔG 333 K, Blue = Δ G373 K) RIJCOSX-ωB97M-D3BJ/def2-TZVPP, for the synthesis of oxazolidinones from CO_2 and **1b** catalysed by Ga(aminotrisphenolate) and TBAI.*

The only difference between the mechanisms of the different aziridines was at **Int1** and **Int2**. **1a** needed to undergo a conformation change at these intermediates to allow for the transition state to occur. This conformation change was not needed for the **1b**. The isomerisation of **Int1α** and **Int1β** is shown in Figure 4.10. The torsional angle (τ) along the atoms N1-C1-C2-O2 is 3.2 ° and -145.0 ° for **Int1α** and **Int1β** respectively. This gives a Δτ 148.2 °. Such a conformational change is needed to pull the phenyl ring bound to the N away from the metal centre creating an easier accessible vacant site for CO_2 activation. This was not needed for substrate **1b** as the metal was already exposed (Figure 4.11).

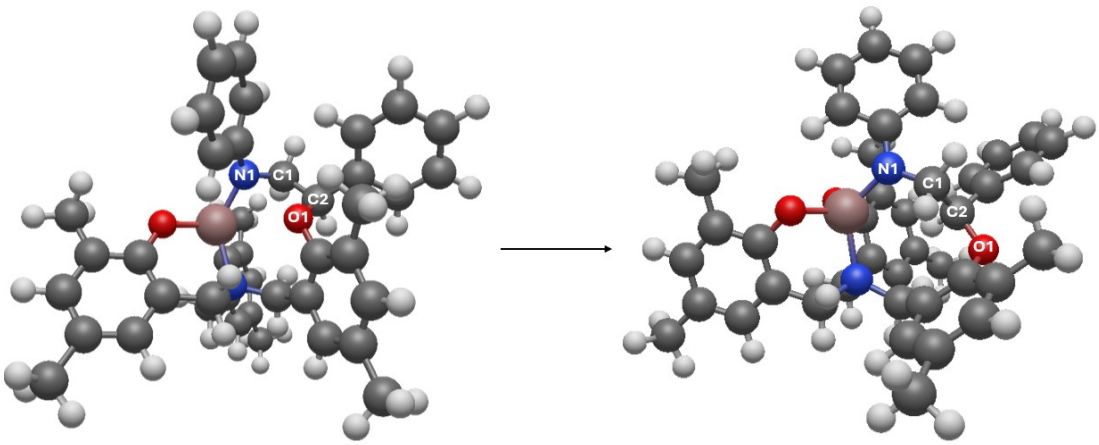

*Figure – Oxazolidinones vs. Piperazines: The Temperature Dependant Conundrum For The Cycloaddition Of Aziridines And CO2.62 - Optimised structures for the isomerisation from **Int1α** (left) to **Int1β** (right) for **1a**.*

Atoms of interest for the conformational change have been labelled. Peach = Ga, grey = C, white = H, red = O and blue = N.

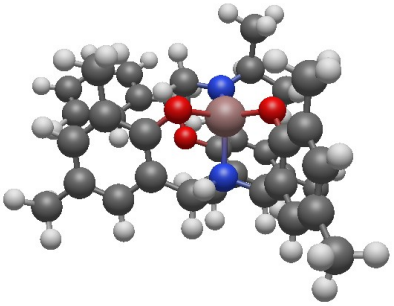

Figure – Oxazolidinones vs. Piperazines: The Temperature Dependant Conundrum For The Cycloaddition Of Aziridines And CO2.63 - ***Int1*** *from the pathway of substrate* ***1b*** *showing the exposed metal for the activation of CO_2. Peach = Ga, grey = C, white = H, red = O and blue = N.*

The isomerisation for **Int2α** to **Int2β** (Figure 4.12) needs to isomerise for a different reason. The oxygen of the ligand arm in **Int2α** is 3.6 Å away from the metal centre. At **Int2α** no transition state could be calculated as the structure would not converge. The calculated bond length for the coordinated ligand arms was 1.9 Å, suggesting that the bond was too far away to find a valid transition state. Therefore, **Int2β** was calculated which saw a $\Delta\tau$ of 11.4 ° along the O1-C1-N1-C2 atoms (Figure 4.12). The conformational change also changed the coordination geometry from a tetrahedral to a pseudo-trigonal bipyramidal. This conformational change brought the oxygen arm of the ligand to 2.1 Å away from the metal centre. This allowed for an elimination/re-coordination **TS3** to be calculated. The reason this conformation change isn't needed for substrate **1b** is after the CO_2 insertion, the complex is already in a pseudo-trigonal bipyramidal coordination with the oxygen of the ligand arm at sufficient distance for the elimination to occur (Figure 4.13).

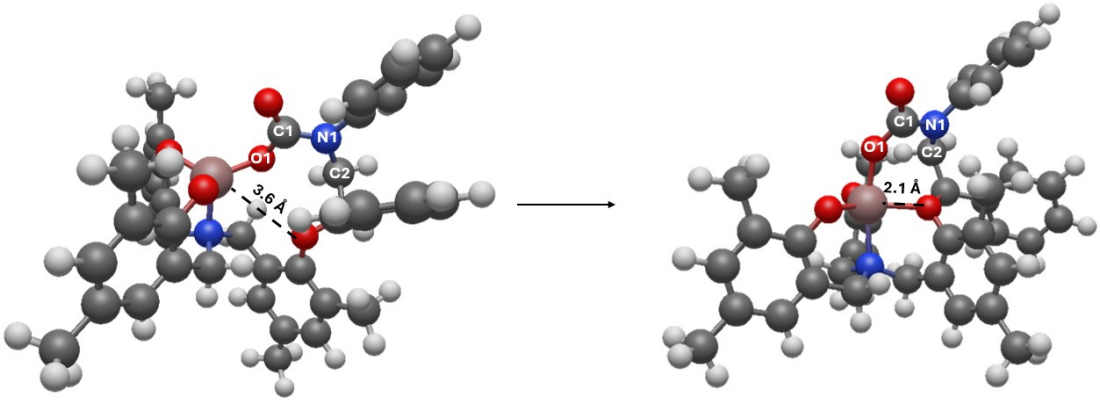

*Figure – Oxazolidinones vs. Piperazines: The Temperature Dependant Conundrum For The Cycloaddition Of Aziridines And CO2.64 - Optimised structures for the isomerisation from **Int2α** (left) to **Int2β** (right) for **1a**. Atoms of interest for the conformational change have been labelled. Peach = Ga, grey = C, white = H, red = O and blue = N.*

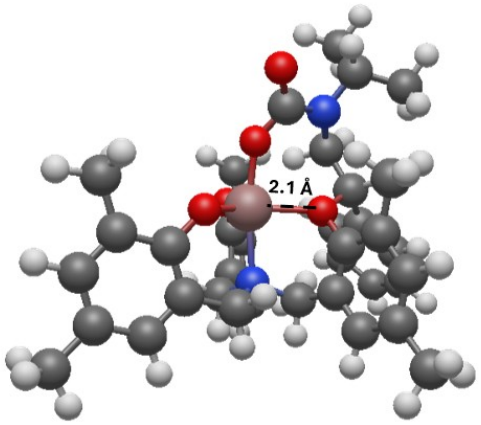

*Figure – Oxazolidinones vs. Piperazines: The Temperature Dependant Conundrum For The Cycloaddition Of Aziridines And CO2.65 – **Int2** from the pathway of substrate **1b** showing the bond distance between the uncoordinated ligand arm and the metal centre after CO_2 insertion. Peach = Ga, grey = C, white = H, red = O and blue = N.*

The calculated free energy spans for **1a** and **1b** are outlined in table 4.2. The calculated energy spans are higher than would be expected for the reaction for the reaction. The optimisation and frequency calculations were undertaken under CPCM solvent conditions at ε 18.5, contributing to higher Gibbs free energies. Including solvation across all calculations affects the entropic and enthalpic components of the free energy. Solvated frequency calculations tend to produce smaller entropy values because the solvent environment dampens translational and rotational contributions. This reduction in entropy makes the calculated Gibbs free energies more positive compared to gas-phase calculations. Furthermore,

the frequency calculations were undertaken at higher temperatures to be more representative of the experimental conditions, also resulting in higher energies.

Table – Oxazolidinones vs. Piperazines: The Temperature Dependant Conundrum For The Cycloaddition Of Aziridines And CO2.11 - The calculated free energy spans (kcal mol^{-1}) for the cycloaddition of aziridines and CO_2 to form oxazolidinones.

Substrate	333 K	373 K
1b	39.7	41.8
1a	38.9	41.5

To confirm that the ligand cooperative pathway was the underlying mechanism, the full mechanism for the adduct association pathway was elucidated (Figures 4.14-4.15; blue). The outline of the mechanism is as follows. The CO_2 associates to the Ga metal centre with a lone pair of electrons on an O atom. The Ga-O interaction activates the C atom by creating a C=O dipole resulting in the carbon becoming electrophilic, allowing for the aziridine associates to the C of CO_2 using lone pair N to form **Int1**. At **Int1**, I^- from TBAI ring opens the aziridine (**TS1**) to form **Int2**. The correct vibrational mode could only be identified for **TS1** with substrate **1a**. From **Int2** a conformational change occurs to afford **Int3** and the ring closure (**TS4**) regenerates the catalyst and forms the oxazolidinone product.

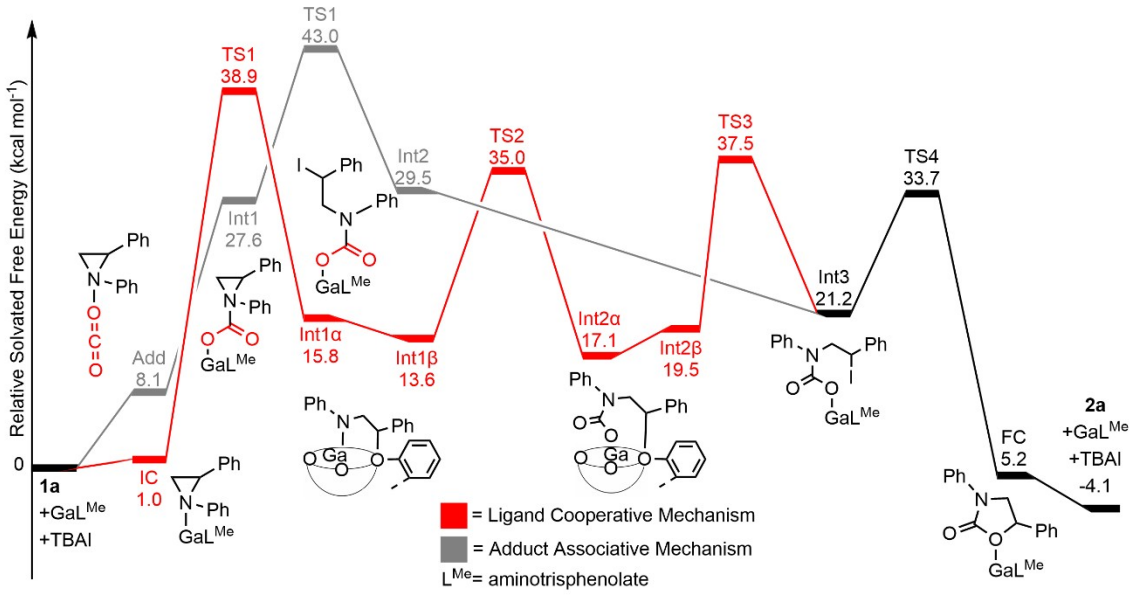

*Figure – Oxazolidinones vs. Piperazines: The Temperature Dependant Conundrum For The Cycloaddition Of Aziridines And CO2.66 - Calculated free energy surface (ΔG 333 K) RIJCOSX-ωB97M-D3BJ/def2-TZVPP, for the synthesis of oxazolidinones from CO_2 and **1a** catalysed by gallium trisaminophenolate and TBAI. Comparing the ligand cooperative pathway (red) and the adduct associative pathway (blue).*

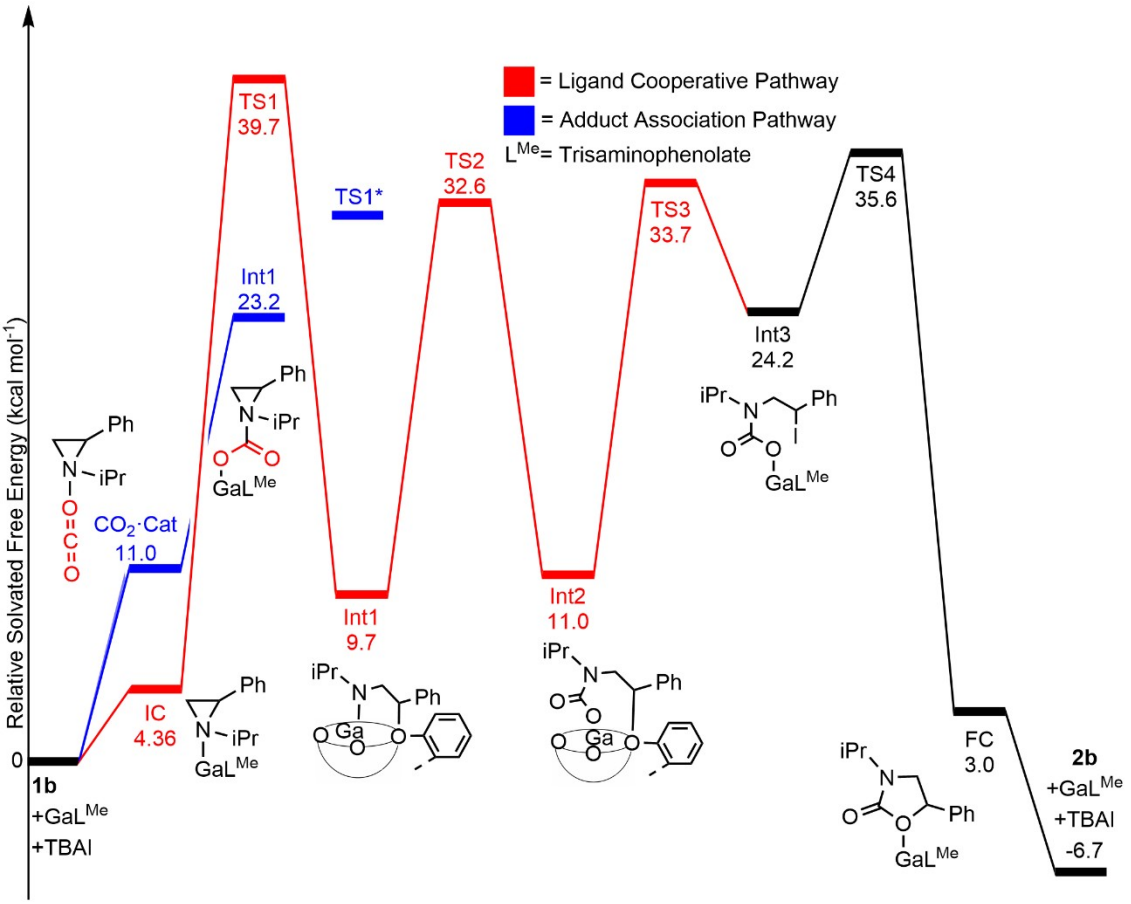

*Figure – Oxazolidinones vs. Piperazines: The Temperature Dependant Conundrum For The Cycloaddition Of Aziridines And CO2.67 - Calculated free energy surface (ΔG 333 K) RIJCOSX-ωB97M-D3BJ/def2-TZVPP, for the synthesis of oxazolidinones from CO_2 and **1b** catalysed by gallium trisaminophenolate and TBAI. Comparing the ligand cooperative pathway (red) and the adduct associative pathway (blue).*

As the ring opening **TS1** for the adduct associative pathway could not be located due to not converging, the ligand cooperative pathway is proposed as the mechanism for the **1b**. Further to this, the calculated energy span for the adduct associative pathway for the **1a** is 43.0 kcal mol^{-1} in comparison to 38.90 kcal mol^{-1} for the ligand cooperative pathway. Therefore, supporting the ligand cooperative route as the overarching mechanism for **1a**. As the calculated energies are high, and to confirm them against an accepted published system, the calculated free energy of the ring opening transition state of propylene oxide with a vanadium trisaminophenolate catalyst was calculated and **Int1** displayed in Figure 4.14. As already discussed, a crystal structure of the ring opened intermediate (**Int1**) had been obtained by Kleij (Figure 4.4), confirming this as a viable mechanism.[15]

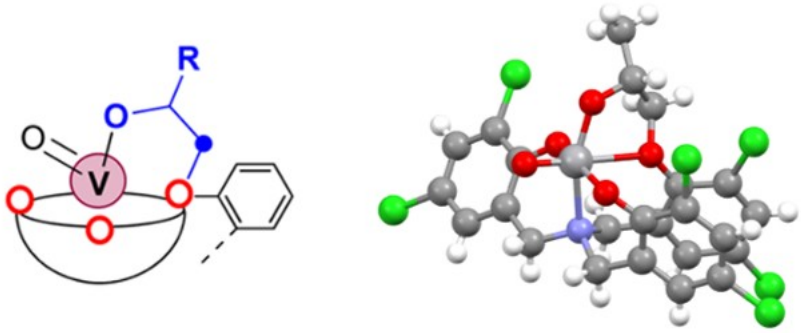

*Figure – Oxazolidinones vs. Piperazines: The Temperature Dependant Conundrum For The Cycloaddition Of Aziridines And CO2.68 - The calculated structure of the ring opened intermediate (**Int1**) by the Vanadium Trisaminophenolate catalyst.*[15]

The only difference in methodology was the dielectric constant value for the CPCM calculations. Propylene oxide (ε16) was used for epoxide reaction compared to the value for MEK used in the aziridine reaction (ε18.5). Calculations were undertaken at 333 K and 373 K to provide a fair comparison. The epoxide cycloaddition reaction was conducted at 353 K meaning the true energies for this reaction would be between the values presented in Figure 4.17. Although the calculated energy spans for the aziridine cyclisation mechanisms in this study are relatively high, they remain lower than those reported for the ring-opening step in Kleij's confirmed mechanism (43.6 kcal mol^{-1} at 333 K and 45.9 kcal mol^{-1} at 373 K). The fact that Kleij's mechanism was supported by crystallographic evidence strongly reinforces the viability of the ligand-cooperative pathway proposed here. These findings indicate that, despite the elevated energy barriers, the mechanism is chemically plausible under the conditions examined.

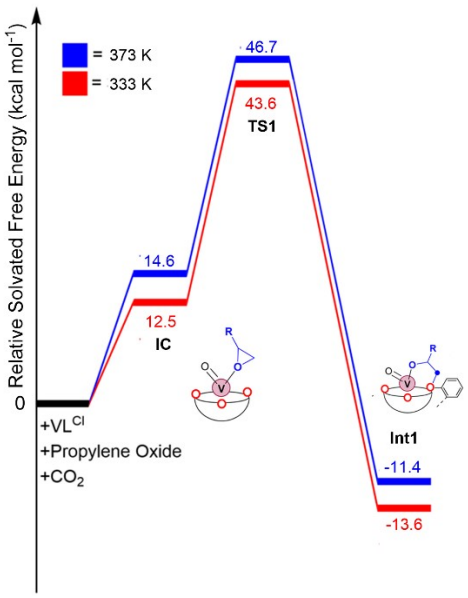

Figure – Oxazolidinones vs. Piperazines: The Temperature Dependant Conundrum For The Cycloaddition Of Aziridines And CO2.69 - Calculated energy of the ligand cooperative ring opening of propylene using a vanadium(V) aminotrisphenolate catalyst at the RIJCOSX-ωB97M-D3BJ/def2-TZVPP level of theory.[15]

In conclusion, a ligand cooperative mechanism has been proposed mechanism for the formation of oxazolidinones. The calculated energy spans appear high, however, considering the DFT methodology employed, and the energy calculated for Kleij's mechanism at equivalent levels of theory, they can be considered accessible. Now an understanding of the oxazolidinone mechanism had been achieved, the full mechanism for the piperazine pathway needed to be elucidated.

4.2.2 Piperazine Mechanistic Investigation

The selective formation of the piperazine was a novel finding by the Whiteoak group. The six-membered rings have been reported as minor byproducts in oxazolidinone synthesis, but never as a targeted product via this synthesis route.[25] As this mechanism has not previously been reported, a novel mechanism was proposed mechanism for the synthesis of the piperazine product (Scheme 4.7).

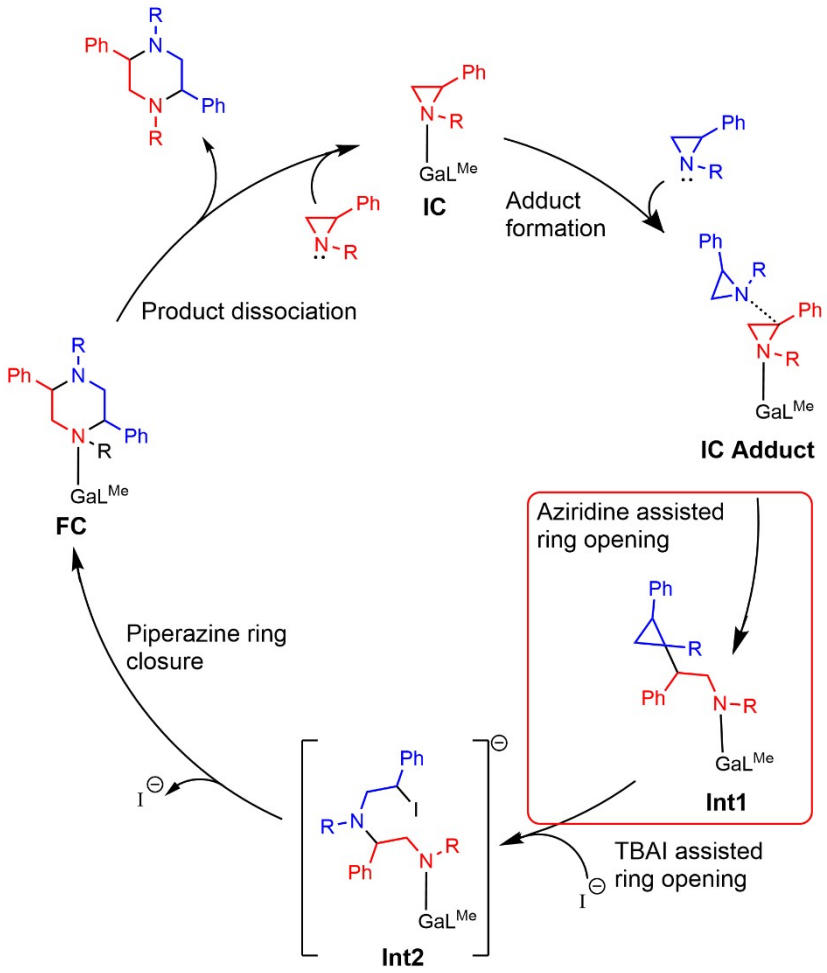

Scheme – Oxazolidinones vs. Piperazines: The Temperature Dependant Conundrum For The Cycloaddition Of Aziridines And CO2.18 - The proposed mechanism for the formation of piperazines via the cyclisation of aziridines with a gallium aminotrisphenolate catalyst.

The proposed mechanism was fully elucidated for the **1a** substrate and only partially elucidated for **1b** due to energies for the aziridine ring opening being too high. The mechanism starts by association of the aziridine substrate to the catalyst (**IC**). At **IC**, an adduct is formed whereby a second aziridine molecule interacts with the electrophilic carbon of the aziridine (**IC Adduct**). Following this, an aziridine assisted ring opening was calculated (**TS1**) to form **Int1**. This would be the divergent step that determines which product is favoured, as the **IC** in the oxazolidinone pathway is ring opened by the ligand arm, and is highlighted in a red box.

From **Int1**, the TBAI assisted ring opening was favourable by 7.1 kcal mol^{-1} at 333 K and by 9.3 kcal mol^{-1} at 373 K compared to a third aziridine molecule facilitating the opening (Figures 4.18-4.19). **Int2** undergoes a conformation change followed by a ring closure (**TS3**) affording the piperazine product and regenerating the catalyst.

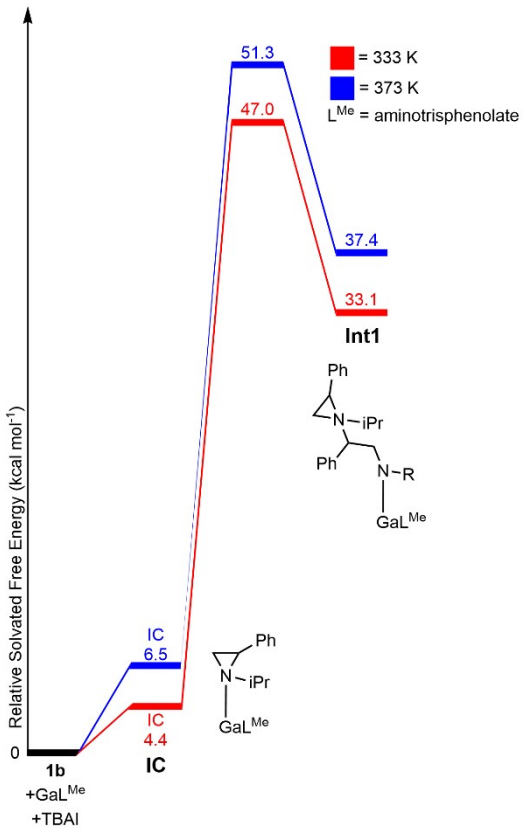

Figure – Oxazolidinones vs. Piperazines: The Temperature Dependant Conundrum For The Cycloaddition Of Aziridines And CO2.70 - Calculated free energy surface (Red = ΔG 333 K, Blue = ΔG 373 K) RIJCOSX-ωB97M-D3BJ/def2-TZVPP, for the synthesis of piperazines from 1b catalysed by gallium aminotrisphenolate.

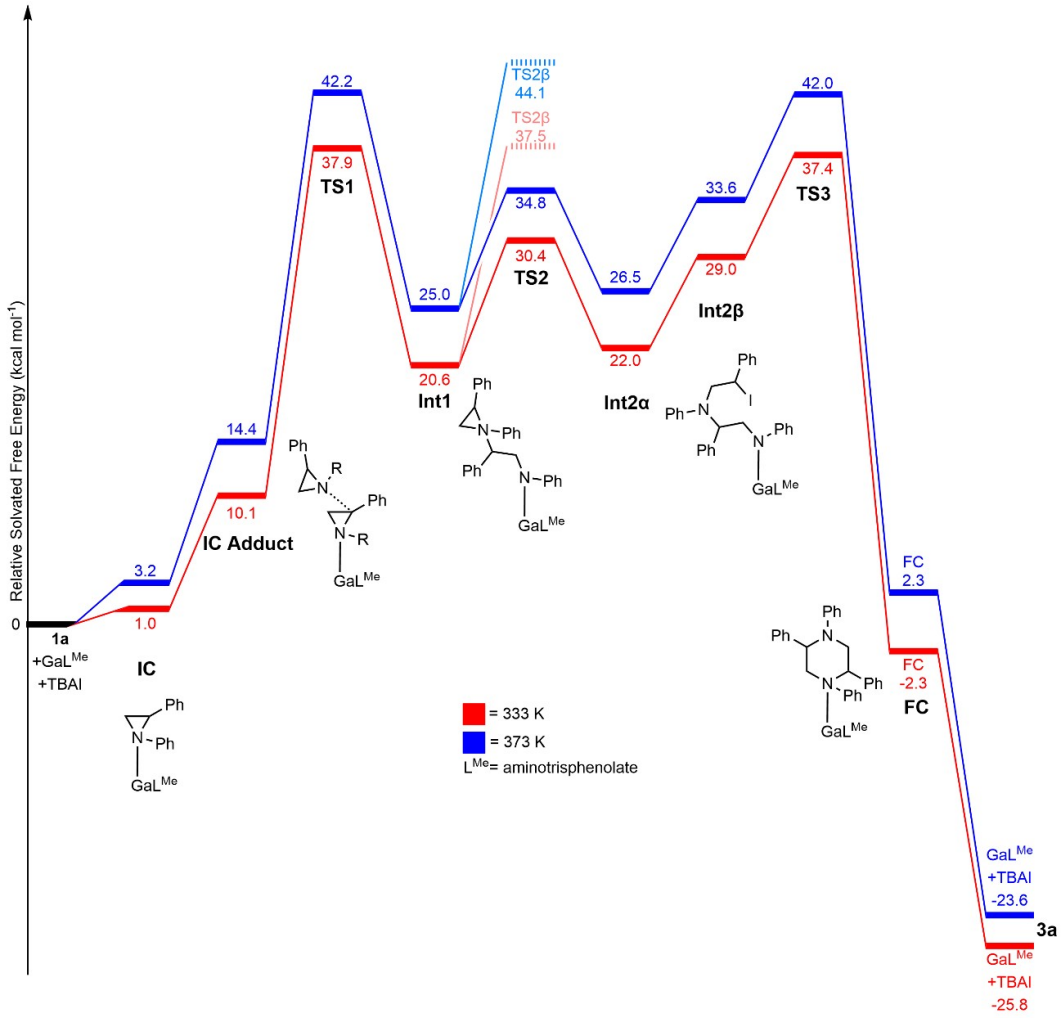

Figure – Oxazolidinones vs. Piperazines: The Temperature Dependant Conundrum For The Cycloaddition Of Aziridines And CO2.71 - Calculated free energy surface (Red = ΔG 333 K, Blue = ΔG 373 K) RIJCOSX-ωB97M-D3BJ/def2-TZVPP, for the synthesis of piperazines from 1as catalysed by gallium aminotrisphenolate and TBAI.

The elucidated mechanism for **1b** was only calculated up to **Int1** due to the calculated free energies of the **TS1** barrier. The aziridine facilitated ring opening is ~6 kcal mol^{-1} higher in energy than the ligand cooperative ring opening forming only **2b** regardless of the temperature in agreement with the Whiteoak group.[1]

Figure 4.20 compares all operative mechanisms for **1a**, at 333 K and 373 K. The free energy spans of the pathways give insight into the temperature-based product selectivity. The TOF-determining transition state (TDTS) for the piperazine at both temperatures and oxazolidinone pathway at 333 K is the ring opening (**TS1**) and at 373 K the ring closure (**TS3**). Comparing the energies of **TS1** for the formation of **2a** and **3a** at 333 K, the aziridine ring opening is favourable over the ligand cooperative ring opening by 1.0 kcal mol^{-1}. This leads to the primary formation of **3a**. On the contrary, at 373 K, the formation of **2a** is more favourable than the formation of **3a** by 0.7 kcal mol^{-1}.

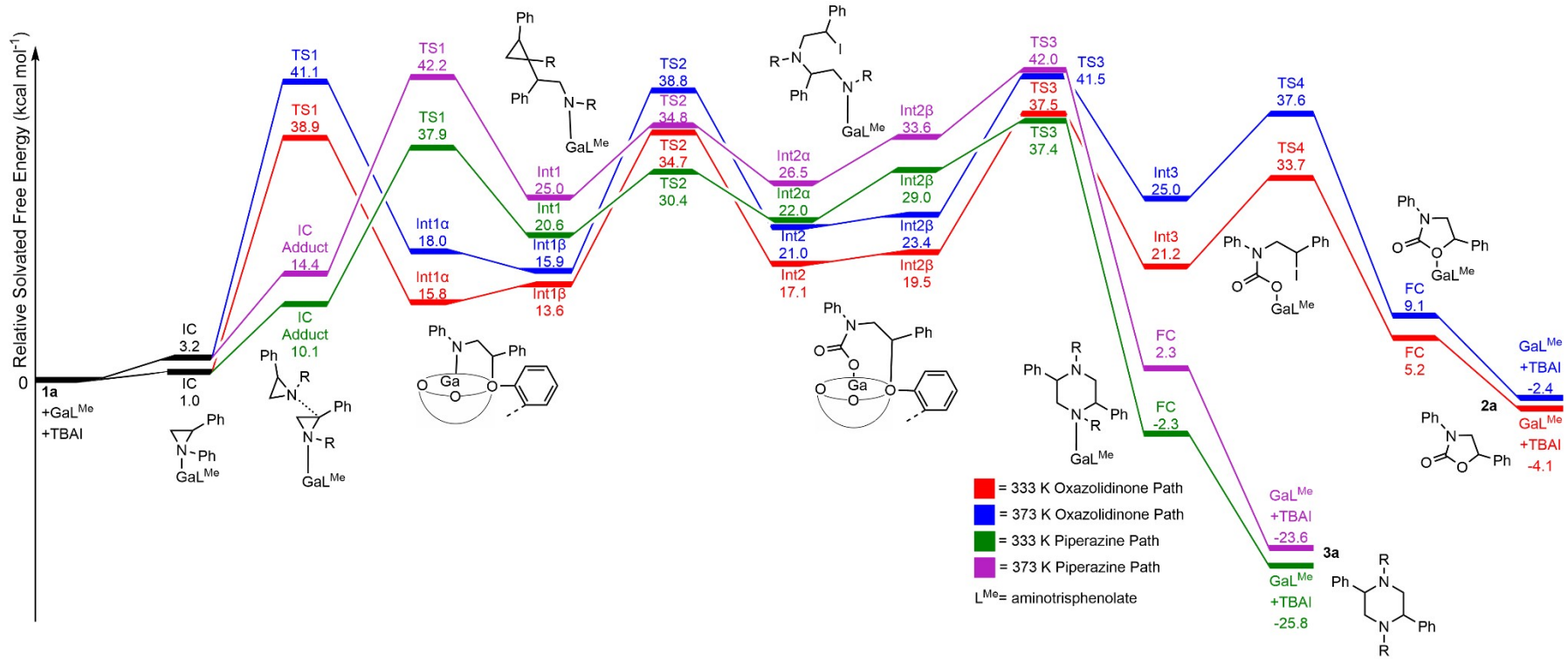

*Figure – Oxazolidinones vs. Piperazines: The Temperature Dependant Conundrum For The Cycloaddition Of Aziridines And CO2.72 - Calculated free energy surface RIJCOSX-ωB97M-D3BJ/def2-TZVPP. The elucidated mechanisms for the formation of **2a** and **3a** have been compared at ΔG 333 K, and ΔG 373 K with the relative zero being all reactants in solution.*

While this provides evidence for the selectivity observed, the energies do not fully explain why no CO_2 insertion occurs at 333 K, but piperazine formation still occurs at 373 K. There is a larger energy difference between the energy span at 333 K compared to 373 K, however, this is only a small difference so would not account for that difference in reactivity. Regardless of this, the results are in good agreement of the observed reactivity experimentally.

4.2.3 Temperature Dependence

To be able to control the stereochemistry of product, solely by changing the temperature, is an attractive prospect for industry. To determine if this is a phenomenon between the two aziridines studied or can be expanded to a wider range of aziridines, a fundamental understanding of the occurrence is needed. Due to the temperature being the dependent variable, the thermal and energetic contributions to the Gibbs energy were recalculated at a range of temperatures (298 – 398 K), to understand how the energy barrier is related to temperature (Figure 4.21).[1]

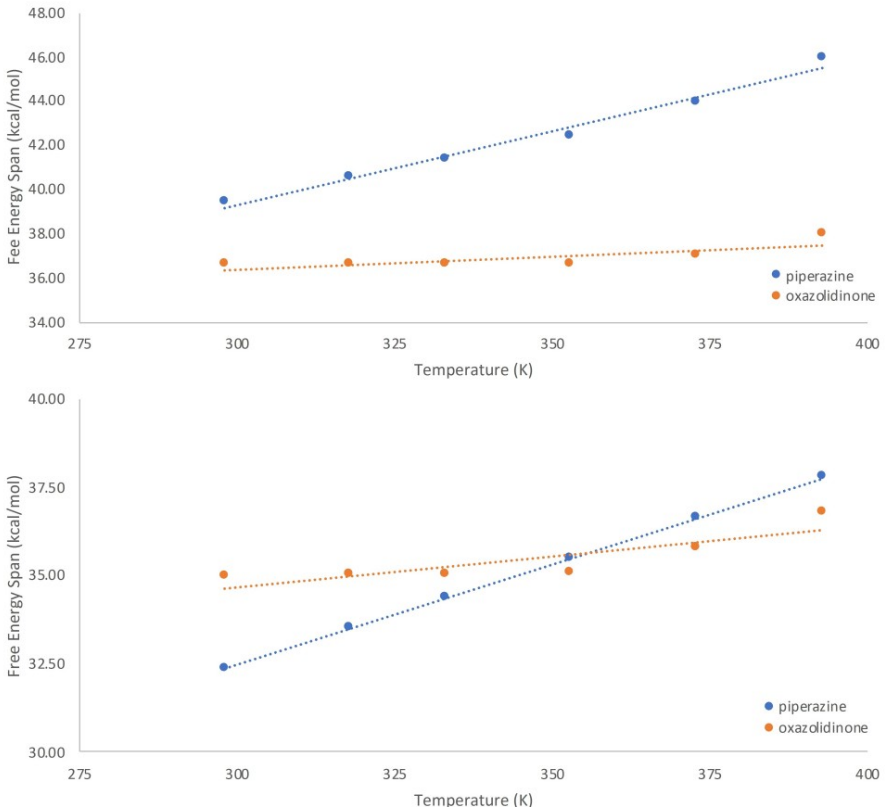

*Figure – Oxazolidinones vs. Piperazines: The Temperature Dependant Conundrum For The Cycloaddition Of Aziridines And CO2.73 - . Temperature dependence of piperazine (blue) vs. oxazolidinone (orange) formation pathways for **1b** (top) and **1a** (bottom), showing free energy span (ΔG) as a function of temperature (K) from 1.*[1]

Figure 4.21 clearly demonstrates that **1b** cannot produce the piperazine product, yet the **1a** is. This can be attributed to the entropic penalty associated with the bi-molecular step of the piperazine pathway. This results in a steeper increase in energy span as a function of temperature and thus, the selectivity. In theory, if the reaction of the **1b** was to happen at a lower temperature, the selective synthesis of the piperazine would be possible.

4.3 Conclusion

This research was highly impactful by providing two novel mechanisms for the formation of oxazolidinone or piperazines and rationalisation for the temperature selective formation of each product for **1a**.

The mechanisms for the formation of oxazolidinones and piperazines have been considered for **1a** and **1b**. The oxazolidinone followed a ligand cooperative mechanism. Once the aziridine associated with the catalyst, the ligand arm of the aminotrisphenolate dissociates to facilitate the aziridine ring opening. CO_2 insertion then occurs followed by a reassociation of the ligand arm through an elimination assisted by **TBAI**. A ring closure of the amide then affords the oxazolidinone and regenerates the catalyst.

Piperazine formation also starts with the aziridine associating to the Ga-catalyst. Instead of a ligand arm assisted ring opening, a second aziridine molecule facilitates the ring opening. The second aziridine molecule is then ring opened by I^- of TBAI which is followed by a ring closure to afford the piperazine product.

The product selectivity based on temperature for the **1a,** is due to a greater entropic penalty using two equivalents of the aziridines in comparison with the oxazolidinone route that sees a greater increase in the energy span of the reaction as the temperature increases. A crossover point between 350-360 K is seen between the favourability of the formation of a piperazine or oxazolidinone product, in reasonable agreement with the experimental findings. Furthermore, it was found that **1b** could not form the piperazine product as it was consistently energetically inferior to the formation of the oxazolidinone.

Justification of the high free energies calculated have been provided in reference to an experimental study by Kleij *et al*.[15] Crystallographic evidence showed that the ligand cooperative mechanism undeniably takes place for the akin reaction

with epoxides. The computed energies for this ring opening with our own methodology exceed the energies displayed in the aziridine mechanisms. As Kleij's system is higher than our system at equivalent methodology, and it is a proven mechanism through crystallographic evidence, it further supports the ligand cooperative mechanism for the aziridine system.

4.4 Computational Methodology

All DFT calculations undertaken using the ORCA 4.2.1 computational software.[26,27] Solvation optimizations and analytical frequency calculations were performed at the RI-B97-D3/def2-SVP (def2-TZVPP on the Ga metal centre) level of theory. [28–31] Final single-point energies and solvation corrections were calculated at RIJCOSX-ωB97M-D3BJ/def2-TZVPP level of theory[30–33] All solvation corrections were calculated using the CPCM model with a dielectric constant value of 18.5 for MEK.[34] Analytical frequencies were calculated for inclusion of the Zero Point Energy (ZPE) correction and entropic contributions to the free energy term (ΔG333 K) and (ΔG373 K), as well as confirming all intermediate were true with no imaginary modes and all transition states had the correct critical frequency of decomposition. All thermodynamic parameters were calculated at 333 K and 373 K with standard pressure (1 atm). Numerical precision integration grids were increased beyond the default settings, to Grid4 for the SCF step and Grid5 for the final energy evaluation. Concentration correction for the individual species was applied as a free energy correction based on RT $\ln(C_i/C_{atm})$[35] where C_i is the experimental concentration of the relevant species. Graphical visualization and structural analysis performed from the DFT calculations using Avogadro 1.2.0.[36]

4.5 References

1 M. D. G. Billacura, R. D. Lewis, N. Bricklebank, A. Hamilton and C. J. Whiteoak, *Adv. Synth. Catal.*, 2023, **365**, 3129–3137.

2 X. Ju, M. Lee, J. C. Leung and J. Lee, *European J. Org. Chem.*, DOI:10.1002/ejoc.202401414.

3 W. Shi, J. Benet-Buchholz and A. W. Kleij, *Nat. Commun.*, 2025, **16**, 1–11.

4 D. A. Evans, J. S. Tedrow, J. T. Shaw and C. W. Downey, *J. Am. Chem. Soc.*, 2002, **124**, 392–393.

5 D. J. Ager, I. Prakash and D. R. Schaad, *Chem. Rev.*, 1996, **96**, 835–875.

6 D. A. Evans, C. W. Downey, J. T. Shaw and J. S. Tedrow, *Org. Lett.*, 2002, 2127–2129.

7 M. R. Barbachyn and C. W. Ford, *Angew. Chem., Int. Ed.*, 2003, **42**, 2010–2023.

8 D. A. Evans, J. Bartroli and T. L. Shih, *Am. Chem. Soc.*, 1981, **103**, 2127–2129.

9 C. Foti, A. Piperno, A. Scala and O. Giuffrè, *Molecules*, 2021, **26**, 1–13.

10 M. Sengoden, M. North and A. C. Whitwood, *ChemSusChem*, 2019, **12**, 3296–3303.

11 C. H. Zhang, Z. L. Wu, R. X. Bai, T. D. Hu and B. Zhao, *ACS Appl. Mater. Interfaces*, 2023, **15**, 1879–1890.

12 W. M. Wang, W. T. Wang, M. Y. Wang, A. L. Gu, T. D. Hu, Y. X. Zhang and Z. L. Wu, *Inorg. Chem.*, 2021, **60**, 9122–9131.

13 T. D. Hu and Y. H. Ding, *Organometallics*, 2020, **39**, 505–515.

14 D. Adhikari, A. W. Miller, M. H. Baik and S. T. Nguyen, *Chem. Sci.*, 2015, 1293–1300.

15 C. Miceli, J. Rintjema, E. Martin, E. C. Escudero-Adán, C. Zonta, G. Licini and A. W. Kleij, *ACS Catal.*, 2017, **7**, 2367–2373.

16 L. Álvarez-Miguel, J. D. Burgoa, M. E. G. Mosquera, A. Hamilton and C. J. Whiteoak, *ChemCatChem*, 2021, **13**, 4099–4110.

17 N. Panza, M. Alberti, S. Galiè, C. Damiano, F. Cargnoni, M. Italo Trioni and A. Caselli, *European J. Org. Chem.*, DOI:10.1002/ejoc.202200908.

18 Y. Song, Q. Sun, B. Aguila and S. Ma, *Catal. Today*, 2020, **356**, 557–562.

19 S. Pulla, C. M. Felton, P. Ramidi, Y. Gartia, N. Ali, U. B. Nasini and A. Ghosh, *J. CO2 Util.*, 2013, **2**, 49–57.

20 J. D. Firth, P. O'Brien and L. Ferris, *J. Am. Chem. Soc.*, 2016, **138**, 651–659.

21 E. Vitaku, D. T. Smith and J. T. Njardarson, *J. Med. Chem.*, 2014, **57**, 10257–10274.

22 M. Bursch, J. M. Mewes, A. Hansen and S. Grimme, *Angew. Chem.*, 2022, **134**, e202205735.

23 K. Fukui, *J. Phys. Chem.*, 1970, **74**, 4161–4163.

24 K. Fukui, *Acc. Chem. Res.*, 1981, **14**, 363–368.

25 Y. Song, Q. Sun, B. Aguila and S. Ma, *Catal. Today*, 2020, **356**, 557–562.

26 F. Neese, *Wiley Interdiscip. Rev. Comput. Mol. Sci.*, 2018, **8**, 4–9.

27 F. Neese, *Wiley Interdiscip. Rev. Comput. Mol. Sci.*, 2012, **2**, 73–78.

28 F. Neese, *J. Comput. Chem.*, 2003, **24**, 1740–1747.

29 S. Grimme, S. Ehrlich and L. Goerick, *J. Comput. Chem.*, 2011, **32**, 1456–1465.

30 A. Schäfer, H. Horn and R. Ahlrichs, *J. Chem. Phys.*, 1992, **97**, 2571–2577.

31 F. Weigend and R. Ahlrichs, *Phys. Chem. Chem. Phys.*, 2005, **7**, 3297–3305.

32 F. Neese, F. Wennmohs, A. Hansen and U. Becker, *Chem. Phys.*, 2009, **356**, 98–109.

33 N. Mardirossian and M. Head-Gordon, *J. Chem. Phys.*, 2016, **144**, 214110.

34 S. Sinnecker, A. Rajendran, A. Klamt, M. Diedenhofen and F. Neese, *J. Phys. Chem. A*, 2006, **110**, 2235–2245.

35 J. N. Harvey, F. Himo, F. Maseras and L. Perrin, *ACS Catal.*, 2019, **9**, 6803–6813.

36 M. Hanwell, D. Curtis, D. Lonie, T. Vandermeersch, E. Zurek and G. Hutchison, *J. Cheminform.*, 2012, **4**, 17.

Chapter 5 – Simple Trihalide Group 13 Catalysts for CO_2 Utilisation: A DFT / Design Criteria Study

5.1 Introduction

The most notable group 13 Lewis acidic catalysts used for the cycloaddition of CO_2 and epoxides have traditionally improved multidentate ligand-structures producing excellent yields in agreeable experimental conditions (Figure 5.1).[1–4] The complex backbones of the ligand are an integral part of controlling catalyst properties and henceforth the catalytic activity. Points of functionalisation are available for complex backbones, such as multiple heterocyclic rings, alkyl chains and arenes, allowing for subtle fine-tuning of the steric and electronic properties through altering substituents. Furthermore, changes in R-groups on the ligand enables control over experimental parameters such as the catalyst solubility.[5]

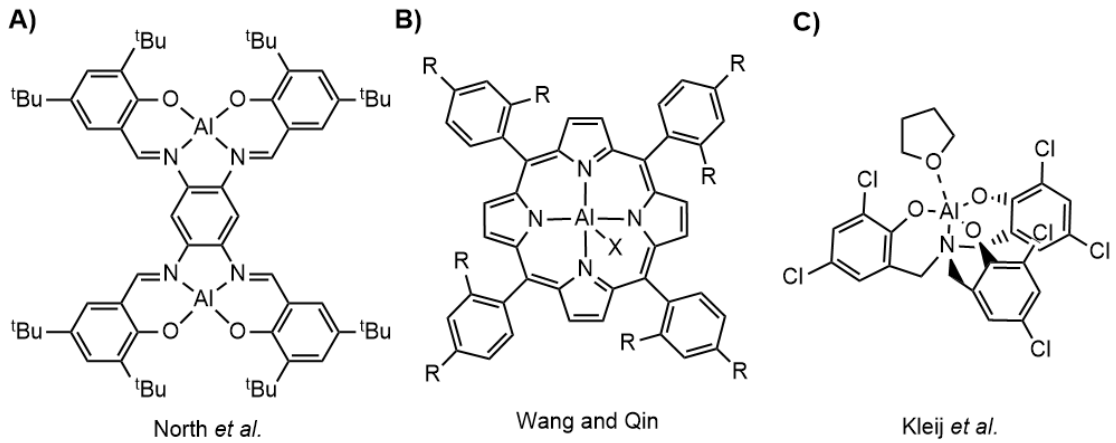

*Figure – Simple Trihalide Group 13 Catalysts for CO2 Utilisation: A DFT / Design Criteria Study.74 - Three notable multidentate catalysts, bi-salphen (**A**), porphyrin (**B**) and aminotrisphenolate (**C**) for the cycloaddition of CO_2 and epoxides.[1,2,4]*

5.1.1 Background

Little attention has been paid to the simpler group 13 Lewis acidic catalysts such as, M(III)X_3, when M = Al, Ga, In; X = small anionic ligand (halides, aloxides and

amides) for the cycloaddition of CO_2 and epoxide.[6] Inductive affects from the ligand have a much greater effect on the metal centre in the small monodentate catalysts compared to larger multidentate structures. The delocalised ring systems which separate the metal centre from the functionalisation points of the catalyst shield the metal centre from inductive effects leading to much more subtle changes in catalyst activity.[7] Despite being less adaptable, a few small catalysts have shown to be promising, particularly GaX_3 and InX_3 where X = (Cl, Br and I).

$GaCl_3$ has proven to be an effective catalyst for the formation of *gem*-acetates (two acetate groups attached to a the same carbon) from aldehydes with short reaction times, high yields, a large substrate scope and non-rigorous reaction conditions.[8] Furthermore, $InCl_3$ catalysts have been reported for use in the [4+2] cycloaddition to form quinolines using the Povrav reaction leading to the formation of a number of novel quinolines.[9] Employment of an $In(OTf)_3$ catalyst for a similar reaction saw the novel synthesis of dihydroacridines which possessed strong photocatalytic properties, highlighting the adaptability of the catalyst for a specific usage.[10]

For the formation of cyclic carbonates, $M(III)X_3$ catalysts have been shown to produce excellent yields as both ionic liquids and as binary Lewis acidic catalysts.[11–13] In 2006, $AlCl_3$ was identified as a good catalyst for the cycloaddition of CO_2 and epoxides displaying conversion percentages in line with $FeCl_3$ and VCl_3 binary systems at low catalyst loading (0.33 mol %).[11]

In 2011, Shibata *et al.* reported InX_3 catalysts (where X = Cl, Br and I) using a PPh_3 co-catalyst yielding cyclic carbonates at ambient conditions.[12] A ligand exchange mechanism was proposed (Figure 5.2). $InBr_3$ and PPh_3 first coordinate to form a complex. A ligand exchange occurs between a Br^- and epoxide molecule. The free Br^- facilitates the epoxide ring opening to afford intermediate **A**. Two separate pathways are available from intermediate **A**. The generally accepted route of a CO_2 insertion followed by a ring closure to afford the cyclic carbonate product and reform the catalyst is denoted on the cycle to the left. An alternate route can occur whereby the PPh_3 ligand disassociates from the In centre and a nucleophilic substitution occurs forming intermediate **A'**. A second epoxide molecule then associates to the In centre and is ring opened by the free

Br^- from the substitution. CO_2 insertion then occurs followed by a ring closure leading to the cyclic carbonate product and the reformation of intermediate **A'**.

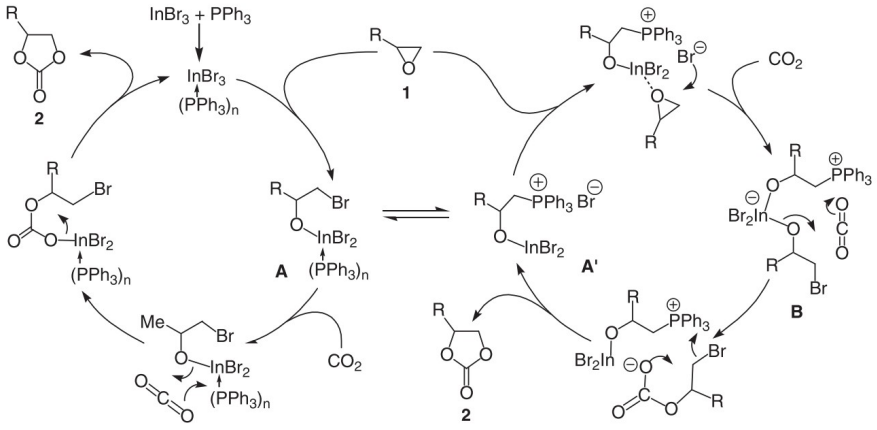

Figure – Simple Trihalide Group 13 Catalysts for CO2 Utilisation: A DFT / Design Criteria Study.75 - The reaction mechanism proposed by Shibata et al. for the cycloaddition of CO_2 and epoxides to from cyclic carbonates catlysed by InX_3 (X = Cl, Br and I) from 13.[12]

5.1.2 Experimental Studies by the Mehrkhodavandi Group

In 2021, the Mehrkhodavandi group systematically studied nine M(III)X_3 catalysts (M = Al, Ga and In; X = Cl, Br and I) using a co-catalyst of TBABr for the cycloaddition of epoxides and CO_2.[14] Table 5.1 gives an outline of the yields achieved for each catalyst. In this study $InBr_3$ gives the highest % yield of cyclic carbonate formation. The In catalysts overall give better yields in comparison to both the Al and Ga trihalides. The difference between Al and Ga catalysts is closer with $AlBr_3$, $GaBr_3$ and GaI_3 yielding around 40 % cyclic carbonate followed by $AlCl_3$ and AlI_3 achieving a lower yield of around 25 %. $GaCl_3$ stands out as inactive producing a yield of 3 %, suggesting mechanistic differences for this catalyst.

Table – Simple Trihalide Group 13 Catalysts for CO2 Utilisation: A DFT / Design Criteria Study.12 - Percentage yields achieved for CO_2 cycloaddition to epoxide. Reaction conditions: Epoxide [1a] = 3.4 mmol, metal halide = 0.17 mmol (5 mol %), NBu_4Br = 0.34 mmol (10 mol %), P (CO_2) = 1 bar, T = 20 °C, time = 1 h. Solvent free.[14]

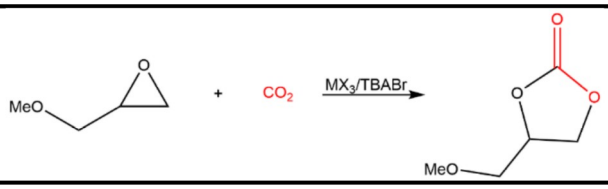

Metal Trihalide (MX_3)	% Yield
$AlCl_3$	23
$AlBr_3$	41
AlI_3	26

$GaCl_3$	3
$GaBr_3$	39
GaI_3	42
$InCl_3$	70
$InBr_3$	90
InI_3	79

Figure 5.3 shows the experimentally proposed catalytic cycle. Due to the high Lewis acidity of the catalysts, and their tendency to form a stable salt with TBABr (i.e. $[TBA^+][MX_4^-]$), the cycle is proposed to start from **IC**. The addition of excess epoxide drives the equilibrium from the salt to **IC**. From **IC**, the TBABr assisted ring opening of the epoxide occurs to form **Int1**, followed by CO_2 insertion to form **Int2** κ^1. As CO_2 can either bind through a κ^1 or κ^2 binding mode, an equilibrium is present. The more prominent κ^1 binding mode undergoes ring closure of the cyclic carbonate to afford **FCR2**. From **FCR2**, a ligand exchange of the cyclic carbonate and an epoxide take place to regenerate the catalyst species and continue the cycle.

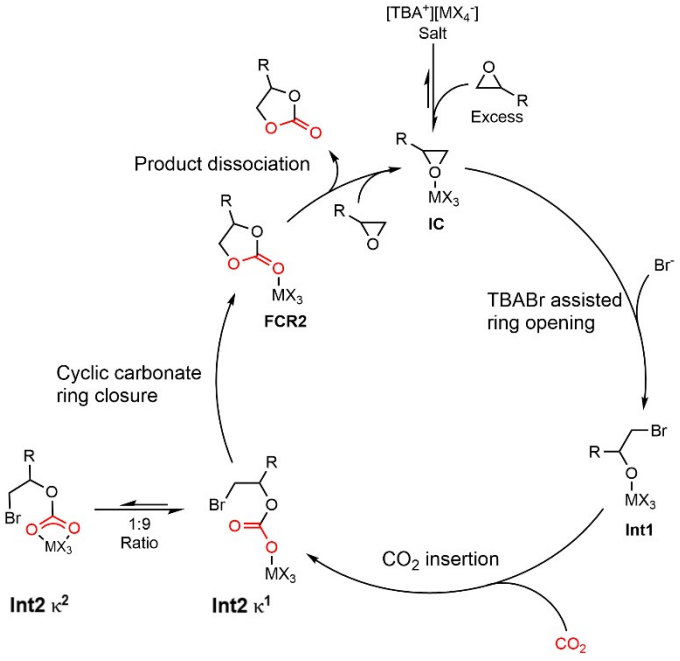

Figure – Simple Trihalide Group 13 Catalysts for CO2 Utilisation: A DFT / Design Criteria Study.76 - Proposed mechanism for cycloaddition of epoxides and CO_2 to form cyclic carbonates catalysed by M(III)X_3 (M = Al, Br and Ga; X = Cl, Br and I).[14]

As $InBr_3$ was found to be the most active catalyst by the mehrkhodavandi group, a detailed kinetic study was conducted to give insight into the mechanism. The reaction was determined to be 1st order with respect to TBABr and $InBr_3$.

Therefore, the mechanism is mononuclear in respect to the catalyst. The observed increase in rate of reaction upon increasing epoxide concentration indicates a positive order dependence on epoxide, consistent with its involvement in the rate-determining step. However, increasing the pressure of CO_2 saw negligible changes to the rate. Therefore, the CO_2 insertion step was ruled out as rate determining.

The rate determining transition state was stated to be the ring opening step because the rate was affected by changes in the concentrations of epoxide, $InBr_3$ and TBABr concentrations. Furthermore, it is also proposed that in the presence of excess epoxide a rapid ring opening would be seen. As both the ring opening and ring closing step are directly affected by the concentrations of the epoxide, $InBr_3$ and TBABr, it leaves the rate determining step open for debate.

To further study the initiation of the reaction and the effect of the salt, an in situ IR experiment monitored the reaction with a $TBAN_3$ nucleophile.[14] Spectra A (Figure 5.4) shows $TBAN_3$ (NBu_4N_3 = $TBAN_3$) in DCM. Spectra B shows that upon the addition of $InBr_3$ with $TBAN_3$, the band at 2000 cm^{-1} is replaced with a band at around 2075 cm^{-1} due to the formation of the $[InBr_3N_3^-][TBA^+]$ salt. Following the addition of the epoxide, little change is seen in spectra C. However, after the addition of the CO_2 two peaks formed rapidly. These peaks can be assigned to free CO_2 (2334 cm^{-1}) and cyclic carbonate (1810 cm^{-1}).

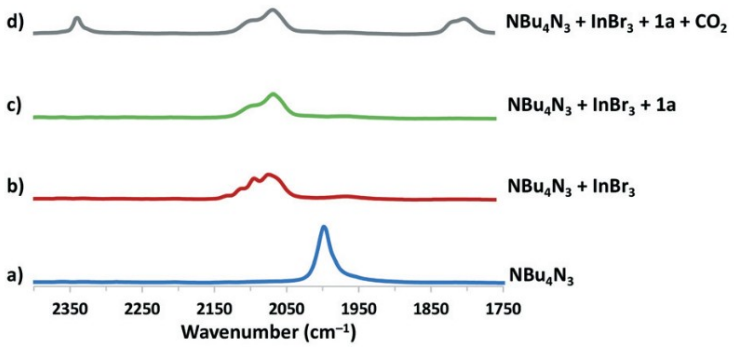

Figure – Simple Trihalide Group 13 Catalysts for CO2 Utilisation: A DFT / Design Criteria Study.77 - Infrared spectra illustrating the different binding modes of azide anion at T = 20 °C. a) NBu_4N_3 in DCM. b) 1 : 1 NBu_4N_3 : $InBr_3$ in DCM. c) 1 : 1 NBu_4N_3 : $InBr_3$, 1a, and DCM. d) 1 : 1 NBu_4N_3 : $InBr_3$, 1a, CO_2 in DCM (the spectrum recorded after 10 min); NBu_4N_3 = $TBAN_3$ from 14.[14]

Figure 5.4 highlights the stability of the salt. Once it has formed in spectra b, the salt remains present until the end of the reaction. To further understand this relationship, the $[InBr_3]$[TBABr] concentration ratio was varied. When $[InBr_3]$ <

[TBABr], the rate increased with increasing [$InBr_3$]. The rate plateaus at 0.89 mol L^{-1} h^{-1} when the ratio reaches 1 (Figure 5.5).[14] When [$InBr_3$] > [TBABr], the rate began to decrease due to the formation of the salt, reducing the chance of a successful ring opening because of a reduced concentration of free Br^- ions. Therefore, excess epoxide and optimal [$InBr_3$]:[TBABr] ratios are needed to drive the equilibrium towards **IC.**

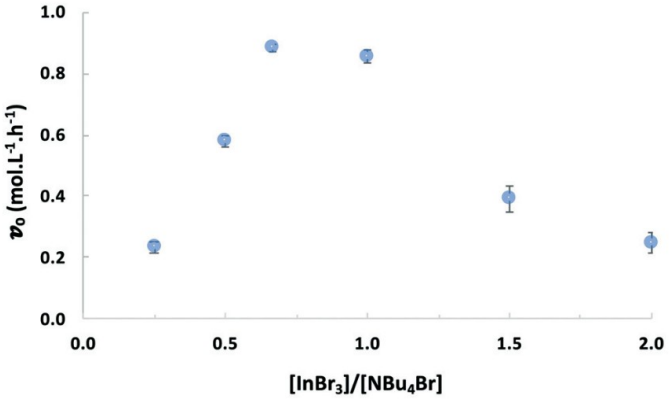

Figure – Simple Trihalide Group 13 Catalysts for CO2 Utilisation: A DFT / Design Criteria Study.78 - Plot of initial rates of product formation with varying concentration ratios of $InBr_3$ and TBABr from 14.[14]

Finally, at **Int2**, there are both κ^1 and κ^2 CO_2 binding modes available. To measure this, a variable temperature NMR was conducted showing a 9:1 favourability for the κ^1 CO_2 coordination. This means that the κ^2 coordination would be present as an off cycle intermediate but the κ^1 coordination would be favoured.[14]

With the indium catalysts providing the best yields, the lesser Lewis acidic catalysts are more active for this synthesis, and this is in good agreement with the groups previous findings.[15–17] The Mehrkhodavandi group reported similar results in a study of small Lewis acid catalysts.[6] In alkoxide complexes in the form of tetradentate salens and tridentate phenolates, the In catalysts were more active compared to Ga.[18] The Ga complexes were found to be more Lewis acidic. However, the calculated Mulliken charges of the different metal centres contradicted this observation showing In as more Lewis acidic. Without conclusive evidence on the measurable Lewis acidities of the compounds, their differences were attributed to steric hinderance around the smaller coordination sphere of Ga.

A different study produced similar results when comparing group 13 trichlorides for the ring opening polymerisation reaction of cyclohexene oxide.[19] The general reactivity of the catalysts was In > Ga > Al > B. This reactivity does not align

directly with Lewis acidities, which would predict BCl_3 as the most active. Instead, the observed order was attributed to the electronic properties of the group 13 (G_{13} which = B, Al, Ga and In) element centres, particularly the degree of covalency in the G_{13}–Cl bonds and the electrophilicity of the metal centres. $InCl_3$ has the most covalent character and lowest Lewis acidity so was better able to better stabilise the transition state during epoxide ring-opening. In contrast, the more Lewis acidic BCl_3 bound overly tight to the epoxide oxygen, hindering turnover and reducing catalytic efficiency.[19]

The Mehrkhodavandi group also conducted an in-depth analysis of varying Lewis's acidity of cationic Ga and In complexes on their activity.[20] The conventional pattern of the heavier group 13 metal catalysts being less Lewis acidic is broken. The article highlights the complex nature of Lewis acidity regarding solvent effects and how it is currently measured. The global electrophilicity index (GEI) calculated In complexes as more Lewis acidic than their Ga counterparts with equivalent coordination spheres. However, due to the preferential formation of lower-coordinate species, in this study, the In complexes did not exist in their higher Lewis acidic form and thus have lower activity.[20]

Despite the reoccurring theme of Lewis acidity not governing a catalysts reactivity, to the best of our knowledge, no chemical descriptors have been determined as the driving force for catalytic activity. This work theoretically expands on the research outlined in this section to obtain a deeper understanding of subtly varying the Lewis acidity, electronic and steric properties on the catalyst's activity. The use of small monodentate catalysts allows for a meaningful comparison of their activity and their Lewis acidity, due to their lower variability in comparison to multidentate catalysts.

5.1.3 Aims of this Work

- To elucidate the mechanisms of all nine group 13 trihalide catalysts.
- Compare the mechanism and calculated free energies of the $InBr_3$ catalyst to the kinetic study by the Mehrkhodavandi group.[14]
- Expand on experimental work by studying three additional GaX_3 catalysts (Figure 5.6).[15,16] By changing the X ligands to Me, ^{t}Bu and Ph, the subtle effects of steric and electronic properties can be elucidated.

- Develop quantitative structure-activity relationship (QSAR) models to gain a better understanding of what catalyst descriptors are driving catalyst activity.

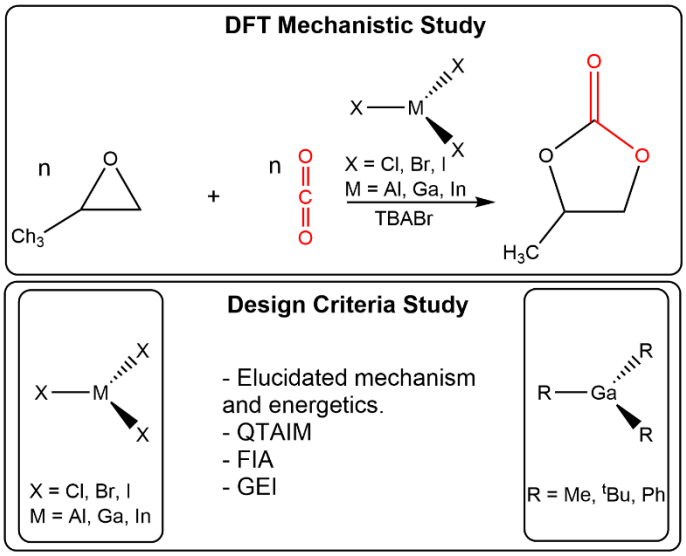

Figure – Simple Trihalide Group 13 Catalysts for CO2 Utilisation: A DFT / Design Criteria Study.79 - An outline of the computational investigations conducted for the cycloaddition of epoxides and CO_2 catalysed by metal halides.

5.2 Results and Discussion

5.2.1 $InBr_3$ Mechanism and Comparison

The calculated mechanism for the cycloaddition of CO_2 and propylene oxide catalysed by $InBr_3$ is shown in Figure 5.7. The mechanism begins at **IC** which is 5.0 kcal mol^{-1} more stable than the reactants. **IC** would be in equilibrium with the **$InBr_4$·TBA** salt which is calculated at 15.6 kcal mol^{-1} more stable in good agreement with the experimental results. Without excess epoxide, the salt would readily form**,** preventing the reaction from proceeding.

From **IC**, TBABr forms pre-transition state adduct, **IC·TBABr**. The epoxide ring opening follows (**TS1·TBA**) to from **Int1·TBA**. A monometallic *vs.* bimetallic **TS1** pathway was calculated. The bimetallic **TS1·TBA Dinuclear** was calculated with a free energy barrier 7.7 kcal mol^{-1} less than **TS1·TBA**. **TS1 Dinuclear**, had a calculated free energy barrier 13.8 kcal mol^{-1} more stable than **TS1·TBA**. However, the correct vibrational mode could not be identified for the monometallic ring opening without the TBA^+ present. Instead, the calculation was converging past the saddle point and the vibrational frequency located was just the bending

of atoms. Therefore, while **TS1 Dinuclear** is lower in free energy, it cannot be attributed as the correct transition state, without the correct imaginary frequency. This is most likely due to the large charge to size ratio of the bromide ion hence it needs the counterion or a second catalyst molecule to be stabilised.

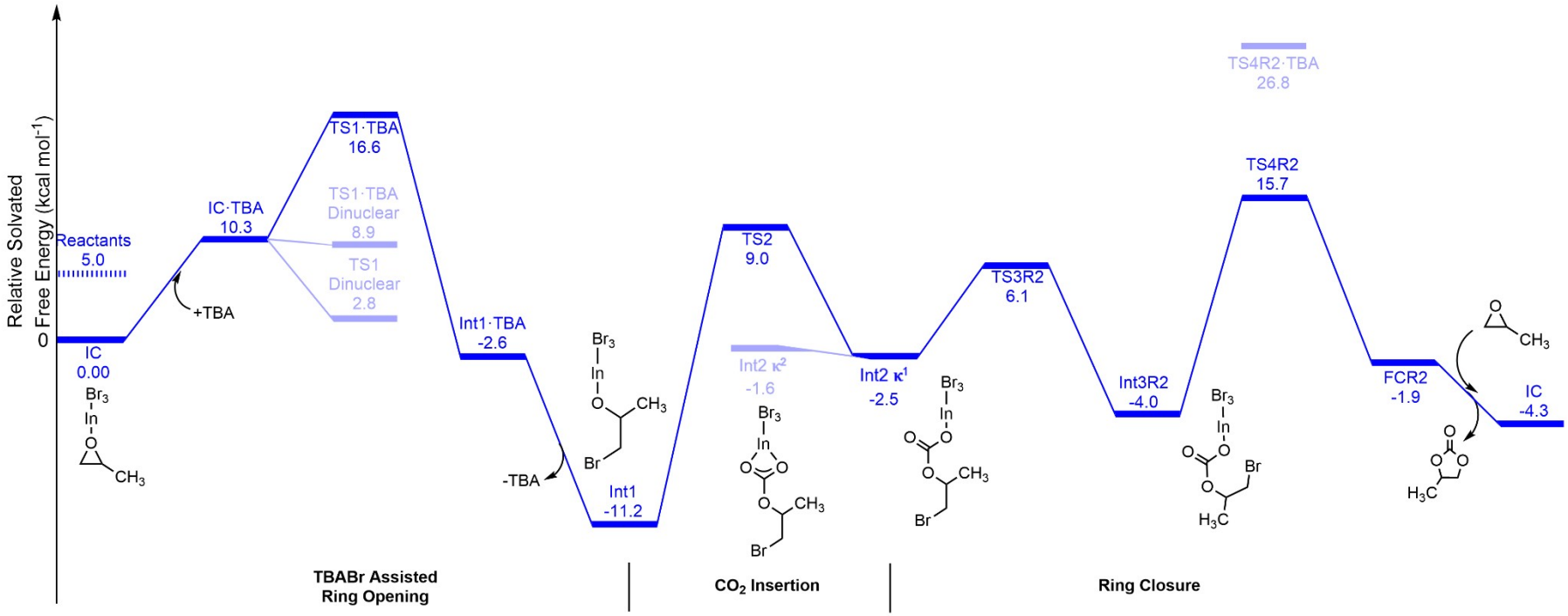

Figure – Simple Trihalide Group 13 Catalysts for CO2 Utilisation: A DFT / Design Criteria Study.80 - Calculated solvated free energy surface in kcal mol^{-1} (ΔG 298 K) for the cycloaddition of CO_2 and propylene oxide catalysed by $InBr_3$, to form propylene carbonate at the ωB97-D3BJ def2-tzvpp def2/j level of theory.

To understand the increased stability of **TS1·TBA Dinuclear**, structural analysis of **TS1·TBA** (Table 5.2, left) and **TS1·TBA Dinuclear** (Table 5.2, right) is presented. The longer Br-C bond of 2.79 Å length seen in **TS1·TBA** shows a weaker interaction between Br and C in comparison with **TS1·TBA Dinuclear** with a Br-C length of 2.409 (Table 5.2). This is much closer to the C-Br bond length of 1.950 Å.

Consequently, **TS1·TBA** exhibits a shorter C-O bond length by 0.312 Å compared to **TS1·TBA Dinuclear**. The observed difference is due to the second catalyst molecule shielding the nucleophile from the strong +1 positive charge of **TBA$^+$**, allowing for the nucleophile to get within a closer proximity to the carbon. The shorter C–O bond in **TS1·TBA** relative to **TS1·TBA Dinuclear** suggests an earlier transition state along the C–O bond cleavage coordinate, consistent with weaker nucleophilic attack. In contrast, the elongation of the C–O bond in the dinuclear system indicates greater progression towards ring opening, consistent with the stronger Br–C interaction and lower activation energy.

*Table – Simple Trihalide Group 13 Catalysts for CO2 Utilisation: A DFT / Design Criteria Study.13 - Comparison of bond lengths (Å) for **TS1·TBA** and **TS1·TBA Dinuclear** with the difference. Figure included to indicate the Br-C bond (blue bond) and C-O bond (red dashed bond) where M = In and X = Br.*

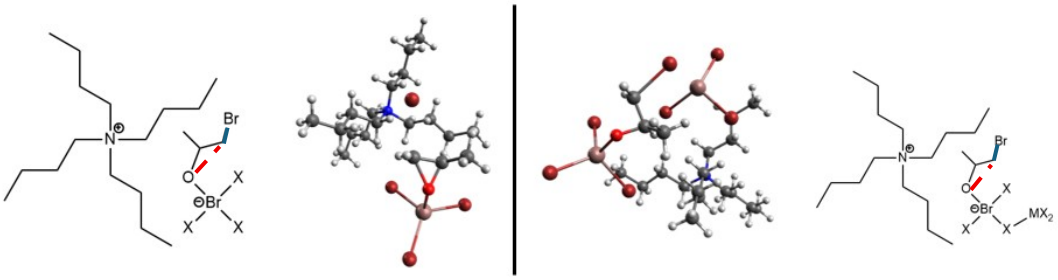

Bond	TS1.TBA	TS1.TBA Dinuclear	Difference
Br-C	2.794 Å	2.409 Å	0.385
C-O	1.581 Å	1.893 Å	0.312

In the case of **TS1 Dinuclear**, **TBA$^+$** was not included explicitly in the geometry optimization or frequency calculation. As a result, the entropy contribution for **TS1 Dinuclear** is significantly less negative (3.6 kcal mol^{-1}) compared to **TS1·TBA Dinuclear** (−72.6 kcal mol^{-1}), where **TBA$^+$** was included fully in the calculation. Consequently, the absolute entropy correction differs substantially from **TS1·TBA Dinuclear**, as inclusion of a large, weakly bound ion introduces many low-frequency modes. This difference in entropic treatment accounts for the lower computed Gibbs free energy of **TS1 Dinuclear**.

For this reaction, **TS1.TBA** is not the TDTS. Due to the energy released because of ring opening the substate, the ring opening step should be fast and readily occur. The difference in the anionic and neutral systems calculated have proven to be a problem for this DFT model. Despite the ring opening step remaining debateable, for the purpose of this study, **TS1·TBA** will be used as the accepted transition state. Furthermore, as **TS1·TBA** is not the TDTS, it does not affect the overall energetics of the calculated mechanism.

To justify the absence of TBA$^+$ for the remainder of the mechanism, **TS4R2·TBA** was calculated to give a comparison of the energy span with and without the TBA$^+$ counterion present. The energy span taken from **Int1** (Turnover Frequency Determining Intermediate (TDI)) to **TS4R2** (TDTS) was calculated at 26.9 kcal mol^{-1}. Between **Int1·TBA** and **TS4R2·TBA** it was calculated at 29.4 kcal mol^{-1}. A 2.4 kcal mol^{-1} difference was observed, however, this would be expected due to the entropic penalty of including the TBA$^+$ in the calculations. Therefore, proceeding **Int1·TBA**, the TBA$^+$ is discounted to reduce computational cost. After **Int1**, CO_2 insertion (**TS2**) occurs with a barrier of 20.2 kcal mol^{-1} to form **Int2 κ^1**. An equilibrium is formed between **Int2 κ^1** and **Int2 κ^2** (Figure 5.8).[14]

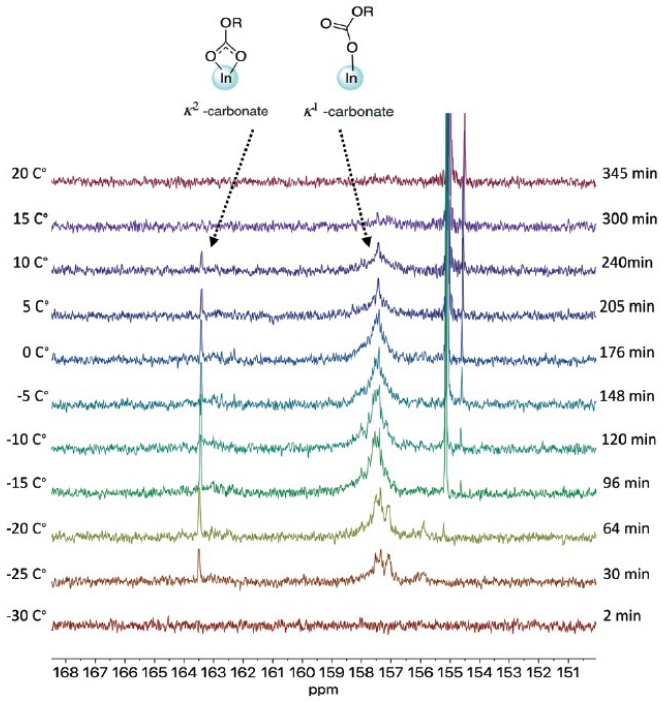

*Figure – Simple Trihalide Group 13 Catalysts for CO2 Utilisation: A DFT / Design Criteria Study.81 - $^{13}C(^{1}H)$ NMR spectrum for the detection of the different CO_2 binding modes for **Int2** κ^1 and κ^2 from 14.[14]*

Experimental results showed a 9:1 ratio between **Int2** κ^1 and κ^2 respectively. The canonical partition function (Eq. 5.1) has been used to calculate the predicted ratio of **Int2** κ^1 and κ^2 to compare computed free energies with experimental data. Using the calculated ΔG 298 K values, a Boltzmann distribution ratio of 7.5:1 was calculated, in good agreement with the 9:1 experimental value.

$$\frac{P_{\int 2\kappa^1}}{P_{\int 2\kappa^2}} = \exp\left(\frac{\varepsilon_{\int 2\kappa^2} - \varepsilon_{\int 2\kappa^1}}{RT}\right) \quad \text{Eq. 5.1}$$

From **Int2** κ^1, an isomerisation occurs (**TS3R2**) to form **Int3R2**. The cyclic carbonate ring closure (**TS4R2**) affords **FCR2**. The energy barrier associated with **TS4R2** was 26.9 kcal mol^{-1} making it the TDTS.[21] An exchange between the cyclic carbonate product and the epoxide then occurs to regenerate **IC** and begin a new catalytic cycle.

Experimentally **TS1** was proposed to be the turnover frequency determining transition state. However, calculations have predicted **TS4R2** as the TDTS by 6 kcal mol^{-1}. As previously mentioned, none of the experimental results presented unambiguously identified the TDTS as either **TS1** or **TS4R2**. **TS2** was ruled out as the TDTS due to negligible changes in the rate of reaction with changing pressures of CO_2. The calculated energy barrier of **TS2** was 6.7 kcal mol^{-1} lower

than **TS4R2** agreeing with this observation. Furthermore, as already discussed, the **TS1·TBA Dinuclear** barrier has been calculated higher due to the entropic penalty with explicitly including the **TBA^+** in the calculation at 16.6 kcal mol^{-1}. This results in an energy span of 20.9 kcal mol^{-1} at **TS1·TBA Dinuclear** in comparison to 26.9 kcal mol^{-1} at **TS4R2**. This indicates **TS4R2** as the TDTS, agreeing with the kinetic study.

5.2.2 Calculated Mechanisms - MX_3 Catalysts (M = Al, Ga, In; X= Cl, Br, I)

To further understand the subtle changes in electronic parameters and Lewis acidity, the mechanism for all nine catalysts were fully elucidated (Figures 5.9-5.11). The general mechanism of each catalyst remains the same as $InBr_3$ (Figure 5.7).

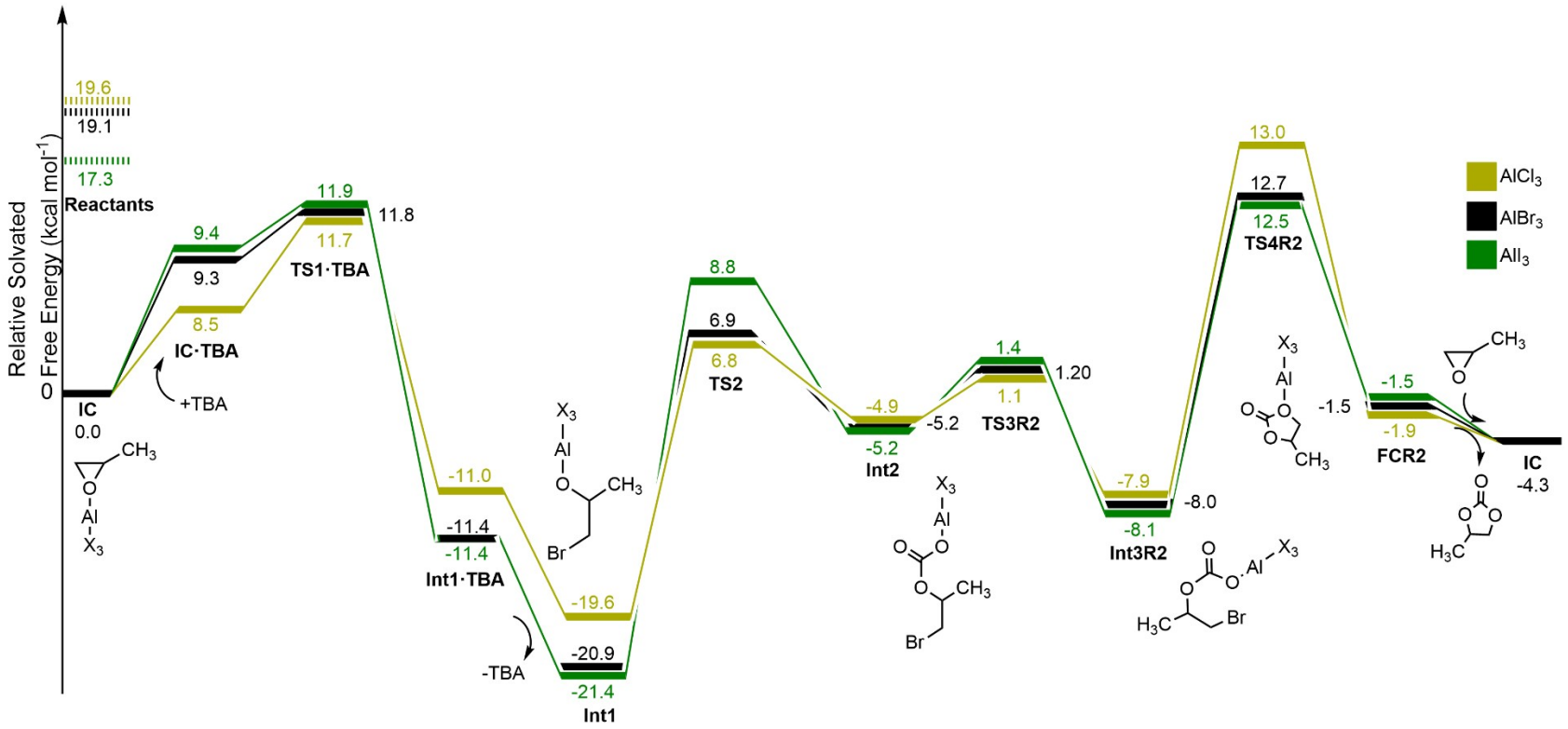

Figure – Simple Trihalide Group 13 Catalysts for CO2 Utilisation: A DFT / Design Criteria Study.82 - Calculated solvated free energy surface in kcal mol^{-1} (ΔG 298 K) for the cycloaddition of CO_2 and propylene oxide catalysed by $AlCl_3$ (Sage), $AlBr_3$ (Black) and AlI_3 (Green) to form propylene carbonate at the ωB97-D3BJ/def2-tzvpp/def2/j level of theory.

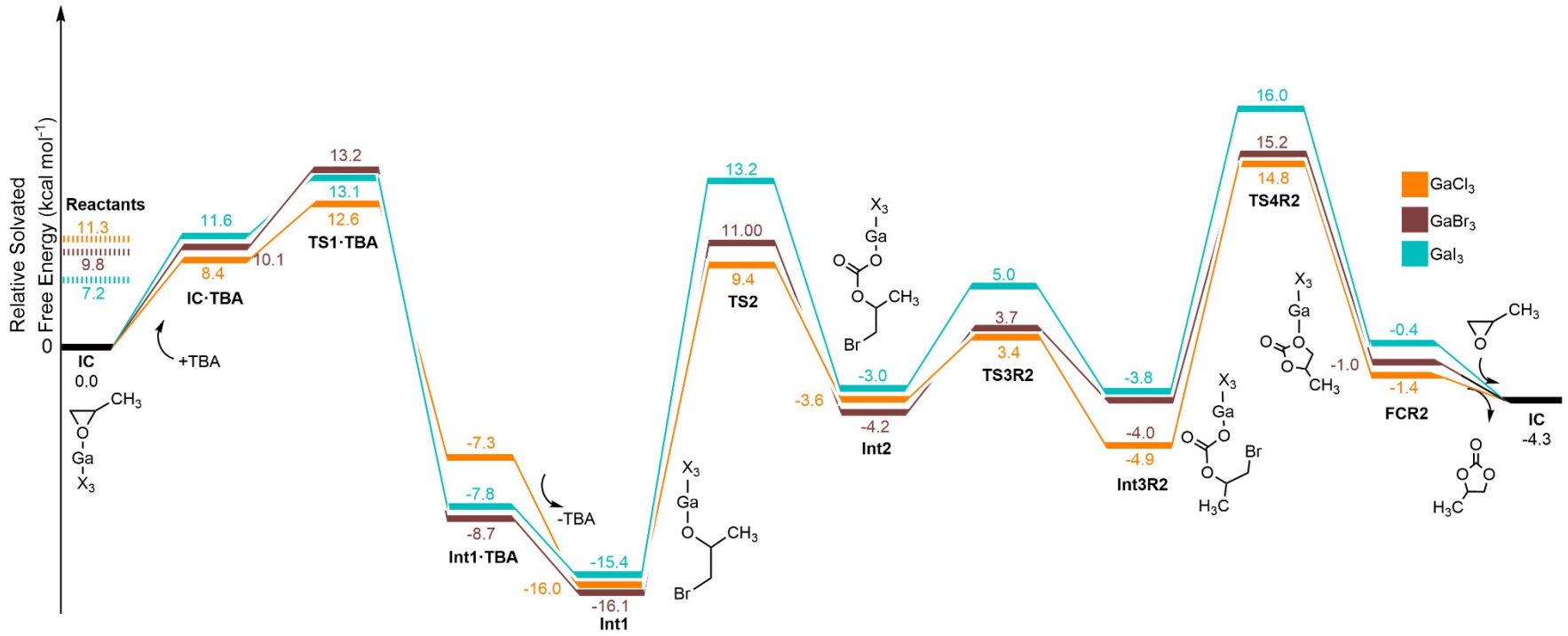

Figure – Simple Trihalide Group 13 Catalysts for CO2 Utilisation: A DFT / Design Criteria Study.83 - Calculated solvated free energy surface in kcal mol^{-1} (ΔG 298 K) for the cycloaddition of CO_2 and propylene oxide catalysed by $GaCl_3$ (Orange), $GaBr_3$ (Brown) and GaI_3 (Cyan) to form propylene carbonate at the ωB97-D3BJ/def2-tzvpp/def2/j level of theory.

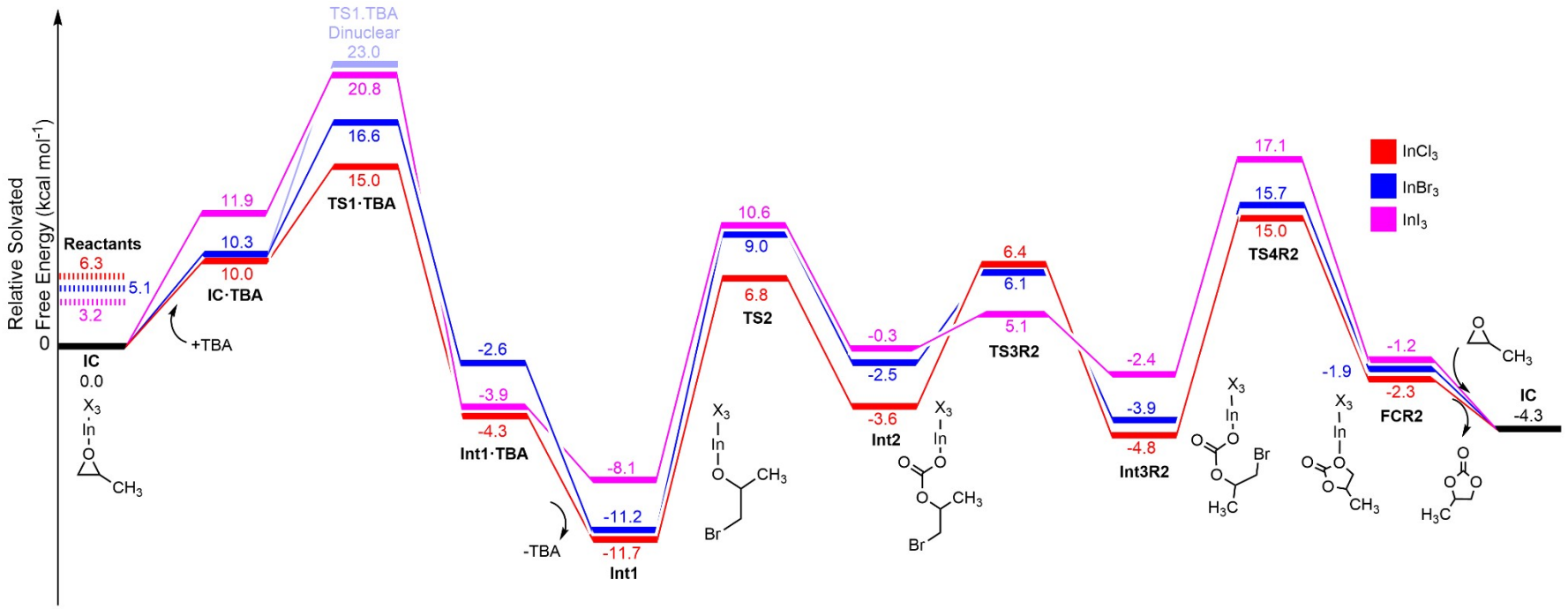

Figure – Simple Trihalide Group 13 Catalysts for CO2 Utilisation: A DFT / Design Criteria Study.84 - Calculated solvated free energy surface in kcal mol^{-1} (ΔG 298 K) for the cycloaddition of CO_2 and propylene oxide catalysed by $InCl_3$ (Red), $InBr_3$ (Blue) and InI_3 (Magenta) to form propylene carbonate at the ωB97-D3BJ/def2-tzvpp/def2/j level of theory.

Across the nine catalysts, several off-cycle dimeric intermediates were calculated. These are summarised in Table 5.3, showing their relative energy in comparison to their non-dimeric partners. There are several non-calculatable (NC) dimers which either did not converge, or the ground state structure could not be confidently identified (contained significant negative modes).

*Table – Simple Trihalide Group 13 Catalysts for CO2 Utilisation: A DFT / Design Criteria Study.14 - The relative stability, in comparison to their non-dimeric intermediates, of possible dimeric structures for all nine catalysts in kcal mol^{-1}. [a] **Int1** and **Int2** dimer for $AlCl_3$ are part of the predicted catalytic cycle and are connected by **TS2** dimer.*

Catalyst	IC Dimer (kcal mol^{-1})	Int1 Dimer (kcal mol^{-1})	Int2 Dimer (kcal mol^{-1})	Int3R2 Dimer (kcal mol^{-1})
	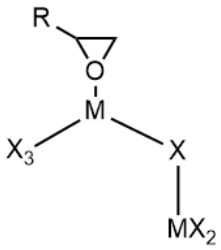	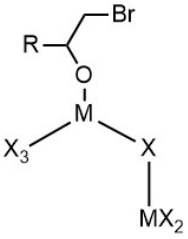	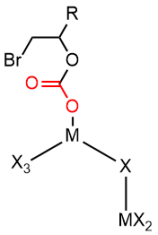	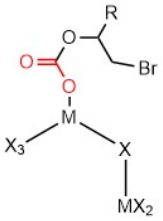
$AlCl_3$	-8.7	-7.7[a]	-6.6[a]	NC
$AlBr_3$	-5.1	-3.2	-1.7	-1.1
AlI_3	-3.5	+0.1	-0.6	+48.4
$GaCl_3$	-2.4	-1.8	+9.4	NC
$GaBr_3$	-3.2	+1.0	+2.5	NC
GaI_3	-2.6	+4.0	+4.9	NC
$InCl_3$	NC	NC	-4.7	NC
$InBr_3$	NC	NC	-1.7	NC
InI_3	-3.2	NC	+0.3	+4.0

NC – Non-calculatable. All dimers with NC contained negative modes. A ground state structure could not be found after several attempts.

The $InBr_3$ reaction was first order in respect to the catalyst. If the dimers were actively involved in the cycle, the reaction would not be first order. Secondly, **Int2 Dimer** sees the CO_2 binding mode move from κ^1 to κ^2 (Figure 5.12), due to one of the Br^- being pulled away from the metal centre giving another vacant site. This means the second oxygen readily interacts with the metal centre in the κ^2 binding mode. The NMR experiment in Figure 5.9 and Boltzmann distribution calculations have shown the clear preference for a κ^1 binding mode. If **Int2 Dimer** was present, the NMR spectra would have shown a stronger band for the κ^2 binding mode.

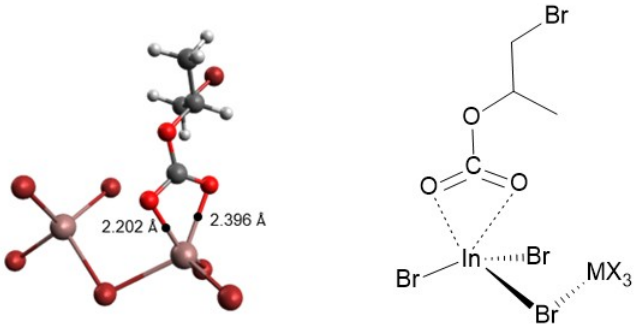

*Figure – Simple Trihalide Group 13 Catalysts for CO2 Utilisation: A DFT / Design Criteria Study.85 - The calculated structure for $InBr_3$ **Int2 Dimer** showing the κ^2 binding mode.*

As already discussed, the reaction proceeds with low catalyst loading as an increase hinders reactivity due to the formation of the $[TBA^+][MX_4^-]$ salt. As the salt is significantly more stable than the **IC dimers**, the equilibrium would shift preferably towards the salt over dimer formation in the event of increased catalyst loading. Furthermore, a lower catalyst loading would not drive the equilibrium towards the formation of a dimeric intermediate (Figure 5.13) as this requires 2 equivalents of a catalyst to form, requiring a higher concentration. To conclude, regardless of several dimers calculated as more energetically favourable in comparison to their monomeric intermediates, they are not taking an active part within the catalytic cycle.

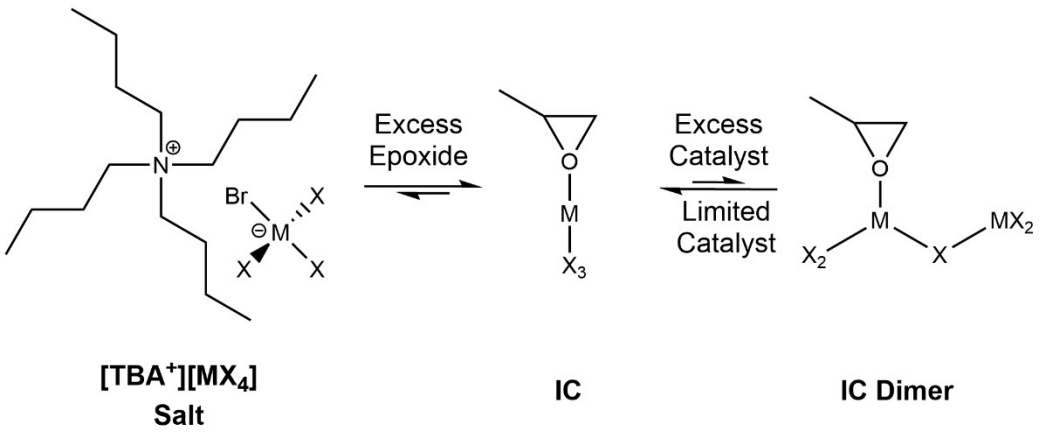

*Figure – Simple Trihalide Group 13 Catalysts for CO2 Utilisation: A DFT / Design Criteria Study.86 - The equilibrium between the $[MX_3Br^-][TBA^+]$ salt, **IC** and **IC Dimer**.*

Table 5.4 outlines the free energy span of the reaction (from the TDI to the TDTS) [21] for each catalyst in comparison to the yield. Two measures of the Lewis acidity, the absolute fluoride ion affinity (FIA) and the global electrophilicity index (GEI), have been included for comparison (details in section 5.3).[22,23]

Table – Simple Trihalide Group 13 Catalysts for CO2 Utilisation: A DFT / Design Criteria Study.15 - A comparison of the calculated free energy span from the TDI to the TDTS with the experimental yield. Fluoride

MX_3	Energy Span (kcal mol^{-1})	Absolute FIA (kJ mol^{-1})	GEI (eV) (x 10^{-2})	Yield%
$AlCl_3$	32.6	506	9.95	23
$AlBr_3$	33.5	511	7.93	41
AlI_3	33.9	510	5.65	26
$GaCl_3$	30.9	433	10.20	3
$GaBr_3$	31.3	429	7.89	39
GaI_3	31.4	420	5.38	42
$InCl_3$	25.2	417	9.64	70
$InBr_3$	26.9	408	7.46	90
InI_3	27.7	395	5.11	79

ion affinity calculations (FIA), global electrophilicity index (GEI) calculations.

As shown in Table 5.4, $InBr_3$ has the lowest calculated energy span of 26.9, in good agreement with the highest yield achieved of 90 %. The In catalysts as a collective have lower calculated energetic spans, 25.2, 26.9, and 27.7 kcal mol^{-1} for $InCl_3$, $InBr_3$ and InI_3 respectively. $GaCl_3$, $GaBr_3$ and GaI_3 have higher calculated energy spans of 30.9, 31.3 and 31.4 kcal mol^{-1} with reported yields of 3, 39 and 42 % respectively, agreeing that Ga catalysts are less active compared to In. The reported yield of $GaCl_3$ was poorly rationalised by the energy span and elucidated reaction mechanism. Therefore, further experiments would be required to explain this. The energy spans of $AlCl_3$, $AlBr_3$ and AlI_3 have been calculated at 32.6, 33.5 and 33.9 kcal mol^{-1} with reported yields of 23, 41 and 26 % respectovely. As a group, the catalysts are generally less active than the Ga catalysts, and have higher energetic spans, again in good agreement with the experimental results.

Figure 5.14 shows that the general trend of increasing Lewis acidity leads to decreasing % yield. The graph shows clusters of each metal with the expected Lewis acidic strength of Al > Ga > In. Furthermore, each metal shows the periodic trend of the halides with decreasing Lewis acidic strength going down the group MCl_3 > MBr_3 > MI_3. Although the graph shows good agreement with other work on group 13 complexes, it cannot be used as a single descriptor to predict the activity in this study.[18]

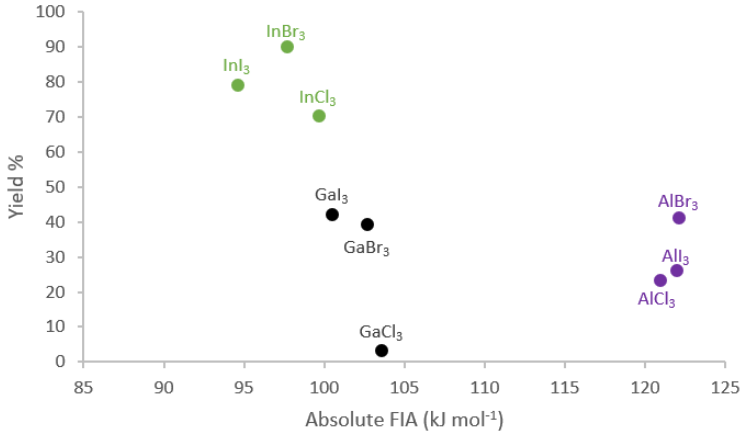

Figure – Simple Trihalide Group 13 Catalysts for CO2 Utilisation: A DFT / Design Criteria Study.87 - A graph showing the relationship between the absolute FIA and the yield for all 9 MX_3 catalysts.

Another measure of the Lewis acidity, the global electrophilicity index (GEI), was calculated (Figure 5.15). The GEI is derived from calculated HOMO and LUMO energies of the catalyst and is a measure of a molecules ability to take up electrons.[23] Figure 5.15 A and Figure 5.15 B show different trendlines the same data. Figure 5.15 A highlights the trend of how changing the halide ligand for a specific metal centre affects the yield. Across all three metals, the periodic trend of Lewis acidity $MBr_3 > MCl_3 > MI_3$, is observed. For the Al and In catalysts, the MBr_3 catalyst produces the best yield. As the MBr_3 catalysts hold the "medium" Lewis acidic strength, this reiterates a point from Chapter 3, that there is an optimum Lewis acidity for catalyst activity. However, the Ga catalysts do not follow this trend with a decline in the yield achieved as the Lewis acidity of the catalyst increases.

Figure 5.15 B highlights the trends across the different metal centres. All three X ligands show that as the Lewis acidic strength of the catalyst increases, the yield achieve decreases. Both the I and Br ligands follow the expected general trend of Lewis acidic strength of Al > Ga > In. For the Br ligand, the Lewis acidic strength is almost equal for $GaBr_3$ and $AlBr_3$ with both producing equivalent yields of cyclic carbonate. For the Cl ligand, the calculated Lewis acidic strength for each metal catalyst is Ga > Al > In. This trend agrees with the study of alkyl-based Lewis acidic structures bearing Cl ligands.[18] The deviation from the expected trend for the Cl ligand means that the $GaCl_3$ catalyst is calculated as the most Lewis acidic using the GEI method. The $GaCl_3$ catalyst is also anomalous in the experimental results only producing a 3 % yield. Although there is no clear link between the deviation and the anomalous yield, the behaviour of the $GaCl_3$ catalyst is unusual.

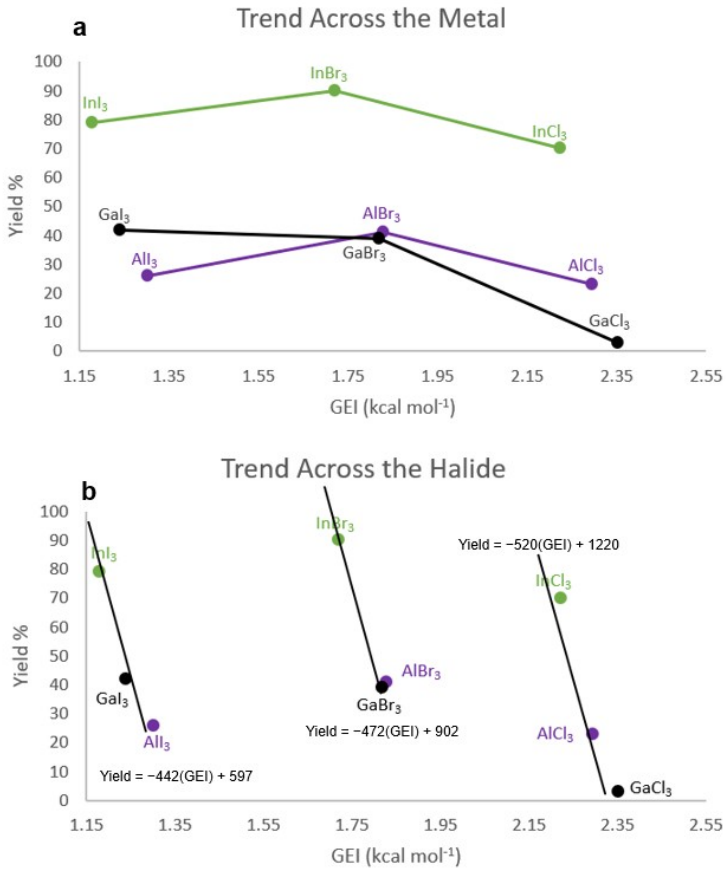

Figure – Simple Trihalide Group 13 Catalysts for CO2 Utilisation: A DFT / Design Criteria Study.88 - Graphs showing the relationship between the GEI and % yield. Graph A highlights the trends between the different halide metal for a single metal centre. Graph B highlights the trends between changing the metal centre with a specific halide ligand and a line of best fit.

It can be concluded that for this study the GEI provides a better prediction of the experimental yield in comparison to the FIA. As FIA calculations are based on the catalysts ability to form an $[LA\text{-}F]^-$ complex, it does not always provide a good representation when the catalyst is binding to other substrates. However, as the GEI is based on the HOMO and LUMO energies of the catalyst structure, this provides a more universally better representation of Lewis acidic strength with a variety of substrates. In this case, this more universal approach of the GEI, led to more accurate predictions. These methods show there is correlation between the Lewis acidic strength and the activity of the catalyst, but this is not a linear relationship. To achieve a deeper understanding of what other properties affect activity, three additional catalysts have been studied computationally ($GaMe_3$, Ga^tBu_3 and $GaPh_3$).

5.2.3 CO_2 Energy of Association ($\Delta G_{assoc‡}$) and insertion (ΔG_{insert})

To evaluate the influence of CO_2 activation on overall catalytic performance, the free energy of CO_2 association ($\Delta G_{assoc‡}$) and the free energy of CO_2 insertion (ΔG_{insert}) were extracted for each catalyst and are summarised in Table 5.5.

Table – Simple Trihalide Group 13 Catalysts for CO2 Utilisation: A DFT / Design Criteria Study.16 - The energy of association and energy of insertion of CO_2 for all nine MX_3 catalysts.

Catalyst	$\Delta G_{assoc‡}$ (kcal mol^{-1})	ΔG_{insert} (kcal mol^{-1})
$AlCl_3$	26.4	14.7
$AlBr_3$	27.8	15.7
AlI_3	30.2	16.2
$GaCl_3$	25.4	12.4
$GaBr_3$	27.0	11.9
GaI_3	28.6	12.4
$InCl_3$	18.5	8.1
$InBr_3$	20.2	8.8
InI_3	18.7	7.7

To better understand the relationship between the CO_2 activation energetics and catalytic performance, graphs were plotted in Figure 5.16. A strong positive correlation is observed between energy span and both $\Delta G_{assoc‡}$ (R^2 = 0.887) and ΔG_{insert} (R^2 = 0.920). The indium systems cluster at lower ΔG values and lower energy spans, whereas the aluminium systems have higher energies, with gallium intermediate. This is correlated with the experimental yields observed by the Mehrkhodavandi group. Both experimentally and computationally, the TDTS was identified as **TS1** for this catalyst series. Although CO_2 insertion (**TS2**) is not thermodynamically defined as the TDTS in these systems, the strong correlation between $\Delta G_{assoc‡}$ / ΔG_{insert} and the overall energy span indicates that CO_2 activation remains kinetically influential within the catalytic cycle. In many related systems, TS2 is commonly found to be turnover determining; therefore, the observed scaling behaviour suggests that even when TS1 formally defines the energy span, the electronic factors governing CO_2 association and insertion

propagate through the reaction coordinate and contribute significantly to the overall catalytic barrier.

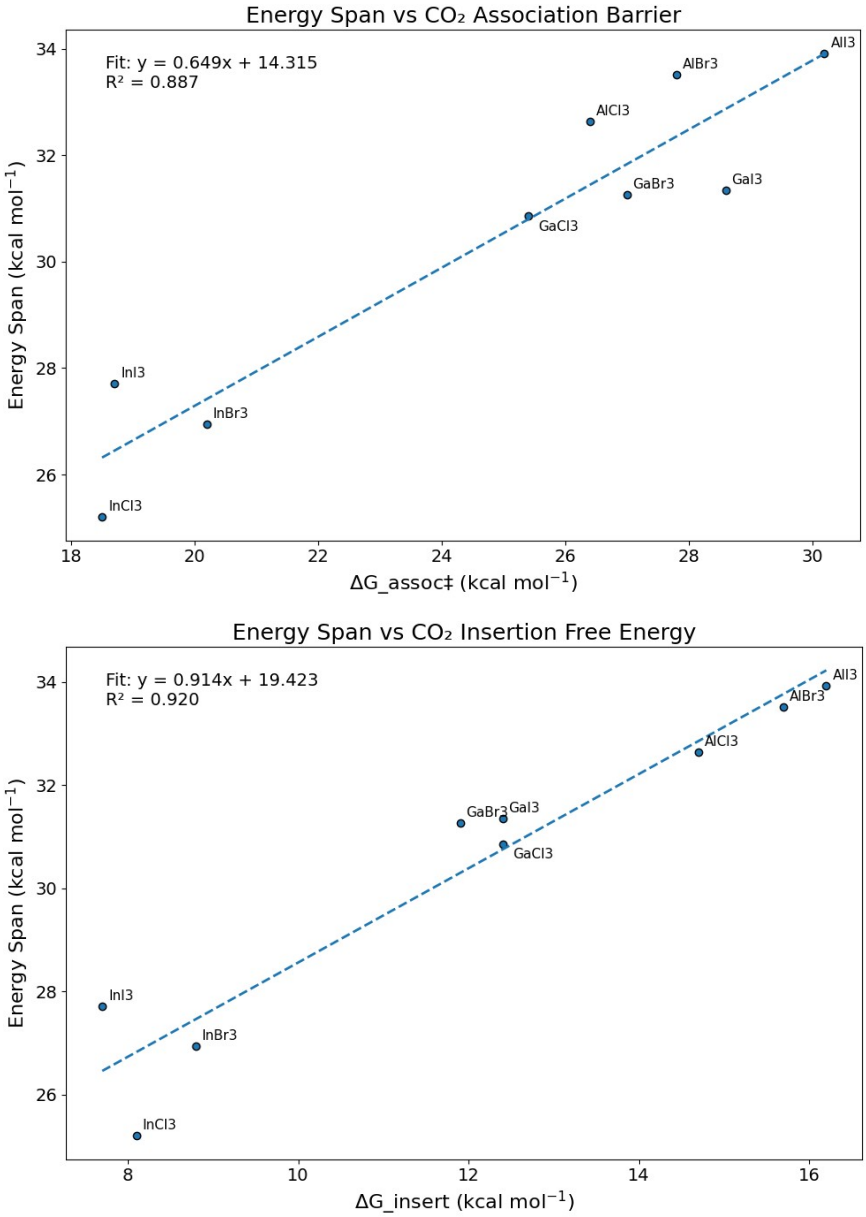

Figure – Simple Trihalide Group 13 Catalysts for CO2 Utilisation: A DFT / Design Criteria Study.89 - Graphs showing the relationship between the free energy span (kcal mol^{-1}) and $\Delta G_{assoc‡}$ (kcal mol^{-1}) (top) and ΔG_{insert} (kcal mol^{-1}) (bottom).

5.2.4 Steric Vs. Electronic Properties

The steric and electronic properties of any catalyst are integral to their activity. The difference in halides in section 5.2.2 are exemplars of how a change in electronic properties can lead to different catalytic activity. To understand how subtle changes to the steric and electronic properties of the catalyst affects activity, three additional catalysts were studied: $GaMe_3$, Ga^tBu_3 and $GaPh_3$. Herein, the mechanism for each catalyst has been calculated in Figure 5.17.

The elucidated mechanisms follow the same general pathway as Figures 5.9-5.11. The Ga metal centre was chosen due to it being highly active in Chapters 3 and 4. The energy span for the Ga complexes ligated with Me, $^{t}Bu_3$ or Ph substituents was 26.5, 24.7 and 23.2 kcal mol^{-1} respectively. In section 5.2.2, the In based catalysts were shown to be the most active. Therefore, it would be expected that an In catalyst with Ph ligands (the best ligand in this section coordinated to Ga), would be calculated as the most active catalyst. However, **TS2** could not be located for an $InPh_3$ catalyst as a structure with a binding mode showing bond formation of an alkoxide and oxygen coordinating with the Ga catalyst could not be calculated.

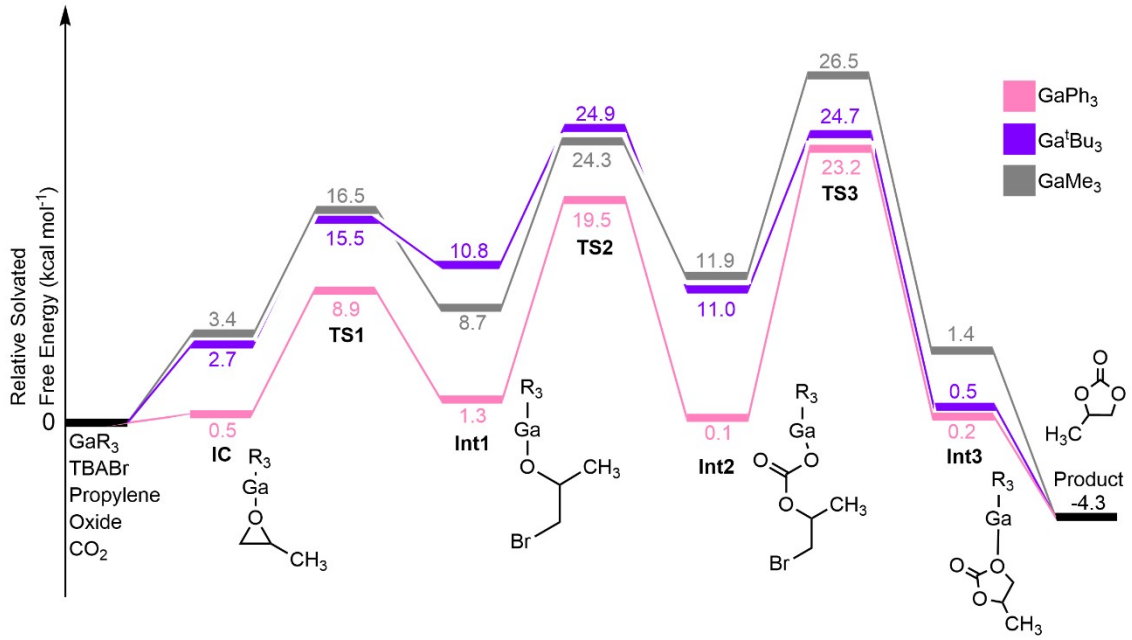

Figure – Simple Trihalide Group 13 Catalysts for CO2 Utilisation: A DFT / Design Criteria Study.90 - Calculated solvated free energy surface in kcal mol^{-1} (ΔG 298 K) for the cycloaddition of CO_2 and propylene oxide catalysed by $GaMe_3$ (Grey), $Ga^{t}Bu_3$ (Purple) and $GaPh_3$ (Pink) to form propylene carbonate at the ωB97-D3BJ def2-tzvpp def2/j level of theory.

One notable difference between Figure 5.17 and Figures 5.9-5.11. Firstly, the three alkyl/aryl catalysts (Ga-R) all start from the reactants due to endergonic formation of **IC** because the Lewis acidic strength of the catalyst is significantly weaker than the halide when L = Ph, ^{t}Bu or Me. Both the calculated FIA values (Figure 5.18) and GEI values (Figure 5.19) have been plotted against the **IC** energy relative to the reactants.

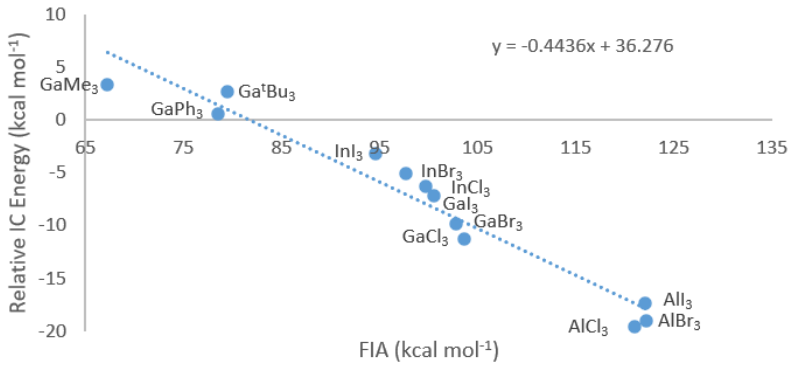

*Figure – Simple Trihalide Group 13 Catalysts for CO2 Utilisation: A DFT / Design Criteria Study.91 - The FIA (kcal mol^{-1}) vs. the **IC** energy (kcal mol^{-1}) relative to the reactants.*

The general trend seen in Figure 5.18 shows that as the calculated Lewis acidic strength decreases, the relative energy of IC increases. As the Ga alkyl and aryl catalysts have an FIA of roughly 15-20 kcal mol^{-1} lower than InI_3 (calculated as the least Lewis acidic of the nine trihalide catalysts), their energy of association with the epoxide becomes positive. Lu *et al.* chose to discount a Ga-salen catalyst from their studies due to it having a low binding energy with the epoxide.[24] In this study, the slightly positive and low binding energies belong to the most active catalysts. Thereby highlighting the importance of exploring new chemical space.

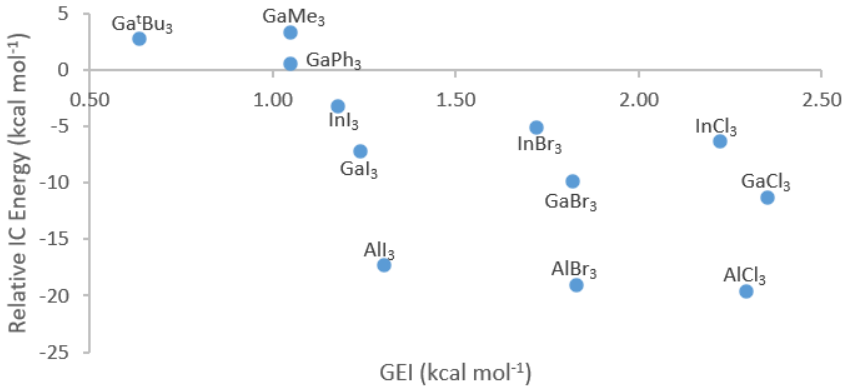

*Figure – Simple Trihalide Group 13 Catalysts for CO2 Utilisation: A DFT / Design Criteria Study.92 - The GEI (kcal mol^{-1}) vs. the **IC** energy (kcal mol^{-1}) relative to the reactants.*

The trend for GEI is less obvious (Figure 5.19) due to the way it is measured in comparison to FIA. The GEI is based on the catalyst's ability to accept electrons based on the HOMO and LUMO energies with the general trend of the higher the calculated Lewis acidity, the larger the relative energy is not seen. However, the graph clearly highlights the periodic trends across the nine trihalide catalysts. Going down group 13, the GEI decreases as the HOMO energy increases. Therefore, the metal cannot accept electrons as easily and the relative **IC** energy increases. Similarly, going down group 17, the GEI of the catalyst decreases due to an increase in HOMO energy because of the electronegativity of the halide decreasing. Therefore, it becomes less electron withdrawing, increasing the electron density around the metal centre and the energy of the HOMO increases, thereby increasing the relative **IC** energy.

Figure 5.19 also demonstrates the differences of making significant changes to the electronic properties of the catalyst. In comparison to the Ga trihalides, the Ga-R catalysts all have a positive relative **IC** energy and a significantly lower GEI. Despite this, the Ga-R catalysts are calculated to have significantly lower energy spans in comparison to the trihalides, suggesting that they would be more active.

The second difference with the mechanisms in Figure 5.18 is the absence of **TS3R2**. From **TS2** the metal-alkoxide is in the correct orientation to access the lower energy ring-closure conformation. A comparison of the minima of the calculated **TS2** structures of $GaBr_3$ (Figure 5.20, left) and $GaMe_3$ (Figure 5.20, right) provide insight into why the isomerisation is not needed for the GaR_3 catalysts. The dihedral angle (O-C_1-C_2-Br) between the ring closing O-C_2 is -63.8 ^{o} with 2.980 Å for the $GaMe_3$ catalyst in comparison to 113.4 ^{o} with 3.826 Å for $GaBr_3$. For $GaMe_3$, the two atoms are aligned closely enough for the ring opening to occur after **Int2,** however, an isomerisation needs to occur for $GaBr_3$ to bring the C_2-O ring closure atoms closer together (2.945 Å).

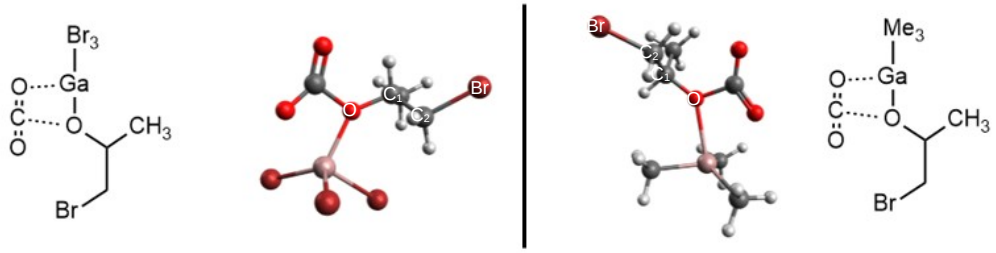

*Figure – Simple Trihalide Group 13 Catalysts for CO2 Utilisation: A DFT / Design Criteria Study.93 - The **TS2** structures for $GaBr_3$ (Left) and $GaMe_3$ (Right).*

As the steric bulk increases from $GaMe_3$ to Ga^tBu_3, there is a 1.6 kcal mol^{-1} lowering of the free energy span. To see the steric effects on **TS3** between $GaMe_3$ and Ga^tBu_3, quantum theory of atoms in molecules (QTAIM) was employed to produce reduced density gradients (RDGs) and non-covalent interaction (NCI) plots (Figure 5.21).

The NCI plots (Figure 5.21, top), highlight a stabilising effect between a ^{t}Bu ligand and the ring closing oxygen through weak interactions and Van der Waals forces (light green). Ga^tBu_3 has a much broader and concentrated patch of light green in comparison to $GaMe_3$.

The RDG plots (Figure 5.21, bottom) show that both catalysts have very similar repulsion profiles (red region) despite the increased steric bulk for ^{t}Bu. Arguably, the $GaMe_3$ catalyst shows a slightly denser region of red at around 0.0375 a.u (ea_0^{-3}). indicating more steric repulsion. The NCI plots indicate this is coming from the formation of the ring. The major difference between the two catalysts lies within the green region (the attractive interaction and Van der Waals forces are lighter green ($-\lambda_2$) and the repulsive are darker green ($+\lambda_2$)). Ga^tBu_3 has a much deeper and concentrated green region in the attractive (0 to -0.01 a.u. (ea_0^{-3})) in comparison to $GaMe_3$, meaning stronger interaction forces are stabilising **TS3** leading to a lower free energy barrier. The Ga^tBu_3 is showing stronger repulsive interactions in the region 0.00-0.01 a.u. (ea_0^{-3}). This can be attributed to the repulsion between the ligands.

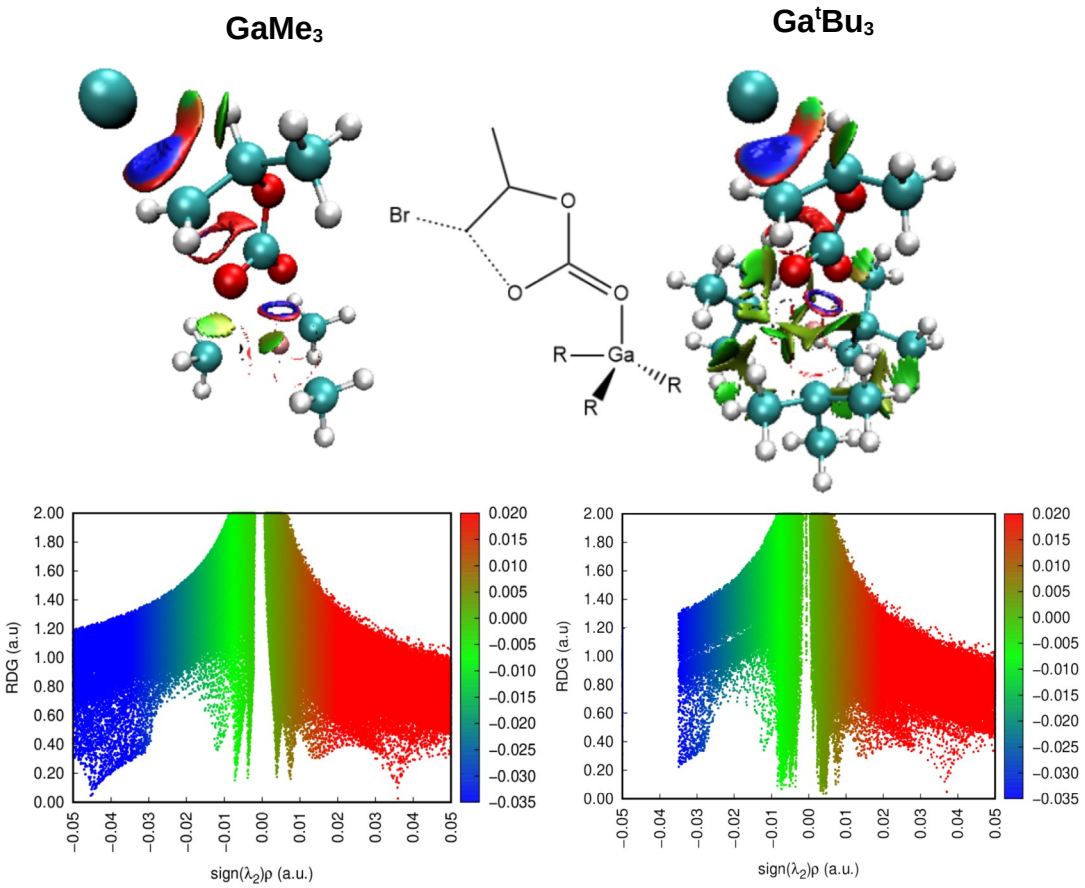

*Figure – Simple Trihalide Group 13 Catalysts for CO2 Utilisation: A DFT / Design Criteria Study.94 – A comparison of the NCI plots (Top) and RDG graphs (Bottom) for **TS3** for both $GaMe_3$ and Ga^tBu_3. The blue colours represent hydrogen bonding, light green (-0.01-0.00 au) represents weak interactions and Van der Waals forces, dark green (0.00-0.01 a.u. (ea_0^{-3})) represents weaker repulsive forces and red represents strong repulsion. RDG values are dimensionless and sign(λ_2)ρ values are reported in atomic units of electron density (ea_0^{-3}), as produced by Multiwfn.*

For completion the NCI plot and RDG graph of **TS3** for $GaPh_3$ is shown in Figure 5.22. The NCI plot shows a lot less green between the ligand and the oxygen than Ga^tBu_3, but displays more than $GaMe_3$, although more dispersed. The RDG, however, closely follows the pattern of Ga^tBu_3, with the large band between -0.01 and 0.00 a.u. (ea_0^{-3}) being present, yet less intense. This would suggest that stabilisation is occurring but weaker. Interestingly, significantly less repulsive forces are present for $GaPh_3$, possibly due to the planar aromatic nature.

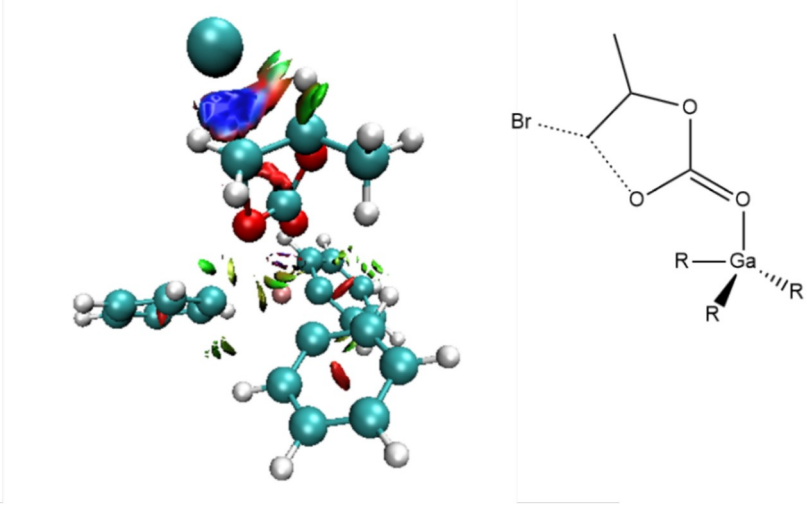

*Figure – Simple Trihalide Group 13 Catalysts for CO2 Utilisation: A DFT / Design Criteria Study.95 - NCI plot (top) and RDG (bottom) for **TS3** with the $GaPh_3$ catalyst. The blue colours represent hydrogen bonding, green represents Van der Waals forces and red represents steric repulsion. RDG values are dimensionless and sign(λ_2)ρ values are reported in atomic units of electron density (ea_0^{-3}), as produced by Multiwfn.*

To quantify this, topology analysis was used to extract bonding critical point (BCP) data for each transition state. Five BCPs have been extracted for each catalyst for the following bonds, Ga-O_1, O_1-C_1, C_1-O_2, O_2-C_2 and C_2-Br (Table 5.5). The electron density values give an indication of the bond strengths. For the Ga-O_1, O_1-C_1 and O_2-C_2 BCPs there are only marginal differences in the observed bond strengths for each catalyst. However, the O_2-C_2 bonds for Ga^tBu_3 and $GaPh_3$ have a higher electron density in comparison to $GaMe_3$ suggesting a stronger interaction between the two atoms. Conversely, the C_2-Br energy density value is larger for $GaMe_3$. These differences agree with the energetics in Figure 5.17 as the ring closure is energetically more favourable for Ga^tBu_3 and $GaPh_3$.

The Laplacian of electron density values give a measure of a bonds covalency, with a negative value meaning a bond is more covalent in character and a positive value more ionic in character. For all five BCPs, the bonding types have been calculated similar in character at almost equivalent Laplacian values; concluding that changing the ligand does not affect the bonding types within the alkoxide.

To compliment the observed results from the NCI analysis (Figures 5.22-5.23), several BCPs have been extracted between the ligand and O_y (Table 5.6). These BCPs were only present for Ga^tBu_3 and $GaPh_3$ agreeing with the NCI that there are limited stabilisation effects for the $GaMe_3$ catalyst. Five BCPs were extracted

for Ga^tBu_3 in comparison to four for $GaPh_3$ as there is more interaction between the ligand and O_y. The electron densities of the BCPs of Ga^tBu_3 are all higher than the comparative ones of $GaPh_3$, further showing the increased stabilisation as ^{t}Bu is an electron donating ligand. In conclusion, both NCI and topology analysis conclude that a sterically bulkier ligand is preferred over a smaller ligand for this set of catalysts.

Ga^tBu_3 and $GaMe_3$ and $GaPh_3$ (electron withdrawing) provide a comparison of different electronic properties. The calculated free energies of the $GaMe_3$ and Ga^tBu_3 pathways are within 1 kcal mol^{-1} of each other except for **Int1** and **TS3** (Figure 5.17). The observed difference in **TS3** free energy has already been accounted for with respect to the stabilisation effects of the larger ligand.

*Table – Simple Trihalide Group 13 Catalysts for CO2 Utilisation: A DFT / Design Criteria Study.17 - The electron density and Laplacian of electron density values for selected bonding critical points to quantify the non-covalent interactions of **TS3** for $GaMe_3$, Ga^tBu_3 and $GaPh_3$. The different types of critical points are bonding critical points (BCP), ring critical points (RCP) and cage critical points (CCP).*

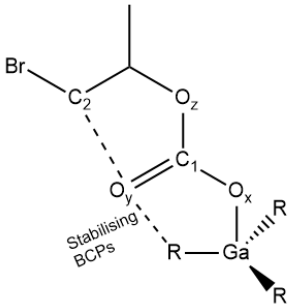

Catalyst	Bond	Type of critical point	Electron Density	Laplacian of Electron Density
Ga^tBu_3	^{t}Bu-O_y	BCP	0.00745	0.0278
	^{t}Bu-O_y	BCP	0.00489	0.0195
	^{t}Bu-Ox-O_y	RCP	0.00459	0.0187
	Ga-O_x	BCP	0.0630	0.269
	O_1-C_x	BCP	0.387	-0.634
	C_1-O_y	BCP	0.376	-0.750
	O_y-C_2	BCP	0.0799	0.112
	C_2-Br	BCP	0.0409	0.0615
$GaMe_3$	Ga-O_x	BCP	0.617	0.260
	O_x-C_1	BCP	0.388	-0.659
	C_1-O_y	BCP	0.378	-0.737

	O_y-C_2	BCP	0.719	0.118
	C_y-Br	BCP	0.0453	0.0615
$GaPh_3$	Ph-O_y	BCP	0.00697	0.0263
	Ph-Ga-O_y	RCP	0.00385	0.0166
	Ph-O_x	BCP	0.00181	0.00549
	Ph-O_x-C1	RCP	0.00137	0.00479
	Ga-O_x	BCP	0.0689	0.299
	O_x-C_1	BCP	0.384	-0.693
	C_1-O_y	BCP	0.377	-0.740
	O_y-C_2	BCP	0.0819	0.110
	C_2-Br	BCP	0.0396	0.0613

The average Ga-L (L = Me, ^{t}Bu or Ph) bond strength for $GaMe_3$ and Ga^tBu_3 for **Int1** is the lowest for both intermediates across the pathway (Table 5.7). The $GaMe_3$ catalyst has a consistent electron density of around 1 x 10^{-1} a.u. (ea_0^{-3}) for intermediates **IC**-**Int2** apart from **Int1,** which sees a weaker interaction. The Ga^tBu_3 catalyst ligand-Ga bond strength varies much more between the same intermediates, but **Int1** has the weakest average bond. The weakening of the Ga-L bonds happens, because of the increased strength of the Ga-O_z bond. As both ligands are electron donating, the bond needs to weaken to allow for a stronger Ga-O_z bond once the O_z-C_2 bond has been broken (Table 5.7). The only correlating factor between calculated **Int1** free energies and the electron density values of Table 5.6 is the inverse relationship between Ga-L bond strength and the free energy of the intermediate. The stronger the bond, the lower the calculated free energy.

Between Ga^tBu_3 and $GaPh_3$, there is a 1.7 kcal mol^{-1} energy span difference in favour of $GaPh_3$. Across the pathway, all intermediates and transition states are lower in energy for $GaPh_3$, more so in the earlier parts of the mechanism. Up to **Int2**, $GaPh_3$ allows for lower energy intermediates and transition states. Due to electron density being pulled away from the metal centre, a stronger Ga-O_z bond can be formed (Table 5.7). Therefore, for **TS1** this allows for a lower energy ring opening step as there is a stronger Ga-O_z bond, thereby weakening the O-C bond making it more prone to nucleophilic attach from the bromide. With less electron density around the metal centre, the CO_2 is also more readily activated. This leads to a significantly lower **TS2** free energy compared to Ga^tBu_3.

Despite Me and ^{t}Bu ligands being preferrable for a lower free energy ring closure (**TS3**), $GaPh_3$ still has a lower free energy. $GaPh_3$ has already shown to have less repulsive forces within **TS3** in comparison to $Ga^{t}Bu_3$. Energy density data from Table 5.6 also show similarities between the $GaPh_3$ and $Ga^{t}Bu_3$ bonds, with the most significant difference when $GaPh_3$ is showing a stronger Ga-O_x bond. This suggests that the **TS3** barrier is not greatly affected by changes from weakly electron donating to weakly electron withdrawing ligands and in the case of this reaction is strongly dictated by the steric properties of the catalyst.

*Table – Simple Trihalide Group 13 Catalysts for CO2 Utilisation: A DFT / Design Criteria Study.18 - Electron density values derived from QTAIM from **IC**-**Int2** for $GaMe_3$, Ga^tBu_3 and $GaPh_3$. Where a bond is not present in the complex a "-" has been included.*

IC	TS1	Int1	TS2	Int2
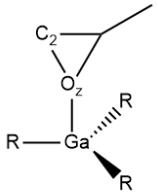	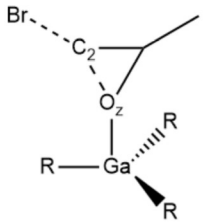	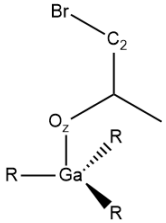	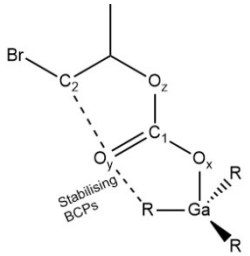	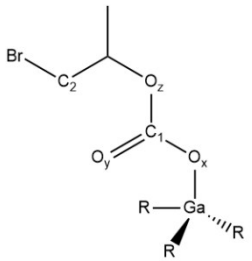

	IC			TS1			Int1		
	$GaMe_3$	**Ga^tBu_3**	**$GaPh_3$**	**$GaMe_3$**	**$GatBu_3$**	**$GaPh_3$**	**$GaMe_3$**	**Ga^tBu_3**	**$GaPh_3$**
Avr. Ga-R	0.105	0.0990	0.109	0.101	0.0953	0.106	0.0971	0.0910	0.101
Ga-O_z	0.0379	0.0362	0.0453	0.0657	0.0643	0.0719	0.0855	0.0862	0.0963
O_z-C_2	0.239	0.241	0.236	-	-	-	-	-	-
C_2-Br	-	-	-	0.0268	0.0262	0.0223	0.119	0.123	0.126

	TS2			Int2		
	$GaMe_3$	**Ga^tBu_3**	**$GaPh_3$**	**$GaMe_3$**	**$GatBu_3$**	**$GaPh_3$**
Avr. Lig-Ga	0.101	0.0935	0.102	0.100	0.0947	0.104
Ga-O_x	0.0252	0.0220	0.0301	0.0700	0.0723	0.0779
Ga-O_z	0.0305	0.0282	0.0451	-	-	-
O_x-C_1	0.401	0.403	0.400	0.373	0.370	0.362
C_1-O_y	0.409	0.410	0.419	0.409	0.409	0.414
C_1-O_z	0.216	0.216	0.204	0.265	0.271	0.274
C_2-Br	0.131	0.131	0.133	0.129	0.131	0.134

One further difference between the Ga-R and Ga-X catalysts is the alkyls have a lower potential for the formation of catalyst wells throughout the reaction. Due to the nature of the Ga-R ligands bound to these catalysts, bridged dimers (Figure 5.12) would be unable to be formed between a second catalyst and the ligand, reducing the formation of off-cycle intermediates.

Secondly, the salt that forms prior to the reaction is much less stable for these three catalysts in comparison to the trihalides (Table 5.8). The calculated energies therefore suggest that by increasing the catalyst loading, the formation of **IC** would be more favourable due to Le Châtlier's principle.

*Table – Simple Trihalide Group 13 Catalysts for CO2 Utilisation: A DFT / Design Criteria Study.19 - The relative stability of the [TBA$^+$][MX$_4^-$] and [TBA$^+$][MR$_3$X$^-$] salts in respect to **IC** and the reactants respectively.*

Catalyst	Salt Stability (kcal mol^{-1})
$AlCl_3$	-7.1
$AlBr_3$	-7.7
AlI_3	-6.3
$GaCl_3$	-13.2
$GaBr_3$	-12.7
GaI_3	-10.8
$GaMe_3$	+0.7
Ga^tBu_3	-2.3
$GaPh_3$	-5.6
$InCl_3$	-16.5
$InBr_3$	-15.6
InI_3	-14.3

A thorough understanding of the mechanisms of the three additional catalysts, $GaMe_3$, Ga^tBu_3 and $GaPh_3$ have been presented. The effects steric and electronic properties have been explored using QTAIM and NCI analysis. To expand beyond the DFT and QTAIM data that has been obtained, Quantitative Structure-Activity Relationship (QSAR) models have been employed to quantitatively analyse the predictive power of different descriptors on the energy span of the reaction based on the catalyst structure.

5.2.4 Quantitative Structure-Activity Relationship (QSAR)

Multivariable QSAR models were constructed using multiple calculated descriptors to predict the energy span (Figure 5.23). In total, 21 different features such as HOMO and LUMO gap, gepol volume and the Mulliken charge on the metal centre were obtained from DFT calculations and post-wavefunction analysis. Due to the number of features outweighing the number of targets, a

recursive feature elimination (RFE) process was employed as a feature engineering method. RFE ranks the features by importance based on the correlation coefficient for a linear regression model (Figure 5.23). The least important feature is removed iteratively until the desired amount is achieved. RFE attempts to reduce collinearity so each iteration would produce a different importance graph because of a loss of correlation with the last removed feature.

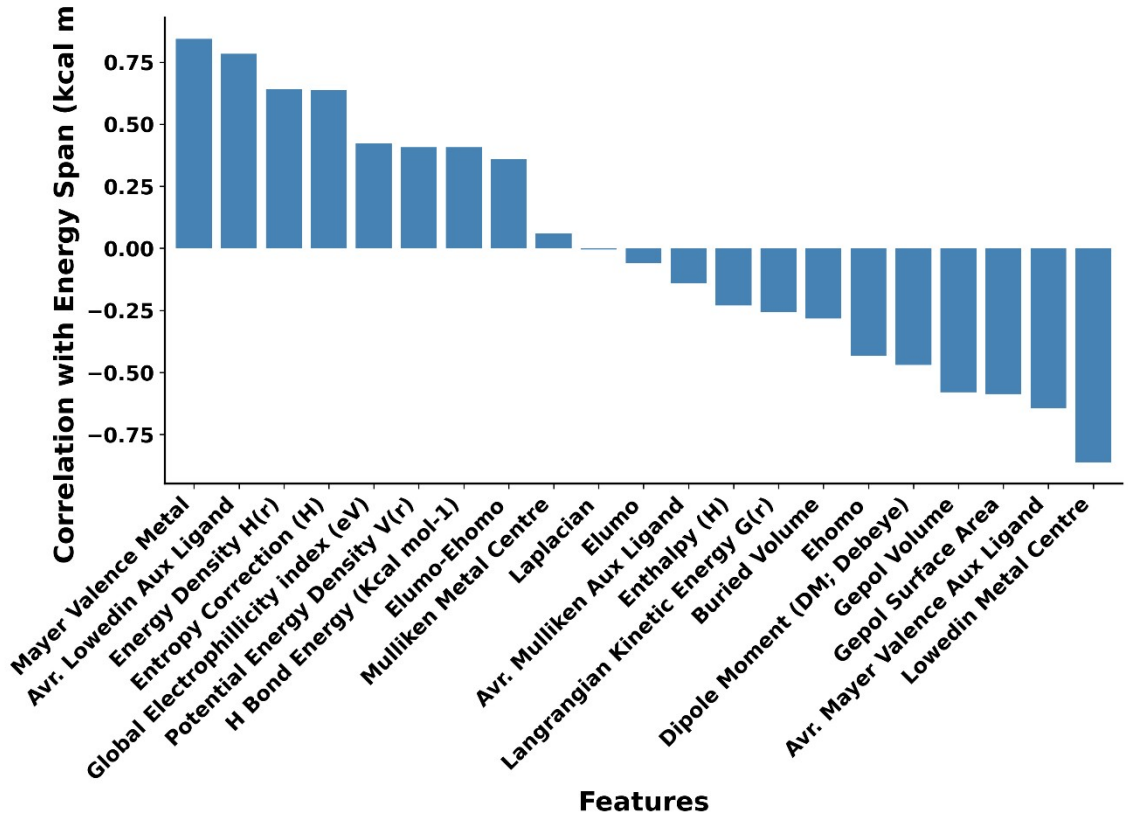

Figure – Simple Trihalide Group 13 Catalysts for CO2 Utilisation: A DFT / Design Criteria Study.96 - Feature importance based on the correlation coefficient with the linear regression model utilising RFE. This importance set is for all of the features collectively. As the number of features reduces, some features may become more/less important due to a change in correlation with other features.

To try and find an optimum number of features, RFE was utilised to give a combination of 2-5 different features. The model settings were coded to try and find the optimal number of features for the best model. Table 5.9 displays the features chosen by RFE and the statistical results obtained from those features.

Using RFE, four different linear regression models were tested. When the features selected were set to two (Model A) and three (Model B), a poor prediction was made by the model with only a R^2 = 0.4 and a poor adjusted R^2. The errors presented in these two models were also excessive. When four features are selected (Model C), the average Lowedin charge of the auxiliary ligands was added into the model. A significant increase in the R^2 value is seen showing an

R^2 = 0.760 and adjusted R^2 = 0.622. Following this, the Lowedin charge of the metal centre is added as the 5th feature with an R^2 of 0.950 and adjusted R^2 of 0.908. Model 5 produced the best model with a good selection of features and was plotted into a graph of predicted versus actual energy span (Figure 5.24).

Table – Simple Trihalide Group 13 Catalysts for CO2 Utilisation: A DFT / Design Criteria Study.20 - Statistical results of four different linear regression models using RFE as the feature selection method.

Model Label	Features Selected	R^2	Adjusted R^2	Mean Squared Error ((kcal mol^{-1})^2)	Root Mean Squared Error (kcal mol^{-1})
A	• Entropy Correction • GEI	0.414	0.284	7.28	2.70
B	• Entropy Correction • GEI • Dipole Moment	0.414	0.194	7.28	2.70
C	• Entropy Correction • GEI • Dipole Moment • Avr. Lowedin Aux Ligand	0.760	0.622	2.98	1.73
D	• Entropy Correction • GEI • Dipole Moment • Avr. Lowedin Aux Ligand • Lowedin Metal Centre	0.950	0.908	0.62	0.79

Across Models A–D, entropy correction and GEI are consistently retained as selected descriptors, with the model predicting both thermodynamic contributions and the GEI play a role in determining the energy span. As the number of features added to the model increases, additional charge-related descriptors such as dipole moment and Löwedin charges (auxiliary ligand and metal centre) are incorporated, meaning they also contribute towards the total energy span. The consistent presence of entropy correction and GEI implies that catalytic performance within this series is governed primarily by the Lewis acidity measured with the HOMO and LUMO energies and entropic modulation.

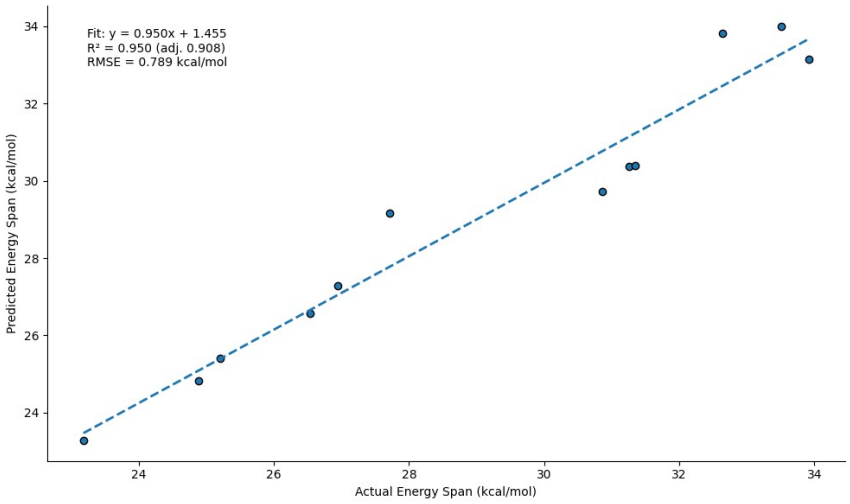

Figure – Simple Trihalide Group 13 Catalysts for CO2 Utilisation: A DFT / Design Criteria Study.97 - A graphical representation of the prediction of the energy span using model D for QSAR analysis of the GaX and Ga-R catalysts.

5.3 Conclusion

In conclusion, the mechanism for all 12 catalysts was successfully elucidated. Calculated energies and elucidated reaction mechanisms were in good agreement with the results from the Mehrkhodavandi group. $InBr_3$ was calculated to have the lowest energy span out of the nine trihalide catalysts in agreement with this catalyst producing the highest yield. Furthermore, the rate determining transition state was identified in agreement with the kinetic experiments. Despite the calculated presence of dimers, the NMR kinetic experiments showed they took no active part in the experiments as a 9:1 ratio of κ^1 to κ^2 CO_2 binding was observed at **Int2**. The **Int2 dimer** had a κ^2 binding mode, which would have been present if it was active in the mechanism. A calculated Boltzmann distribution of the different binding modes showed a 7.5:1 ratio of κ^1 to κ^2 binding in good agreement with experimental results.

The steric and electronic effects of the catalysts were explored using $GaMe_3$, Ga^tBu_3 and $GaPh_3$. The steric properties of the catalyst showed that a larger ligand helped stabilise the TDTS (**TS3**) leading to a lower energetic span. The $GaPh_3$ was predicted to be the most active catalyst. The energetics across the pathway were lower for $GaPh_3$, including **TS3,** which prefers electron donating groups.

To quantify and highlight which calculated descriptors best described the energy span, QSAR models were employed. The features, entropy correction, GEI,

dipole moment, average Lowedin charge on the auxiliary ligand, Lowedin charge on the metal centre, provided the best model (model D).

After evaluating the obtained results in this study, the following criteria would be recommended for the design of small tri-ligated catalysts:

- *Weak electron donating ligands:* As the $GaPh_3$ had the lowest calculated energy span, it was predicted as the most active. Weakly electron donating groups also appear to provide a more active catalyst in comparison to the stronger electron withdrawing halides.
- *Larger ligands:* The larger Ph and ^{t}Bu ligands have calculated energy spans lower than all the halides and the Me ligand due to the stabilisation of **TS3**.
- *Non-dimeric ligands:* Ligands that have the potential to lead to dimerization products should be avoided. The Lewis acidic nature of these catalysts means that they can easily dimerise and risk off-cycle intermediates being formed.
- *Lewis Acidity:* While there is no clear indication of how Lewis acidic a catalyst should perform well, the higher Lewis acidic catalysts in this study appeared to perform worse. The GEI suggests an optimum range for Lewis acidity. However, more experimental evidence would be needed to conclude on this point.

5.4 Computational Methodology

5.4.1 DFT and Post-Wavefunction Analysis

Computational calculations were undertaken using Orca 4.2.1.[25,26] Optimisation and frequency calculations were performed at the RI-B97-D3/def2-tzvpp/j level of theory.[27–33] Final single point energies and solvent corrections were calculated at the RIJCOSX-ωB97-D3BJ/def2-tzvpp/j level of theory.[30–32,34,35] Solvation corrections were implemented with a dielectric constant of 16 for the epoxide using the CPCM model.[35] Analytical frequencies were calculated for inclusion of the Zero Point Energy (ZPE) correction and entropic contributions to the free energy term (ΔG 298.15 K) as well as confirming all intermediate were true with no imaginary modes and all transition states had the correct critical frequency of decomposition. All thermodynamic parameters were calculated in the standard

state (298.15 K and 1 atm). A larger numerical integration grid4 was used for the SCF steps of the calculation with grid5 being applied to the final energy evaluation step. Concentration correction, to account for the low catalyst loading was applied as a free energy correction based on the Van't Hoff reaction quotient equation RT ln(Q) where Q accounts for the 20-fold concentration gradient between the epoxide and the MX_3 catalyst.[36,37] Avogadro 1.2.0 was utilised to perform all structural analysis and graphical visualisations.[38] Post-wavefunction analysis methods (QTAIM and NCI) were performed using the Multiwfn package.[39]

GEI values were calculated using HOMO and LUMO energy values from the output files of the Optimisation/Frequency calculuations.[40] FIA calculations were performed at the recommended RIJSCOSX-PW6B95/def2-qzvpp level of theory using the TMS-anchored isodesmic reaction scheme method (Figure 2.3).[22,25,29,30,41,42]

5.4.2 QSAR Methodology

Python was employed to create a linear regression model.[43–45] The dataset was standardised to ensure features have a mean of zero and standard deviation of 1 using "standardscaler" from the scikit-learn library.[46] Feature engineering utilised the python libraries Matplotlib and Seaborn to plot the importance of each feature based on the correlation coefficients of each feature with the energy span.[47,48] The feature importance graph was used to manually select features using chemical intuition. Furthermore, RFE methods were employed from the scikit-learn library.[46] Residual diagnostics were performed to validate the model and measure the fit of the model by the linearity and normality of the residuals.[49]

5.5 References

1 C. J. Whiteoak, N. Kielland, V. Laserna, E. C. Escudero-Adán, E. Martin and A. W. Kleij, *J. Am. Chem. Soc.*, 2013, **135**, 1228–1231.

2 X. Wu and M. North, *ChemSusChem*, 2017, **10**, 74–78.

3 S. Dagorne and R. Wehmschulte, *ChemCatChem*, 2018, **10**, 2509–2520.

4 Y. Qin, H. Guo, X. Sheng, X. Wang and F. Wang, *Green Chem.*, 2015, **17**, 2853–2858.

5 R. Vilar, M. Bartlett, J. Burke, P. Sherin, M. K. Kuimova and M. Barahona, *Chem. - Eur. J.*, 2024, **30**, e202402465.

6 A. B. Kremer, R. J. Andrews, M. J. Milner, X. R. Zhang, T. Ebrahimi, B. O. Patrick, P. L. Diaconescu and P. Mehrkhodavandi, *Inorg. Chem.*, 2017, **56**, 1375–1385.

7 N. Heppe, C. Gallenkamp, S. Paul, N. Segura-Salas, N. von Rhein, B. Kaiser, W. Jaegermann, A. Jafari, I. Sergueev, V. Krewald and U. I. Kramm, *Chem. - Eur. J.*, 2023, **29**, e202202465.

8 S. Kumar, A. Saini and J. S. Sandhu, *Arkivoc*, 2007, **14**, 27–33.

9 R. R. Singh, T. P. Singh, N. P. Singh, S. S. Naorem and O. M. Singh, *J. Fluoresc.* 2021, **31**, 247–257.

10 J. Nan, G. Huang, S. Liu, J. Wang, Y. Ma and X. Luan, *Chem. Sci.*, 2023, 5160–5166.

11 T. Bok, K. N. Eun and Y. L. Bun, *Bull. Korean Chem. Soc.*, 2006, **27**, 1171–1174.

12 I. Shibata, I. Mitani, A. Imakuni and A. Baba, *Tetrahedron Lett.*, 2011, **52**, 721–723.

13 Y. J. Kim and R. S. Varma, *J. Org. Chem.*, 2005, **70**, 7882–7891.

14 H. A. Baalbaki, H. Roshandel, J. E. Hein and P. Mehrkhodavandi, *Catal. Sci. Technol.*, 2021, **11**, 2119–2129.

15 L. Álvarez-Miguel, J. D. Burgoa, M. E. G. Mosquera, A. Hamilton and C. J. Whiteoak, *ChemCatChem*, 2021, **13**, 4099–4110.

16 M. D. G. Billacura, R. D. Lewis, N. Bricklebank, A. Hamilton and C. J. Whiteoak, *Adv. Synth. Catal.*, 2023, **365**, 3129–3137.

17 D. J. Cabrera, R. D. Lewis, C. Díez-Poza, L. Álvarez-Miguel, M. E. G. G. Mosquera, A. Hamilton and C. J. Whiteoak, *Dalton Trans.*, 2023, **52**, 5882–5894.

18 A. B. Kremer, R. J. Andrews, M. J. Milner, X. R. Zhang, T. Ebrahimi, B. O. Patrick, P. L. Diaconescu and P. Mehrkhodavandi, *Inorg. Chem.*, 2017, **56**, 1375–1385.

19 S. Sarkar, S. Singha Roy and D. Chakraborty, *J. Polym. Res.*, 2024, **31**, 1–8.

20 C. Goonesinghe, H. Jung, I. O. Betinol, J. R. Gaffen, C. N. Garrard, J. Chang, K. Hosseini, H. Roshandel, K. Nyamayaro, B. Patrick, M. Ezhova, C. B. Caputo, T. Baumgartner, J. P. Reid and P. Mehrkhodavandi, *ACS Catal.*, 2023, **13**, 16148–16157.

21 S. Kozuch and S. Shaik, *Acc. Chem. Res.*, 2011, **44**, 101–110.

22 P. Erdmann, J. Leitner, J. Schwarz and L. Greb, *ChemPhysChem*, 2020, **21**, 987–994.

23 A. R. Jupp, T. C. Johnstone and D. W. Stephan, *Dalton Trans.*, 2018, **47**, 7029–7035.

24 T. Wu, T. Wang, L. Sun, K. Deng, W. Deng and R. Lu, *ChemistrySelect*, 2017, **2**, 4533–4537.

25 F. Neese, *Wiley Interdiscip. Rev. Comput. Mol. Sci.*, 2018, **8**, 4–9.

26 F. Neese, *Wiley Interdiscip. Rev. Comput. Mol. Sci.*, 2012, **2**, 73–78.

27 S. Grimme, S. Ehrlich and L. Goerick, *J. Comput. Chem.*, 2011, **32**, 1456–1465.

28 F. Neese, *J. Comput. Chem.*, 2003, **24**, 1740–1747.

29 S. Grimme, *J. Comput. Chem.*, 2006, **27**, 1787–1799.

30 A. Schäfer, H. Horn and R. Ahlrichs, *J. Chem. Phys.*, 1992, **97**, 2571–2577.

31 F. Weigend and R. Ahlrichs, *Phys. Chem. Chem. Phys.*, 2005, **7**, 3297–3305.

32 F. Weigend, *Phys. Chem. Chem. Phys.*, 2006, **8**, 1057–1065.

33 A. D. Becke, *J. Chem. Phys.*, 1997, **8560**, 8554–8560.

34 F. Neese, F. Wennmohs, A. Hansen and U. Becker, *Chem. Phys.*, 2009, **356**, 98–109.

35 S. Sinnecker, A. Rajendran, A. Klamt, M. Diedenhofen and F. Neese, *J. Phys. Chem. A*, 2006, **110**, 2235–2245.

36 J. N. Harvey, F. Himo, F. Maseras and L. Perrin, *ACS Catal.*, 2019, **9**, 6803–6813.

37 H. Ryu, J. Park, H. K. Kim, J. Y. Park, S. T. Kim and M. H. Baik, *Organometallics*, 2018, **37**, 3228–3239.

38 M. Hanwell, D. Curtis, D. Lonie, T. Vandermeersch, E. Zurek and G. Hutchison, *J. Cheminform.*, 2012, **4**, 17.

39 T. Lu and F. Chen, *J. Comput. Chem.*, 2012, **33**, 580–592.

40 A. R. Jupp, T. C. Johnstone and D. W. Stephan, *Dalton Transactions*, 2018, **47**, 7029–7035.

41 R. J. Meier, *Faraday Discuss.*, 2003, **124**, 405–412.

42 Y. Zhao and D. G. Truhlar, *J. Phys. Chem. A*, 2005, **109**, 5656–5667.

43 G. A. F. Seber and A. J. Lee, *Linear Regression Analysis*, John Wiley & Sons, Inc., 2003.

44 N. R. Draper and H. Smith, *Applied Regression Analysis*, John Wiley & Sons, Inc., 1998.

45 Google, Google Colab, https://colab.research.google.com/, (accessed 22 July 2024).

46 F. Pedregosa, G. Varoquaux, A. Gramfort, V. Michel, B. Thirion, O. Grisel, M. Blondel, P. Prettenhofer, R. Weiss, V. Dubourg, J. Vanderplas, A. Passos, D. Cournapeau, M. Brucher, M. Perrot and E. Duchesnay, *J. Mach. Learn. Res.*, 2011, **12**, 2825–2830.

47 J. D. Hunter, *Comput. Sci. Eng.*, 2007, **9**, 90–95.

48 M. Waskom, O. Botvinnik, D. O'Kane, P. Hobson, S. Lukauskas, D. C. Gemperline, T. Augspurger, Y. Halchenko, J. B. Cole, J. Warmenhoven, J. De Ruiter, C. Pye, S. Hoyer, J. Vanderplas, S. Villalba, G. Kunter, E. Quintero, P. Bachant, M. Martin, K. Meyer, A. Miles, Y. Ram, T. Yarkoni, M. L. Williams, C.

Evans, C. Fitzgerald, Brian, C. Fonnesbeck, A. Lee and A. Qalieh, *Zenodo*, 2017, preprint.

49 C. F. Dormann, J. Elith, S. Bacher, C. Buchmann, G. Carl, G. Carré, J. R. G. Marquéz, B. Gruber, B. Lafourcade, P. J. Leitão, T. Münkemüller, C. Mcclean, P. E. Osborne, B. Reineking, B. Schröder, A. K. Skidmore, D. Zurell and S. Lautenbach, *Ecography*, 2013, **36**, 27–46.

Chapter 6 – Conclusions and Future Directions

6.1 Conclusions

The utilisation of CO_2 as a sustainable C1 feedstock remains a significant challenge due to its inherent thermodynamic stability and kinetic inertness, requiring the development of efficient catalytic systems to enable its transformation into value-added products. Group 13 Lewis acidic catalysts have shown promise in this area; however, their activity and underlying structure–reactivity relationships are not fully understood, particularly for the less commonly explored heavier group 13 elements. This work therefore aimed to provide a detailed mechanistic and electronic understanding of Al, Ga and In catalysts in CO_2 cycloaddition reactions, to rationalise their behaviour and inform future catalyst design.

From this work has provided a greater understanding of the utilisation of Al, Ga and In homogeneous Lewis acidic catalysts for the cyclisation of CO_2 and epoxides to form cyclic carbonates using DFT. For the reactions explored in this study, heavier group 13 catalysts have shown to catalyse the cycloaddition more effectively in comparison to Al. The mechanistic work presented herein provided insight into the reasons for the increased activity. This increased activity arises from a combination of factors, including a more favourable coordination environment at the metal centre (as reflected in the τ_5 values in **Chapter 3**), a balanced Lewis acidity that enables activation of CO_2 without over-stabilisation of intermediates, and a reduced tendency to form off-cycle or aggregated species that inhibit catalytic turnover.

These findings provide inspiration to other groups to go beyond Al when considering a group 13 Lewis acidic catalyst and utilise underexplored Ga and In catalysts. Reaction mechanisms have been elucidated for a series of different group 13 metal catalysts with varying steric and electronic properties. In **chapter 3** and **chapter 5**, calculations determine general reaction mechanism was followed except from a few deviations. When using the salphen ligand, a novel halide abstraction step was seen in the M[(salphen)X] mechanism for a stronger activation of CO_2 and allowing for a reaction to proceed. This mechanistic insight

provides a foundation for the rational design of next-generation catalysts and may be applied to address limitations in CO_2 activation across related catalytic systems.

In **chapter 3**, the experimental work alongside the Whiteoak group showed the higher activity of Ga[(salphen)X] and In[(salphen)X] in comparison to the poor activity of the Al[(salphen)X] went against the traditional thinking that a more Lewis acidic catalyst would better activate CO_2 and facilitate the reaction more effectively. QTAIM revealed that the harder, more Lewis acidic Al bonded to the ligand with more ionic character in comparison to Ga and In. The more ionic nature meant that the $Al[(salphen)X_2]^-$ complex formed by chloride ligand abstraction could be more susceptible to forming long chain ionic complexes in comparison to the heavier Ga and In analogues.[1]

Future work could focus on the application of quantum or semi-empirical molecular dynamics to investigate the aggregation behaviour of the Al system and the formation of the insoluble product. Such approaches would allow for the exploration of intermolecular interactions and the proposed formation of an ionic chain, which is not readily captured by static DFT calculations. Understanding these aggregation processes could provide broader insight into catalyst deactivation pathways in homogeneous catalysis, particularly in systems where highly polar or ionic intermediates are formed and inform on catalyst design to mitigate solubility limitations in related catalytic systems.

This thesis uses FIA and GEI calculations to highlight and rationalise that a stronger Lewis acid catalyst does not produce a more active catalyst for the cycloaddition of CO_2 and epoxide contrary to considered opinions.[2] Calculated values from Figures 3.16 and 5.14-5.15 show that Lewis acidic for the M[(salphen)X] catalysts of **chapter 3** and the MX_3 catalysts of **chapter 5** do not follow this trend. For the M[(salphen)X] catalysts, the more Lewis acidic Al[(salphen)X] was predicted to exhibit comparable activity to In[(salphen)X]; however, this was not realised experimentally due to the formation of off-cycle intermediates. The lower Lewis acidic Ga[(salphen)X] catalysts performed the worst due to greater free energy spans arising from less effective activation of CO_2. In **chapter 5**, the calculated intermediates for the more Lewis acidic AlX_3 catalysts were calculated thermodynamically more stable than the Ga and In counterparts. This increased stability requires higher free energy spans for the

reaction to proceed and would consequently result in lower catalytic activity. The most active catalyst, $InBr_3$, had a calculated Lewis acidity in the middle of the range of the nine MX_3 catalysts.

The key result from these findings is that the Lewis acidity is not linearly related to the catalysts activity. Assumptions such as this can prevent further exploration of chemical space, such as using metals of higher cost, such as Ga and In in comparison to Al. Future work could extend the FIA and GEI dataset across a wider range of group 13 catalysts to further explore the relationship between Lewis acidity and catalytic activity. Expanding this dataset would allow for a more systematic investigation into whether an optimum range of Lewis acidity exists for this transformation, rather than a simple linear relationship.[3] Such an approach could help identify a balance between sufficient activation of CO_2 and avoidance of overly stabilised intermediates or off-cycle species, providing a more general framework for catalyst design in related cycloaddition reactions.

The complexity of the relationship of a catalysts activity also goes far beyond a single descriptor. In **chapter 5**, a range of steric and electronic properties were selected and QSAR was used to predict which descriptors had the greatest influence on the activity of the catalyst. Despite only using a small sample of 12 data points, the model predicted that an MX_3 catalyst, ligated with a larger, weak electron withdrawing ligand, would produce the most active catalyst. To achieve a more in-depth understanding of these relationships, a further study would need to be undertaken as discussed in section 6.2.

Reaffirming the importance of expanding chemical space, **chapter 4** explored the cyclisation of 1,2-diphenylaziridine and 1-isopropyl-2-pehnylaziridine with CO_2 to form oxazolidinones using a Ga-aminotrisphenolate catalyst.[4,5] It was found that the 1,2-diphenylaziridine could selectively form an oxazolidinone or piperazine depending on the temperature of the reaction, as a result of the entropic differences at the point of divergence between the different mechanisms. This understanding could inform future design of catalysts and reactions in attempt to replicate reactivity and gain access to areas of chemical space which would otherwise be more difficult (i.e. require harsher conditions or reagents).

Building on these findings, further computational work could be undertaken to expand the mechanistic understanding of this system. Calculation of the full free

energy profiles for the aluminium and indium aminotrisphenolate catalysts would allow for direct comparison across the group 13 series and clarify how metal identity influences selectivity. In addition, full elucidation of the mechanism leading to piperazine formation from 1-isopropyl-2-pehnylaziridine would help determine whether factors beyond entropy, such as kinetic barriers or intermediate stability, limit its formation under the conditions studied. Together, these studies would provide a more complete picture of the factors governing product selectivity and reactivity within this system.

In conclusion, a thorough computational study has been conducted on Al, Ga and In homogeneous catalysts for the cycloaddition of 3-membered heterocycles and CO_2. Calculations have been utilised to provide theoretical explanations to experimental results. This increased understanding could encourage other groups to explore chemical space beyond the traditional.

6.2 Machine Learning for Group 13 Catalysts

The results of this work highlight the complexity of catalyst performance, where multiple electronic and steric factors contribute to activity and no single descriptor is sufficient to predict behaviour. In recent years, machine learning (ML) approaches have emerged as a powerful tool for addressing this challenge by enabling the analysis of large, multidimensional datasets and identifying non-linear relationships between catalyst properties and reactivity. Unlike traditional descriptor-based approaches, ML methods allow for the simultaneous consideration of multiple interacting variables, making them particularly well suited to systems such as those studied here, where optimal performance arises from a balance of competing effects rather than a single dominant parameter.

To further expand the scope of this study, machine learning methodologies could be employed to explore the relationships between catalyst descriptors and catalytic activity, as demonstrated in recent AI-driven approaches to homogeneous catalysis.[6] With sufficiently large datasets, these methods can identify complex, non-linear relationships between electronic and steric descriptors and catalytic performance, enabling the prediction of key properties such as reaction barriers and yields.[6] Recent developments show that machine learning can be used not only to screen catalyst candidates but also to gain mechanistic insight and guide catalyst optimisation through data-driven

approaches.[6] Applying similar methodologies to group 13 systems would allow the contributions of descriptors such as Lewis acidity, charge distribution, and steric environment to be quantified more rigorously. These predictions could then be used to define design criteria for highly active catalysts, enabling the targeted synthesis of new systems and providing a high-throughput and cost-effective route to exploring chemical space beyond that accessible through conventional computational studies.

6.3 Other Future Directions Related to This Work

The findings of this thesis demonstrate that catalytic performance in group 13 systems is governed by a balance of electronic and steric factors, rather than by Lewis acidity alone.[2] This suggests that future catalyst design should focus on targeting an optimal range of Lewis acidity, where sufficient activation of CO_2 is achieved without over-stabilisation of intermediates or the formation of off-cycle species. Based on the FIA and GEI analysis presented in **Chapters 3** and **5**, this optimal region appears to lie between the extremes of group 13 represented by aluminium and indium, indicating that catalysts with intermediate electronic character may provide the most favourable reactivity.

One key direction for future work is the rational design of ligand frameworks that can tune the electronic environment of the metal centre to approach this optimal region. Importantly, this work demonstrates that catalyst design should avoid the extremes observed within the group 13 series; highly Lewis acidic systems such as aluminium promote over-stabilisation of intermediates and the formation of off-cycle species, while less activating systems fail to sufficiently interact with CO_2. This insight extends beyond the specific systems studied here, demonstrating that heavier group 13 catalysts, which are often overlooked due to cost and availability, can offer improved reactivity when compared to traditional aluminium systems. As such, this work provides a framework for re-evaluating catalyst selection in CO_2 utilisation and related transformations, where assumptions based solely on one chemical descriptor may limit exploration of more effective systems. The principles identified here could therefore be applied to other aluminium-based catalytic systems and more broadly across homogeneous catalysis, encouraging the exploration of alternative metals and challenging established design strategies.

Beyond ligand design, the exploration of new catalyst architectures represents an important opportunity for expanding chemical space. Mixed donor ligands, partially flexible ligand systems, or catalysts capable of dynamic coordination behaviour could provide a means of balancing activation and stability throughout the catalytic cycle. Systems that can adapt their coordination environment during the reaction may help avoid the formation of strongly stabilised intermediates that increase the overall energy span.

In addition to catalyst development, the extension of this chemistry to alternative substrates offers significant potential. While this work has focused on epoxides and aziridines, the principles identified here could be applied to other strained heterocycles or CO_2-derived transformations like carbon disulfide or thiiranes. **Chapter 4** also suggests that catalyst design could be used not only to improve activity but also to access new synthesis routes to valuable carbon heterocyclic products under mild conditions. This has important implications for the development of more sustainable and versatile CO_2 utilisation strategies.

Overall, this work highlights that the future of group 13 catalysis for CO_2 utilisation is not determined by creating a catalyst with the highest Lewis acidity, but in achieving a balance of interacting properties that govern the full catalytic cycle. The identification of an optimal region of catalyst behaviour, combined with rational ligand and catalyst design, suggests that there remains significant opportunity for further development, and that the best performing systems have yet to be realised.[3]

From a broader perspective, the future of CO_2 utilisation will likely depend on the development of catalytic systems that are not only active but also scalable, robust and compatible with industrial processes. While group 13 catalysts have demonstrated significant potential in homogeneous systems, particularly using Ga and In as shown in this work, their wider application may be limited by factors such as cost, availability and catalyst recovery. As such, these systems may represent an important step towards understanding the fundamental requirements for effective CO_2 activation, rather than the final solution for large-scale deployment. The mechanistic and electronic insights gained from this work could therefore be transferred to the design of more practical catalytic systems, including heterogeneous or supported catalysts, where similar principles of balanced Lewis acidity and controlled coordination environments can be applied.

A recent example of this transition towards practical application is demonstrated in continuous CO_2 cycloaddition processes using immobilised ionic liquid catalysts within fixed-bed reactors. In these systems, the catalyst is supported on a solid material, allowing continuous operation, improved heat management, and simplified separation compared to homogeneous systems. However, the study highlights that reaction performance is not governed solely by intrinsic catalytic activity but is strongly influenced by mass transfer limitations and catalyst stability under flow conditions.[7] As such, the concept of an optimal balance in catalyst properties extends beyond molecular design and into reactor performance, reinforcing the importance of tuning both electronic structure and physical behaviour when translating homogeneous catalysts into scalable processes.

6.3 References

1 D. J. Cabrera, R. D. Lewis, C. Díez-Poza, L. Álvarez-Miguel, M. E. G. G. Mosquera, A. Hamilton and C. J. Whiteoak, *Dalton Trans.*, 2023, **52**, 5882–5894.

2 R. D. Lewis, M. D. G. Billacura, A. Hamilton and C. J. Whiteoak, in *Organometallic Chemistry: Volume 45*, Royal Society of Chemistry, 2024.

3 T. Yan, H. Liu, Z. X. Zeng and W. G. Pan, *J. CO2 Util.*, 2023, **68**, 102355.

4 M. D. G. Billacura, R. D. Lewis, N. Bricklebank, A. Hamilton and C. J. Whiteoak, *Adv. Synth. Catal.*, 2023, **365**, 3129–3137.

5 L. Álvarez-Miguel, J. D. Burgoa, M. E. G. Mosquera, A. Hamilton and C. J. Whiteoak, *ChemCatChem*, 2021, **13**, 4099–4110.

6 L. Morán-González, A. L. Burnage, A. Nova and D. Balcells, *ACS Catal.*, 2025, **15** 9089–9105.

7 J. Sun, K. Yu, D. Zhou, Q. Xu, J. Yin, X. Li, H. Sun and J. Wu, *Chem. Eng. Sci.*, 2024, **283**, 119415.

Appendices

Ethics Approval

Computational Chemistry Driven Understanding for Group-13 Catalysts in CO_2 Utilisation

Ethics Review ID: ER31417403

Workflow Status: Application Approved

Type of Ethics Review Template: No human participants, human tissue or personal data

Primary Researcher / Principal Investigator

Ryan Lewis
(Health and Wellbeing)

Converis Project Application:

Q1. Is this project ii) Doctoral research

Director of Studies

Thomas
Bassindale
(Health and
Wellbeing)

Supervisory Team

Alex Shenfield
(Communication and Computing Research Centre)

Alex Hamilton (Victoria university of wellington)